The CN Perspective on Dense Gas and Star Formation

Using the Cyanide Radical to Trace Dense Molecular Gas in Nearby Star-Forming Galaxies

By Blake Ledger
Hon. BSc. (University of Calgary, Calgary, AB, Canada)

A Thesis Submitted to the School of Graduate Studies in Partial Fulfilment of the Requirements for the Degree Doctor of Philosophy

McMaster University
Doctor of Philosophy (2024)
Hamilton, Ontario (Physics & Astronomy)

TITLE: Using the Cyanide Radical to Trace Dense Molecular Gas in Nearby Star-Forming Galaxies
AUTHOR: Blake Ledger (McMaster University)
SUPERVISOR: Dr. Christine D. Wilson
NUMBER OF PAGES: xxvi, 191

Abstract

Dense molecular gas is the fuel for star formation in galaxies. Empirical scaling relations show that dense gas mass correlates nearly linearly with star formation rate in normal and star-forming galaxies. To understand the connection between dense gas and star formation, astronomers have previously relied on observations of molecules like hydrogen cyanide (HCN). Recently, it has been shown that the cyanide radical (CN) can be used to study dense gas in a similar way to HCN. In this thesis, I investigate the properties of dense molecular gas using new and archival observations of CN and HCN from the Atacama Large Millimeter/Submillimeter Array (ALMA) for Ultraluminous and Luminous Infrared Galaxies (U/LIRGs).

I begin with a multi-transition line study of CN and HCN to compare the excitation conditions of these two molecules in a sample of three galaxies: IRAS 13120-5453, NGC 3256, and NGC 7469. I find variations between individual lines of each molecule which are connected with regions of enhanced star formation or the presence of an active galactic nuclei. I then focus on using CN as a tracer of dense gas and dense gas fraction when compared with carbon monoxide (CO). I measure the CN/CO intensity ratio in a sample of 16 galaxies and find that CN/CO is higher, on average, in ULIRGs compared to LIRGs. LIRGs have a larger spread in CN/CO ratios compared to ULIRGs, which I attribute to their variation in star formation, AGN, and morphological properties. Finally, I use the CN/CO ratio to estimate the dense gas fraction and find that it correlates with star formation rate and hard X-ray luminosity at the location of peak X-ray emission. The results of this thesis imply that CN can be used as a tool to study the physical and chemical properties of dense gas in extreme star-forming galaxies.

To Victoria,
My universe is better with you in it.

You just never know - FJB

Acknowledgements

These last five years at McMaster have been incredible and I have many folks to highlight and thank for helping me to get to the end of this journey. I would like to start with my supervisor, Dr. Christine Wilson. Thank you for your guidance and direction. It has been a privilege to be a part of your research team and to learn from you. I am a better scientist because of you and the opportunities that you provided for me. To the past and present members of the Wilson group: Toby, Jiayi, Woorak, Ashley, Nathan, Ryan, Hao, Celine, Jennifer, Osvald, Taavishi, Babara, and Emily - thank you for making the office a fun place to be, creating interesting and fulfilling group meetings, and for sharing your science with me. Thank you to Dr. Eva Schinnerer for being my external examiner and your insights, feedback, and questions during my thesis defense. Thank you to Dr. Doug Welch for chairing my thesis defense.

Thank you to those who have mentored me along the way. To my supervisory committee, Dr. Laura Parker and Dr. Ralph Pudritz - it has been an honour to share my results with you and to have you help shape the path I took to get here at the end of my PhD. Thank you for asking important and challenging questions that helped to focus my projects and to remember the big picture. Thank you to Dr. Toshiki Saito and Dr. Daisuke Iono for hosting me at NAOJ and growing my international network. The summer I spent with you in Japan led to so much opportunity and career growth and I am forever grateful. From the University of Calgary, thank you to Dr. René Plume for introducing me to the world of research in astrophysics - you are the reason I started grad school. Thank you to Dr. Jason Donev for your incredible enthusiasm, contagious passion for teaching and learning, and inspiring me to become an educator.

Thank you to Dr. Rob Cockcroft. I don't really have the words to describe the gratitude I have for you and your place in my life these last few years. You have taught me so much about how to treat people and what it means to be an ally, an advocate, a leader, a mentor, and a friend. I will always remember the partnership we had teaching astronomy and running the planetarium together. I aspire to one day have students that look up to me the same way that I look up to you.

To the grad students at McMaster who have made Hamilton feel like home - thank you. Claude - you inspire me so much and I know you will go so far. I am proud to have had you as a friend from the start and to have experienced this adventure together. Lauren and Megan - you two are the daily spark when I need to laugh and remember to not take things too seriously. I am proud to have you both as my friends, whether it is down bad at the gym, on the softball field, singing Taylor Swift, dog-sitting Bear, or going out for treats. Thank you to Carmen, Jacqueline, Joey, Veronika, Jeremy, Kate, Hannah, Dylan, and Mathew for being a part of my life. Big shout out to the members of the CASCA GSC who also helped me feel at home in the world of Canadian astronomy. Thank you to Pamela for taking on the GSC with me. I am proud we climbed the mountains together.

My heart has always had a place back in Calgary where I created so many friendships and memories. I owe so much to Prosser, Haydon, Johnny, Kelsie, Jess, Kevin, Joel, and Sierra for years of shenanigans and adventures. I am proud to have seen you all grow so much and start your lives together. I am so privileged to have still been a part of it all while following my own path in Hamilton. Thank you to Sam WC for the study trips to the mountains, for the card and cribbage games, and for reminding me that we can accomplish anything.

I am blessed to have families who have contributed so much to my success and what I have grown into as a person. A minha família brasileira - obrigado por tudo. Vocês são uma parte muito importante na minha vida e espero que continuemos a criar memórias juntos. A minha mãe Roseli - você está sempre presente no meu coração. Igor - ter você como irmão é um dos maiores privilégios que alguém pode obter. Cauê, Mayara, e Rebeca - a família que estão formando é incrivel e eu sou grato por tudo que tenha me dado. Paulo - obrigado por ter me acolhido na sua vida como filho também. O meu pai Rogelio - a convicção que você criou em mim como pessoa nunca será esquecido. Roger - você é uma inspiração e sempre estou tentando a chegar ao seu nível de sabedoria e forteleza. Rosangela, Tamara, e Ísis - a sua família é muito simpática e sou muito grato por tê-las em minha vida. Eu amo muito todos vocês.

To my Canadian family - I don't even know where to start. Arriving at the end of this path has seen us spend nearly 10 years apart with only a few moments shared in person. I am grateful for every one of them. Granny and Grandpa - I am so thankful for the numerous phone calls, time spent together, and being able to share my success with you. Teralynn and Chanel - I have loved watching you both grow as passionate and strong individuals. I am a proud brother and know that you will both continue to have such successful and fulfilling lives. Mom - your strength has carried me. I owe all of my success to you. I am so grateful for your unconditional love and support as I pursued my dreams. Dad - I have always looked up to you. You have set an incredible example with your work ethic and determination to provide and care for our family. Thank you for setting the bar so high as a father. I hope I have kids one day who are as proud of me as I am of you. I love you all.

To my new family - Peter, Sonia, Pete, Margaret, Chloe, Will, Cam, Sevin, Pat, and Emma - thank you for being so supportive of me and for creating a welcoming and loving environment that I could be a part of. You were a big part of this journey and I love that I can celebrate it with you as well.

He will never read this, but shout out to Bear for rescuing me and bringing me so much joy, frustration, laughter, anxiety, panic, and love. You saved me.

To Victoria - it feels like you have been there since the start. It is nearly 5 years exactly since we met and started our journey together. Look at how much we have accomplished. You have always supported me - through the transition from my MSc to PhD, during my comprehensive exam grind, while I have been away at conferences, and at the end while I scrambled to finish everything I needed to on time. Thank you. Celebrating this milestone with you makes it so much better. I cannot wait to see what we can achieve together on our next adventure moving to BC and all of the other ones we have in store. You bring out so much good in me and I could not have done this without you. I dedicate it all to you and to us.

Contents

List of Figures

List of Tables

List of Abbreviations

Science terms

ΛCDM	Cosmological model with cosmological constant and cold dark matter
AD	Anderson-Darling
AGN(s)	Active galactic nucleus (nuclei)
C	Carbon
CASA	Common Astronomy Software Applications
CGM	Circumgalactic medium
CMB	Cosmic microwave background
CN	Cyanide radical
CND	Circumnuclear disk
CNM	Cold neutral medium
CO	Carbon monoxide
CR	Cosmic ray
CS	Carbon monosulfide
DEC	Declination
DIG	Diffuse ionized gas
FUV	Far ultraviolet
FIR	Far infrared
GMC	Giant molecular cloud
GOALS	Great Observatories All-sky LIRG Survey
H	Hydrogen
H_2	Molecular hydrogen
HCN	Hydrogen cyanide
HCO^+	Formyl cation
HERUS	HERschel Ultra Luminous InfraRed Galaxy Survey
HIM	Hot intercloud medium
HMXB	High-mass X-ray binaries
ICM	Intracluster medium
IR	Infrared
ISM	Interstellar medium

KS	Kennicutt-Schmidt
LTE	Local thermodynamic equilibrium
PA	Position angle
PAH	Polycyclic aromatic hydrocarbon
PDR	Photon dominated region
PE	Photoelectric
PHANGS	Physics at High Angular resolution in Nearby GalaxieS
RA	Right Ascension
RMS	Root mean square
S/N	Signal-to-noise
SED	Spectral energy distribution
SFR	Star formation rate
SFE	Star formation efficiency
SN(e)	Supernova(e)
SNR(s)	Supernova(e) remnant
U/LIRG	Ultraluminous/luminous infrared galaxy
UV	Ultraviolet
WIM	Warm ionized medium
WNM	Warm neutral medium
XDR	X-ray dominated region

Telescope facilities

ACA	Morita Atacama Compact Array
ALMA	Atacama Large Millimeter/Submillimeter Array
GALEX	Galaxy Evolution Explorer
HST	Hubble Space Telescope
IRAM	Institut de Radioastronomie Millimetrique
IRAS	Infrared Astronomical Satellite
JWST	James Webb Space Telescope
SDSS	Sloan Digital Sky Survey
SKA	Square Kilometer Array
TP	Total Power array

UVIT	Ultraviolet Imaging Telescope
VLA	Very Large Array
WMAP	Wilkinson Microwave Anisotropy Probe

Institutes and organizations

ADC	Astronomy Data Centre
ApJ	The Astrophysical Journal
ASIAA	Academia Sinica Institute of Astronomy and Astrophysics
AUI	Associated Universities, Inc.
CSA	Canadian Space Agency
ESA	European Space Agency
ESO	European Space Observatory
IPAC	Infrared Processing and Analysis Center
JSPS	Japan Society for the Promotion of Science
KASI	Korea Astronomy and Space Science Institute
MDAS	Multi-wavelength Data Analysis System
MOST	Ministry of Science and Technology in Taiwan
MNRAS	Monthly Notices of the Royal Astronomical Society
NAOJ	National Astronomical Observatory of Japan
NASA	National Aeronautics and Space Administration
NED	NASA/IPAC Extragalactic Database
NINS	National Institutes of Natural Sciences of Japan
NRAO	National Radio Astronomy Observatory of USA
NRC	National Research Council
NSERC	Natural Sciences and Engineering Research Council of Canada
NSF	National Science Foundation
STScI	Space Telescope Science Institute

Co-authorship

Chapters 2, 3, and 4 of this thesis contain original scientific research written by myself, Blake Ledger.

Chapter 2 has been published as a peer-reviewed journal article in the Monthly Notices of the Royal Astronomical Society (MNRAS). The citation for this work is: Ledger B., Wilson C. D., Michiyama T., Iono D., Aalto S., Saito T., Bemis A., Aladro R., 2021, MNRAS, Volume 504, Issue 4, pp. 5863–5879. This work is co-authored with my supervisor, Dr. Christine D. Wilson, who led the observing proposal for acquiring the new ALMA observations analysed in this work. The remaining authors, Dr. Tomonari Michiyama, Dr. Daisuke Iono, Dr. Susanne Aalto, Dr. Toshiki Saito, Dr. Ashley Bemis, and Dr. Rebecca Aladro aided in preparing the observing proposal and provided helpful comments and feedback on the article draft. While not co-authors on the published article, Dr. Nanase Harada, Dr. Kazimierz Sliwa, and Dr. Kazushi Sakamoto also aided in preparing the observing proposal for the data used in this work.

Chapter 3 has been published as a peer-reviewed journal article in MNRAS. The citation for this work is: Ledger B., Saito T., Iono D., Wilson C. D., 2024, MNRAS, Volume 527, Issue 2, pp. 2963–2990. This work was supported by and co-authored with Dr. Toshiki Saito and Dr. Daisuke Iono, who hosted me at the National Astronomical Observatory of Japan for 10-weeks to conduct the research in this publication. Dr. Toshiki Saito provided supported for the data analysis of this project and feedback on much of the text of the article draft. Dr. Daisuke Iono provided the facilities used for the analysis and storage of the data, as well as helpful comments on the article draft. Additionally, this work is co-authored with my supervisor, Dr. Christine D. Wilson, who provided comments and feedback on the article draft.

Chapter 4 has been submitted to the peer-reviewed journal the Astrophysical Journal. This work is co-authored with my supervisor, Dr. Christine D. Wilson. The third author, Osvald Klimi, conducted the radio continuum analysis on the ALMA observations used in this work. The fourth author, Dr. Núria Torres-Albà, provided the X-ray analysis from *Chandra* data which was necessary for this work. Dr. Toshiki Saito provided helpful comments on the article draft and assisted in the precursor to this article published as Chapter 3 of this thesis.

Chapter 5 and the future work section also contains preliminary research work which is in preparation and will be submitted to a peer-reviewed journal. The author list for this work is: Ledger, B. and Wilson, C. D. This work is co-authored with my supervisor, Dr. Christine D. Wilson.

I hereby grant an irrevocable, non-exclusive license to McMaster University and Library and Archives Canada to reproduce the material as part of this thesis.

1 | Introduction

Humans have been observing the universe since long before sophisticated instruments and telescopes existed, looking up at the sky as astronomers and wondering about fundamental questions like are we alone, where did we come from, can we describe the objects we are seeing, and how was the universe created? While we do not yet have the answers to all of these questions, our ability to observe the universe, particularly through the creation of modern day telescopes, has opened our eyes to many unexplored regions of space. In this thesis, I will discuss my contribution to our understanding of the universe by using observations of dense molecular gas from one of the world's most powerful instruments, the Atacama Large Millimeter/Submillimeter Array (ALMA).

I introduce how astronomers observe the Universe in Section 1.1, galaxies in Section 1.2, the interstellar medium (ISM) in Section 1.3, molecular gas in Section 1.4, dense molecular gas in Section 1.5, star formation in Section 1.6, and the primary instrument for my thesis observations, ALMA, in Section 1.7. Finally, I introduce the main science questions and individual chapters of this thesis in Section 1.8.

1.1 Observing the Universe

1.1.1 Radiation fields, photons, and telescope observations

The main way that humans observe and interact with the universe is through light and radiation, or photons. Photons are electromagnetic waves that propagate through space at the speed of light, $c \approx 3.0 \times 10^{10}$ cm s^{-1}, with both a wave- and particle-like nature. The major identifying characteristics associated with these photons are their frequency, ν, which is interchangeable with their wavelength, λ, using $c = \lambda\nu$, and the energy associated with that frequency, $E_\nu = h\nu$. The energy of the photon can be roughly thought of as a temperature, $T \approx E/k_{\mathrm{B}}$ (Rybicki & Lightman 1986). Here, h and k_{B} are two fundamental constants of physics, Planck's constant and the Boltzmann constant, respectively. An easy rule of thumb to follow is that 1 eV $\sim$ 1000 nm $\sim 10^4$ K. Photons are classified based on their energies and wavelengths.

Gamma rays and X-rays

The highest energy radiation in the universe comes in the form of gamma rays and X-rays. Gamma rays are photons with incredibly high energies $\gtrsim$ 100 keV and temperatures

$\gtrsim 10^9$ K, although the specific values are not well-constrained (Rybicki & Lightman 1986; Funk 2015). Gamma rays come from sources like compact neutron stars, stellar mass black holes, active galactic nuclei (AGN), and gamma ray bursts (Funk 2015). Although there is a continuum of X-ray energies, X-rays are often split into two separate classifications: soft X-rays (0.5 – 2 keV) and hard X-rays (2 – 10 keV or higher; Rybicki & Lightman 1986). Soft X-rays originate from the hot gas in the universe ($T \sim 10^6 - 10^7$ K), often associated with the intracluster medium (ICM) in galaxy clusters (Forman & Jones 1982) and gaseous regions which have been heated by star formation (Gorenstein & Tucker 1976; Iwasawa et al. 2011; Torres-Albà et al. 2018). Hard X-rays come from sources like AGN, black hole accretion, and high-mass X-ray binaries which are the end products of star formation (Iwasawa et al. 2011; Torres-Albà et al. 2018). The temperatures required to produce hard X-rays are of order $T \gtrsim 10^7$ K. X-rays can also be produced by stars (Rosner et al. 1985) or from supernova remnants (SNRs; Raymond 1984).

Ultraviolet, visible and optical light

Ultraviolet (UV) light dominates the spectrum of massive O and B stars, which ionize a significant fraction of the gaseous material in galaxies to create HII regions (further discussed in Section 1.3). UV photons can also be used to trace recent star formation (Kennicutt & Evans 2012) and are also emitted by stellar remnants, such as white dwarfs and SNRs. UV light has energies of $\sim 4 - 100$ eV and temperatures of $10^4 - 10^6$ K (Rybicki & Lightman 1986).

Visible, or optical, light is the most commonly known type of light because it is the type of radiation that the human eye has evolved to see. The Earth's atmosphere is also quite transparent at these wavelengths (Figure 1.1). Sources of visible light are all stars (O to M type), HII regions, SNRs, quasars, and emission lines from the ISM (Carroll & Ostlie 2017). Visible light has wavelengths of 300 nm -1 μm and temperatures of $10^3 - 10^4$ K (Rybicki & Lightman 1986).

Infrared light

Infrared (IR) light has wavelengths of 1 μm -1 mm and $T \sim 10 - 10^3$ K (Rybicki & Lightman 1986). IR radiation can be of stellar origin, from cooler stars like K and M

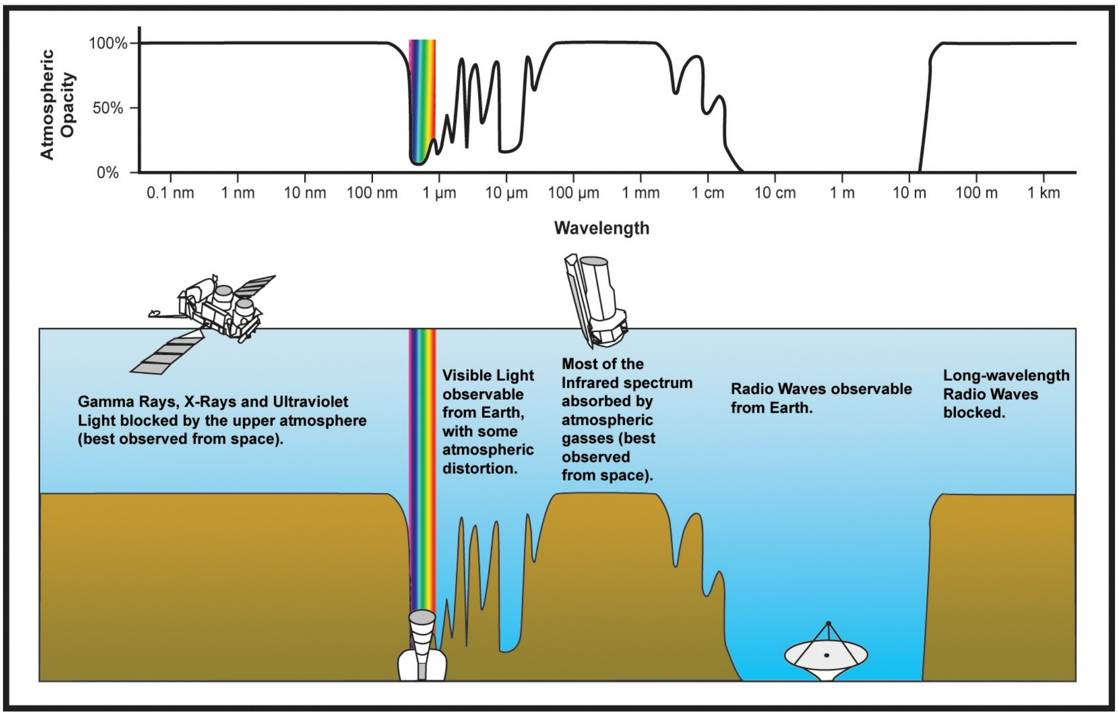

FIGURE 1.1: Earth's atmosphere has different opacities at different wavelengths. The top plot shows the percentage of blocked light by the atmosphere as a function of wavelength, highlighting the visible range. The lower graphic describes what telescopes are needed, either space-based or ground-based, to observe different parts of the electromagnetic spectrum. Image credit: European Space Agency (ESA)/Hubble Space Telescope (HST; F. Granato).

type stars (Carroll & Ostlie 2017). Interstellar dust is also a significant contributor to IR emission (Draine 2003). Large, carbonaceous structures like polycyclic aromatic hydrocarbon (PAHs) create excesses in the observed IR spectra of galaxies (Rigopoulou et al. 2024 and references therein). Finally, the main cooling lines (Section 1.3.3) in the ISM of galaxies, like [OI] and [CII] lines, emit at IR wavelengths (Tielens 2005).

Millimeter, submillimeter and radio waves

Finally, photons with longer wavelengths ($\gtrsim$ 1 mm), smaller energies ($\lesssim$ 0.001 eV), and cold temperatures ($\lesssim$ 20 K) are associated with millimeter, submillimeter, and radio waves (Rybicki & Lightman 1986). Effectively, these types of radiation allow astronomers to probe the coldest corners of the universe. Observations of the 2.7 K cosmic microwave background (CMB) probe the earliest phases of the universe (Weiss 1980), and anisotropies in this microwave radiation led to the development of the Lambda Cold Dark Matter (ΛCDM) model (Planck Collaboration et al. 2020). Cold baryonic matter, such as molecules and atomic hydrogen (HI), emits at centimeter, millimeter, and submillimeter wavelengths. Molecular line emission is a crucial component of this thesis that I discuss in detail in Section 1.4. HI and its 21 cm spontaneous spin flip transition are heavily utilized to understand the atomic structure of the Milky Way (McClure-Griffiths et al. 2023) and other galaxies (e.g., Giovanelli et al. 2005). Plasmas at the coldest temperatures emit at the longest radio wavelengths (Rybicki & Lightman 1986). Synchrotron radiation can also produce radio waves, as well as star formation processes, pulsars, and quasars.

Figure 1.1 shows that the Earth's atmosphere is transparent for mm – cm wavelength photons, particularly at high altitudes. In this thesis, I use millimeter and submillimeter observations to target the chemical and physical properties of molecular gas, which exist at cold temperatures in the ISM ($\leq$ 100 K; introduced further in Section 1.3).

1.1.2 Equation of radiative transfer

As photons travel through space, they can undergo the processes of scattering (photons leaving the path), absorption (photons destroyed in the path), or emission (new photons added into the path; Condon & Ransom 2016). The light traveling along the path to Earth from the source is often referred to as the "specific intensity" or "brightness", I_ν [erg s^{-1} cm^{-2} sr^{-1} Hz^{-1}], which is independent of the distance of the source (Rybicki & Lightman 1986; Condon & Ransom 2016). The intensity of light along its path is described using the equation of radiative transfer,

$$\frac{dI_\nu}{ds} = -\alpha_\nu I_\nu + j_\nu. \tag{1.1}$$

In this equation, α_ν [cm^{-1}] and j_ν [erg s^{-1} cm^{-3} sr^{-1} Hz^{-1}] are the absorption and emission coefficients, respectively, and ds is the path length. An additional quantity is the optical depth, $\tau_\nu = \alpha_\nu ds$, which measures the transparency of a medium to radiation. Using the optical depth, the generalized, formal solution to the equation of radiative transfer is:

$$I_\nu\left(\tau_\nu\right) = I_\nu\left(0\right) e^{-\tau_\nu} + \int_0^{\tau_\nu} e^{-\left(\tau_\nu - \tau'_\nu\right)} S_\nu\left(\tau'_\nu\right) d\tau'_\nu. \tag{1.2}$$

This equation contains two terms: the initial intensity diminished by some absorption $e^{-\tau_\nu}$, and emission from an intervening source, $S_\nu \equiv \frac{j_\nu}{\alpha_\nu}$, which is also affected by absorption (Rybicki & Lightman 1986). Specific examples and simplifications of this complicated equation are applicable for millimeter wavelength observations. Equation 1.2 can be connected to the Planck function, $B_\nu\left(T\right)$, for the specific intensity ($I_\nu = B_\nu$) of blackbody radiation or for the source function ($S_\nu = B_\nu$) of thermal radiation (Rybicki & Lightman 1986). Planck's law is written as

$$B_\nu\left(T\right) = \frac{2h\nu^3}{c^2}\frac{1}{e^{\nu/k_{\rm B}T} - 1}. \tag{1.3}$$

In the radio and millimeter regimes $h\nu \ll k_{\rm B}T$, and this leads to the Rayleigh Jean's approximation

$$I_\nu = B_\nu = \frac{2\nu^2}{c}k_{\rm B}T_{\rm B}. \tag{1.4}$$

This is an important equation for millimeter and radio astronomy because it means that the specific intensity of an observed source can be described as if it were emitting as a blackbody at the same temperature and frequency (Rybicki & Lightman 1986; Condon & Ransom 2016). The brightness temperature, $T_{\rm B}$ [K] is a more useful measure of intensity for radio and millimeter telescope observations, particularly for thermal sources, and the majority of my ALMA observations throughout this thesis are described using the brightness temperature.

The flux density, F_ν [erg s^{-1} cm^{-2} Hz^{-1}], received at a telescope can be determined from the specific intensity by integrating over the solid angle ($d\Omega$) observed in the sky,

$$F_\nu = \int I_\nu \cos\left(\theta\right) d\Omega, \tag{1.5}$$

with θ the angle between the incidence of the radiation and the normal to the plane of the telescope. Finally, the flux density of the emitting source is connected with its intrinsic, monochromatic luminosity, L_ν [erg s^{-1} Hz^{-1}], via

$$L_\nu = 4\pi D_{\rm L}^2\ \left(1+z\right)^{-1}\ F_\nu, \tag{1.6}$$

where the luminosity distance is D_{L} and z is the redshift of the source (Solomon & Vanden Bout 2005).

1.2 Galaxies

Galaxies are large, gravitationally bound objects in the universe that are comprised of stars, gas, dust, and embedded in a massive dark matter halo. Edwin Hubble was a pioneer in observing these "island universes" and found that galaxies tend to fall into specific morphological categories (Hubble 1926). Most galaxies populate what is referred to as the Hubble tuning fork, with early-type galaxies which are elliptical at one end and late-type galaxies at the other, divided into spirals with and without a bar (e.g., Binney & Merrifield 1998). A classification of irregular galaxies was added as more unique morphologies and subclasses were discovered (de Vaucouleurs 1959). I discuss the properties and composition of the most common types of galaxies in Section 1.2.1. I describe galaxy interactions and mergers of galaxies in Section 1.2.2. Finally, I introduce the main types of galaxies observed in this thesis, the extreme starburst systems known as Ultraluminous and Luminous Infrared Galaxies (U/LIRGs), in Section 1.2.3.

1.2.1 Galaxy types, morphologies, and composition

Galaxy properties depend on whether they are early-type, elliptical and S0s, late-type and spiral, or irregular. Spiral galaxies are sometimes known as disk galaxies, as a large portion of their material is situated in a gravitationally bound rotating disk surrounded by an extended stellar halo and embedded within an even larger dark matter halo (Binney & Merrifield 1998). The bulk of the baryonic matter (e.g., the stars, dust, and gas) is in the disk itself, while smaller objects like globular clusters can be found in the halo. The surface brightness profiles of the stellar disks of spiral galaxies are approximately given by Binney & Tremaine (2008) as

$$I(R) = I_{\mathrm{d}} e^{-(R/R_{\mathrm{d}})}, \tag{1.7}$$

where R_{d} is the disk scale length and I_{d} is the surface brightness of the galaxy at $R = R_{\mathrm{d}}$. The density profile of stars vertically in the disk is given by

$$\rho\left(R,z\right)=\rho\left(R,0\right)e^{-\left|z\right|/z_{\mathrm{d}}\left(R\right)},\tag{1.8}$$

where z and $z_{\mathrm{d}}\left(R\right)$ are the distance from the midplane and the disk scale height, respectively (Binney & Tremaine 2008). The typical range of masses for spiral galaxies is $10^{9}-10^{12}$ $\mathrm{M}_{\odot}$, with disk diameters of $5-100$ kpc and rotational velocities of a few hundred km s^{-1} (Carroll & Ostlie 2017). Spiral galaxies have a diversity of morphologies depending on, for example, the number and tightness of spiral arms, the relative size of the bulge, or the presence of a central bar. In this thesis, words like "normal", "disk", "late-type", and "spiral" may be used interchangeably to label the type of galaxy described above.

Elliptical galaxies contain less gas and dust than spiral galaxies, and are mostly relaxed systems with older stellar populations and elliptical surface brightness profiles. The surface brightness profiles can be described by the de Vaucouleurs $\mathrm{R}^{1/4}$ law (de Vaucouleurs 1948), given by Binney & Merrifield (1998) as

$$I\left(R\right)=I_{\mathrm{e}}10^{-3.33\left[\left(R/R_{\mathrm{e}}\right)^{1/4}-1\right]},\tag{1.9}$$

where R_{e} is the effective radius and I_{e} is the surface brightness at $R=R_{\mathrm{e}}$. Note that the bright bulges at the centres of disk-like galaxies can also follow this type of surface brightness profile (Binney & Merrifield 1998). Elliptical galaxies tend to have a wider range of masses than spiral galaxies ($10^{7}-10^{14}$ $\mathrm{M}_{\odot}$) and a significant difference in sizes depending on the type of elliptical, with cD galaxies reaching $\sim 100-1000$ kpc diameters and dwarf ellipticals <10 kpc (Carroll & Ostlie 2017).

Irregular galaxies are those which do not fit the typical observed profiles and properties of early- and late-type galaxies. They tend to be smaller, on average, than both ellipticals and spirals, but can be comparable in both stellar mass ($10^{7}-10^{10}$ $\mathrm{M}_{\odot}$) and size (<50 kpc, Carroll & Ostlie 2017). Irregulars do not possess a common set of distinguishing properties due to their diverse morphologies, deviation from spiral structure, and low surface brightnesses (Binney & Tremaine 2008).

1.2.2 Galaxy interactions and mergers

Galaxies are not always completely isolated systems, where the local properties and dynamics are governed solely by internal processes and interaction with the ICM. Galaxies can live in small collections of galaxies called groups or large complexes of galaxies called clusters. The large-scale environment that a galaxy lives in can play a significant role in the evolution of a galaxy (e.g., Vollmer 2013). Interactions between galaxies can lead to changes in their morphologies, such as some of the first "bridges" and "tails" observed and catalogued between interacting galaxies (Arp 1966; Toomre & Toomre 1972; Arp & Madore 1987). Interactions which eventually lead to galaxy coalescence are referred to as mergers. A simplistic picture of hierarchical galaxy formation and evolution suggests that galaxy mergers allow smaller galaxies to collide and merge, repeatedly, to form large systems (Toomre & Toomre 1972; White & Rees 1978; Fall 1979; Barnes 2002; Binney & Tremaine 2008). Mergers can be classified as "major" or "minor", depending on the mass ratios of the merging galaxies (Binney & Tremaine 2008). Major mergers occur when the mass ratio of the merging systems is nearly unity, and minor mergers, which are much more common than major mergers, have a mass ratio of $\sim 1:4$ or larger (Lotz et al. 2011).

Simulations of galaxy mergers show that they can produce a large gaseous disk (Noguchi 1988; Mihos & Hernquist 1996; Barnes 2002; Hopkins et al. 2013; Patton et al. 2013; Moreno et al. 2015, 2019), which can serve as a reservoir of molecular gas to sustain enhanced star formation (further discussed in Sections 1.4.3 and 1.6). Interactions and mergers of galaxies also play a significant role in the activation of AGN at the centres of galaxies (Ellison et al. 2011; Khabiboulline et al. 2014; Satyapal et al. 2014; Weston et al. 2017; Goulding et al. 2018). Simulations of merging galaxies allow astronomers to observe the merger sequence from initial interaction through coalescence and obtain detailed properties of the merging galaxies as a function of time. Large optical surveys of galaxies like the Sloan Digital Sky Survey (SDSS), have produced tens of thousands of images (most recent SDSS data release − DR18 − Almeida et al. 2023), including galaxy pairs and mergers. The enormous number of galaxy images that are required to be visually inspected for galaxy morphologies has led to citizen science projects, such as Galaxy Zoo (Lintott et al. 2008), and using artificial intelligence models (e.g., Ferreira et al. 2024) to identify galaxy mergers.

Larson & Tinsley (1978) showed that some galaxies host an incredibly intense burst of star formation compared with normal galaxies, and these systems are often termed "starbursts". One of the first uses of the term "starburst galaxy" was by Weedman et al. (1981), who observed an intense nuclear enhancement of star formation in NGC

7714. Starburst galaxies that also have an abundance of gas and dust and are incredibly luminous at IR wavelengths are called U/LIRGs (Sanders & Mirabel 1996; Lonsdale et al. 2006; Armus et al. 2009; Pérez-Torres et al. 2021).

1.2.3 Ultraluminous and luminous infrared galaxies

Observations using the Infrared Astronomical Satellite (IRAS) found that there are a large number of IR bright galaxies in the universe (e.g., Sanders et al. 2003). The classifications of LIRGs and ULIRGs are that they have IR luminosities of $10^{11} - 10^{12}\ L_\odot$ and $\geq 10^{12}\ L_\odot$, respectively. The IR luminosities from U/LIRGs are thought to originate from dust that has been heated by intense star formation triggered by a merger or interaction or by an AGN (Sanders & Mirabel 1996; Lonsdale et al. 2006; Pérez-Torres et al. 2021). At low redshift, $\sim 25 - 40\%$ of LIRGs are major mergers, and this fraction only increases ($\sim 50 - 80\%$) for ULIRGs (Kartaltepe et al. 2010; Ellison et al. 2013a). Major collaborations, such as the Great Observatories All-sky LIRG Survey (GOALS[1]), have dedicated years of multi-wavelength observational campaigns to understanding the physical properties of U/LIRGs (e.g., Armus et al. 2009; Howell et al. 2010; Iwasawa et al. 2011; Stierwalt et al. 2013; Díaz-Santos et al. 2017; Barcos-Muñoz et al. 2017; Song et al. 2021; Armus et al. 2023). The molecular gas content and star formation properties of U/LIRGs can be quite different than normal galaxies, and I highlight some differences in Sections 1.4.3 and 1.6.

All of the galaxies studied in this thesis are U/LIRGs and a full list of galaxy names is given in Table 3.1. The sample contains 4 ULIRGs and 12 LIRGs, with IR luminosities spanning $\log_{10}(L_{\rm IR}) = 11.08 - 12.28\ L_\odot$ (Armus et al. 2009) and various AGN types (see Chapter 3 and 4). These galaxies also cover a range of merger stages, as identified spectroscopically using Spitzer data (Stierwalt et al. 2013): 4 galaxies are non-mergers, 3 galaxies are pre-mergers, 1 galaxy is a late-stage merger, and 8 galaxies are post-mergers (further details in Chapter 4). Chapter 2 focuses on two nearby LIRGs with a strong starburst (NGC 3256, Figure 1.2) and a Seyfert 2 nucleus (NGC 7469), and the second nearest bright ULIRG, IRAS 13120-5453. Chapters 3 and 4 include all 16 galaxies from the sample.

[1] https://goals.ipac.caltech.edu/

FIGURE 1.2: HST image of the nearby LIRG NGC 3256. This galaxy is an active merger, as can be seen by the chaotic morphology, and the presence of obscuring dust blocks much of the starlight near the centre of the merger. NGC 3256 has a bright starburst in the northern nucleus and an edge on disk with an obscured embedded active galactic nucleus in the south. Image credit: ESA/HST, National Aeronautics and Space Administration (NASA).

1.3 The Interstellar Medium

Within galaxies, the space between the stars is referred to as the ISM. The ISM is comprised primarily of gas-phase hydrogen (H) and helium, with trace amounts of heavier elements (Tielens 2005). Additionally, roughly 1% of the ISM exists in macroscopic silicates and carbonaceous dust grains (Draine 2003). In the following sections, I briefly describe the structure of the ISM and its different phases, radiation fields and their interaction with the ISM, and the most important heating and cooling mechanisms in the ISM.

1.3.1 ISM structure and phases

The components of the ISM can be described by different phases, each with its own temperature, T, and density, n. Early models of the ISM (McKee & Ostriker 1977) split it into three components which were primarily regulated by supernovae (SNe) explosions and an equilibrium balance between the phases (Figure 1.3, left). Since then, observations and theory have expanded and astronomers now describe the ISM as a combination of many interacting phases including molecular clouds, the cold neutral medium (CNM), the warm neutral medium (WNM), the warm ionized medium (WIM), and the hot ionized medium (HIM). As molecular gas is an integral part of this thesis, I describe this phase of the ISM and how it is observed in Section 1.4. Figure 1.3 (right) shows new James Webb Space Telescope (JWST) observations, combined with archival Hubble Space Telescope (HST) data, of the IR and visible emission from the ISM in the galaxy NGC 628. Clearly, the observational picture is much more complex than the original three-phase models introduced by McKee & Ostriker (1977).

The CNM is the densest phase of the ISM after molecular clouds and is mostly occupied by neutral atomic gas with temperatures of $\sim$ 100 K and densities between 10 – 100 cm^{-3} (Tielens 2005). Along with molecular clouds, the CNM represents a major reservoir of atomic H which serves as fuel for star formation. Some textbooks identify the CNM as diffuse clouds of atomic matter, which lack a distinct structure or morphology and can be translucent to interstellar light (Kwok 2007). The CNM is primarily observed using the 21 cm spin-flip transition of atomic H. Major telescopes that are crucial for observing the CNM include the Very Large Array (VLA), previously

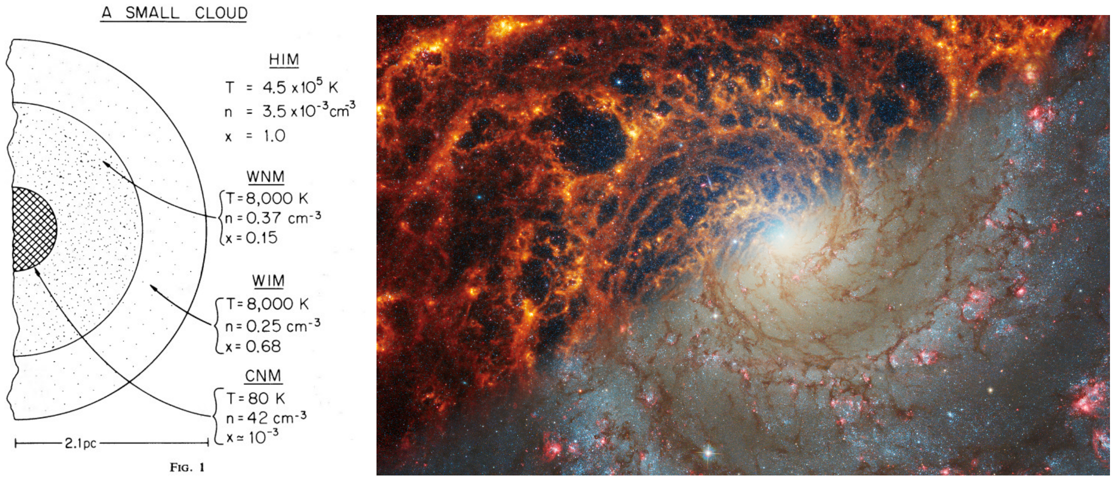

FIGURE 1.3: *Left:* Figure 1 from McKee & Ostriker (1977) demonstrating a schematic cross section a small cloud in their three-phase model of the ISM. In this model, the CNM is embedded within the WNM and WIM, surrounded by an outer layer of HIM. T, n, and x are the temperature, density, and ionization fraction of each phase, respectively. Image credit: McKee & Ostriker (1977). *Right:* A combined JWST and HST image of the nearby spiral galaxy NGC 628. The top left half of the image shows the IR JWST data and warm glowing dust in the ISM. The bottom right half shows the visible light from HST, with extincting dust lanes overlaid on top of stellar complexes and HII regions scattered in bright red. Image credit: NASA, ESA, Canadian Space Agency (CSA), Space Telescope Science Institute (STScI), Janice Lee (STScI), Thomas Williams (Oxford), Physics at High Angular resolution in Nearby GalaxieS (PHANGS) Team.

Arecibo, and the Square Kilometer Array (SKA) in the future, which should see first light before 2030. Like the CNM, the WNM consists of neutral gas but with significantly warmer temperatures of $\sim$ 8000 K and lower densities of 1 cm^{-3} (Tielens 2005). The WNM primarily occupies the intercloud space between diffuse clouds (about 30% of the total galaxy volume) and is "puffier" than the CNM, with galaxy disk scale heights roughly 2 times larger ($\sim$ 200 pc compared to $\sim$ 100 pc, Tielens 2005).

The WIM has similar temperatures and densities to the WNM ($\sim$ 8000 K and 0.1 cm^{-3}, Tielens 2005), with the critical difference being that this phase of the ISM is now ionized (Cox 2005). A diffuse ionized gas component of the WIM extends above the disks of galaxies, reaching scale heights of $\sim$ 1 kpc, and fills about 25% of the volume of a galaxy (Tielens 2005). HII regions are ionized regions in the ISM which are located around regions of massive O and B star formation where the radiation is strong enough to have completely ionized the atomic H. Both diffuse ionized gas and HII regions can be observed with Hα recombination lines (Tielens 2005).

Finally, the hottest ($> 10^6$ K) and most diffuse (< 0.01 cm^{-3}) component of the ISM is the HIM (Tielens 2005). The HIM is diffcult to observe because it is so diffuse and extends up into the halos of galaxies, occupying nearly 50% of the volume of the ISM (Tielens 2005). The possibility of observing the HIM was first discussed by Spitzer (1956), and most early observations were of a soft X-ray emitting background (Cox & Smith 1974; Williamson et al. 1974) and highly ionized metal absorption lines, like O[VI] (Rogerson et al. 1973; York 1974; Jenkins & Meloy 1974). The HIM is thought to play a critical role in the recycling of material from the halo of a galaxy through the gas cooling, condensing, and raining back down onto the disk (e.g., the "galactic fountain model" Shapiro & Field 1976). The HIM is also observed in UV absorption surveys via pencil beams observations through galaxy halos.

1.3.2 Photon and X-ray dominated regions

More than 90% of the ISM exists in what is known as photon dominated regions regions (PDRs; also known as photodissocation regions, Tielens & Hollenbach 1985). PDRs are regions of the neutral or ionized ISM where the chemical and physical properties are dominated by far ultraviolet (FUV; energies of 6 – 13.6 eV) radiation field effects (Tielens & Hollenbach 1985; Wolfire et al. 2022). The FUV photons are emitted by massive O and B type stars, which are often embedded within the ISM and surrounded by an HII region (Figure 1.4, right), and the strength of the FUV photons depends on the proximity of the OB stars to the surrounding medium. Both heating (via the FUV photoelectric effect on dust grains) and cooling (via line emission) processes in the ISM play a critical role in the regulation of star formation rates (SFRs) in galaxies (e.g., Ostriker et al. 2010; Wolfire et al. 2022).

The simplest PDR model is a one-dimensional slab with an FUV photon source on one side (Figure 1.4, left). This schematic, introduced by Tielens & Hollenbach (1985), shows a transition between different atomic and molecular components as the FUV photons interact with the baryonic matter and produce different chemical effects. One major feature in Figure 1.4 (left) is the H^+/H transition at the edge of the cloud where the ionizing photons dip below energies of 13.6 eV and lose the ability to ionize H into H^+.

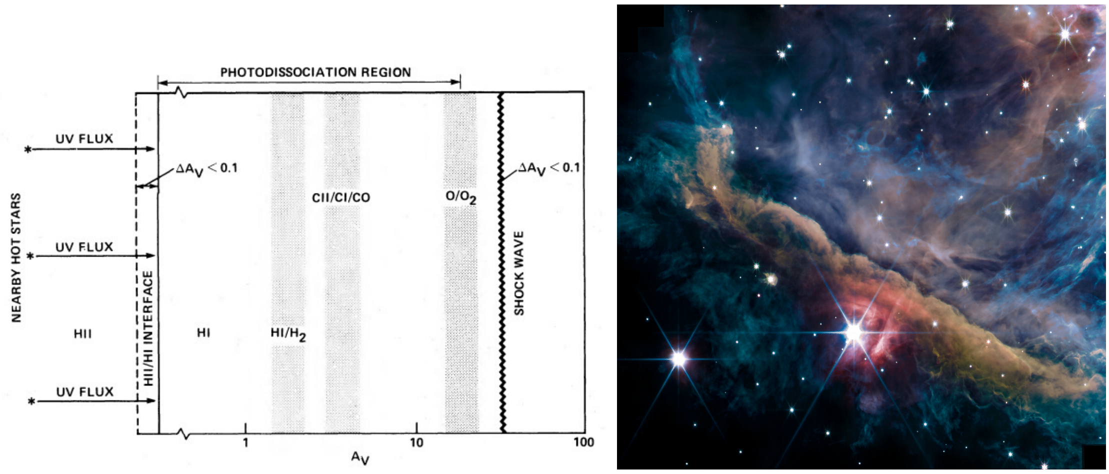

FIGURE 1.4: *Left:* A simple 1-dimensional schematic of a PDR region from Tielens & Hollenbach (1985). Cloud depth increases from left to right as a function of A_V. UV radiation from hot massive stars enters from the left and passes through layers of material, attentuating and weakening with increasing A_V. The various chemical components of the PDR are shown in different vertical layers. Image credit: Tielens & Hollenbach (1985). *Right:* A JWST NIRcam image of the Orion Nebula and PDR. Stars are the bright spots in the image, with radiation shining on the surrounding dust and gas. Compared with the 1D schematic on the *left*, real PDRs are 3D complex structures with multiple embedded stars producing radiation that interacts with the gas and dust. Image credit: NASA, ESA, CSA, Data reduction and analysis: PDRs4All ERS Team; graphical processing S. Fuenmayor.

A second important feature is the transition at $A_v \sim 2$ when atomic H forms molecular hydrogen, H_2 (Wolfire et al. 2022). The carbon transition occurs around $A_v \sim 4$, when electrons recombine with C^+ (one of the major coolants of the ISM; Section 1.3.3) to form neutral carbon (C) before undergoing ion-neutral reactions to create carbon monoxide (CO; van Dishoeck & Black 1988; Sternberg & Dalgarno 1995). CO lines dominate the cooling budget at these depths and radiate at millimeter wavelengths, which can be observed with telescopes like ALMA and the Institut de radioastronomie millimétrique (IRAM) 30 m telescope.

A region that is dominated by X-ray emission instead of FUV photons is known as an X-ray dominated region (XDR; also known as X-ray dissociation regions, Maloney et al. 1996). XDRs are regions where the energy input and chemical and physical properties of the ISM are set by the presence of X-rays. Since X-rays have higher energies than FUV photons, they are able to penetrate deeper into molecular clouds without the radiation fields being attenuated as quickly. However, the sources of these X-rays are often much smaller or more compact compared to a large star formation region producing a large area of FUV photons. Therefore, XDRs have a strong, but more localized effect, for example in the molecular gas around an AGN (Maloney et al. 1996; Izumi et al. 2016). Highly energetic particles known as cosmic rays (CRs) can also play a critical role in the densest regions of PDRs, where the FUV and X-ray photons have been mostly attenuated and the heating balance is set by the CR ionization rate (Tielens 2005).

Both PDRs and XDRs are relevant for this thesis, as extreme galaxies have incredible SFRs (large PDRs) and can have strong X-ray emission (XDRs) from AGN and/or star formation that can affect the dense molecular gas.

1.3.3 Heating and cooling mechanisms

The heating and cooling balance in the ISM is regulated through various different physical and chemical mechanisms. The energy balance can be different in different components of the ISM, such as ionized HII regions, PDRs, and molecular clouds (Tielens 2005). Different types of galaxies can also be dominated by different heating and cooling rates and mechanisms.

In order for the ISM to cool, energy needs to leave the system in some way. This is most typically done through different line emission processes. For most cooling processes, the cooling rates will depend primarily on gas densities and temperatures (Tielens 2005). The dominant coolants in the ionized phases of the ISM are atomic transitions such as [OIII] and [NII] (Tielens 2005). In the neutral ISM, line emission comes from different atomic and molecular species, and often the cooling rates have a strong temperature dependences. For example, the most important coolant of the neutral ISM changes from the [CII] 158 μm line at $T \sim 100$ K to the [OI] 63 μm line $T \sim 10^3$ K to the Lyman α line at $T \sim 10^4$ K, with the latter regime beginning to reach temperatures sufficient to ionize most of the atomic H (Tielens 2005). At the highest temperatures in the ISM, $T \sim 10^7$ K, free-free radiation, also known as Bremsstrahlung or braking radiation, will dominate the cooling as there are vast amounts of free electrons that can interact and emit photons (Tielens 2005).

The ISM can gain energy and heat in a variety of different ways, most of which involve some interaction with radiation fields. Photo-ionization, the process where an energetic photon interacts with an atom or molecule and ejects an electron which carries away some of the energy of the initial photon kinetically, contributes to ISM heating in regions with strong radiation fields and many photons (Tielens 2005). The most dominant heating mechanism in the ISM, however, is the photoelectric (PE) heating of dust grains and PAHs, whereby a photon removes an electron from a dust grain and the electron collisionally dissipates its energy into the rest of the ISM (Tielens 2005). The dominant heating mechanisms depend on the phase of the ISM, with diffuse regions in high radiation fields dominated by PE heating of dust, the WNM dominated by PE heating at high densities and CRs and X-rays at low densities, and molecular cloud heating dominated mostly by CR heating (Tielens 2005).

1.4 Molecular gas

Molecular clouds, which are made of primarily molecular hydrogen (H_2) gas, are the coldest and densest component of the ISM. The temperatures in this phase are on the order of $10 - 50$ K, and densities reach $> 10^2$ cm^{-3} (Tielens 2005). The molecular gas that is observed in galaxies appears to be organized into what are referred to as giant molecular clouds (GMCs), with masses of $\sim 10^2 - 10^7 M_{\odot}$ and sizes of $10 - 100$ pc (Solomon et al. 1979, 1987; Heyer et al. 2001, 2009; Sun et al. 2018, 2020; Rosolowsky et al. 2021; Brunetti & Wilson 2022; Chevance et al. 2023). The GMCs live in the filamentary structure of the ISM (André et al. 2010; Pillsworth & Pudritz 2024) and have average lifetimes of a few to several times 10^7 Myr (Kim et al. 2022; Pan et al. 2022; Chevance et al. 2023). The molecular ISM is not necessarily in equilibrium with the other ISM phases, but instead is a turbulent medium (Larson 1981) that is self-gravitating and in a constant battle of magnetic, radiation and turbulent pressures counteracting gravitational collapse (Tielens 2005). Dense cores are found in GMCs and are the sites of future star formation (Lada et al. 1991; Lada & Lada 2003; Lada et al. 2012; André 2017), with sizes of ~ 1 pc, densities $> 10^4$ cm^{-3}, and masses of $10 - 10^3 M_{\odot}$ (Tielens 2005). Incredible, multi-wavelength surveys in recent years have expanded the understanding of molecular gas in normal galaxies. In particular, the Physics at High Angular resolution in Nearby GalaxieS (PHANGS, Leroy et al. 2021) survey has revolutionized the number of cloud-scale observations of molecular gas and cloud properties.

H_2 can form through a number of formation channels, but the most efficent involve reactions with dust grains (Tielens 2005). Individual H atoms stick to a dust grain surface and through quantum mechanical processes migrate around until they encounter another H atom, forming H_2 and then evaporating back into the gas phase (Tielens 2005). Gas phase reactions are very inefficient with slow reaction rates (Tielens 2005; Kwok 2007). H_2 is destroyed primarily through photodissociation by energetic photons from a FUV radiation field (Tielens 2005). If H_2 is abundant enough, it can self-shield from the radiation field and H_2 begins to accumulate. H_2 is the most abundant molecule in the ISM and is therefore influential in the excitation and reactions with all other species in the ISM.

1.4.1 Molecular line emission

In this thesis, I use observations of the emission lines of molecules to study the properties of the molecular ISM. While molecules can also be observed through absorption lines, those are not a focus of this work. The strength of an emission line depends on a number of factors, including gas temperature and density, optical depth, and the abundance of the emitting molecule relative to H_2. Excitation primarily occurs through collisions with H_2, but radiative processes can also excite the transitions.

The simplest case to consider is a two-level system without radiative trapping, where a molecule is excited/de-excited by absorption/emission of a photon of energy $E = h\nu$ between two transition levels. This process can occur by spontaneous emission, absorption, or stimulated emission, described by the Einstein coefficients (Rybicki & Lightman 1986). When the system is in thermodynamic equilibrium, the rate of photons entering and leaving one energy state is balanced. The Boltzmann equation, which describes the number of atoms in each energy state, n_i and n_0, is given as

$$\frac{n_i}{n_0} = \frac{g_i}{g_0} e^{\frac{h\nu_{i0}}{k_B T_{ex}}}. \tag{1.10}$$

Here, g_i and g_0 describe the degeneracy of each state, $h\nu_{i0}$ is the energy separating the two transitions, and T_{ex} is the excitation temperature (Rybicki & Lightman 1986; Kwok 2007). In Local Thermodynamic Equilibrium (LTE), T_{ex} is equivalent to the kinetic temperature of the gas and n_i and n_0 are determined by collisonal processes (Kwok 2007).

The critical density, $n_{\rm crit} = A_{ij}/\gamma_{ij}$ of a molecule is defined as the ratio between the Einstein A coefficient describing the rate of spontaneous emission between levels i and j, A_{ij}, and the rate of collisional excitation, γ_{ij} (Tielens 2005). The critical density can be used to describe if the excitation is dominated by radiative or collisional processes. In a two level system, the excitation temperature of a molecule can be connected with its kinetic temperature as (Tielens 2005)

$$T_{\rm ex} = \frac{T}{1 + \frac{k_{\rm B}T}{h\nu_{i0}} \ln\left(1 + \frac{n_{\rm crit}}{n}\right)}, \tag{1.11}$$

where T and n are the kinetic temperature and density of the gas, respectively. When $n \gg n_{\rm crit}$, the system is in LTE and $T_{\rm ex} = T$. Once the excitation temperature is known, it can be connected to the optical depth in order to determine the molecular abundance (Kwok 2007).

1.4.2 Observations of molecular gas

H_2 is largely invisible under the typical gas temperatures (< 50 K) and conditions seen in the ISM. To directly observe the lowest transition of H_2, which has an energy of $E/k_{\rm B} \approx 510$ K, gas temperatures of $\gtrsim 80$ K are required (Togi & Smith 2016). Only in the warm molecular ISM do the rotational transitions of H_2 become visible, such as can be observed in the IR regime with JWST (e.g., Armus et al. 2023).

Since there is no direct access to H_2 in cold GMCs, observes use other tracers as a proxy for H_2 column density. Commonly used tracers of molecular gas mass are dust, with an assumed dust-to-gas ratio (Sandstrom et al. 2013), [CI] emission, particularly at high redshift (Papadopoulos et al. 2004), and CO emission (e.g., Bolatto et al. 2013; Schinnerer & Leroy 2024). By far the most important molecular gas tracer for observers is CO. The lowest rotational transition, CO $J = 1-0$, has an energy of ≈ 5.53 K, meaning that it is easily excited in cold molecular gas and clouds that are ~ 10 K (Bolatto et al. 2013). The critical density for CO $J = 1-0$ is $n_{\rm crit} \approx 2200$ cm^{-3} (Bolatto et al. 2013); however, it is commonly excited in even lower gas densities as it is optically thick (Shirley 2015).

The molecular gas mass, $M_{\rm mol}$, is estimated via $M_{\rm mol} = \alpha_{\rm CO} L_{\rm CO}$, where $L_{\rm CO}$ is the CO luminosity in K km s^{-1} pc^2 (Bolatto et al. 2013) and $\alpha_{\rm CO}$ is the well-known "CO-to-H_2 conversion factor". There has been much discussion in recent years about the conversion factor and its dependencies using observations in the Milky Way (Lee et al. 2014; Chen et al. 2015; Sofue & Kohno 2020; Kohno & Sofue 2024b,a), observations in extragalactic systems (Bothwell et al. 2014; Carleton et al. 2017; Cormier et al. 2018; Chiang et al. 2021; Jiao et al. 2021; Teng et al. 2022, 2023; Hunt et al. 2023; Yasuda et al. 2023; den Brok et al. 2023; Pereira-Santaella et al. 2024; Chiang et al. 2024; Lee et al. 2024; Teng et al. 2024; He et al. 2024), and through modeling and simulations (Gong et al. 2018, 2020; Keating et al. 2020; Borchert et al. 2022; Hu et al. 2022). In disk galaxies, like the Milky Way, the canonical value is $\alpha_{CO} = 4.35$, which includes a factor of 1.36 for helium (Bolatto et al. 2013). In galaxies with high gas surface densities, like U/LIRGs, α_{CO} tends to decrease (Downes et al. 1993; Solomon et al. 1992; Papadopoulos et al. 2012) and the canonical value, including helium, is $\alpha_{CO} = 1.1$ (Bolatto et al. 2013; He et al. 2024).

1.4.3 Molecular gas in U/LIRGs

The molecular gas content of the ISM in U/LIRGs can be strikingly different than that of normal galaxies. U/LIRGs have higher gas surface densities with molecular gas masses $\gtrsim 10^{10} M_{\odot}$ (Sanders et al. 1991; Downes et al. 1993; Downes & Solomon 1998). The densities of the entire molecular medium in U/LIRGs are likely high enough to excite CO ubiquitously (Wilson et al. 2019). The CO-to-H_2 conversion factor is lower in U/LIRGs so a higher L_{CO} is expected for the same molecular gas mass (Downes et al. 1993; Downes & Solomon 1998; Solomon et al. 1997). Additionally, higher line widths will lead to lower values of α_{CO} in starbursts and U/LIRGs (Bolatto et al. 2013; He et al. 2024). Mergers and interactions can trigger incredible starbursts which power the enormous IR luminosities observed in these systems (Solomon et al. 1997; Ueda et al. 2021). Empirical scaling relations have been observed linking the molecular gas content to star formation rate in both normal star-forming galaxies and U/LIRGs (see Sections 1.6.2 and 1.6.2). Additionally, large circumnuclear disks of molecular gas drive mass accretion onto supermassive black holes in the centres of U/LIRGs and power strong IR luminous AGN (e.g., Izumi et al. 2016).

Molecular gas in U/LIRGs can pervade the space between GMCs such that the intercloud medium is molecular (Solomon et al. 1997; Downes & Solomon 1998). For example, in the nearby merger, NGC 3256, Brunetti & Wilson (2022) find a "smooth" ISM with molecular cloud properties in this LIRG that differ than those of normal galaxies. The GMCs in this galaxy have gas surface densities as high as $5500 M_\odot$ pc^2, velocity dispersions ($\leq$ 200 km s^{-1}) well above those observed for normal spirals, and turbulent pressures of $10^5 - 10^{10}$ K cm^{-3} (Brunetti et al. 2021). To fully understand the molecular gas properties in U/LIRGs, observations of a large sample of galaxies at high resolution, like what was done for normal galaxies with PHANGs, would be a major advance.

1.5 Dense molecular gas

1.5.1 Commonly used dense gas tracers

The dense phase of molecular gas is typically traced by molecules with higher dipole moments and critical densities. The usual threshold for what is consider "dense" is $n_{H_2} \gtrsim 10^4$ cm^{-3}, and observers use molecules like hydrogen cyanide (HCN), the formyl cation (HCO^+), and carbon monosulfide (CS) as tracers (Nguyen-Q-Rieu et al. 1989; Gao & Solomon 2004a; Wu et al. 2010; García-Burillo et al. 2012; Kennicutt & Evans 2012). By far the most commonly used dense gas tracer for external galaxies is HCN. Before 2004, roughly 30 galaxies had been detected in HCN (Nguyen-Q-Rieu et al. 1989; Nguyen et al. 1992; Henkel et al. 1990; Solomon et al. 1992; Helfer & Blitz 1993; Aalto et al. 1995; Curran et al. 2000; Israel 1992; Sorai et al. 2002; Kuno et al. 2002). Gao & Solomon (2004a) published an HCN survey of 53 galaxies and paved the way for future dense gas studies in the Milky Way and other galaxies.

HCN $J = 1 - 0$ has an excitation energy of 4.25 K[2] and a critical density of $n_{\rm crit} \gtrsim 10^5$ (Shirley 2015). Collisional excitation of HCN with H_2 occurs in the presence of molecular gas close to or above this critical density, but subthermal excitation of HCN can also occur due to IR pumping from strong X-ray emission near an AGN (Kohno 2005; Izumi et al. 2013, 2016). In U/LIRGs, HCN is expected to have higher temperatures, densities, and line widths than in spiral galaxies (Solomon et al. 1992; Downes & Solomon 1998; Gao & Solomon 2004b,a; Graciá-Carpio et al. 2006, 2008; Privon et al. 2015; Imanishi et al. 2019). HCN is also thought to be optically thick (Nguyen et al. 1992; Wild et al. 1992; Jiménez-Donaire et al. 2017), with optical depths of $\tau = 2 - 11$ (Jiménez-Donaire et al. 2017). Gao & Solomon (2004b) established the

[2]https://home.strw.leidenuniv.nl/~moldata/

$\alpha_{\rm HCN}$ conversion factor to convert HCN $J = 1-0$ luminosity to dense gas mass as $M_{\rm dense} = \alpha_{\rm HCN} L_{\rm HCN}$. They determined $\alpha_{\rm HCN} = 10$, which becomes 13.6 after including the Helium factor. Variations in $\alpha_{\rm HCN}$ have been observed or predicted theoretically to vary with environmental factors (Graciá-Carpio et al. 2008; Vega et al. 2008; García-Burillo et al. 2012; Usero et al. 2015; Onus et al. 2018; Jones et al. 2023), including a dependence on UV radiation field strength (Shimajiri et al. 2017).

The fraction of dense molecular gas, $f_{\rm dense}$, is commonly estimated using the HCN/CO intensity ratio (Gao & Solomon 2004b). High dense gas fractions are observed in the Central Molecular Zone of the Milky Way (e.g., Mills et al. 2018), the centres of other galaxies (e.g., Bešlić et al. 2021; Li et al. 2024), U/LIRGs (e.g., (Sanders & Mirabel 1996; Baan et al. 2008; Juneau et al. 2009; Papadopoulos et al. 2012; Pérez-Torres et al. 2021)), and galaxies at high redshift ($z > 1$, e.g., Gowardhan et al. 2017; Oteo et al. 2017). Simulations have shown that $f_{\rm dense}$ will increase once a galaxy has experienced a merger event (Juneau et al. 2009; Moreno et al. 2019). In contrast, however, observational work does not agree that $f_{\rm dense}$ has any connection with merger stage (e.g., Ueda et al. 2021). Post-starburst galaxies, often the result of a merger, have been discovered to have a distinctly large molecular gas reservoir (French et al. 2015). However, follow up studies of post-starbursts in dense gas tracers like HCN has shown that they may not have much, if any, dense molecular gas despite their large gas reservoir (French et al. 2018). More studies of post-starbursts and mergers are required to understand $f_{\rm dense}$ and the dense gas content in these complicated systems.

1.5.2 The Cyanide Radical

Recently, Wilson et al. (2023) observed a nearly constant ratio between the HCN $J = 1-0$ and the cyanide radical (CN) $N = 1-0$ lines in a sample of 9 nearby star-forming galaxies. The ratio is constant across nearly 3 orders of magnitude in both molecular gas (Figure 1.5, left) and star formation rate surface density (Figure 1.5, right) on 30 – 400 pc scales. Although there is a standard deviation of 0.20 in the average line ratio of CN/HCN $= 0.86 \pm 0.07$, it is clear that CN and HCN are likely tracing a similar component of the dense ISM at these spatial scales. Wilson (2018) used Cycle 0 ALMA observations to measure the CN/CO intensity ratio in 8 galaxies and found variations both within and between galaxies, including higher ratios in regions/galaxies containing starbursts.

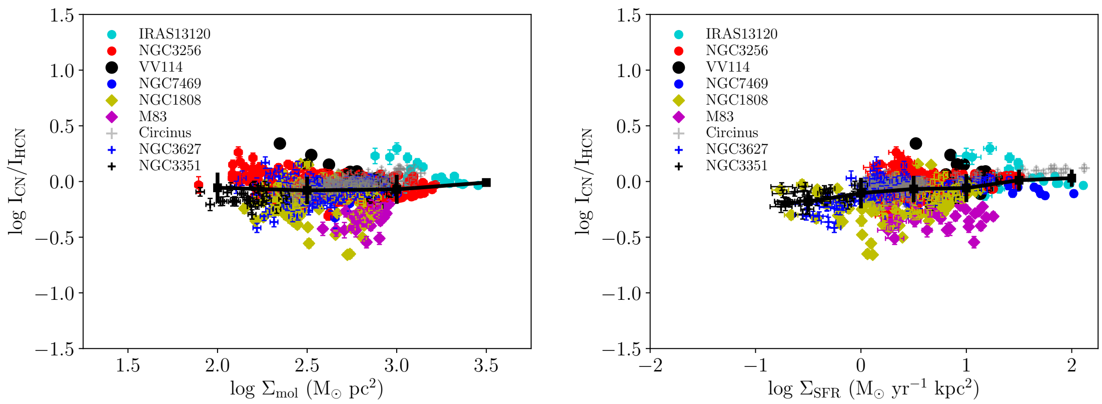

FIGURE 1.5: Figure 2 from Wilson et al. (2023) showing the CN/HCN intensity ratio as a function of molecular gas (*left*) and star formation rate (*right*) surface densities in a sample of 9 resolved normal and star-forming galaxies. A nearly constant ratio is seen over 3 orders of magnitude in both $\Sigma_{\rm mol}$ and $\Sigma_{\rm SFR}$, with a slight positive trend in $\Sigma_{\rm SFR}$ versus $I_{\rm CN}/I_{\rm HCN}$. The black lines show the mean and standard deviation in bins of 0.5 in log space. Image credit: Wilson et al. (2023).

These works together stand as the motivation for my thesis project focusing on using CN to measure the properties of dense molecular gas.

Early detections of CN in the Milky Way and other galaxies began toward the end of the 20th century (Henkel et al. 1990; Fuente et al. 1993, 1995; Greaves & Church 1996; Bachiller et al. 1997; Rodriguez-Franco et al. 1998). The critical density of CN $N = 1-0$ is very similar to that of HCN $J = 1-0$, with $n_{\rm crit} \gtrsim 10^5$ cm^{-3} (Shirley 2015), and the excitation of the $N = 1-0$ transition line is 5.4 K. The CN/HCN abundance ratio is theoretically predicted to vary with UV radiation field, e.g., in a PDR, peaking near the edge of clouds where the UV radiation field and molecular dissociation is the highest and decreasing with higher cloud depths (Sternberg & Dalgarno 1995; Rodriguez-Franco et al. 1998; Boger & Sternberg 2005). The first observations of the CN/HCN intensity ratio were converted to an abundance ratio using chemical models and suggested that the CN/HCN abundance ratio was good tracer of UV radiation field in PDRs (Fuente et al. 1993, 1995; Greaves & Church 1996). This is in constrast with the recently observed constant CN/HCN intensity ratio (Figure 1.5) with star formation surface density, which is roughly tracing UV radiation field strength (Wilson et al. 2023).

CN formation occurs through a few different chemical reaction pathways. CN is primarily formed by photodissociation of HCN by energetic photons (Aalto et al. 2002; Boger & Sternberg 2005; Chapillon et al. 2012) and the reactions HCN + ν $\rightarrow$ CN + H or HCN + cosmic ray $\rightarrow$ CN + H. Neutral-neutral reactions of N + C_2 $\rightarrow$ CN + C and N + CH $\rightarrow$ CN + H can occur toward the edges of molecular clouds in PDRs (Aalto et al. 2002; Boger & Sternberg 2005). CN can form through two-step reactions as OH + N $\rightarrow$ NO + H followed by NO + C $\rightarrow$ CN + O (Boger & Sternberg 2005). Finally, dissociative recombination can create CN as $H_2CN^+ + e^- \rightarrow CN + H_2$ (Boger & Sternberg 2005).

It is also important to consider CN destruction. When the radiation field is particularly strong, CN can also dissociate like HCN and become CN + ν $\rightarrow$ C + N (Boger & Sternberg 2005). When shielded within a cloud, neutral-neutral reactions can remove CN as CN + N $\rightarrow$ N_2 + C and CN + O $\rightarrow$ CO + N (Boger & Sternberg 2005).

X-ray radiation fields and cosmic rays may also play a role in changing the CN abundance in the ISM. CN can preferentially form in XDRs (Krolik & Kallman 1983; Lepp & Dalgarno 1996; Meijerink & Spaans 2005; Meijerink et al. 2007; García-Burillo et al. 2010), although in regions of very high temperature ($>$ 800 K) CN becomes depleted as it begins to form HCN through CN + H_2 $\rightarrow$ HCN + H (Harada et al. 2010, 2013). Higher cosmic ray ionization rates also support an increase in CN abundance, either by dissociation of HCN or by creating a larger supply of atoms and molecules required in the CN formation reaction pathways (Boger & Sternberg 2005; Bayet et al. 2011; Aladro et al. 2013).

In Chapter 3, I introduce the literature surrounding observations of CN using ALMA and other telescopes. It has become a target molecule for observations of molecular gas in spirals, starbursts, AGN, molecular outflows, early type galaxies, U/LIRGs, mergers, merger remnants, and is even detected in absorption lines. My thesis focuses on using new and archival ALMA observations of CN to investigate the dense molecular gas in nearby U/LIRGs.

1.6 Star Formation

The process of star formation is a direct result of gravitational forces within molecular clouds overcoming the supporting pressures within the cloud, leading to collapse and core contraction, compressing the gas and igniting a star. The physical process which govern how stars form in galaxies, however, span a range of scales and environments.

Inflows from the circumgalactic medium (CGM) surrounding galaxies replenishes the gas reservoir for a galaxy on the largest scales (Dekel & Birnboim 2006; Tumlinson et al. 2017), which then cools to form neutral gas in the ISM. The gas condenses further into molecular clouds and filaments (André et al. 2010; Pillsworth & Pudritz 2024), gravitationally unstable cores (André et al. 2014), and, eventually, stars and planets. The initial fuel for star formation begins as atomic H gas, which makes up a significant fraction of the cold gas mass in the ISM (e.g., Saintonge et al. 2017). As the H gas cools and condenses, it interacts with grains of dust to form H_2 molecules (Tielens 2005). The molecular gas, then, becomes the reservoir from which stars form. The different phases and components of the ISM cycle through one another, from atomic gas into molecular gas, which further condenses into dense cores which go on to form stars. The stars then produce ionizing radiation, radiation pressures, stellar winds, and eventually supernovae and SNRs as they evolve. These processes inject energy and matter back into the ISM, enhancing the metallicity and rejuvenating the ISM. The entire process controls the evolution and future cycle of a galaxy and is often referred to as the "baryon cycle" in galaxies.

In IR-bright galaxies like starbursts and U/LIRGs, a significant fraction of the IR power comes from star formation. Merging galaxies, which are often ULIRGs, have been shown to have higher SFRs than their normal galaxy counterparts (Ellison et al. 2013a,b; Pérez-Torres et al. 2021). Ellison et al. (2013b) find that both central star formation enhancement and starbursts peak in a post-merger sample of ~ 100 galaxies compared to a test sample of > 10000 galaxies. Clearly, gas-rich mergers and galaxy interactions can lead to enhanced star formation rates and properties.

While observations of star formation rates and star formation tracers are not a direct focus of this thesis, Chapter 4 uses measurements of star formation rates using the IR and radio continuum tracers. I will briefly introduce some of the tracers used in this research, before discussing empirically observed star formation scaling relations.

1.6.1 Tracers of star formation

Observationally, star formation can be measured either by counting the number of very young stars, or inferred by measuring the radiation emitted from young stars. This thesis uses SFRs measured by two observational tracers: the IR luminosity and the radio continuum. I briefly introduce these two diagnostics, as well as give a short discussion of star formation traced by UV and Hα photons.

Infrared luminosity

One of the best star formation tracers is the IR luminosity from $8 - 1000\ \mu$m photons. IR emission originates from dust that has been heated by massive star formation (Mooney & Solomon 1988; Kennicutt 1998a; Kennicutt & Evans 2012) and traces SFR on timescales of $100 - 200$ Myr (Kennicutt & Evans 2012). IR is a particularly good tracer of SFR in dusty U/LIRGs as the amount of dust means that nearly all of the starlight will be absorbed by dust grains and re-emitted. Telescopes like IRAS, the Spitzer Space Telescope, the Herschel Space Observatory, and most recently JWST have revolutionized observations of IR emission and the ability to estimate SFRs locally and at high redshift. A major sources of uncertainty in IR-SFR estimates, particularly in U/LIRGs, is the presence of an AGN which can contribute significantly to the IR luminosity and therefore result in an overestimate of the actual SFR.

Radio continuum

Radio continuum originates from free-free electron emission from the ionized regions surrounding recently formed stars and also from the synchrotron radiation ($\nu < 5$ GHz) coming from SNRs (Murphy et al. 2011; Kennicutt & Evans 2012). Multi-frequency measurements are often necessary to separate the star formation and SNe components of the radio continuum, often referred to as "thermal" and "non-thermal" components (Murphy et al. 2011). Thermal radio continuum traces recent star formation in the last ~ 10 Myr (Murphy et al. 2011; Arango-Toro et al. 2023), and is useful as a tracer in U/LIRGs as it is not attenuated by dust in the ISM. Two major sources of uncertainty in radio continuum SFR estimates in U/LIRGs come from non-thermal contributions from synchrotron emission originating around AGN and contamination from dust emission. In NGC 3256, Wilson et al. (2019) estimate that the dust contribution to the 93 GHz (106 GHz) radio continuum was 10% (15%). In the highly obscured dusty system Arp 220, Sakamoto et al. (2017) found the dust contribution to the 3 mm continuum was as high as 47% in one of the nuclei.

UV and Hα

UV radiation is emitted from young, massive stars and is therefore one of the best observational ways to directly trace the number of stars forming in galaxies (Kennicutt & Evans 2012). However, UV photons are also susceptible to absorption by interstellar dust grains and other baryonic matter in the ISM. Therefore, the UV emission from star formation is often heavily obscured and sometimes entirely blocked. Space telescopes, like the Galaxy Evolution Explorer (GALEX; Martin et al. 2005), and the Canadian-made UV Imaging Telescope (UVIT) on AstroSat, observe UV light and allow for an estimate of a global SFR for UV bright galaxies, although with the uncertainty that calibration factors require an intrinsic understanding of the extinction of UV light in the ISM (Kennicutt & Evans 2012).

Hα is a transition in the Balmer series and comes from an electron transitioning from $n = 3 \rightarrow n = 2$ and emitting a photon at 656.28 nm. Hα emission is observed primarily from HII regions which have been ionized by the UV photons of recently formed massive stars. It is therefore one of the best tracers of recent star formation, on timescales of ~ 10 Myrs (e.g., Glazebrook et al. 1999). Hα is primarily affected by dust attenuation and non-star formation related contributions from the diffuse ionized gas (DIG) in the WNM (Haffner et al. 2009). The DIG emission must be removed before estimating the SFR using Hα (Oey et al. 2007; Tomičić et al. 2021). The dust attenuation is often estimated by using the "Balmer decrement", comparing the Hα and Hβ ($n = 4 \rightarrow n = 2$) emission (Kennicutt & Evans 2012). Although it is a well-calibrated SFR tracer both locally and at high-redshift (Shivaei et al. 2015; Tacchella et al. 2022), Hα is less useful as an SFR tracer in U/LIRGs because of the large amount of dust and attenuation in these galaxies.

1.6.2 Observed star formation laws

The first theoretical scaling relation for a connection between gas and star formation was proposed by Schmidt (1959), who suggested that SFR volume density should be a power law of the gas volume density, $\rho_{\rm SFR} \propto \rho_{\rm gas}^N$, with an index of $N = 2$. Incorporating the free-fall time, $t_{\rm ff}$, which is the time it takes for a cloud to completely collapse under its own self-gravity, the relation becomes $\rho_{\rm SFR} \propto \rho_{\rm gas}/t_{\rm ff} \propto \rho_{\rm gas}^{1.5}$, since $t_{\rm ff} \propto \rho_{\rm gas}^{-1/2}$. The gas and SFR volume densities can be converted to surface densities by an assumption made

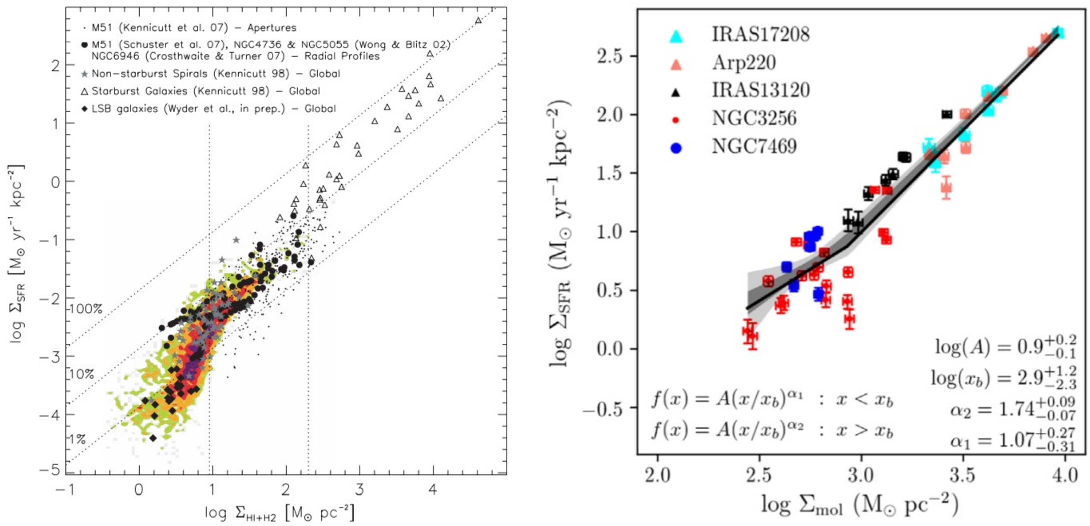

FIGURE 1.6: *Left*: Figure 15 from Bigiel et al. (2008) showing the combined atomic and molecular gas ($\Sigma_{gas} = \Sigma_{HI} + \Sigma_{H_2}$) Kennicutt-Schmidt (KS) relation in a sample of spiral and starburst galaxies. Vertical dotted lines show transitions from atomic to molecular gas (left) and normal to starburst regimes (right). Diagonal dotted lines represent different values of star formation efficiency. Image credit: Bigiel et al. (2008). *Right*: Figure 1 from Wilson et al. (2019) showing the resolved KS relation in a sample of five U/LIRGs. The data are fit with a broken power law pivoting around $\Sigma_{mol} = 10^3\ M_\odot\ \mathrm{pc}^{-2}$. The power law index for Σ_{mol} is higher (1.74) than expected for normal and starburst galaxies (~ 1.4). Image credit: Wilson et al. (2019).

about the gas scale height (e.g., Wilson et al. 2019), leading to the well-known "Schmidt relation":

$$\Sigma_{SFR} \propto A\Sigma_{gas}^{N}. \tag{1.12}$$

A is a constant and N is the power-law index which, as I will describe, may vary between normal galaxies and star-forming galaxies like mergers and U/LIRGs (Wilson et al. 2019; Kennicutt & De Los Reyes 2021).

Kennicutt (1998b) expanded upon the Schmidt relation with observations in disk and starburst galaxies of molecular gas traced by CO and SFR traced by Hα and measured the empirical "Kennicutt-Schmidt (KS) law" to have a power-law index of $N = 1.4 \pm 0.15$. Since then, the KS law has been confirmed with observations in galaxies of all types, including both the atomic and molecular gas contributions to $\Sigma_{HI} + \Sigma_{H_2} = \Sigma_{gas}$ (Bigiel et al. 2008; Schruba et al. 2011; de los Reyes & Kennicutt 2019; Kennicutt & De Los Reyes 2021). Figure 1.6 (left) shows the KS law measured by Bigiel et al. (2008). A transition can be seen around $\Sigma_{\rm gas} = 10\ M_\odot\ {\rm pc}^{-2}$ where the gas changes from atomic to molecular. The fit lines in Figure 1.6 (left) are measurements of the star formation efficiency (SFE), defined here as SFE $= \Sigma_{\rm SFR}/\Sigma_{\rm gas}$, which is the inverse of the gas depletion time (Bigiel et al. 2008). The depletion time is defined as the time it would take for the galaxy to completely deplete its gas reservoir due to star formation. An average SFE per free-fall time is of order 1%, although this is uncertain and variations are seen on multiple scales and in different galaxies (e.g., Bigiel et al. 2008; Leroy et al. 2008; Daddi et al. 2010; Genzel et al. 2010; Wilson et al. 2019; Kennicutt & De Los Reyes 2021). For example, in a sample of 5 U/LIRGs, Wilson et al. (2019) show that the KS law is best fit by a broken power law (Figure 1.6, right), where gas surface densities above $\Sigma_{\rm mol} = 10^3 M_\odot\ {\rm yr}^{-1}$ have an index of $N = 1.74$ and mean SFE per free-fall time of $\sim 5-7\%$. The observed KS scaling relations imply that the process of star formation and the efficiency with which gas converts to stars is inherently different in U/LIRGs compared to normal galaxies (Daddi et al. 2010; Genzel et al. 2010; Wilson et al. 2019; Kennicutt & De Los Reyes 2021).

Dense gas relations to star formation

As I discussed is Section 1.5, the densest molecular gas in the ISM is traced by molecular line emission from molecules like HCN, HCO^+, CS, and CN. A nearly linear scaling relation was found by Gao & Solomon (2004b) between HCN luminosity and IR luminosity including both normal galaxies and U/LIRGs in their sample (Figure 1.7, left), indicating that there is perhaps a more fundamental law governing star formation than the KS law. The empirical relation between HCN and IR luminosities has since been confirmed in individual molecular clouds, spiral galaxies, U/LIRGs, and in higher redshift galaxies (e.g., Wu et al. 2005; Graciá-Carpio et al. 2006, 2008; García-Burillo et al. 2012; Jiménez-Donaire et al. 2019). In Figure 1.7 (right), I show a figure from Jiménez-Donaire et al. (2019) which compiles nearly all HCN and IR luminosity measurements from the literature onto one relation. A clear linear trend between dense gas and SFR is observed.

The scatter in the dense gas KS relation can be attributed to differences in the star formation efficiency of dense gas, defined as $\mathrm{SFE}_{\rm dense} = \Sigma_{\rm SFR}/\Sigma_{\rm dense}$. Jiménez-Donaire

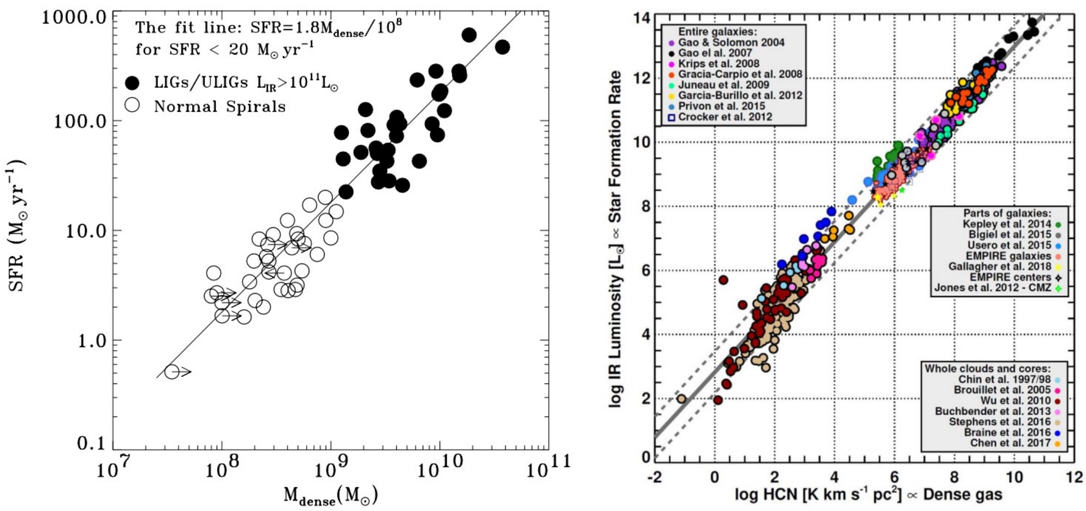

FIGURE 1.7: Dense gas mass correlates with star formation rate. *Left*: Figure 6 from Gao & Solomon (2004b) showing SFR as a function of dense molecular gas mass in a sample of spirals (open circles) and U/LIRGs (black circles). The black line is linear fit to the data. Image credit: Gao & Solomon (2004b). *Right*: Figure 13 from Jiménez-Donaire et al. (2019) showing a literature compilation of IR and HCN luminosity measurements in clumps and cores, clouds, GMCs, low-metallicity galaxies, and extragalactic systems. The data points and their original references are described on the plot, and the gray line is the mean IR-to-HCN ratio of 776 $L_\odot$/(K km^{-1} pc^2) with a 1σ rms scatter. Image credit: Jiménez-Donaire et al. (2019).

et al. (2019) find that SFE$_{\text{dense}}$ varies on kiloparsec scales in their sample of 9 nearby star-forming galaxies. The authors attribute the variations to local variations in gas pressure and environment, e.g., stellar and gas surface densities. Variations have also been observed for SFE$_{\text{dense}}$ on resolved scales using ALMA and other telescopes in normal and star-forming galaxies (e.g., Gallagher et al. 2018; Bemis & Wilson 2019, 2023; Neumann et al. 2023). Both Graciá-Carpio et al. (2008) and García-Burillo et al. (2012) show that the SFE$_{\text{dense}}$ is a factor of 2 – 3 higher in U/LIRGs compared to normal galaxies. García-Burillo et al. (2012) indicate that dense gas depletion times in their U/LIRG sample are ~ 14 Myr, compared to ~ 50 Myr in normal galaxies. Clearly, the star formation processes in the dense gas of U/LIRGs are different than those in normal galaxies.

1.7 The Atacama Large Millimeter/Submillimeter Array

1.7.1 Interferometry and radio astronomy

For submillimeter, millimeter, and radio wavelengths (corresponding to $\sim$ 10 MHz to $\sim$ 1 THz frequencies; Condon & Ransom 2016), high angular resolution observations require incredibly large telescope diameters. This is because Θ, the angular resolution in radians (1 radian = 206265”), is given by

$$\Theta \approx 1.22\,\frac{\lambda}{D}, \tag{1.13}$$

where λ is the wavelength and D is the diameter of the telescope (Carroll & Ostlie 2017). In order to achieve an angular resolution of 1” at a wavelength of 1 mm, which physically corresponds to $\sim$ 50 pc at a distance of $\sim$ 10 Mpc, one would need a telescope of diameter $\sim$ 250 m. A telescope of this size would be incredibly challenging, if not impossible, to build logistically. Therefore, millimeter and radio astronomers use an array of radio dishes in an interferometer. Two examples of modern interferometric telescope arrays are the VLA and ALMA.

ALMA is one of the most powerful, modern, ground-based telescopes on Earth. It is run by an international consortium of countries from three major regions: North America, Europe, and East Asia. As a funding partner, Canada has contributed greatly to the success of ALMA by contributing financially, supporting with hardware and instrumentation on the telescopes and array itself, and hosting a large community of scientists performing state-of-the-art research with ALMA data. ALMA construction began in 2004, with first light achieved in 2011, and cost in excess of 1.5 billion USD. Since 2011, ALMA has conducted more than 75000 observations for more than 4500 projects producing $\sim$ 4000 publications.

1.7.2 The ALMA site

The ALMA site was chosen because of its altitude (above most of the precipital water vapour contamination to millimeter observations) and dry and desert-like climate. Accessing the ALMA site is challenging, and only local engineers and workers typically

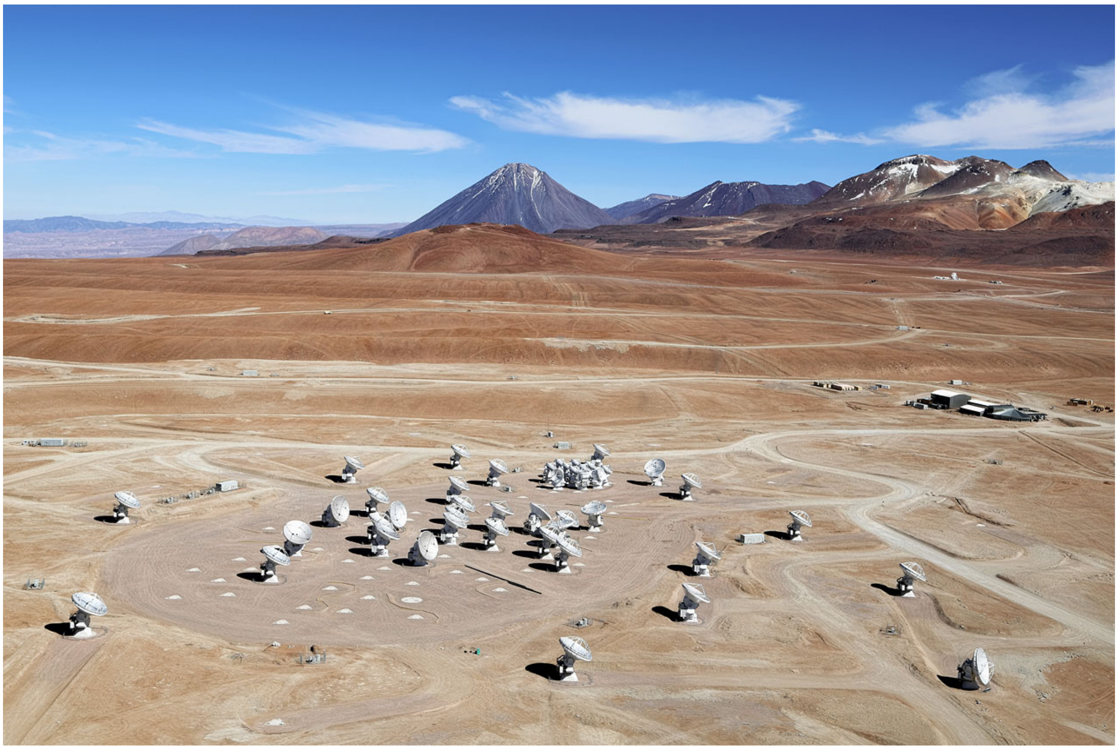

FIGURE 1.8: The ALMA telescope array situated on the Chajnantor plateau in the Atacama desert in northern Chile. The ALMA site is perfect for submillimeter observations as it is far from light and radio pollution, in a dry desert climate, and at an altitude of 5000 m, significantly reducing the precipital water vapour in the atmosphere. Image credit: Clem & Adri Bacri-Normier (wingsforscience.com)/European Southern Observatory (ESO).

visit the telescope site itself. ALMA sits at an altitude of 5000 m in the Chajnantor plateau in the Atacama Desert in northern Chile (Figure 1.8), and has an annual average precipital water vapour column of just 1.1 mm (Bustos et al. 2014). The local Indigenous population of the Chajnantor plateau are the Atacameño people, known as Likan Antai.

1.7.3 The ALMA telescopes, arrays, and archive

ALMA is a radio interferometer with many antennae which can be moved and set up in different configurations to achieve various angular resolutions. ALMA makes use of 66 individual telescope dishes, which are split between 12 m diameters (54 dishes) and 7 m diameters (12 dishes). Fifty of the 12 m dishes make up ALMA's "main array", while the 7 m dishes are known as the "Atacama Compact Array" (ACA). ALMA has an additional small grouping of four 12 m dishes known as the "Total Power" (TP) array, which effectively work as a single-dish telescope to provide short-spacing data missed by the two arrays. In its most compact configuration, ALMA has a baseline of $\sim$ 150 m. The most extended configuration allows a maximum baseline of 16 km. As an example, for a wavelength of 2.6 mm (that of the CO $J = 1 - 0$ transition) and the maximum baseline of 16 km, Equation 1.13 gives $\theta = 1.22 \times \frac{2.6 \text{ mm}}{16 \text{ km}} \times 206265\text{"} = 0.04\text{"}$ - unprecedented resolution at these wavelengths, comparable to HST.

The separation of individual antennae in a configuration means that arriving radio waves from different sources in the field of view have a slight time and phase delay. A powerful instrument on the back end of the telescope, known as the correlator, then converts the information into an electronic signal. The resulting observations harbour an incredible amount of data, with more than 1 PB of data stored and annual growth rates of 300 – 400 TB. One of the major challenges for ALMA and the scientific community is the sheer processing power required to store and analyze the data itself.

The science community of ALMA has access to a public archive[3] where, after a proprietary period for Primary Investigators, data becomes available for users to conduct their own science projects. The ALMA archive has hubs in each of the three main partner regions and is continually being upgraded to better store the incredible amount of data and facilitate downloading, calibrating, and providing science ready data products. In Chapters 3 and 4 of this thesis, I harness the power of the ALMA archive and all of my observations and data products are obtained from a combination of previously observed ALMA projects. The archive is an amazing tool for the science community where observers can search for data which answers their science questions without needing to rely on the oversubscribed proposal application for new ALMA observations and telescope time.

1.8 This thesis

The broad goals of this thesis are to measure the physical and chemical properties of dense molecular gas in the ISM of U/LIRGs. The instrument I use is the ALMA telescope and I target the CN, HCN, and CO molecules as my molecular tracers. My hypothesis is that observers can use CN in a similar way to HCN to study dense molecular gas,

[3] https://almascience.nrao.edu/aq/

particularly in extreme star-forming systems, but that the underlying connection between CN and HCN will uncover the gas conditions in response to the presence of PDR and XDR chemistry. This thesis will explore three main science questions:

1. What is the utility of CN as a tracer of dense molecular gas? What are the implications of CN as a tracer moving forward?

2. How does the dense molecular gas differ in LIRGs compared to ULIRGs?

3. How does the dense gas fraction in U/LIRGs connect to global galaxy properties?

The rest of this thesis contains four additional chapters, which are organized as follows.

In Chapter 2, I discuss the results of a multi-transition line survey of CN and HCN in three U/LIRGs: NGC 3256, NGC 7469, and IRAS 13120-5453. I find variations in the intensity ratios of the lines for the individual molecules, as well as between the two molecules. In particular, the variations are associated with regions of enhanced star formation in starbursts and the presence of an AGN.

In Chapter 3, I discuss the observed CN/CO intensity ratio in 16 U/LIRGs. Observations were compiled from the ALMA archive for CN and CO on 500 pc scales in a sample containing starbursts, AGN, and mergers. I find higher CN/CO intensity ratios in ULIRGs compared to LIRGs. The larger spread in CN/CO ratios in the LIRGs is attributed to the different galaxy environments, e.g., disk regions, starbursts, and AGN, while the ULIRGs show less of a spread in CN/CO ratios as they are more compact. I find higher CN/CO intensity ratios in nuclear regions compared to the disk. Finally, I use the hyperfine structure of CN to estimate the optical depth.

In Chapter 4, I use the measured CN/CO intensity ratios from Chapter 3 to estimate the dense gas fraction and compare it with global galaxy properties. I convert CN/CO to a global dense gas fraction and find that it correlates with global SFR traced by both infrared and radio continuum. Global dense gas fractions do not correlate with merger stage or global hard X-ray luminosity. I measure the dense gas fraction at the location of peak hard X-ray emission and find that it correlates with global hard X-ray luminosity. The peak dense gas fraction does not correlate with SFR or merger stage.

In Chapter 5, I summarize my results and synthesize the discussion from Chapters 2, 3, and 4. I highlight the main findings of this thesis and discuss the implications of my work in the broader dense gas community. Finally, I motivate future work and present preliminary results measuring CN and HCN abundances in NGC 3256, NGC 7469, and IRAS 13120 using RADEX modeling.

Bibliography

Aalto S., Booth R. S., Black J. H., Johansson L. E. B., 1995, A&A, 300, 369

Aalto S., Polatidis A. G., Hüttemeister S., Curran S. J., 2002, A&A, 381, 783

Aladro R., et al., 2013, A&A, 549, A39

Almeida A., et al., 2023, ApJS, 267, 44

André P., 2017, Comptes Rendus Geoscience, 349, 187

André P., et al., 2010, A&A, 518, L102

André P., Di Francesco J., Ward-Thompson D., Inutsuka S. I., Pudritz R. E., Pineda J. E., 2014, in Beuther H., Klessen R. S., Dullemond C. P., Henning T., eds, Protostars and Planets VI. pp 27–51 (arXiv:1312.6232), doi:10.2458/azu_uapress_9780816531240-ch002

Arango-Toro R. C., Ciesla L., Ilbert O., Magnelli B., Jiménez-Andrade E. F., Buat V., 2023, A&A, 675, A126

Armus L., et al., 2009, PASP, 121, 559

Armus L., et al., 2023, ApJ, 942, L37

Arp H., 1966, ApJS, 14, 1

Arp H. C., Madore B., 1987, A catalogue of southern peculiar galaxies and associations. Cambridge University Press

Baan W. A., Henkel C., Loenen A. F., Baudry A., Wiklind T., 2008, A&A, 477, 747

Bachiller R., Fuente A., Bujarrabal V., Colomer F., Loup C., Omont A., de Jong T., 1997, A&A, 319, 235

Barcos-Muñoz L., et al., 2017, ApJ, 843, 117

Barnes J. E., 2002, MNRAS, 333, 481

Bayet E., Williams D. A., Hartquist T. W., Viti S., 2011, MNRAS, 414, 1583

Bemis A., Wilson C. D., 2019, AJ, 157, 131

Bemis A. R., Wilson C. D., 2023, ApJ, 945, 42

Bešlić I., et al., 2021, MNRAS, 506, 963

Bigiel F., Leroy A., Walter F., Brinks E., de Blok W. J. G., Madore B., Thornley M. D., 2008, AJ, 136, 2846

Binney J., Merrifield M., 1998, Galactic Astronomy. Princeton University Press

Binney J., Tremaine S., 2008, Galactic Dynamics: Second Edition. Princeton University Press

Boger G. I., Sternberg A., 2005, ApJ, 632, 302

Bolatto A. D., Wolfire M., Leroy A. K., 2013, ARA&A, 51, 207

Borchert E. M. A., Walch S., Seifried D., Clarke S. D., Franeck A., Nürnberger P. C., 2022, MNRAS, 510, 753

Bothwell M. S., et al., 2014, MNRAS, 445, 2599

Brunetti N., Wilson C. D., 2022, MNRAS, 515, 2928

Brunetti N., Wilson C. D., Sliwa K., Schinnerer E., Aalto S., Peck A. B., 2021, MNRAS, 500, 4730

Bustos R., Rubio M., Otárola A., Nagar N., 2014, PASP, 126, 1126

Carleton T., et al., 2017, MNRAS, 467, 4886

Carroll B. W., Ostlie D. A., 2017, An introduction to modern astrophysics, Second Edition. Cambridge University Press

Chapillon E., Guilloteau S., Dutrey A., Piétu V., Guélin M., 2012, A&A, 537, A60

Chen B. Q., Liu X. W., Yuan H. B., Huang Y., Xiang M. S., 2015, MNRAS, 448, 2187

Chevance M., Krumholz M. R., McLeod A. F., Ostriker E. C., Rosolowsky E. W., Sternberg A., 2023, in Inutsuka S., Aikawa Y., Muto T., Tomida K., Tamura M., eds, Astronomical Society of the Pacific Conference Series Vol. 534, Protostars and Planets VII. p. 1 (`arXiv:2203.09570`), doi:10.48550/arXiv.2203.09570

Chiang I.-D., et al., 2021, ApJ, 907, 29

Chiang I.-D., et al., 2024, ApJ, 964, 18

Condon J. J., Ransom S. M., 2016, Essential Radio Astronomy. Princeton University Press

Cormier D., et al., 2018, MNRAS, 475, 3909

Cox D. P., 2005, ARA&A, 43, 337

Cox D. P., Smith B. W., 1974, ApJ, 189, L105

Curran S. J., Aalto S., Booth R. S., 2000, A&AS, 141, 193

Daddi E., et al., 2010, ApJ, 714, L118

Dekel A., Birnboim Y., 2006, MNRAS, 368, 2
Díaz-Santos T., et al., 2017, ApJ, 846, 32
Downes D., Solomon P. M., 1998, ApJ, 507, 615
Downes D., Solomon P. M., Radford S. J. E., 1993, ApJ, 414, L13
Draine B. T., 2003, ARA&A, 41, 241
Ellison S. L., Patton D. R., Mendel J. T., Scudder J. M., 2011, MNRAS, 418, 2043
Ellison S. L., Mendel J. T., Scudder J. M., Patton D. R., Palmer M. J. D., 2013a, MNRAS, 430, 3128
Ellison S. L., Mendel J. T., Patton D. R., Scudder J. M., 2013b, MNRAS, 435, 3627
Fall S. M., 1979, Nature, 281, 200
Ferreira L., et al., 2024, MNRAS, 533, 2547
Forman W., Jones C., 1982, ARA&A, 20, 547
French K. D., Yang Y., Zabludoff A., Narayanan D., Shirley Y., Walter F., Smith J.-D., Tremonti C. A., 2015, ApJ, 801, 1
French K. D., Zabludoff A. I., Yoon I., Shirley Y., Yang Y., Smercina A., Smith J. D., Narayanan D., 2018, ApJ, 861, 123
Fuente A., Martin-Pintado J., Cernicharo J., Bachiller R., 1993, A&A, 276, 473
Fuente A., Martin-Pintado J., Gaume R., 1995, ApJ, 442, L33
Funk S., 2015, Annual Review of Nuclear and Particle Science, 65, 245
Gallagher M. J., et al., 2018, ApJ, 858, 90
Gao Y., Solomon P. M., 2004a, ApJS, 152, 63
Gao Y., Solomon P. M., 2004b, ApJ, 606, 271
García-Burillo S., et al., 2010, A&A, 519, A2
García-Burillo S., Usero A., Alonso-Herrero A., Graciá-Carpio J., Pereira-Santaella M., Colina L., Planesas P., Arribas S., 2012, A&A, 539, A8
Genzel R., et al., 2010, MNRAS, 407, 2091
Giovanelli R., et al., 2005, AJ, 130, 2598
Glazebrook K., Blake C., Economou F., Lilly S., Colless M., 1999, MNRAS, 306, 843
Gong M., Ostriker E. C., Kim C.-G., 2018, ApJ, 858, 16
Gong M., Ostriker E. C., Kim C.-G., Kim J.-G., 2020, ApJ, 903, 142
Gorenstein P., Tucker W. H., 1976, ARA&A, 14, 373
Goulding A. D., et al., 2018, PASJ, 70, S37
Gowardhan A., Riechers D. A., Daddi E., Pavesi R., Dannerbauer H., Carilli C., 2017,

ApJ, 838, 136
Graciá-Carpio J., García-Burillo S., Planesas P., Colina L., 2006, ApJ, 640, L135
Graciá-Carpio J., García-Burillo S., Planesas P., Fuente A., Usero A., 2008, A&A, 479, 703
Greaves J. S., Church S. E., 1996, MNRAS, 283, 1179
Haffner L. M., et al., 2009, Reviews of Modern Physics, 81, 969
Harada N., Herbst E., Wakelam V., 2010, ApJ, 721, 1570
Harada N., Thompson T. A., Herbst E., 2013, ApJ, 765, 108
He H., Wilson C. D., Sun J., Teng Y.-H., Rosolowsky E., Bemis A. R., 2024, arXiv e-prints, p. arXiv:2401.16476
Helfer T. T., Blitz L., 1993, ApJ, 419, 86
Henkel C., Whiteoak J. B., Nyman L. A., Harju J., 1990, A&A, 230, L5
Heyer M. H., Carpenter J. M., Snell R. L., 2001, ApJ, 551, 852
Heyer M., Krawczyk C., Duval J., Jackson J. M., 2009, ApJ, 699, 1092
Hopkins P. F., Cox T. J., Hernquist L., Narayanan D., Hayward C. C., Murray N., 2013, MNRAS, 430, 1901
Howell J. H., et al., 2010, ApJ, 715, 572
Hu C.-Y., Schruba A., Sternberg A., van Dishoeck E. F., 2022, ApJ, 931, 28
Hubble E. P., 1926, ApJ, 64, 321
Hunt L. K., et al., 2023, A&A, 675, A64
Imanishi M., Nakanishi K., Izumi T., 2019, ApJS, 241, 19
Israel F. P., 1992, A&A, 265, 487
Iwasawa K., et al., 2011, A&A, 529, A106
Izumi T., et al., 2013, PASJ, 65, 100
Izumi T., Kawakatu N., Kohno K., 2016, ApJ, 827, 81
Jenkins E. B., Meloy D. A., 1974, ApJ, 193, L121
Jiao Q., Gao Y., Zhao Y., 2021, MNRAS, 504, 2360
Jiménez-Donaire M. J., et al., 2017, MNRAS, 466, 49
Jiménez-Donaire M. J., et al., 2019, ApJ, 880, 127
Jones G. H., Clark P. C., Glover S. C. O., Hacar A., 2023, MNRAS, 520, 1005
Juneau S., Narayanan D. T., Moustakas J., Shirley Y. L., Bussmann R. S., Kennicutt R. C. J., Vanden Bout P. A., 2009, ApJ, 707, 1217
Kartaltepe J. S., et al., 2010, ApJ, 721, 98

Keating L. C., et al., 2020, MNRAS, 499, 837

Kennicutt Robert C. J., 1998a, ARA&A, 36, 189

Kennicutt Robert C. J., 1998b, ApJ, 498, 541

Kennicutt Robert C. J., De Los Reyes M. A. C., 2021, ApJ, 908, 61

Kennicutt R. C., Evans N. J., 2012, ARA&A, 50, 531

Khabiboulline E. T., Steinhardt C. L., Silverman J. D., Ellison S. L., Mendel J. T., Patton D. R., 2014, ApJ, 795, 62

Kim J., et al., 2022, MNRAS, 516, 3006

Kohno K., 2005, in Hüttmeister S., Manthey E., Bomans D., Weis K., eds, American Institute of Physics Conference Series Vol. 783, The Evolution of Starbursts. pp 203–208 (`arXiv:astro-ph/0508420`), doi:10.1063/1.2034987

Kohno M., Sofue Y., 2024a, PASJ,

Kohno M., Sofue Y., 2024b, MNRAS, 527, 9290

Krolik J. H., Kallman T. R., 1983, ApJ, 267, 610

Kuno N., Nakai N., Sorai K., Nishiyama K., Vila-Vilaó B., 2002, PASJ, 54, 555

Kwok S., 2007, Physics and Chemistry of the Interstellar Medium. University Science Books

Lada C. J., Lada E. A., 2003, ARA&A, 41, 57

Lada E. A., Bally J., Stark A. A., 1991, ApJ, 368, 432

Lada C. J., Forbrich J., Lombardi M., Alves J. F., 2012, ApJ, 745, 190

Larson R. B., 1981, MNRAS, 194, 809

Larson R. B., Tinsley B. M., 1978, ApJ, 219, 46

Lee M.-Y., Stanimirović S., Wolfire M. G., Shetty R., Glover S. C. O., Molina F. Z., Klessen R. S., 2014, ApJ, 784, 80

Lee A. M., Koda J., Hirota A., Egusa F., Heyer M., 2024, ApJ, 968, 97

Lepp S., Dalgarno A., 1996, A&A, 306, L21

Leroy A. K., Walter F., Brinks E., Bigiel F., de Blok W. J. G., Madore B., Thornley M. D., 2008, AJ, 136, 2782

Leroy A. K., et al., 2021, ApJS, 257, 43

Li F., Zhang Z.-Y., Wang J., Luo G., Lin L., Zhou J., 2024, MNRAS, 527, 531

Lintott C. J., et al., 2008, MNRAS, 389, 1179

Lonsdale C. J., Farrah D., Smith H. E., 2006, in Mason J. W., ed., , Astrophysics Update 2. Springer, p. 285, doi:10.1007/3-540-30313-8_9

Lotz J. M., Jonsson P., Cox T. J., Croton D., Primack J. R., Somerville R. S., Stewart K., 2011, ApJ, 742, 103

Maloney P. R., Hollenbach D. J., Tielens A. G. G. M., 1996, ApJ, 466, 561

Martin D. C., et al., 2005, ApJ, 619, L1

McClure-Griffiths N. M., Stanimirović S., Rybarczyk D. R., 2023, ARA&A, 61, 19

McKee C. F., Ostriker J. P., 1977, ApJ, 218, 148

Meijerink R., Spaans M., 2005, A&A, 436, 397

Meijerink R., Spaans M., Israel F. P., 2007, A&A, 461, 793

Mihos J. C., Hernquist L., 1996, ApJ, 464, 641

Mills E. A. C., Ginsburg A., Immer K., Barnes J. M., Wiesenfeld L., Faure A., Morris M. R., Requena-Torres M. A., 2018, ApJ, 868, 7

Mooney T. J., Solomon P. M., 1988, ApJ, 334, L51

Moreno J., Torrey P., Ellison S. L., Patton D. R., Bluck A. F. L., Bansal G., Hernquist L., 2015, MNRAS, 448, 1107

Moreno J., et al., 2019, MNRAS, 485, 1320

Murphy E. J., et al., 2011, ApJ, 737, 67

Neumann L., et al., 2023, MNRAS, 521, 3348

Nguyen-Q-Rieu Nakai N., Jackson J. M., 1989, A&A, 220, 57

Nguyen Q. R., Jackson J. M., Henkel C., Truong B., Mauersberger R., 1992, ApJ, 399, 521

Noguchi M., 1988, A&A, 203, 259

Oey M. S., et al., 2007, ApJ, 661, 801

Onus A., Krumholz M. R., Federrath C., 2018, MNRAS, 479, 1702

Ostriker E. C., McKee C. F., Leroy A. K., 2010, ApJ, 721, 975

Oteo I., et al., 2017, ApJ, 850, 170

Pan H.-A., et al., 2022, ApJ, 927, 9

Papadopoulos P. P., Thi W. F., Viti S., 2004, MNRAS, 351, 147

Papadopoulos P. P., van der Werf P. P., Xilouris E. M., Isaak K. G., Gao Y., Mühle S., 2012, MNRAS, 426, 2601

Patton D. R., Torrey P., Ellison S. L., Mendel J. T., Scudder J. M., 2013, MNRAS, 433, L59

Pereira-Santaella M., González-Alfonso E., García-Bernete I., García-Burillo S., Rigopoulou D., 2024, A&A, 681, A117

Pérez-Torres M., Mattila S., Alonso-Herrero A., Aalto S., Efstathiou A., 2021, AAPR, 29, 2

Pillsworth R., Pudritz R. E., 2024, MNRAS, 528, 209

Planck Collaboration et al., 2020, A&A, 641, A6

Privon G. C., et al., 2015, ApJ, 814, 39

Raymond J. C., 1984, ARA&A, 22, 75

Rigopoulou D., et al., 2024, MNRAS, 532, 1598

Rodriguez-Franco A., Martin-Pintado J., Fuente A., 1998, A&A, 329, 1097

Rogerson J. B., York D. G., Drake J. F., Jenkins E. B., Morton D. C., Spitzer L., 1973, ApJ, 181, L110

Rosner R., Golub L., Vaiana G. S., 1985, ARA&A, 23, 413

Rosolowsky E., et al., 2021, MNRAS, 502, 1218

Rybicki G. B., Lightman A. P., 1986, Radiative Processes in Astrophysics. Wiley-VCH

Saintonge A., et al., 2017, ApJS, 233, 22

Sakamoto K., et al., 2017, ApJ, 849, 14

Sanders D. B., Mirabel I. F., 1996, ARA&A, 34, 749

Sanders D. B., Scoville N. Z., Soifer B. T., 1991, ApJ, 370, 158

Sanders D. B., Mazzarella J. M., Kim D. C., Surace J. A., Soifer B. T., 2003, AJ, 126, 1607

Sandstrom K. M., et al., 2013, ApJ, 777, 5

Satyapal S., Ellison S. L., McAlpine W., Hickox R. C., Patton D. R., Mendel J. T., 2014, MNRAS, 441, 1297

Schinnerer E., Leroy A. K., 2024, arXiv e-prints, p. arXiv:2403.19843

Schmidt M., 1959, ApJ, 129, 243

Schruba A., et al., 2011, AJ, 142, 37

Shapiro P. R., Field G. B., 1976, ApJ, 205, 762

Shimajiri Y., et al., 2017, A&A, 604, A74

Shirley Y. L., 2015, PASP, 127, 299

Shivaei I., Reddy N. A., Steidel C. C., Shapley A. E., 2015, ApJ, 804, 149

Sofue Y., Kohno M., 2020, MNRAS, 497, 1851

Solomon P. M., Vanden Bout P. A., 2005, ARA&A, 43, 677

Solomon P. M., Scoville N. Z., Sanders D. B., 1979, ApJ, 232, L89

Solomon P. M., Rivolo A. R., Barrett J., Yahil A., 1987, ApJ, 319, 730

Solomon P. M., Downes D., Radford S. J. E., 1992, ApJ, 387, L55

Solomon P. M., Downes D., Radford S. J. E., Barrett J. W., 1997, ApJ, 478, 144

Song Y., et al., 2021, ApJ, 916, 73

Sorai K., Nakai N., Kuno N., Nishiyama K., 2002, PASJ, 54, 179

Spitzer Lyman J., 1956, ApJ, 124, 20

Sternberg A., Dalgarno A., 1995, ApJS, 99, 565

Stierwalt S., et al., 2013, ApJS, 206, 1

Sun J., et al., 2018, ApJ, 860, 172

Sun J., et al., 2020, ApJ, 901, L8

Tacchella S., et al., 2022, MNRAS, 513, 2904

Teng Y.-H., et al., 2022, ApJ, 925, 72

Teng Y.-H., et al., 2023, ApJ, 950, 119

Teng Y.-H., et al., 2024, ApJ, 961, 42

Tielens A. G. G. M., 2005, The Physics and Chemistry of the Interstellar Medium. Cambridge University Press

Tielens A. G. G. M., Hollenbach D., 1985, ApJ, 291, 722

Togi A., Smith J. D. T., 2016, ApJ, 830, 18

Tomičić N., et al., 2021, ApJ, 907, 22

Toomre A., Toomre J., 1972, ApJ, 178, 623

Torres-Albà N., et al., 2018, A&A, 620, A140

Tumlinson J., Peeples M. S., Werk J. K., 2017, ARA&A, 55, 389

Ueda J., et al., 2021, ApJS, 257, 57

Usero A., et al., 2015, AJ, 150, 115

Vega O., Clemens M. S., Bressan A., Granato G. L., Silva L., Panuzzo P., 2008, A&A, 484, 631

Vollmer B., 2013, in Oswalt T. D., Keel W. C., eds, , Vol. 6, Planets, Stars and Stellar Systems. Volume 6: Extragalactic Astronomy and Cosmology. Springer, p. 207, doi:10.1007/978-94-007-5609-0_5

Weedman D. W., Feldman F. R., Balzano V. A., Ramsey L. W., Sramek R. A., Wuu C. C., 1981, ApJ, 248, 105

Weiss R., 1980, ARA&A, 18, 489

Weston M. E., McIntosh D. H., Brodwin M., Mann J., Cooper A., McConnell A., Nielsen J. L., 2017, MNRAS, 464, 3882

White S. D. M., Rees M. J., 1978, MNRAS, 183, 341

Wild W., Harris A. I., Eckart A., Genzel R., Graf U. U., Jackson J. M., Russell A. P. G., Stutzki J., 1992, A&A, 265, 447

Williamson F. O., Sanders W. T., Kraushaar W. L., McCammon D., Borken R., Bunner A. N., 1974, ApJ, 193, L133

Wilson C. D., 2018, MNRAS, 477, 2926

Wilson C. D., Elmegreen B. G., Bemis A., Brunetti N., 2019, ApJ, 882, 5

Wilson C. D., Bemis A., Ledger B., Klimi O., 2023, MNRAS, 521, 717

Wolfire M. G., Vallini L., Chevance M., 2022, ARA&A, 60, 247

Wu J., Evans Neal J. I., Gao Y., Solomon P. M., Shirley Y. L., Vanden Bout P. A., 2005, ApJ, 635, L173

Wu J., Evans Neal J. I., Shirley Y. L., Knez C., 2010, ApJS, 188, 313

Yasuda A., et al., 2023, PASJ, 75, 743

York D. G., 1974, ApJ, 193, L127

de Vaucouleurs G., 1948, Annales d'Astrophysique, 11, 247

de Vaucouleurs G., 1959, Handbuch der Physik, 53, 275

de los Reyes M. A. C., Kennicutt Robert C. J., 2019, ApJ, 872, 16

den Brok J. S., et al., 2023, A&A, 676, A93

van Dishoeck E. F., Black J. H., 1988, ApJ, 334, 771

2 | Observed CN and HCN intensity ratios exhibit subtle variations in extreme galaxy environments

This chapter represents an unchanged version of the paper *Observed CN and HCN intensity ratios exhibit subtle variations in extreme galaxy environments*, published in the refereed journal, *Monthly Notices of the Royal Astronomical Society*. The full reference is given below:

Ledger B.[1], Wilson C. D.[1], Michiyama T.[2], Iono D.[3,4], Aalto S.[5], Saito T.[6], Bemis A.[7], Aladro R.[8], 2021, MNRAS, Volume 504, Issue 4, pp. 5863–5879

[1]*Department of Physics and Astronomy, McMaster University, 1280 Main St. W., Hamilton, Ontario L8S 4M1, Canada*
[2]*Kavli Institute for Astronomy and Astrophysics, Peking University, 5 Yiheyuan Road, Haidian District, Beijing 100871, P.R.China*
[3]*National Astronomical Observatory of Japan, National Institutes of Natural Sciences, 2-21-1 Osawa, Mitaka, Tokyo, 181-8588*
[4]*Department of Astronomical Science, The Graduate University for Advanced Studies, SOKENDAI, 2-21-1 Osawa, Mitaka, Tokyo, 181-8588*
[5]*Department of Space, Earth and Environment, Chalmers University of Technology, Onsala Observatory, SE-439 92 Onsala, Sweden*
[6]*Max-Planck-Institut für Astronomie, Königstuhl 17, 69117 Heidelberg, Germany*
[7]*Leiden Observatory, Leiden University, PO Box 9513, 2300 RA Leiden, The Netherlands*

[8]*Max-Planck-Institut fur Radioastronomie, Auf dem Hügel 69, 53121 Bonn, Germany*

Abstract

We use both new and archival ALMA data of three energy lines each of CN and HCN to explore intensity ratios in dense gas in NGC 3256, NGC 7469, and IRAS 13120-5453. The HCN (3-2)/HCN (1-0) intensity ratio varies in NGC 3256 and NGC 7469, with superlinear trends of 1.53 ± 0.07 and 1.55 ± 0.05, respectively. We find an offset to higher HCN (3-2)/HCN (1-0) intensity ratios (~ 0.8) in IRAS 13120-5453 compared to NGC 3256 ($\sim 0.3 - 0.4$) and NGC 7469 ($\sim 0.3 - 0.5$). The HCN (4-3)/HCN (3-2) intensity ratio in NGC 7469 has a slope of 1.34 ± 0.05. We attribute the variation within NGC 3256 to excitation associated with the northern and southern nuclei. In NGC 7469, the variations are localized to the region surrounding the active galactic nucleus. At our resolution ($\sim$ 700 pc), IRAS 13120-5453 shows little variation in the HCN intensity ratios. Individual galaxies show nearly constant CN (2-1)/CN (1-0) intensity ratios. We find an offset to lower CN (2-1)/CN (1-0) intensity ratios (~ 0.5) in NGC 3256 compared to the other two galaxies (~ 0.8). For the CN (3-2)/CN (2-1) intensity ratio, NGC 7469 has a superlinear trend of 1.55 ± 0.04, with the peak localized toward the active galactic nucleus. We find high (~ 1.7) CN (1-0)/HCN (1-0) intensity ratios in IRAS 13120-5453 and in the northern nucleus of NGC 3256, compared to a more constant ratio (~ 1.1) in NGC 7469 and non-starbursting regions of NGC 3256.

Key words: ISM: molecules – galaxies: ISM – galaxies: nuclei – galaxies: starburst.

2.1 Introduction

In dense regions of molecular clouds, observers use molecules with high critical densities such as HCN, HCO^+, and CS to identify regions of active and future star formation (Wu et al. 2010; Kennicutt & Evans 2012). In particular, HCN luminosity has been shown to correlate well with total far-infrared (FIR) luminosity, a tracer of the star formation rate in galaxies (Gao & Solomon 2004; Wu et al. 2005), especially in intense starbursts and Ultra-Luminous and Luminous Infrared Galaxies (U/LIRGs). Sub-mm thermal pumping of HCN has also been shown to increase its excitation in the presence of strong X-ray emission around active galactic nuclei (AGN) in these luminous galaxies (Kohno 2005; Izumi et al. 2013, 2016).

An interesting molecule that is astrochemically related to HCN is the cyanide radical (CN). CN also has a high critical density and is primarily formed from photodissociation of HCN and neutral-neutral reactions with N, C_2, CH_2, and CH (Aalto et al. 2002; Boger & Sternberg 2005; Chapillon et al. 2012). Intermediate stages in the reaction pathways involve neutral and ionized carbon (C and C^+; Boger & Sternberg 2005). CN is thus thought to preferentially form in regions illuminated by intense radiation fields, including the ultra-violet (UV) radiation fields of photo-dissociation regions (PDRs) surrounding massive stars (Fuente et al. 1993, 1995; Greaves & Church 1996; Bachiller et al. 1997; Rodriguez-Franco et al. 1998; Boger & Sternberg 2005; Ginard et al. 2015). CN will also be more likely to form when exposed to radiation in X-ray dominated regions (XDRs) near AGNs (Meijerink & Spaans 2005; Meijerink et al. 2007; García-Burillo et al. 2010) and increased cosmic ray ionization rates (Boger & Sternberg 2005; Bayet et al. 2011; Aladro et al. 2013). The CN/HCN abundance ratio is therefore predicted to increase where photodestruction rates of HCN are high and carbon is ionized, and to decrease with cloud depth as HCN is protected from external radiation (Sternberg & Dalgarno 1995; Rodriguez-Franco et al. 1998; Boger & Sternberg 2005).

Galaxies with starbursts and/or AGN are prime environments for probing CN and HCN and their interactions with radiation fields. U/LIRGs are typically interacting or merging galaxies characterized by high infrared luminosities (Sanders et al. 2003), large fractions of dense molecular gas (Solomon et al. 1992; Gao & Solomon 2004; Privon et al. 2017; Sliwa et al. 2017), and high star formation rate surface densities (Σ_{SFR}, Vollmer et al. 2017; Privon et al. 2017). Additionally, many of these systems host an AGN, indicating the presence of both PDRs and XDRs. We refer the reader to Lonsdale et al. (2006) and Pérez-Torres et al. (2021) for comprehensive reviews on U/LIRGs. U/LIRGs are typically found at large distances, but the high sensitivity and spatial resolution of modern telescopes, like the Atacama Large Millimeter/Sub-millimeter Array (ALMA), have made these galaxies accessible for detailed observations. With ALMA, we can achieve spatial resolutions that allow us to identify and isolate starburst regions and AGN in these extreme galaxy environments.

In this paper, we present the results of an observational study of the intensity ratios of CN and HCN in three U/LIRGs. We use both new and archival ALMA observations of three lines each of CN and HCN. The higher energy lines allow us to explore the interaction between these molecules in a variety of radiation environments. Section 2.2 describes our galaxy sample, observations, data reduction, imaging, and analysis. Section 2.3 presents the observed intensity ratios of CN and HCN, the line ratio maps, and scatter plots of the line intensities. We briefly discuss potential physical drivers of the ratios in Section 2.4, with a summary of our conclusions in Section 2.5. We will present non-LTE radiative transfer modelling directly comparing abundance ratios to PDR and XDR models, such as those from Boger & Sternberg (2005), Meijerink & Spaans (2005), and Meijerink et al. (2007), in a follow-up paper. Throughout this paper, our discussion of 'ratios' refers to 'integrated line intensity ratios' and not 'molecular abundance ratios', unless otherwise indicated.

2.2 Observations and Data Reduction

2.2.1 U/LIRG sample

Our sample consists of two LIRGs, NGC 3256 and NGC 7469, and one ULIRG, IRAS 13120-5453 (hereafter referred to as IRAS 13120). The individual properties of these galaxies are summarized in Table 2.1. The different galaxy environments available in this sample allow us to probe the effects of both UV and X-ray radiation fields on the molecular gas.

[1]The NASA/IPAC Extragalactic Database (NED) is operated by the Jet Propulsion Laboratory, California Institute of Technology, under contract with the National Aeronautics and Space Administration. http://ned.ipac.caltech.edu/

[2]The SIMBAD astronomical database. http://simbad.u-strasbg.fr/simbad/

TABLE 2.1: Basic properties of the galaxy sample.

Property^a	NGC 3256	NGC 7469	IRAS 13120
Luminosity class	LIRG	LIRG	ULIRG
$\log(L_{\rm IR})$ ($L_\odot$)^b	11.75	11.60	12.29
AGN contribution^c	$<$ 5 per cent	32 – 40 per cent	17 – 33 per cent
RA (J2000)	$10^h27^m51^s.3$	$23^h03^m15^s.6$	$13^h15^m06^s.4$
Dec. (J2000)	$-43°54'13''.5$	$+08°52'26''$	$-55°09'22''.6$
Diameter	3.8 arcmin × 2.1 arcmin	1.5 arcmin × 1.1 arcmin	0.33 arcmin × 0.33 arcmin
Redshift	0.00935	0.01632	0.03076
$D_{\rm L}$ (Mpc)^d	44	66	134
$\langle$SFR$\rangle$ ($M_\odot$ yr^{-1})^e	84	60	292

Notes. ^{a}NGC 3256 and NGC 7469 properties are retrieved from the NASA/IPAC Extragalactic Database (NED[1]). IRAS 13120 properties come from Simbad[2].
$^b L_{\rm IR}$ data from Sanders et al. (2003) and are corrected for luminosity distance.
^{c}The AGN contribution to $L_{\rm IR}$ is estimated from 6 μm and 24 μm emission for NGC 3256 and NGC 7469 (Alonso-Herrero et al. 2012). For IRAS 13120, the AGN contribution is estimated from 15 μm and 30 μm (Veilleux et al. 2013), 60 μm (Teng et al. 2015), and total 8-1000 μm emission (Iwasawa et al. 2011).
^{d}Luminosity distances from redshifts (corrected to the 3K CMB reference frame) and assuming H_0 = 70.5 km s^{-1} Mpc^{-1}. For NGC 7469, the SN Type Ia distance is from Ganeshalingam et al. (2013).
^{e}SFRs calculated from $L_{\rm IR}$ using equation (12) in Kennicutt & Evans (2012); not corrected for AGN contribution.

NGC 3256 is a nearby luminous galaxy merger that can be separated into northern and southern nuclear regions. The northern nucleus is fairly face-on and has a nuclear disk with significant starburst activity (Sakamoto et al. 2014). The southern nucleus is mostly edge-on and thought to host an embedded dormant AGN (Sakamoto et al. 2014). NGC 3256 is a complicated system containing molecular outflows from both nuclei (Sakamoto et al. 2014) and high fractions of shocked and dense gas (Harada et al. 2018). Sakamoto et al. (2014) find that the outflows in the southern nucleus are highly collimated, bipolar nuclear jets with velocities of ~ 2000 km s^{-1}. Brunetti et al. (2021) argue that, due to a lack of significant trends in molecular gas surface density, brightness temperature, and velocity dispersion with physical scale, NGC 3256 must contain a smooth interstellar medium down to ~ 55 pc scales.

NGC 7469 hosts a nuclear luminous type-1 AGN ($L_{\rm 2\text{-}10keV} = 1.5 \times 10^{43}$ erg s^{-1}; Liu et al. 2014) and has a starburst ring surrounding the central portion of the galaxy (Izumi et al. 2015, 2020). The AGN is creating an XDR ~ 50 pc in size in the nuclear region, and this XDR is surrounded by a circumnuclear disc of star-forming gas (Izumi et al. 2020). Izumi et al. (2015) find the integrated intensities of HCN $(4-3)$, HCO$^+$ $(4-3)$, and CS (7-6) are higher in the nucleus than in the starburst ring and predict that the HCN abundance is enhanced in the nucleus due to increased sub-mm radiation near the AGN (Izumi et al. 2013, 2016).

IRAS 13120 has been optically classified as a Seyfert 2 galaxy (Véron-Cetty & Véron 2010). Teng et al. (2015) find that observations of IRAS 13120 are consistent with the galaxy hosting an inactive, Compton-thick AGN ($N_{\rm H} > 10^{24}$ cm^{-2}). ^{12}CO observations by Sliwa et al. (2017) show evidence for a young starburst (< 7 Myr) in the central ~ 500 pc region. Privon et al. (2017) find the HCN/HCO$^+$ ratio is higher in the central starburst and suggest this is from mechanical heating of the gas by supernovae feedback.

2.2.2 Data and imaging

Table 2.2 lists the project IDs for the new and archival ALMA data used in our analysis. The data were reduced and imaged with the Common Astronomy Software Application (CASA; McMullin et al. 2007). The raw *uv* data were calibrated for each project using the relevant CASA version. All subsequent data reduction was performed using CASA version 5.6.1. Continuum subtraction was performed on each *uv* dataset using line-free channels and CASA's UVCONTSUB task.

TABLE 2.2: New and archival ALMA projects with HCN ($J = 1-0, 3-2, 4-3$) and CN ($N = 1-0, 2-1, 3-2$) observations of the three target galaxies.

Line	Project code	PI	ALMA data reference
NGC 3256			
HCN $(1-0)$	2015.1.00993.S	Michiyama, T.	Michiyama et al. (2018)
HCN $(3-2)$	2015.1.00412.S	Harada, N.	Harada et al. (2018)
HCN $(4-3)$	2018.1.00493.S	Wilson, C.	This paper
CN $(1-0)$	2011.0.00525.S	Sakamoto, K.	Sakamoto et al. (2014)
CN $(2-1)$	2015.1.00412.S	Harada, N.	Harada et al. (2018)
CN $(3-2)$	2018.1.00493.S	Wilson, C.	This paper
NGC 7469			
HCN $(1-0)$	2012.1.00165.S	Izumi T.	Izumi et al. (2015)
HCN $(3-2)$	2012.1.00034.S	Imanishi M.	Imanishi et al. (2016)
HCN $(4-3)$	2012.1.00165.S	Izumi T.	Izumi et al. (2015)
CN $(1-0)$	2013.1.00218.S	Izumi T.	Wilson et al. (2019)[a]
CN $(2-1)$	2015.1.00412.S	Harada, N.	Harada et al. (2018)
CN $(3-2)$	2018.1.00493.S	Wilson, C.	This paper
IRAS 13120			
HCN $(1-0)$	2013.1.00379.S	Sliwa, K.	Sliwa et al. (2017)
HCN $(3-2)$	2018.1.00493.S	Wilson, C.	This paper
HCN $(4-3)$	2015.1.00102.S	Iono D.	Fluetsch et al. (2019)[b]
CN $(1-0)$	2015.1.00287.S	Sliwa, K.	Wilson et al. (2019)[a]
CN $(2-1)$	2016.1.00777.S	Sliwa, K.	–
CN $(3-2)$	2018.1.00493.S	Wilson, C.	This paper

Notes. [a]Reference uses the CO $(1-0)$ transition from these project IDs. [b]Reference uses the CO $(3-2)$ transition from this project ID.

Given the large collection of ALMA observations from which our data were obtained, we put significant effort into matching the spatial and spectral resolutions of the lines. The *uv* data for each galaxy were imaged individually with CASA's TCLEAN task. All imaging was done using Brigg's weighting (Briggs 1995). Making use of TLCEAN's CELL, UVTAPER, UVRANGE, and WIDTH parameters, the *uv* coverage, spectral channel width, and dirty beam sizes were compared and matched for each galaxy. The limiting factors were the largest minimum *uv* coverage, the largest spectral channel width, and the largest dirty beam size. We note that applying a *uv* cut-off and taper with the UVRANGE and UVTAPER parameters in TCLEAN will limit the number of short baselines in our data and thus could potentially lead to missing flux on the largest angular scales. The UVRANGE parameter was matched between all lines in each galaxy in order to recover similar flux scales for each line. We tried to limit the problem of missing flux in our interferometric observations by choosing the largest minimum UVRANGE cut-off while still matching all lines.

A measure of the mean RMS noise was found from both the dirty and final smoothed image cubes for each spectral line in CASA using the IMSTAT task on line-free channels. The sensitivities varied for each line in each galaxy depending on the specific ALMA observations and can be found in Tables 2.3 and 2.6. The imaging of all galaxies was limited to regions where the primary beam response was greater than 20 per cent and cleaning was performed using CASA's AUTO-MULTITHRESH (Kepley 2019) down to the 2σ level using the line sensitivities from the dirty cubes. Masks produced by TCLEAN's auto-masking algorithm were checked for consistency during major cleaning cycles. Most observations were completed with a single pointing and imaged with matched phase centres in TCLEAN, except for the ALMA Band 7 observations of CN $(3-2)$ and HCN $(4-3)$ in NGC 3256 which had multiple pointings. In these cases, the imaging was done as a mosaic with the same matched phase centres. A final smoothing to a common round beam was completed for all lines in each galaxy with the CASA task IMSMOOTH.

NGC 3256 processing

The spectral resolution in NGC 3256 was limited by the CN $(1-0)$ line at 26.43 km s^{-1} and all lines were binned in velocity to this channel width. The limiting dirty beam size was set by the HCN $(1-0)$ observations at 2.1 arcsec $\times$1.7 arcsec, PA = 88°. The parameter UVTAPER was used to taper the longest baselines in each data set until

TABLE 2.3: Data reduction imaging properties and line sensitivities.

Imaging property	NGC 3256	NGC 7469	IRAS 13120
Beam size[a]	2.2 arcsec	0.95 arcsec	1.1 arcsec
Beam (pc)	469	304	715
Velocity resolution (km s^{-1})[b]	26.43	20.68	20.64
Pixel size[b]	0.3 arcsec	0.15 arcsec	0.15 arcsec
Re-binned pixel size[b]	1.1 arcsec	0.475 arcsec	0.55 arcsec
UVRANGE cut-off (kλ)[c]	> 15	> 19.8	> 15.9
Maximum recoverable scale[c]	8.25 arcsec	6.25 arcsec	7.78 arcsec
Sensitivities (mJy $beam^{-1}$)[d]			
HCN(1 – 0)	0.24	0.27	0.95
HCN(3 – 2)	1.53	0.44	0.58
HCN(4 – 3)	0.99	0.81	2.00
CN(1 – 0)	0.66	0.49	1.11
CN(2 – 1)	0.95	0.26	0.39
CN(3 – 2)	0.53	0.71	0.97

Notes. [a]Beams smoothed, rounded, and matched to this resolution for all lines.
[b]The velocity resolution and pixel size were matched between all lines.
[c]UVRANGE cut-off based on the minimum *uv* range covered by all lines in each galaxy and has also been converted to a maximum recoverable scale of emission.
[d]Sensitivities determined using line-free channels of dirty image cubes.

the beams were matched relatively well, before a final smoothing to a 2.2 arcsec round beam was applied. For the HCN (3 – 2), HCN (4 – 3), CN (2 – 1), and CN (3 – 2) lines, natural weighting (Brigg's with robust = 2.0) was used to increase sensitivity and naturally increase the dirty beam size before tapering. For HCN (1 – 0) and CN (1 – 0), the resolution was close enough to the target size of 2.2 arcsec that little tapering was required and Brigg's weighting with robust = 0.5 was sufficient.

NGC 7469 processing

The three CN transitions in NGC 7469 had limiting spectral resolutions of ~ 5.17 km s^{-1}; however, the channel widths were increased to an integer multiple of $4 \times 5.17 = 20.68$ km s^{-1} to smooth the data spectrally and increase the signal-to-noise. This smoothing helped match the spectral resolution of the NGC 3256 and IRAS 13120 data. The CN (1 – 0) line limited our resolution to a beam size of 0.89 arcsec $\times$0.55 arcsec, PA = $-47.3°$. We thus targeted a smoothed 0.95 arcsec round beam, and adjusted weighting and UVTAPER parameters to match this target. HCN (1 – 0), CN (1 – 0), and CN (3 – 2) were imaged using robust = 0.5. HCN (3 – 2), HCN (4 – 3), and CN (3 – 2) were imaged using natural weighting.

IRAS 13120-5453 processing

In the IRAS 13120 data, the native spectral resolution varied for each of the three CN lines. The HCN lines all had the same ~ 3.3 km s^{-1} velocity resolution. Channel widths were fixed at 20.64 km s^{-1}, an integer multiple of the CN (1 – 0) transition line. This spectral smoothing enhanced the signal-to-noise ratio for the large velocity dispersions seen in IRAS 13120. The limiting beam size was the HCN (1 – 0) line at 1.01 arcsec $\times$0.51 arcsec, PA = 73.7°, imaged with robust = 0.5. The remaining lines were imaged with robust = 2.0, as they all had dirty beams with better than 0.6 arcsec resolution. Tapers were applied and we smoothed the data to a final target 1.1 arcsec round beam.

2.2.3 Integrated intensities and measured ratios

We produced integrated intensity (moment 0) maps of all lines in our three galaxies. Cleaned, smoothed data cubes were extracted from CASA and subsequent processing, including the creation of the moment 0 maps, was done using the ASTROPY software

TABLE 2.4: CN and HCN measured intensity ratios.

Region	$\frac{\text{HCN (3 – 2)}}{\text{HCN (1 – 0)}}$	$\frac{\text{HCN (4 – 3)}}{\text{HCN (3 – 2)}}$	$\frac{\text{CN (2 – 1)}}{\text{CN (1 – 0)}}$	$\frac{\text{CN (3 – 2)}}{\text{CN (2 – 1)}}$	$\frac{\text{CN (1 – 0)}}{\text{HCN (1 – 0)}}$	$\frac{\text{CN (3 – 2)}}{\text{HCN (3 – 2)}}$
NGC 3256						
N. nucl.	0.39(4)	0.48(7)	0.47(5)	0.27(4)	1.7(1)	0.55(8)
S. nucl.	0.33(4)	0.46(7)	0.44(5)	0.22(3)	1.12(9)	0.34(5)
Non-nucl.	0.27(3)	0.45(6)	0.43(5)	0.21(3)	1.14(8)	0.38(5)
NGC 7469						
Nucl.	0.52(6)	0.48(7)	0.80(9)	0.45(6)	1.13(9)	0.8(1)
Non-nucl.	0.33(4)	0.37(5)	0.76(9)	0.30(4)	1.11(8)	0.8(1)
IRAS 13120						
Global	0.80(9)	0.8(1)	0.77(9)	0.53(8)	1.7(1)	0.8(1)
Peak	0.79(9)	0.9(1)	0.80(9)	0.57(8)	1.5(1)	0.8(1)

Notes. Uncertainties are measurement plus calibration uncertainties and are given as the uncertainty on the last digit (i.e. 0.39(4) = 0.39 ± 0.04).
ALMA calibration uncertainties are 5 per cent (Band 3) and 10 per cent (Band 6 and 7).

TABLE 2.5: Slopes from pixel-by-pixel comparisons.[a]

Ratio	NGC 3256	NGC 7469	IRAS 13120	All pixels
$\frac{\text{HCN (3 – 2)}}{\text{HCN (1 – 0)}}$	1.53 ± 0.07	1.55 ± 0.05	0.84 ± 0.06	1.46 ± 0.04
$\frac{\text{HCN (4 – 3)}}{\text{HCN (3 – 2)}}$	0.99 ± 0.04	1.34 ± 0.05	1.3 ± 0.1	1.12 ± 0.03
$\frac{\text{CN (2 – 1)}}{\text{CN (1 – 0)}}$	0.95 ± 0.03	0.93 ± 0.03	0.91 ± 0.02	1.07 ± 0.02
$\frac{\text{CN (3 – 2)}}{\text{CN (2 – 1)}}$	1.26 ± 0.05	1.55 ± 0.04	1.11 ± 0.04	1.33 ± 0.02
$\frac{\text{CN (1 – 0)}}{\text{HCN (1 – 0)}}$	1.49 ± 0.06	1.26 ± 0.05	0.83 ± 0.05	1.25 ± 0.03
$\frac{\text{CN (3 – 2)}}{\text{HCN (3 – 2)}}$	1.06 ± 0.09	1.17 ± 0.05	0.94 ± 0.06	1.21 ± 0.04

Notes: [a]Fit parameters determined from Linmix linear fitting of the form $\log(y) = m \log(x) + b$.

in Python 3.7. The cubes were trimmed to include only channels with line emission (found using the CASA viewer). The HCN (1 − 0), HCN (3 − 2), and HCN (4 − 3) line cubes were trimmed to include the same range in velocity. The CN lines were trimmed depending on their hyperfine structure so that all hyperfine lines were included in the calculation of the integrated intensities. Exact velocity ranges for all six lines can be found in Table 2.6. An RMS cut-off of 3.5σ was used to mask the cleaned cubes to include strong emission while avoiding noisy emission in lines with lower S/N. This 3.5σ limit used the line sensitivities calculated in the smoothed cubes and was chosen to overcome the varying sensitivities between different lines in each galaxy. The moment 0 maps were further masked to only include pixels with emission in all six spectral lines. In cases where multiple hyperfine lines are present (the HCN (1 − 0), CN (1 − 0), CN (2 − 1), and CN (3 − 2) lines), the integrated intensities include all hyperfine lines that were observed. The moment 0 maps were converted to physical units of K km s^{-1} and corrected for the primary beam response. Moment 0 maps for each line can be found in the Appendix (Figs. 2.5, 2.6, and 2.7). Uncertainty maps were made to match each moment 0 map. Individual uncertainties on each pixel were calculated as $\sigma = \mathrm{rms} \cdot \sqrt{\Delta V_{\mathrm{chan}} \cdot V_{\mathrm{line}}}$, where ΔV_{chan} is the velocity width of an individual channel and V_{line} is the width of the line integrated in that pixel. The integrated intensity maps were used to calculate total intensities and intensity ratios. Maps of the ratios covering the high S/N regions in each galaxy are shown in Figs. 2.1 and 2.2.

We calculate global line ratios for each galaxy using the average line intensities in K km s^{-1}. Along with the global ratios, we measured line ratios in the northern and southern nuclei of NGC 3256 and the nucleus of NGC 7469. The central nuclear pixels were identified using the 93 GHz radio continuum emission peak for NGC 3256 and NGC 7469. To isolate the nuclear regions, we used an aperture centred on the nuclear pixel. The size of the aperture is equal to the full-width at half-maximum of the beam in each galaxy. Additionally, for NGC 3256 and NGC 7469 we calculated non-nuclear line ratios using all non-nuclear pixels. For IRAS 13120, we measured the line ratios at a single pixel at the 93 GHz radio continuum peak. Table 2.4 presents the results of this analysis and the measured ratios in the different regions of each galaxy.

2.2.4 Pixel-by-pixel comparisons

We explored correlations between spectral lines using a pixel-by-pixel comparison of the intensities. We first re-sampled the imaged data cubes to half the full-width at half-maximum of the beam. The number of pixels sampled across the beam was reduced by a factor of 3 for all galaxies, and the new pixel sizes can be found in Table 2.3. Following the same process as described in Section 2.2.3, moment 0 maps with associated uncertainties were made using masked, matched pixels in the re-sampled image cubes in physical units of K km s^{-1}. For NGC 7469, we corrected the measured intensities in the scatter plots for an inclination angle of 45 ± 5 deg (Davies et al. 2004). The intensities of the other two galaxies were not corrected for inclination angle[3].

We present pixel-by-pixel comparisons of the integrated intensities in the scatter plots of Figs. 2.3 and 2.4. We used the Linmix linear regression method to fit the integrated intensity pixels in log-log space and account for the higher uncertainties seen in the lower S/N pixels (Kelly 2007; Meyers 2018). The resulting slopes found for each intensity ratio are presented in Table 2.5. Full details of all calculated slopes and intercepts for all line ratio combinations can be found in Table 2.7 in the Appendix.

2.3 Variations in the CN and HCN intensity ratios

In this section, we present the measured intensity ratios and slopes from our CN and HCN line analysis. Discussion and physical interpretation of the ratios is deferred until Section 2.4.

2.3.1 Regions of enhanced HCN ratios

We find variations in the HCN (3 − 2)/HCN (1 − 0) ratio in NGC 3256 and NGC 7469 (Fig. 2.3a), with spatial variations in the ratio within these galaxies (Figs. 2.1a and 2.1e). Both galaxies show a similar superlinear trend (1.53 ± 0.07 for NGC 3256, 1.55 ± 0.05

[3]NGC 3256 is a complicated system where the northern and southern nuclei are fairly face-on and edge-on, respectively ($i_N \approx 30°$ and $i_S \approx 80°$; Sakamoto et al. 2014), making it challenging to correct for any specific angle. No inclination angle for IRAS 13120 was found in the literature. We performed the same analysis applying a conservative estimate for inclination angles of 60° to NGC 3256 and IRAS 1320 and found that the resulting slopes and intercepts match the results in Table 2.5 within one standard deviation.

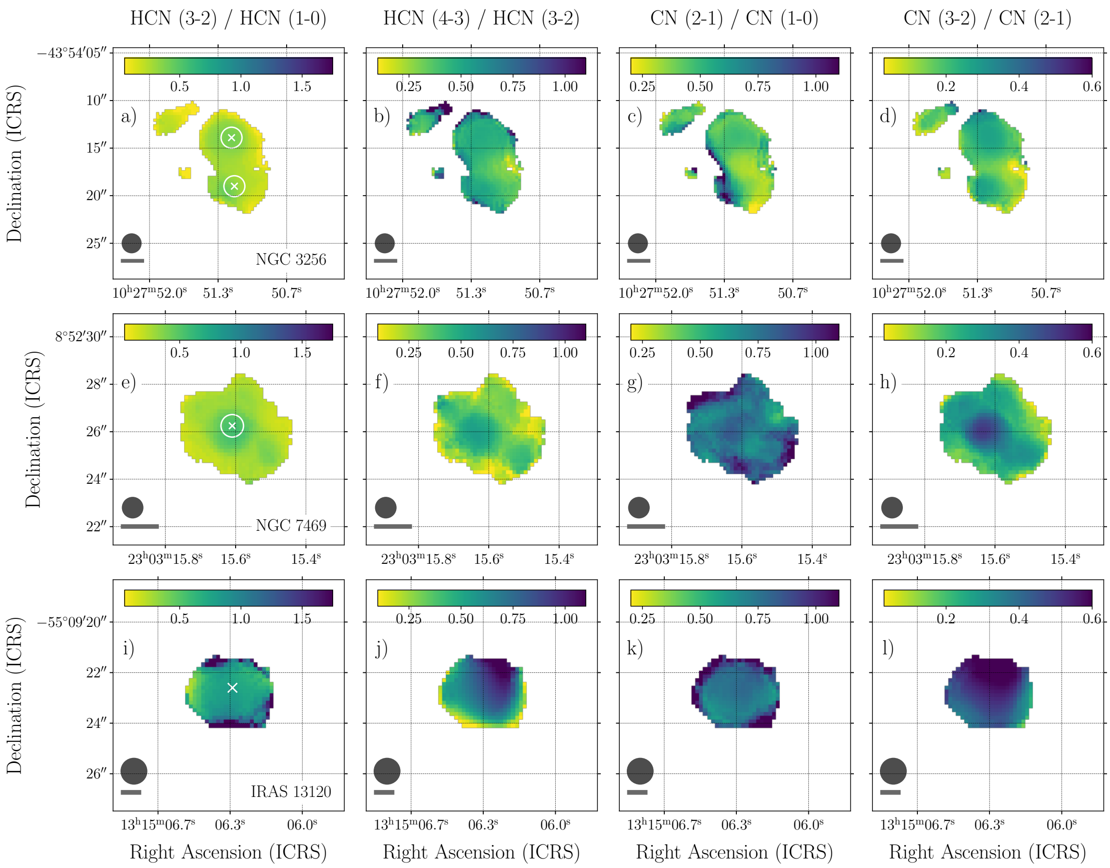

FIGURE 2.1: Top row (a-d): NGC 3256 ratio maps. Middle row (e-h): NGC 7469 ratio maps. Bottom row (i-l): IRAS 13120 ratio maps. Ratio maps are calculated from the integrated intensities in K km s^{-1}. The beam size is shown as the black circle and the scale bars are set to 500 pc. Intensity ratios in each column are (from left to right) HCN $(3-2)$/HCN $(1-0)$, HCN $(4-3)$/HCN $(3-2)$, CN $(2-1)$/CN $(1-0)$, and CN $(3-2)$/CN $(2-1)$. White crosses indicate the 93 GHz radio continuum peaks in each galaxy and white circles represent the apertures within which nuclear ratios were measured. The coordinates of the continuum peaks in each galaxy are: NGC 3256 north nucleus: ($10^h27^m51^s.23$, $-43°54'14''.23$); NGC 3256 south nucleus: ($10^h27^m51^s.20$, $-43°54'19''.29$); NGC 7469 nucleus: ($23^h3^m15^s.62$, $8°52'26''.10$); IRAS 13120 nucleus: ($13^h15^m6^s.34$, $-55°9'22''.75$).

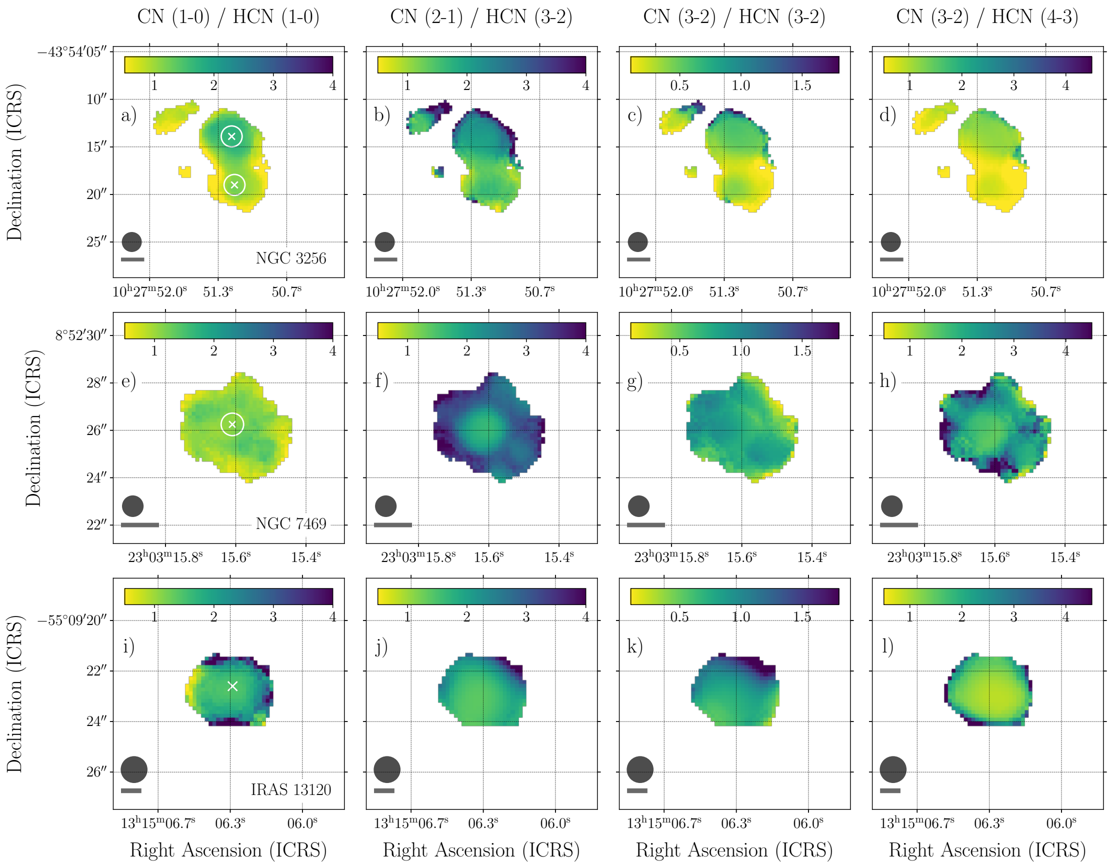

FIGURE 2.2: Top row (a-d): NGC 3256 ratio maps. Middle row (e-h): NGC 7469 ratio maps. Bottom row (i-l): IRAS 13120 ratio maps. Ratio maps are calculated from the integrated intensities in K km s^{-1}. Beam sizes, scale bars, white circles, and crosses are as described in Fig. 2.1. Intensity ratios in each column are (from left to right) CN $(1-0)$/HCN $(1-0)$, CN $(2-1)$/HCN $(3-2)$, CN $(3-2)$/HCN $(3-2)$, and CN $(3-2)$/HCN $(4-3)$.

for NGC 7469). The northern nucleus of NGC 3256 shows a marginal increase in the HCN (3 – 2)/HCN (1 – 0) ratio to a value of 0.39 ± 0.04, in contrast to the value of 0.27 ± 0.03 in the non-nuclear pixels. In NGC 7469, the HCN (3 – 2)/HCN (1 – 0) ratio is significantly higher (0.52 ± 0.06) in the central ~ 500 pc compared to the value of the non-nuclear pixels (0.33 ± 0.04) in the rest of the disc.

Comparing the two galaxies, the HCN (3 – 2)/HCN (1 – 0) and HCN (4 – 3)/HCN (1 – 0) global and non-nuclear ratios in NGC 3256 and NGC 7469 are similar within our uncertainties (Table 2.4 and 2.8). In the nuclear regions, however, both ratios are higher in NGC 7469 than in NGC 3256.

There is no difference in the HCN (3 – 2)/HCN (1 – 0) ratio for IRAS 13120 between the global ratio and the continuum peak. IRAS 13120 shows a slight sublinear trend in the HCN (3 – 2)/HCN (1 – 0) ratio, with a slope of 0.84 ± 0.06 (Fig. 2.3a), significantly different from the superlinear trends with slopes > 1.5 found in NGC 3256 and NGC 7469. The HCN (3 – 2)/HCN (1 – 0) ratio of the ULIRG is higher (~ 0.8) than both the global and nuclear values of the LIRGs (~ 0.3 – 0.5).

The HCN (4 – 3)/HCN (3 – 2) ratio in NGC 3256 has a slope consistent with unity (0.99 ± 0.04). This ratio in NGC 3256 has nearly identical values of 0.48 ± 0.07, 0.46 ± 0.07, and 0.45 ± 0.06 in the northern nucleus, southern nucleus, and non-nuclear pixels, respectively. Slight variations can be seen in the HCN (4 – 3)/HCN (3 – 2) ratio in NGC 3256 in Fig. 2.1. In contrast, NGC 7469 and IRAS 13120 show variations in the HCN (4 – 3)/HCN (3 – 2) ratio with superlinear trends of 1.34 ± 0.05 and 1.3 ± 0.1, respectively. A fit to the pixels from all galaxies in the HCN (4 – 3)/HCN (3 – 2) ratio gives a slightly superlinear slope of 1.13 ± 0.03 (Fig. 2.3c).

2.3.2 Consistency in the CN ratios

The slopes for the CN (2 – 1)/CN (1 – 0) ratio are consistent within one standard deviation for all three galaxies in our sample, with an average value of 0.93 ± 0.05 (Fig. 2.3b). We do not resolve any structure in the line ratio maps of individual galaxies (2.1). There is, however, an offset to lower values for the CN (2 – 1)/CN (1 – 0) intensity ratio in NGC 3256 (~ 0.4) compared to NGC 7469 and IRAS 13120 (~ 0.8).

The CN (3 – 2)/CN (2 – 1) ratio varies in all the galaxies in our sample (superlinear trends in Table 2.4 and Fig. 2.3). The slopes of the CN (3 – 2)/CN (2 – 1) ratio in NGC 3256 and IRAS 13120 are smaller (1.26 ± 0.05 and 1.11 ± 0.04, respectively) than the

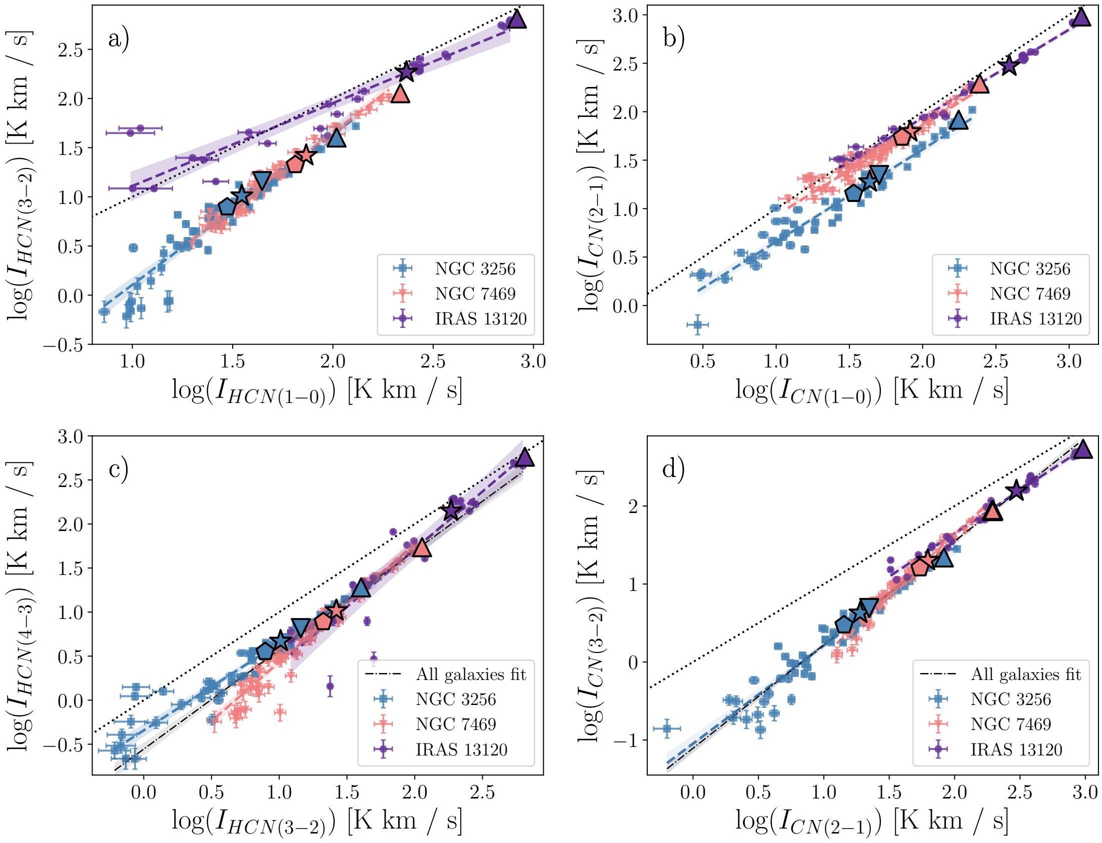

FIGURE 2.3: Pixel-by-pixel comparisons of individual line intensities in each galaxy. The higher-J/N transition of the two lines is always plotted on the y-axis. The black dotted line is the one-to-one line. Blue squares correspond to NGC 3256; pink inverted triangles correspond to NGC 7469; purple circles correspond to IRAS 13120. The dashed lines in each colour represent the Linmix fits for each galaxy, with the shaded region representing the 95 per cent confidence interval of these fits. Large stars show the global ratio in each galaxy and large pentagons show the non-nuclear ratios in NGC 3256 and NGC 7469. Large triangles show ratios for the northern nucleus of NGC 3256, the nucleus of NGC 7649, and the continuum peak in IRAS 13120, while the large inverted triangle shows the ratio for the southern nucleus of NGC 3256. The black dot-dashed lines and shaded regions in (c) and (d) show Linmix fits to all three galaxies. Comparison plots of the additional J/N-level transition lines of CN and HCN can be found in the Appendix.

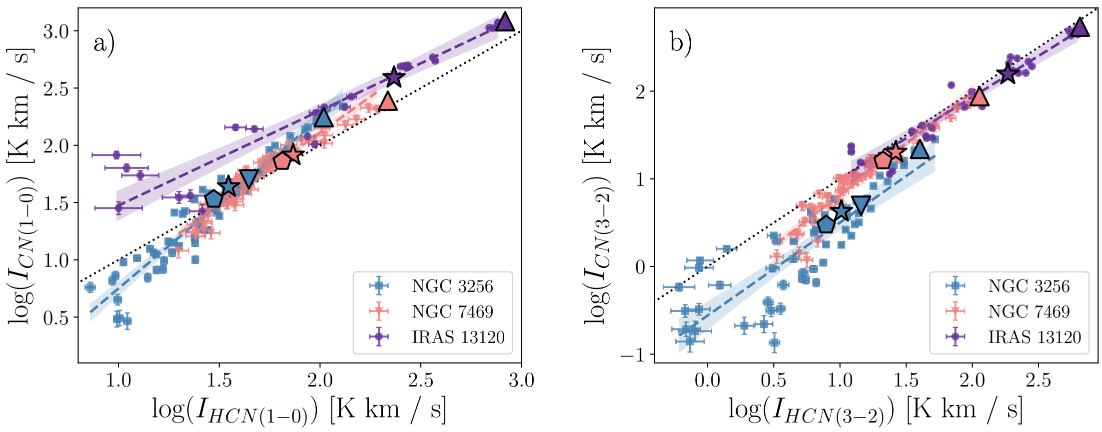

FIGURE 2.4: Pixel-by-pixel comparisons for CN compared to HCN for selected transitions. For plot descriptions, refer to the caption of Fig. 2.3. Comparison plots of the additional J/N-level transition lines of CN and HCN can be found in the Appendix.

strong superlinear trend seen in NGC 7469 (1.55 ± 0.04). We find a higher CN $(3-2)$/CN $(2-1)$ ratio of 0.45 ± 0.06 in the nucleus of NGC 7469 compared to the non-nuclear value of 0.30 ± 0.04. The nuclear CN $(3-2)$/CN $(2-1)$ ratio in NGC 7469 more closely resembles the ratio in IRAS 13120 (~ 0.5) than NGC 3256 (~ 0.2). Fitting the pixels from all galaxies, the CN $(3-2)$/CN $(2-1)$ ratio has a superlinear slope of 1.33 ± 0.02 (Fig. 2.3d). The superlinear trend in this CN $(3-2)$/CN $(2-1)$ ratio is stronger than the trend in the HCN $(4-3)$/HCN $(3-2)$ ratio, with values of 1.33 ± 0.02 and 1.13 ± 0.03, respectively.

2.3.3 Subtle variations in CN/HCN intensity ratios

We find a higher CN $(1-0)$/HCN $(1-0)$ intensity ratio of 1.7 ± 0.1 in the northern nucleus of NGC 3256, compared to the non-nuclear value of 1.14 ± 0.09. The global CN $(1-0)$/HCN $(1-0)$ ratio in IRAS 13120 is also 1.7 ± 0.1. The CN $(1-0)$/HCN $(1-0)$ ratios in IRAS 13120 and in the northern nucleus of NGC 3256 are significantly higher than the ratio of ~ 1.1 in NGC 7469. The southern nucleus and non-nuclear regions of NGC 3256 also have smaller ratios of ~ 1.1.

The variations in the CN $(1-0)$/HCN $(1-0)$ ratio in NGC 3256 result in a superlinear slope of 1.49 ± 0.06 (Fig. 2.4a). Despite the lack of obvious variations in the different regions of NGC 7469 and IRAS 13120, the slopes indicate subtle variations in the CN

(1 − 0)/HCN (1 − 0) ratio with values of 1.26 ± 0.05 for NGC 7469 and 0.83 ± 0.05 for IRAS 13120.

For the CN (3 − 2)/HCN (3 − 2) ratio, we measure the same ratio of 0.8 ± 0.1 for all regions in NGC 7469 and IRAS 13120. The CN (3 − 2)/HCN (3 − 2) ratio in NGC 3256 has lower values between 0.35 − 0.55 (Fig. 2.4b). The lower CN (3 − 2)/HCN (3 − 2) ratio in NGC 3256 occur primarily toward the southern half of the galaxy (Fig. 2.2c). In NGC 3256, the highest CN (3 − 2)/HCN (3 − 2) ratio of 0.55 ± 0.08 occurs in the northern nucleus.

2.4 Potential Physical Drivers for the Observed Ratio Variations

2.4.1 Driving the excitation of HCN

Molecular excitation is dependent on the temperature, density, and optical depth of the molecular gas, as well as the presence of an external radiation source, such as a PDR and/or an XDR (Boger & Sternberg 2005; Meijerink & Spaans 2005; Meijerink et al. 2007). Additionally, molecular excitation can be affected by shocks, which will increase the temperature in the shocked regions of the gas (Martín et al. 2015). The $J = 1 - 0$, $3 - 2$ and $4 - 3$ rotational transitions of HCN have energies of 4.25 K, 25.52 K and 42.53 K above the ground state, respectively[4]. HCN excitation to the $J = 3 - 2$ and $4 - 3$ transitions thus requires much warmer, dense gas conditions than the $J = 1 - 0$ transition. An increase in HCN excitation and intensity ratios is expected in regions surrounding AGN sources (Boger & Sternberg 2005; Meijerink & Spaans 2005; Meijerink et al. 2007; Izumi et al. 2013, 2016). In addition, Saito et al. (2018) find a positive correlation between HCN excitation and SFR surface density when excluding AGN contributions from their analysis. Therefore, we expect to find increased HCN intensity ratios in regions with starburst and/or AGN activity. All galaxies in our sample host some combination of AGN and starburst activity that we often cannot separate at our resolutions.

[4]The LAMBDA database. https://home.strw.leidenuniv.nl/~moldata/

Increased nuclear HCN $(3-2)$/HCN $(1-0)$ ratio in NGC 7469

The nuclear region of NGC 7469 has an HCN $(3-2)$/HCN $(1-0)$ ratio of ~ 0.5. There is a circumnuclear disc of cold molecular gas surrounding the AGN of this galaxy and forming stars in the inner ~ 100 pc region (Davies et al. 2004; Izumi et al. 2015). Our observations of NGC 7469 have a resolution of ~ 300 pc and thus blend the influence of both AGN and starburst activity in the circumnuclear disc. This blending makes it challenging to disentangle the effect of the AGN and starburst on the molecular gas, as both will help to increase the HCN $(3-2)$/HCN $(1-0)$ ratio.

There is evidence of an XDR that is < 50 pc in radius around the AGN in NGC 7469 (Izumi et al. 2015, 2020). This XDR will influence the higher HCN excitation we find in the nuclear region. Izumi et al. (2013, 2016) conclude that there will be high intensities in the HCN sub-mm lines due to IR-pumping in the presence of XDRs. This IR-pumping is a result of X-ray radiation heating dust grains in the vicinity of the XDR and producing strong IR radiation that affects the HCN chemistry. Our future non-LTE analysis with accurate modelling of gas temperatures and densities will help interpret the HCN $(4-3)$/HCN $(3-2)$ and HCN $(3-2)$/HCN $(1-0)$ ratios we find in the nucleus of NGC 7469.

Another plausible scenario for the higher HCN line ratios we find around the AGN in NGC 7469 could be shocks from the AGN outflow increasing the temperature of the gas. Shocked gas will have increased temperatures that favour the warm gas chemistry required to produce HCN (Harada et al. 2013; Martín et al. 2015). Martín et al. (2015) find enhanced HCN abundances around the Seyfert 1 AGN in NGC 1097 due to the shocked material produced by the outflows. The peak HCN intensity in their observations is found ~ 200 pc from the galaxy centre, where the X-ray radiation is weaker and the shocks at the base of the outflow are prominent. At our resolution, we cannot distinguish between the effects of the central XDR in NGC 7469 and any shocks in the outflowing gas that could also increase the gas temperature and affect the HCN excitation in this galaxy.

Higher HCN $(3-2)$/HCN $(1-0)$ ratios in IRAS 13120 than NGC 3256

The HCN $(3-2)$/HCN $(1-0)$ ratio should increase with increasing starburst contribution due to the positive correlation between HCN excitation and SFR surface density (Saito et al. 2018). Wilson et al. (2019) find ranges of $\Sigma_{\rm SFR}$ between 10 – 100 $M_\odot$ yr^{-1} kpc^{-1} for IRAS 13120 compared to 1 – 25 $M_\odot$ yr^{-1} kpc^{-1} for NGC 3256. Teng et al. (2015) find the 2 – 10 keV absorption-corrected luminosity of IRAS 13120 is 1.25×10^{43} erg s^{-1} and thermal and non-thermal components of the 0.5 – 2 keV luminosity are consistent with a star formation rate of $\sim$ 170 $M_\odot$ yr^{-1}. The lower $\Sigma_{\rm SFR}$ in NGC 3256 could lead to less HCN excitation (Saito et al. 2018). IRAS 13120 has the highest HCN (3 – 2)/HCN (1 – 0) ratio ($\sim$ 0.8), while the northern nucleus of NGC 3256 is lower ($\sim$ 0.4). We note that the different resolutions in our observations of NGC 3256 ($\sim$ 470 pc) and IRAS 13120 ($\sim$ 700 pc) mean that we are comparing different spatial scales in the starburst regions of these two galaxies, which might lead to a difference in the HCN (3 – 2)/HCN (1 – 0) ratios.

There is no difference in the HCN (3 – 2)/HCN (1 – 0) ratio for IRAS 13120 between the global ratio and the continuum peak. Our resolution of $\sim$ 700 pc is insufficient to isolate the nuclear region and so the line ratio will have contributions from both the starburst and AGN components in this galaxy. Veilleux et al. (2013) find that IRAS 13120 has a fast, wide-angle outflow seen in the FIR OH line and suggest an AGN contribution to $L_{\rm IR}$ up to 33.4 per cent. This outflow could impact the excitation of HCN through the presence of shocks that could increase the temperature of the gas (Martín et al. 2015).

The southern nucleus of NGC 3256 contains an embedded AGN. Previous work has described this AGN as being inactive or dormant (Sakamoto et al. 2014). The strength of the X-ray emission from this AGN would likely be lower than the other AGN in our sample and we would not expect as significant an increase in the HCN excitation due to X-rays here. Alonso-Herrero et al. (2012) place a 5 per cent upper limit on the contribution from any AGN to the total bolometric luminosity of NGC 3256. Both nuclei in NGC 3256 have been detected in X-rays with Chandra by Lira et al. (2002), although, the authors found no evidence for an AGN in either nucleus. Ohyama et al. (2015) used *Spitzer* data and SED fitting to starburst and AGN templates to suggest there is an AGN in the southern nucleus with $L_{8\text{-}1000\,\mu\rm m} \sim 10^{9.7} L_\odot$. The northern nucleus is more likely to host an extreme starburst than an AGN (Neff et al. 2003). These limitations on the AGN in NGC 3256 indicate that the HCN excitation conditions will be almost completely driven by starburst effects on the molecular gas. Any contribution from the AGN in this galaxy to HCN excitation would more likely come from shocks in the outflows from the AGN (e.g. Aalto et al. 2012; Martín et al. 2015).

With higher resolution images and the ability to resolve individual XDRs, we would be able to compare individual ratios based on the relative strengths of the X-rays and outflows created by the AGN.

2.4.2 Driving the excitation of CN

As with HCN, the excitation conditions of CN will depend on the temperature, density, optical depth, and presence of external radiation fields in the molecular gas. The CN $N = 1 - 0$, $2 - 1$, and $3 - 2$ lines have energies of 5.4 K, 16.3 K, and 32.6 K above ground, respectively. As with HCN, gas traced by higher CN line excitation will be both warmer and/or denser than the $N = 1 - 0$ line.

Superlinear trend in CN (3 − 2)/CN (2 − 1)

The superlinear trend we see in the CN (3 − 2)/CN (2 − 1) intensity ratio indicates that the different global ratios between our galaxies are correlated with increased intensity of line emission. We observe higher intensities on average in IRAS 13120 than in NGC 3256 and NGC 7469 for both CN lines. These higher ratios could indicate molecular gas that is more dense with higher temperatures, leading to higher CN excitation. Additionally, because IRAS 13120 is a ULIRG with a high SFR surface density, we could expect a higher external UV field interacting with the molecular gas and leading to an increase in CN abundance by activating the CN formation pathways (i.e. HCN photodissociation and ionization of carbon; Boger & Sternberg 2005).

In NGC 7469, the CN (3 − 2)/CN (2 − 1) ratio appears to be lowest toward the edges of the map, with mid-range values in the gas surrounding the nucleus, and the highest ratio in the nuclear pixels. We find that the CN (3 − 2)/CN (2 − 1) ratio increases from the non-nuclear value of 0.30 ± 0.04 to a value of 0.45 ± 0.06 in the nucleus. The increased CN excitation in this galaxy can thus be attributed to the conditions near the central AGN and surrounding starburst ring. It is apparent that the environment in the nucleus of NGC 7469 has a significant impact on the higher CN excitation. X-rays from the AGN will enhance the bulk temperature of the gas, while PDRs will have higher surface temperatures. In this way, the heating of the gas in the centre of NGC 7469 could be reflected in the CN excitation. We note that it is unclear how far the X-rays will reach, however, and that at our resolution of ~ 300 pc in this galaxy we do not resolve the XDR to localize the extent of AGN gas heating.

While we do not find any localized enhancement in the CN $(3-2)$/CN $(2-1)$ ratio in IRAS 13120, the CN $(3-2)$ emission is high throughout the galaxy. We find higher CN $(3-2)$/CN $(2-1)$ ratios (> 0.5) in both the global and continuum peak measurements of IRAS 13120 than in any regions of NGC 3256 (< 0.3) or the non-nuclear region of NGC 7469 (~ 0.3). The nuclear region of NGC 7469 has a CN $(3-2)$/CN $(2-1)$ ratio of 0.45, that is similar to the global ratio in IRAS 13120. Our ability to resolve different contributions to the excitation to CN $(3-2)$ in IRAS 13120 is limited, while we are better able to localize the effect of the AGN on this ratio in NGC 7469. In any case, both the starburst and AGN contributions in IRAS 13120 will help to increase the excitation of CN to higher values than we find in NGC 3256 and the non-nuclear region of NGC 7469.

We also find a local increase in the CN $(3-2)$/CN $(2-1)$ ratio in the northern nucleus of NGC 3256 (~ 0.27) compared to the southern nucleus (~ 0.22) and non-nuclear pixels (~ 0.21). However, these ratios are not significantly different once uncertainties on the measured values are taken into account. The higher CN $(3-2)$/CN $(2-1)$ ratio in the northern nucleus of NGC 3256 could be caused by the more widespread starburst in the northern nucleus. At our resolution (~ 470 pc), we do not completely resolve the edge-on southern nucleus and therefore will have lower excitation gas from non-nuclear regions mixed into the beam. Sakamoto et al. (2014) also observed enhanced CN emission associated with the molecular outflows in the northern nucleus of NGC 3256. The CN emission could thus be enhanced as a result of outflow chemistry that is influenced by far-UV emission from massive stars that are formed in the outflow (e.g. Cicone et al. 2020). Cicone et al. (2020) note, however, that CN enhancement in the outflow of NGC 3256 is weaker than in Mrk 231.

The CN $(2-1)$/CN $(1-0)$ intensity ratio

The CN $(2-1)$/CN $(1-0)$ ratio has a consistent slope (~ 0.9) and ratio (~ 0.8) in NGC 7469 and IRAS 13120. This result suggests that the conditions in these two galaxies produce similar excitation conditions for CN. Radiation in the nuclear region of NGC 7469 is dominated by X-rays from the AGN. However, at our resolution of ~ 304 pc, we will include more than just the X-ray effects on the circumnuclear disc of molecular gas contained within the central beam. The $2-10$ keV luminosity of the type 1 Seyfert nucleus is $L_{2\text{-}10\,\mathrm{keV}} = 1.5 \times 10^{43}$ erg s^{-1} (Liu et al. 2014). The AGN accounts for $30-40$ per cent of the IR luminosity in NGC 7469 (Alonso-Herrero et al. 2012). IRAS 13120 has a Compton thick AGN that accounts for $17-33.4$ per cent of the total IR luminosity (Iwasawa et al. 2011; Teng et al. 2015; Veilleux et al. 2013). Teng et al. (2015) find the $2-10$ keV absorption-corrected luminosity of IRAS 13120 is 1.25×10^{43} erg s^{-1}, which is comparable to that in NGC 7469. At our resolution, we are unable to distinguish between effects from the AGN and/or starburst activity in IRAS 13120. The presence of both UV and X-ray radiation fields should increase the CN abundance (Boger & Sternberg 2005; Meijerink & Spaans 2005; Meijerink et al. 2007). Our results indicate that the different radiation fields in NGC 7469 and IRAS 13120 seem to affect the molecular gas in a similar way.

The offset to lower CN $(2-1)$/CN $(1-0)$ ratios on the whole in NGC 3256 is interesting. The CN $(1-0)$ data for NGC 3256 is our only data set from ALMA Cycle 0. As such, the flux measurements and intensity ratios using this line in this galaxy have the highest calibration uncertainties of our sample. Given the similarity of the slopes in the CN $(2-1)$/CN $(1-0)$ ratio of all three galaxies, the offset in the ratio in NGC 3256 could be due to large observational uncertainties. The difference in the CN $(2-1)$/CN $(1-0)$ ratio in NGC 3256 of ~ 0.45 compared to the ratios in NGC 7469 and IRAS 13120 of ~ 0.8 (Fig. 2.3) should be treated with caution until this is confirmed with follow-up observations. If real, the offset to lower ratios could be due to different excitation conditions in the dense gas of this galaxy. The small contribution from any AGN in NGC 3256 (< 5 per cent; Alonso-Herrero et al. 2012) could perhaps contribute to the lower (< 0.5) CN $(2-1)$/CN $(1-0)$ ratio compared to those in NGC 7469 and IRAS 13120 (both > 0.75). The X-ray luminosity in NGC 3256 is $L_{2\text{-}10\,\mathrm{keV}} = 1.5 \times 10^{40}$ erg s^{-1} (Ohyama et al. 2015), three orders of magnitude smaller than both NGC 7469 and IRAS 13120. The models by Meijerink et al. (2007) indicate that CN abundance will be more strongly affected in the presence of XDRs than PDRs, suggesting that the higher CN intensity ratios we find in IRAS 13120 and NGC 7469 could be a result of the influence of the AGN. If both the UV and X-ray fields created in NGC 3256 are weaker than those found in IRAS 13120 or NGC 7469, the CN $(1-0)$ emission could dominate over the CN $(2-1)$ as conditions are not favourable for CN to be excited to higher levels. Future non-LTE modelling to estimate the opacities, temperatures, and densities in these galaxies will allow us to better explain the offset we see in the CN $(2-1)$/CN $(1-0)$ ratio in NGC 3256.

2.4.3 The CN/HCN intensity ratio as a probe of radiation field

The HCN $J = 1-0$ and CN $N = 1-0$ transitions have energies of ~ 4.25 K and ~ 5.4 K, respectively, suggesting they trace molecular gas of similar temperatures and densities. In fact, recent work using ALMA observations has found that the global observed CN $(1-0)$/HCN $(1-0)$ intensity ratio is nearly constant over 3 orders of magnitude change in Σ_{SFR} across a number of different galactic environments, making CN a potentially novel molecule with which to study dense gas (Wilson et al. *in prep*). The average CN $(1-0)$/HCN $(1-0)$ ratio[5] in their sample of 9 galaxies is 0.866 ± 0.096, with a standard deviation of 0.29. Wilson et al. (*in prep*) use an additional criteria of detecting 93 GHz radio continuum emission in order to compare their CN $(1-0)$/HCN $(1-0)$ ratios to Σ_{SFR}. Since we are not requiring 93 GHz continuum detections, we can extend our analysis to the lower line intensities where we find most of our variations in the CN $(1-0)$/HCN $(1-0)$ ratios. Including both CN $N = 1-0$ hyperfine groups, we find ratios of $1.1 - 1.7$ for the CN $(1-0)$/HCN $(1-0)$ ratio.

We find variations in the observed intensity ratios between CN and HCN lines, particularly in regions associated with high starburst activity. For example, the CN $(1-0)$/HCN $(1-0)$ ratio in IRAS 13120 has a value of 1.7 ± 0.1. IRAS 13120 is a ULIRG with a higher Σ_{SFR} than both NGC 3256 and NGC 7469. The increased star formation activity in this galaxy should be indicative of an increase in UV radiation due to young, massive star formation, which could indicate that the UV radiation more strongly affects the gas properties. The northern nucleus of NGC 3256 has the same CN $(1-0)$/HCN $(1-0)$ ratio of 1.7 ± 0.1 and is also a starburst with a high UV field (Sakamoto et al. 2014). These results will be explored further using non-LTE analysis to calculate the CN/HCN abundance ratio in the presence of UV fields using a PDR model in a future paper.

The CN $(1-0)$/HCN $(1-0)$ ratio in the southern nucleus of NGC 3256 (~ 1.1) is more comparable with that of NGC 7469 (~ 1.1). In the southern nucleus of NGC

[5] In their analysis, which includes the galaxies NGC 3256, NGC 7469, and IRAS 13120, they consider only the strong CN $(1-0)$ hyperfine line, which accounts for ~ 70 per cent of the total CN $(1-0)$ line emission for optically thin lines (Shirley 2015; Meier et al. 2015).

3256, the AGN and disc are more compact and therefore the sphere of influence of any enhancement from a UV field due to star formation or X-rays from the AGN is relatively small compared to the extent of the starburst in the northern nucleus. The exact impact of X-ray versus UV radiation fields on CN and HCN excitation is beyond the scope of this work.

We find a relatively constant CN $(1-0)$/HCN $(1-0)$ intensity ratio across NGC 7469, suggesting that the presence of an AGN and XDR does not affect the ratio as significantly as the starbursts do in IRAS 13120 and the northern nucleus of NGC 3256. Non-LTE modelling to determine the CN and HCN abundance ratio is needed to determine if the CN/HCN abundance ratio is also constant. Izumi et al. (2015) suggest that high-temperature gas-phase chemistry in NGC 7469 could significantly enhance the abundance of HCN through an activated formation pathway from CN when $T > 300$ K (e.g. Harada et al. 2010).

Throughout this paper, we have described the CN/HCN intensity ratios from observations of multiple CN and HCN lines in three galaxies. We find variations in the CN $(1-0)$/HCN $(1-0)$ intensity ratio in NGC 3256, from values of ~ 1 in the non-nuclear pixels to values of ~ 1.7 in the northern nucleus. A simple LTE calculation suggests that the CN and HCN column densities should be in the range of $10^{13}-10^{17}$ cm^{-2}. We used this column density range to perform a simple non-LTE calculation with the online version of RADEX[6] (van der Tak et al. 2007). Using a gas temperature of 40 K, an H_2 number density of 10^7 cm^{-3}, and a line width of 10 km s^{-1}, we reproduce CN $(1-0)$/HCN $(1-0) \sim 1$ in the non-nuclear pixels of NGC 3256 with a column density ratio of $N_{CN}/N_{HCN} \sim 10$. The intensity ratio of CN $(1-0)$/HCN $(1-0) \sim 1.7$ in the northern nucleus of NGC 3256 is reproduced with $N_{CN}/N_{HCN} \sim 24$. Further non-LTE analysis will be performed in future work, with more analysis on the specific gas properties and optical depths in NGC 3256, NGC 7469, and IRAS 13120 that can produce our observed CN and HCN intensity ratios. In this way, we will be able to compare our data to the expectation that the CN/HCN abundance ratio should increase in the presence of a starburst or increased radiation field (c.f. Fuente et al. 1993, 1995; Aalto et al. 2002; Boger & Sternberg 2005; Meijerink & Spaans 2005).

[6] https://home.strw.leidenuniv.nl/ moldata/radex.html

2.5 Conclusions

In our observational study of CN and HCN lines in a sample of three U/LIRG galaxies, we find subtle variations in line intensity ratios within and among galaxies. These variations can be localized to regions of starburst and/or AGN activity. Both CN and HCN excitation are enhanced in the higher intensity regions.

Our main conclusions are summarized as follows:

(i) We find variations in the HCN $(3-2)$/HCN $(1-0)$ ratio in NGC 3256 and NGC 7469. Both galaxies have superlinear trends with slopes > 1.5. The global and non-nuclear HCN $(3-2)$/HCN $(1-0)$ and HCN $(4-3)$/HCN $(1-0)$ ratios are the same (~ 0.3) in the two galaxies, which suggests similar excitation conditions. The enhanced HCN excitation is seen in both nuclei of NGC 3256 and in the nucleus of NGC 7469. The HCN $(3-2)$/HCN $(1-0)$ ratio in NGC 7469 shows the largest difference between non-nuclear (0.33 ± 0.04) and nuclear (0.52 ± 0.06) regions. We attribute the regions of enhanced HCN excitation in NGC 7469 to the central AGN, where both an XDR and shocks in outflows can heat the gas and increase HCN excitation. The HCN $(3-2)$/HCN $(1-0)$ ratios are increased relative to the disk in both nuclei of NGC 3256 due to both starburst and AGN effects, although to a lesser extent than in the nucleus of NGC 7469.

(ii) The HCN $(3-2)$/HCN $(1-0)$ ratio in IRAS 13120 is higher (~ 0.8) than both NGC 3256 ($\sim 0.27-0.39$) and NGC 7469 ($\sim 0.33-0.52$). We find little spatial variation in the HCN excitation of IRAS 13120. We attribute the higher HCN $(3-2)$/HCN $(1-0)$ ratios to the higher star formation rate surface density and contribution of the Compton-thick AGN to the total IR luminosity.

(iii) We find relatively constant CN $(2-1)$/CN $(1-0)$ ratios and subtle variations in the CN $(3-2)$/CN $(2-1)$ ratio in our galaxy sample. We find an offset to lower ratios of ~ 0.45 in the CN $(2-1)$/CN $(1-0)$ ratio in NGC 3256 compared to ~ 0.8 in NGC 7469 and IRAS 13120. We note that this offset could arise from the difference in the fraction of AGN contribution to the total IR luminosity in NGC 3256 (< 5 per cent) compared to NGC 7469 ($32-40$ per cent) and IRAS 13120 ($17-33.4$ per cent). Further non-LTE modelling analysis may help explain the origin of this offset.

(iv) The CN $(1-0)$/HCN $(1-0)$ ratio is higher (1.7) in the northern nucleus of NGC 3256 than in the rest of the galaxy. We find a similarly high CN $(1-0)$/HCN $(1-0)$ ratio in the starburst galaxy IRAS 13120. The intense starburst activity in the regions with large CN $(1-0)$/HCN $(1-0)$ ratios suggests the enhanced ratio may be due to increased exposure to UV radiation fields. We note that opacity effects could potentially be important and determining the CN/HCN abundance ratios is the next step in this analysis. The CN $(1-0)$/HCN $(1-0)$ ratio in NGC 7469 is ~ 1.1 and is relatively constant across the entire galaxy. NGC 7469 is dominated by a nuclear AGN, which does not appear to affect the CN/HCN ratio as significantly as the starbursts in the other galaxies.

The more detailed examination of CN and HCN conducted in this work helps confirm the conclusion of Wilson et al. (in preparation) that CN is a viable tracer of dense gas in galaxies. However, it is clear that more work is needed to understand the complex relationship between CN and HCN in dense gas exposed to strong UV and X-ray radiation fields. Future non-LTE radiative transfer modelling of the CN and HCN lines in this galaxy sample will allow us to determine physical properties such as gas temperature, density, opacity, and molecular abundance. Using the molecular abundances, we will be able to compare our results to models predicting CN/HCN abundance ratios and further explore the effects of radiation fields on molecular gas properties.

Acknowledgements

We thank the anonymous referee for detailed comments that significantly improved the content of this paper. We would like to thank Kazushi Sakamoto for his insightful comments and important feedback on this work. We also thank Nanase Harada for her collaboration and contribution of ALMA data to this work. This paper makes use of the following ALMA data:
ADS/JAO.ALMA#2011.0.00525.S,
ADS/JAO.ALMA#2012.1.00034.S,
ADS/JAO.ALMA#2012.1.00165.S,
ADS/JAO.ALMA#2013.1.00218.S,
ADS/JAO.ALMA#2013.1.00379.S,
ADS/JAO.ALMA#2015.1.00102.S,
ADS/JAO.ALMA#2015.1.00287.S,
ADS/JAO.ALMA#2015.1.00412.S,
ADS/JAO.ALMA#2015.1.00993.S,

ADS/JAO.ALMA#2016.1.00777.S,
ADS/JAO.ALMA#2018.1.00493.S. ALMA is a partnership of ESO (representing its member states), NSF (USA), and NINS (Japan), together with NRC (Canada), MOST and ASIAA (Taiwan), and KASI (Republic of Korea), in cooperation with the Republic of Chile. The Joint ALMA Observatory is operated by ESO, AUI/NRAO, and NAOJ. The National Radio Astronomy Observatory is a facility of the National Science Foundation operated under cooperative agreement by Associated Universities, Inc.

This research has made use of the NASA/IPAC Extragalactic Database (NED), which is funded by the National Aeronautics and Space Administration and operated by the California Institute of Technology, and the SIMBAD database, operated at CDS, Strasbourg, France (Wenger et al. 2000). The LAMDA database is supported by the Netherlands Organization for Scientific Research (NWO), the Netherlands Research School for Astronomy (NOVA), and the Swedish Research Council. This research has also made use of ASTROPY[7], a community-developed core PYTHON package for Astronomy (Astropy Collaboration et al. 2013; Price-Whelan et al. 2018). A significant amount of this research has also made use of the MATPLOTLIB (Hunter 2007), NUMPY (van der Walt et al. 2011), JUPYTER NOTEBOOK (Kluyver et al. 2016) and LINMIX[8] (Meyers 2018) PYTHON packages.

CDW acknowledges financial support from the Canada Council for the Arts through a Killam Research Fellowship. The research of CDW is supported by grants from the Natural Sciences and Engineering Research Council of Canada and the Canada Research Chairs program. BL wishes to acknowledge partial support from a Natural Sciences and Engineering Research Council of Canada Alexander Graham Bell Canada Graduate Scholarship-Master's (CGS-M) and a Jim & Annette Ray Ontario Graduate Scholarship (OGS).

Data Availability

This research is based on public data available in the ALMA archive and the exact project IDs can be found in Table 2.2. The whole dataset and processed data cubes can be obtained from the authors by request.

[7]http://www.astropy.org
[8]https://linmix.readthedocs.io/en/latest/src/linmix.html

TABLE 2.6: Data reduction imaging properties and line sensitivities.

Imaging property	NGC 3256	NGC 7469	IRAS 13120
Beam size[a]	2.2 arcsec	0.95 arcsec	1.1 arcsec
Velocity resolution (km s^{-1})[b]	26.43	20.68	20.64
Moment 0 map velocity ranges (km s^{-1})			
HCN(1 – 0)	2584.30 – 2980.75	4632.72 – 5087.68	8744.48 – 9363.68
HCN(3 – 2)	2584.30 – 2980.75	4624.08 – 5079.04	8744.48 – 9363.68
HCN(4 – 3)	2584.30 – 2980.75	4632.72 – 5087.68	8744.48 – 9363.68
CN(1 – 0)	2555.72 – 3850.79	4503.40 – 5087.68	8744.48 – 9363.68
CN(2 – 1)	1805.72 – 3021.50	3865.44 – 4940.80	8003.20 – 9262.24
CN(3 – 2)	1905.72 – 3121.50	3944.76 – 5082.16	8044.48 – 9179.68
Smoothed cube line sensitivities (mJy beam^{-1})[c]			
HCN(1 – 0)	0.241	0.280	0.958
HCN(3 – 2)	1.624	0.478	0.628
HCN(4 – 3)	1.059	0.872	2.166
CN(1 – 0)	0.635	0.508	1.220
CN(2 – 1)	1.021	0.277	0.424
CN(3 – 2)	0.570	0.753	1.035

Notes. [a]The beams were smoothed, rounded, and matched to this resolution for all lines.
[b]The velocity resolution and pixel size were matched between all lines.
[c]The smoothed cube line sensitivities were determined using the same line-free channels as for the dirty cubes. Integrated intensity map 3.5σ cut-offs used these smoothed cube sensitivities.

2.A Appendix: Moment maps and additional line ratio measures

2.A.1 Integrated intensity maps

The moment 0 maps of all lines in our three galaxies are shown in Figs. 2.5, 2.6, and 2.7. The RMS noise measured from the smoothed cubes and the velocity ranges used are given in Table 2.6.

2.A.2 Full measured intensity ratios

Table 2.8 presents the measured CN and HCN intensity ratios in the global, nuclear, and non-nuclear regions of NGC 3256, NGC 7469, and IRAS 13210 for additional pairs of lines beyond those given in Table 2.4.

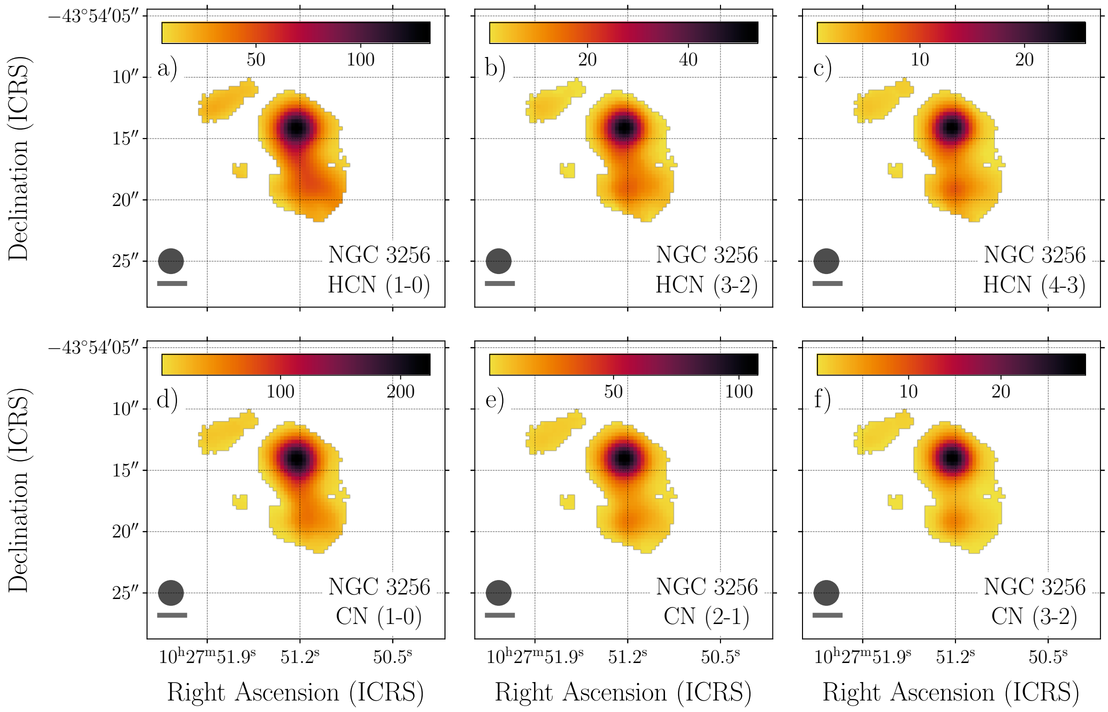

FIGURE 2.5: Integrated intensity maps in K km s^{-1} of NGC 3256 for all six lines. In the lower left corner, the circle indicates the beam size of 2.2 arcsec and the scale bar is set at 500 pc. NGC 3256 clearly has a peak intensity in the northern nucleus. The southern nucleus also shows a local increase in intensity. One spiral arm feature can be seen at our sensitivity in the top left corner of the maps.

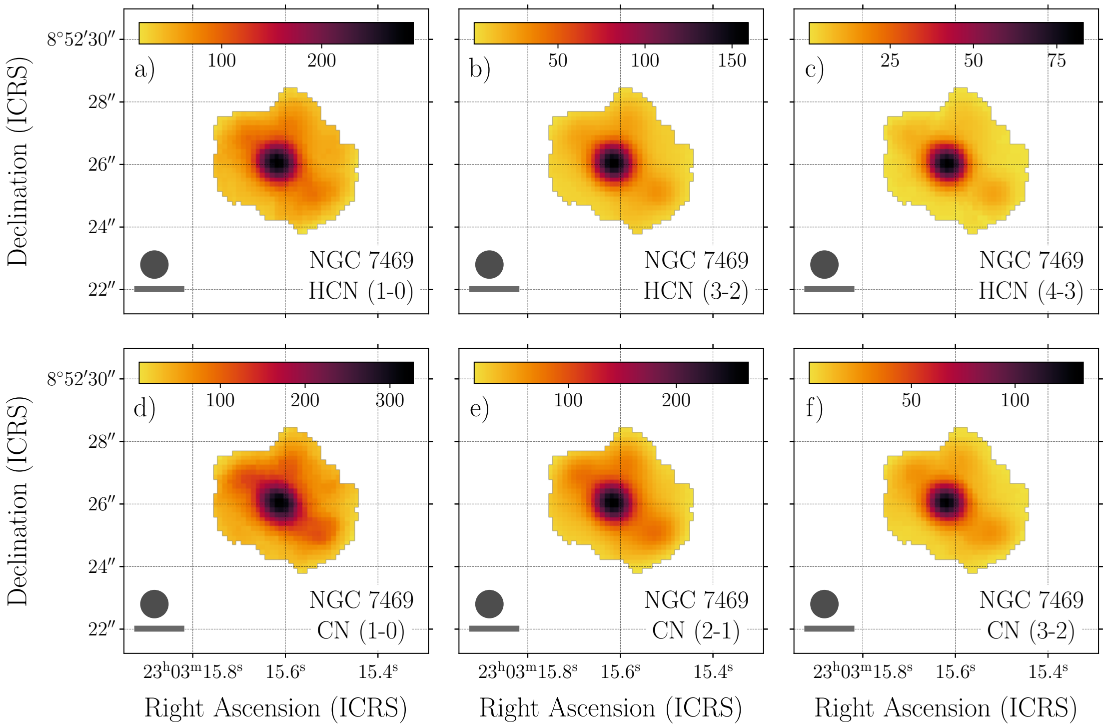

FIGURE 2.6: Integrated intensity maps in K km s^{-1} of NGC 7469 for all six lines. In the lower left corner, the circle indicates the beam size of 0.95 arcsec and the scale bar is set at 500 pc. The peak intensity corresponds to the central nuclear region hosting the AGN. We see some increase in intensity in the region surrounding the nucleus, potentially corresponding to the starburst ring found in this galaxy.

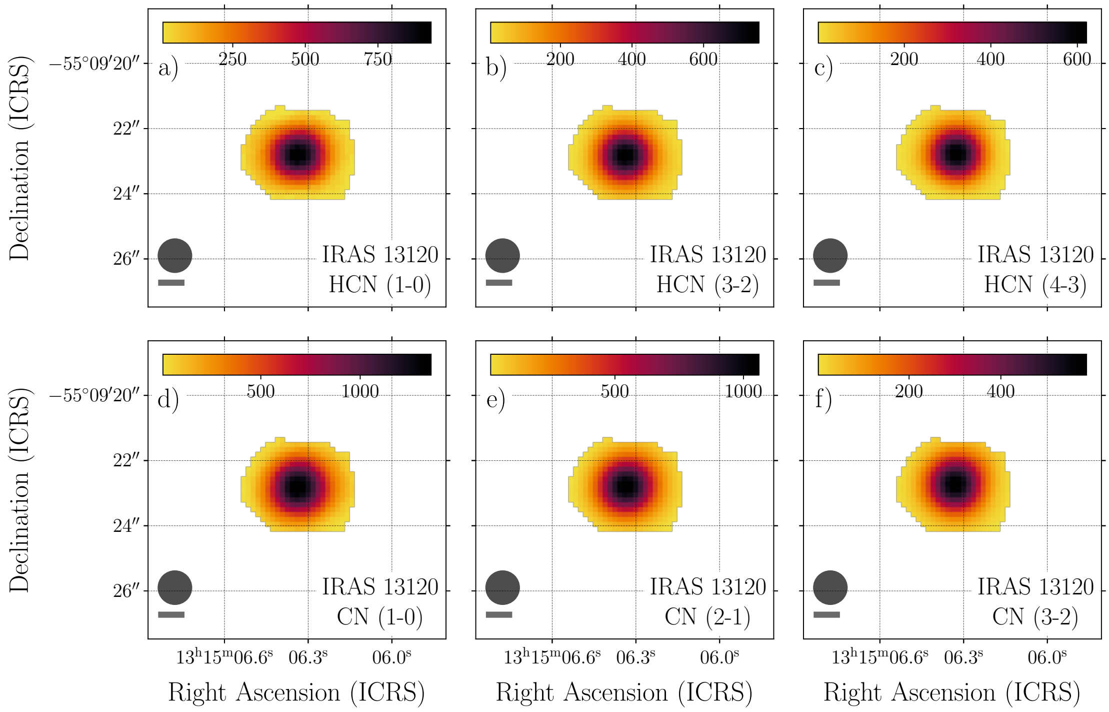

FIGURE 2.7: Integrated intensity maps in K km s^{-1} of IRAS 13120 for all six lines. In the lower left corner, the circle indicates the beam size of 1.1 arcsec and the scale bar is set at 500 pc. The furthest galaxy in our sample, IRAS 13120 has quite a symmetric appearance. The intensities of individual lines at the central peak are much higher than those detected in NGC 3256 and NGC 7469.

TABLE 2.7: Slope and intercept from pixel-by-pixel comparisons.

Ratio	Parameters[a]	NGC 3256	NGC 7469	IRAS 13120	All pixels
$\frac{\text{HCN (3 – 2)}}{\text{HCN (1 – 0)}}$					
	m	1.53 ± 0.07	1.55 ± 0.05	0.84 ± 0.06	1.46 ± 0.04
	b	−1.4 ± 0.1	−1.45 ± 0.08	0.3 ± 0.1	−1.26 ± 0.07
$\frac{\text{HCN (4 – 3)}}{\text{HCN (1 – 0)}}$					
	m	1.50 ± 0.08	2.1 ± 0.1	1.19 ± 0.07	1.46 ± 0.04
	b	−1.7 ± 0.1	−2.9 ± 0.2	−0.7 ± 0.1	−1.26 ± 0.07
$\frac{\text{HCN (4 – 3)}}{\text{HCN (3 – 2)}}$					
	m	0.99 ± 0.04	1.34 ± 0.05	1.3 ± 0.1	1.13 ± 0.03
	b	−0.34 ± 0.04	−0.91 ± 0.06	−0.9 ± 0.2	−0.55 ± 0.04
$\frac{\text{CN (2 – 1)}}{\text{CN (1 – 0)}}$					
	m	0.95 ± 0.03	0.93 ± 0.03	0.91 ± 0.02	1.07 ± 0.02
	b	−0.29 ± 0.05	−0.00 ± 0.06	0.11 ± 0.06	−0.33 ± 0.04
$\frac{\text{CN (3 – 2)}}{\text{CN (1 – 0)}}$					
	m	1.16 ± 0.07	1.42 ± 0.07	0.99 ± 0.05	1.07 ± 0.02
	b	−1.4 ± 0.1	−1.4 ± 0.1	−0.4 ± 0.1	−0.33 ± 0.04
$\frac{\text{CN (3 – 2)}}{\text{CN (2 – 1)}}$					
	m	1.26 ± 0.05	1.55 ± 0.04	1.11 ± 0.04	1.33 ± 0.02
	b	−1.05 ± 0.06	−1.47 ± 0.06	−0.56 ± 0.08	−1.11 ± 0.03
$\frac{\text{CN (1 – 0)}}{\text{HCN (1 – 0)}}$					
	m	1.49 ± 0.06	1.26 ± 0.05	0.83 ± 0.05	1.25 ± 0.03
	b	−0.74 ± 0.09	−0.40 ± 0.08	0.6 ± 0.1	−0.38 ± 0.06
$\frac{\text{CN (2 – 1)}}{\text{HCN (3 – 2)}}$					
	m	0.89 ± 0.05	0.77 ± 0.02	0.86 ± 0.04	0.91 ± 0.02
	b	0.35 ± 0.05	0.70 ± 0.03	0.54 ± 0.08	0.44 ± 0.03
$\frac{\text{CN (3 – 2)}}{\text{HCN (3 – 2)}}$					
	m	1.06 ± 0.09	1.17 ± 0.05	0.94 ± 0.06	1.21 ± 0.04
	b	−0.56 ± 0.08	−0.35 ± 0.06	0.1 ± 0.1	−0.52 ± 0.05
$\frac{\text{CN (3 – 2)}}{\text{HCN (4 – 3)}}$					
	m	1.14 ± 0.07	0.85 ± 0.03	0.69 ± 0.04	1.01 ± 0.04
	b	−0.23 ± 0.05	0.46 ± 0.03	0.75 ± 0.07	0.12 ± 0.04

Notes. [a]Fit parameters are determined from Linmix linear fitting of the form $\log(y) = m \log(x) + b$.

TABLE 2.8: Additional CN and HCN measured intensity ratios.

Region	$\frac{\text{HCN}\,(3-2)}{\text{HCN}\,(1-0)}$	$\frac{\text{HCN}\,(4-3)}{\text{HCN}\,(1-0)}$	$\frac{\text{HCN}\,(4-3)}{\text{HCN}\,(3-2)}$	$\frac{\text{CN}\,(2-1)}{\text{CN}\,(1-0)}$	$\frac{\text{CN}\,(3-2)}{\text{CN}\,(1-0)}$	$\frac{\text{CN}\,(3-2)}{\text{CN}\,(2-1)}$	$\frac{\text{CN}\,(1-0)}{\text{HCN}\,(1-0)}$	$\frac{\text{CN}\,(2-1)}{\text{HCN}\,(3-2)}$	$\frac{\text{CN}\,(3-2)}{\text{HCN}\,(3-2)}$	$\frac{\text{CN}\,(3-2)}{\text{HCN}\,(4-3)}$
NGC 3256										
Global	0.29(3)	0.13(2)	0.46(7)	0.44(5)	0.10(1)	0.22(3)	1.24(9)	1.9(3)	0.42(6)	0.9(1)
North nucleus	0.39(4)	0.18(2)	0.48(7)	0.47(5)	0.13(1)	0.27(4)	1.7(1)	2.1(3)	0.55(8)	1.2(2)
South nucleus	0.33(4)	0.15(2)	0.46(7)	0.44(5)	0.10(1)	0.22(3)	1.12(9)	1.5(2)	0.34(5)	0.8(1)
Non-nuclear	0.27(3)	0.12(1)	0.45(6)	0.43(5)	0.09(1)	0.21(3)	1.14(8)	1.8(3)	0.38(5)	0.8(1)
NGC 7469										
Global	0.36(4)	0.14(2)	0.40(6)	0.76(9)	0.25(3)	0.32(5)	1.12(8)	2.4(3)	0.8(1)	1.9(3)
Nucleus	0.52(6)	0.25(3)	0.48(7)	0.80(9)	0.36(4)	0.45(6)	1.13(9)	1.7(2)	0.8(1)	1.6(2)
Non-nuclear	0.33(4)	0.12(1)	0.37(5)	0.76(9)	0.22(3)	0.30(4)	1.11(8)	2.6(4)	0.8(1)	2.1(3)
IRAS 13120										
Global	0.80(9)	0.61(7)	0.8(1)	0.77(9)	0.40(5)	0.53(8)	1.7(1)	1.6(2)	0.8(1)	1.1(2)
Continuum peak	0.79(9)	0.70(8)	0.9(1)	0.80(9)	0.45(5)	0.57(8)	1.5(1)	1.5(2)	0.8(1)	0.9(1)

Notes. The uncertainties presented here are the measurement and calibration uncertainties and given as the uncertainty on the last digit (i.e. $0.29(3) = 0.29 \pm 0.03$). Ratios include the 5 per cent (Band 3) and 10 per cent (Band 6 and 7) ALMA calibration uncertainties for each line.

2.A.3 Additional pixel-by-pixel comparisons

We present additional pixel-by-pixel correlations between HCN $(4-3)$ and HCN $(1-0)$, CN $(3-2)$ and CN $(1-0)$, CN $(2-1)$ and HCN $(3-2)$, and CN $(3-2)$ and HCN $(4-3)$ using the intensities in the re-sampled moment 0 maps in the scatter plots of Figs. 2.9 and 2.8. In Table 2.7, we present the measured slopes and intercepts from the Linmix linear regression fits to the various line ratios explored in the pixel-by-pixel comparisons. In this table we also include the HCN $(4-3)$/HCN $(1-0)$, CN $(3-2)$/CN $(1-0)$, CN $(2-1)$/HCN $(3-2)$, and CN $(3-2)$/HCN $(4-3)$ ratios. The linear fits were in the form $\log(y) = m \log(x) + b$ on to the pixel-by-pixel comparisons of the re-sampled moment 0 maps and we present both m and b values here. Inclination corrections are as described in Section 2.2.4. Fits to all pixels from all galaxies for the various line ratios are presented in Table 2.7, as well.

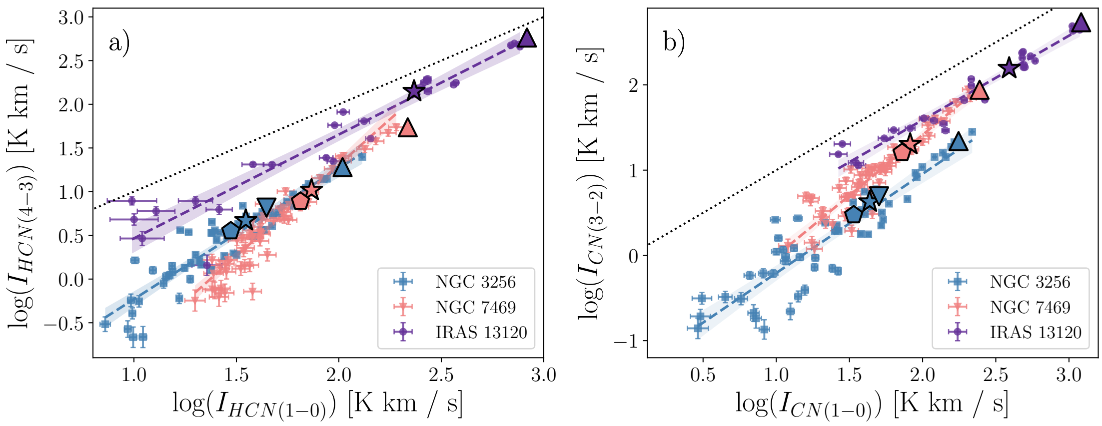

FIGURE 2.8: Pixel-by-pixel comparisons of individual line intensities in each galaxy. The higher-J/N transition of the two lines is always plotted on the y-axis. The black dotted line is the one-to-one line. Blue squares correspond to NGC 3256; pink inverted triangles correspond to NGC 7469; purple circles correspond to IRAS 13120. The dashed lines in each colour represent the Linmix fits for each galaxy, with the shaded region representing the 95 per cent confidence interval of these fits. Large stars show the global ratio in each galaxy and large pentagons show the non-nuclear ratios in NGC 3256 and NGC 7469. Large triangles show ratios for the northern nucleus of NGC 3256, the nucleus of NGC 7649, and the continuum peak in IRAS 13120, while the large inverted triangle shows the ratio for the southern nucleus of NGC 3256.

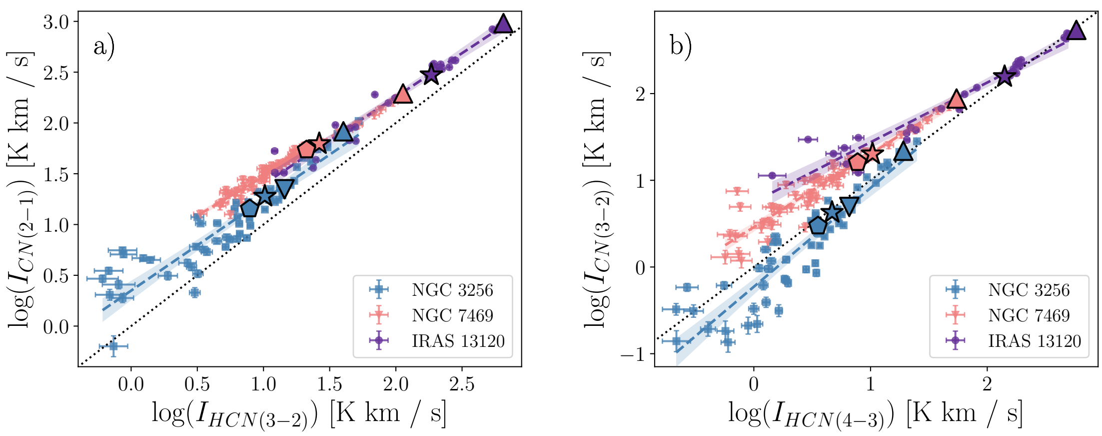

FIGURE 2.9: Pixel-by-pixel comparisons for CN compared to HCN for selected transitions. For plot descriptions, refer to the caption of Fig. 2.8.

Bibliography

Aalto S., Polatidis A. G., Hüttemeister S., Curran S. J., 2002, A&A, 381, 783

Aalto S., Garcia-Burillo S., Muller S., Winters J. M., van der Werf P., Henkel C., Costagliola F., Neri R., 2012, A&A, 537, A44

Aladro R., et al., 2013, A&A, 549, A39

Alonso-Herrero A., Pereira-Santaella M., Rieke G. H., Rigopoulou D., 2012, ApJ, 744, 2

Astropy Collaboration et al., 2013, A&A, 558, A33

Bachiller R., Fuente A., Bujarrabal V., Colomer F., Loup C., Omont A., de Jong T., 1997, A&A, 319, 235

Bayet E., Williams D. A., Hartquist T. W., Viti S., 2011, MNRAS, 414, 1583

Boger G. I., Sternberg A., 2005, ApJ, 632, 302

Briggs D. S., 1995, in American Astronomical Society Meeting Abstracts. p. 112.02

Brunetti N., Wilson C. D., Sliwa K., Schinnerer E., Aalto S., Peck A. B., 2021, MNRAS, 500, 4730

Chapillon E., Guilloteau S., Dutrey A., Piétu V., Guélin M., 2012, A&A, 537, A60

Cicone C., Maiolino R., Aalto S., Muller S., Feruglio C., 2020, A&A, 633, A163

Davies R. I., Tacconi L. J., Genzel R., 2004, ApJ, 602, 148

Fluetsch A., et al., 2019, MNRAS, 483, 4586

Fuente A., Martin-Pintado J., Cernicharo J., Bachiller R., 1993, A&A, 276, 473

Fuente A., Martin-Pintado J., Gaume R., 1995, ApJ, 442, L33

Ganeshalingam M., Li W., Filippenko A. V., 2013, MNRAS, 433, 2240

Gao Y., Solomon P. M., 2004, ApJ, 606, 271

García-Burillo S., et al., 2010, A&A, 519, A2

Ginard D., et al., 2015, A&A, 578, A49

Greaves J. S., Church S. E., 1996, MNRAS, 283, 1179

Harada N., Herbst E., Wakelam V., 2010, ApJ, 721, 1570

Harada N., Thompson T. A., Herbst E., 2013, ApJ, 765, 108

Harada N., Sakamoto K., Martín S., Aalto S., Aladro R., Sliwa K., 2018, ApJ, 855, 49

Hunter J. D., 2007, Computing in Science & Engineering, 9, 90

Imanishi M., Nakanishi K., Izumi T., 2016, AJ, 152, 218

Iwasawa K., et al., 2011, A&A, 528, A137

Izumi T., et al., 2013, PASJ, 65, 100

Izumi T., et al., 2015, ApJ, 811, 39

Izumi T., et al., 2016, ApJ, 818, 42

Izumi T., et al., 2020, ApJ, 898, 75

Kelly B. C., 2007, ApJ, 665, 1489

Kennicutt R. C., Evans N. J., 2012, ARA&A, 50, 531

Kepley A. A., 2019, Auto-multithresh: Automated masking for clean (ascl:1909.001)

Kluyver T., et al., 2016, in Loizides F., Scmidt B., eds, Positioning and Power in Academic Publishing: Players, Agents and Agendas. IOS Press, pp 87–90, https://eprints.soton.ac.uk/403913/

Kohno K., 2005, in Hüttmeister S., Manthey E., Bomans D., Weis K., eds, American Institute of Physics Conference Series Vol. 783, The Evolution of Starbursts. pp 203–208 (arXiv:astro-ph/0508420), doi:10.1063/1.2034987

Lira P., Ward M., Zezas A., Alonso-Herrero A., Ueno S., 2002, MNRAS, 330, 259

Liu T., Wang J.-X., Yang H., Zhu F.-F., Zhou Y.-Y., 2014, ApJ, 783, 106

Lonsdale C. J., Farrah D., Smith H. E., 2006, Ultraluminous Infrared Galaxies. Springer, p. 285, doi:10.1007/3-540-30313-8_9

Martín S., et al., 2015, A&A, 573, A116

McMullin J. P., Waters B., Schiebel D., Young W., Golap K., 2007, in Shaw R. A., Hill F., Bell D. J., eds, Astronomical Society of the Pacific Conference Series Vol. 376, Astronomical Data Analysis Software and Systems XVI. p. 127

Meier D. S., et al., 2015, ApJ, 801, 63

Meijerink R., Spaans M., 2005, A&A, 436, 397

Meijerink R., Spaans M., Israel F. P., 2007, A&A, 461, 793

Meyers J. E., 2018, linmix package, https://github.com/jmeyers314/linmix/blob/master/linmix/linmix.py

Michiyama T., et al., 2018, ApJ, 868, 95

Neff S. G., Ulvestad J. S., Campion S. D., 2003, ApJ, 599, 1043

Ohyama Y., Terashima Y., Sakamoto K., 2015, ApJ, 805, 162

Pérez-Torres M., Mattila S., Alonso-Herrero A., Aalto S., Efstathiou A., 2021, AAPR, 29, 2

Price-Whelan A. M., et al., 2018, AJ, 156, 123

Privon G. C., et al., 2017, ApJ, 835, 213

Rodriguez-Franco A., Martin-Pintado J., Fuente A., 1998, A&A, 329, 1097

Saito T., et al., 2018, ApJ, 863, 129

Sakamoto K., Aalto S., Combes F., Evans A., Peck A., 2014, ApJ, 797, 90

Sanders D. B., Mazzarella J. M., Kim D. C., Surace J. A., Soifer B. T., 2003, AJ, 126, 1607

Shirley Y. L., 2015, PASP, 127, 299

Sliwa K., Wilson C. D., Aalto S., Privon G. C., 2017, ApJ, 840, L11

Solomon P. M., Downes D., Radford S. J. E., 1992, ApJ, 387, L55

Sternberg A., Dalgarno A., 1995, ApJS, 99, 565

Teng S. H., et al., 2015, ApJ, 814, 56

Veilleux S., et al., 2013, ApJ, 776, 27

Véron-Cetty M. P., Véron P., 2010, A&A, 518, A10

Vollmer B., Gratier P., Braine J., Bot C., 2017, A&A, 602, A51

Wenger M., et al., 2000, A&AS, 143, 9

Wilson C. D., Elmegreen B. G., Bemis A., Brunetti N., 2019, ApJ, 882, 5

Wu J., Evans Neal J. I., Gao Y., Solomon P. M., Shirley Y. L., Vanden Bout P. A., 2005, ApJ, 635, L173

Wu J., Evans Neal J. I., Shirley Y. L., Knez C., 2010, ApJS, 188, 313

van der Tak F. F. S., Black J. H., Schöier F. L., Jansen D. J., van Dishoeck E. F., 2007, A&A, 468, 627

van der Walt S., Colbert S. C., Varoquaux G., 2011, Computing in Science Engineering, 13, 22

3 | Stored in the archives: Uncovering the CN/CO intensity ratio with ALMA in nearby U/LIRGs

This chapter represents an unchanged version of the paper *Stored in the archives: Uncovering the CN/CO intensity ratio with ALMA in nearby U/LIRGs*, published in the refereed journal, *Monthly Notices of the Royal Astronomical Society*. The full reference is given below:

Ledger B.[1], Saito T.[2], Iono D.[2,3], Wilson C. D.[1], 2024, MNRAS, Volume 527, Issue 2, pp. 2963– 2990

[1]*Department of Physics and Astronomy, McMaster University, 1280 Main St. W., Hamilton, Ontario L8S 4M1, Canada*
[2]*National Astronomical Observatory of Japan, National Institutes of Natural Sciences, 2-21-1 Osawa, Mitaka, Tokyo, 181-8588*
[3]*Department of Astronomical Science, The Graduate University for Advanced Studies, SOKENDAI, 2-21-1 Osawa, Mitaka, Tokyo 181-8588*

Abstract

We present an archival Atacama Large Millimeter/submillimeter Array (ALMA) study of the cyanide radical (CN) $N = 1 - 0$ /carbon monoxide (CO) $J = 1 - 0$ intensity ratio in nearby ($z < 0.05$) ultra-luminous and luminous infrared galaxies (U/LIRGs). We identify 16 U/LIRGs that have been observed in both CN and CO lines at $\sim$ 500 pc resolution based on 16 different ALMA projects. We measure the (CN bright)/CO and (CN bright)/(CN faint) intensity ratios at an ensemble of molecular clouds scales (CN bright = CN $N = 1-0$, $J = 3/2-1/2$; CN faint = CN $N = 1-0$, $J = 1/2-1/2$ hyperfine groupings). Our global measured (CN bright)/CO ratios range $0.02 - 0.15$ in LIRGs and $0.08 - 0.17$ in ULIRGs. We attribute the larger spread in LIRGs to the variety of galaxy environments included in our sample. Overall, we find that the (CN bright)/CO ratio is higher in nuclear regions, where the physical and excitation conditions favour increased CN emission relative to the disc regions. 10 out of 11 galaxies which contain well-documented active galactic nuclei show higher ratios in the nucleus compared with the disc. Finally, we measure the median resolved (CN bright)/(CN faint) ratio and use it to estimate the total integrated CN line optical depth in ULIRGs ($\tau \sim 0.96$) and LIRGs ($\tau \sim 0.23$). The optical depth difference is likely due to the higher molecular gas surface densities found in the more compact ULIRG systems.

Keywords: ISM: molecules – ISM: photodissociation region (PDR) – galaxies: ISM – galaxies: nuclei – galaxies: Seyfert – galaxies: starburst.

3.1 Introduction

The processes of galaxy formation and evolution are guided by the rates at which stars are formed in galaxies, which makes understanding the connection between the interstellar medium (ISM) and star formation a major area of research in modern astronomy (see the review by Kennicutt & Evans 2012 and references therein). The molecular gas content of galaxies plays an important role in regulating star formation, as it is the fuel from which future stars are formed. Observers typically use carbon monoxide (CO) and a corresponding conversion factor, $\alpha_{\rm CO}$, to estimate the cold molecular gas content of galaxies (see the review by Bolatto et al. 2013 and references therein). The lowest energy rotational line, ^{12}CO ($J = 1-0$) – hereafter referred to as simply 'CO' unless otherwise specified – is often found to be optically thick and can thus be excited and observed even in the coldest parts of molecular clouds with a low excitation energy (~ 5 K) and gas densities of $n < 10^2$ cm^{-3}(Shirley 2015). CO can also be excited in the diffuse molecular gas when there is sufficient column density for self-shielding to occur (Bolatto et al. 2013). Thus, CO is a good tracer for the bulk cold gas content in the ISM. However, stars are formed in the densest regions of molecular clouds (Lada et al. 1991) and to target this dense gas ($n_{\rm H_2} \gtrsim 10^4$ cm^{-3}), molecules with higher critical densities need to be used. Molecules like hydrogen cyanide (HCN), the formyl cation (HCO^+), and carbon monosulfide (CS) are the common tracers used by observers (Wu et al. 2010; García-Burillo et al. 2012; Kennicutt & Evans 2012), with the HCN ($1-0$) line representing a well-established empirical tracer of dense gas in galaxies. Dense molecular gas has been found to correlate with the star formation rate (SFR) in galaxies on global scales with a nearly linear power law slope (Gao & Solomon 2004; Usero et al. 2015; Gallagher et al. 2018), and the correlation extends to individual molecular clouds on Galactic scales (Wu et al. 2005; Shimajiri et al. 2017).

The HCN line luminosity converts to a dense gas mass through a conversion factor ($\alpha_{\rm HCN}$, Gao & Solomon 2004). Variations in this conversion factor have been observed or predicted in the Milky Way and nearby galaxies (Graciá-Carpio et al. 2008; Vega et al. 2008; García-Burillo et al. 2012; Usero et al. 2015; Shimajiri et al. 2017; Onus et al. 2018; Jones et al. 2023). Additionally, dense gas will be exposed to strong stellar feedback and ultra-violet (UV) radiation fields from newly formed stars. Shimajiri et al. (2017) demonstrate that the HCN conversion factor depends on the strength of this UV radiation field. HCN emission has also been found to be optically thick when observed in the centres of galaxies (Jiménez-Donaire et al. 2017 and references therein), with optical depths in the range of $\tau = 2 - 11$. Since the link between HCN and dense gas is complicated due to its high optical depth and the variations in $\alpha_{\rm HCN}$, it is useful to explore other bright dense gas tracers; in this work, we use an astrochemically related molecule to HCN, the cyanide radical (CN), as our dense gas tracer ($n_{\rm crit} \gtrapprox 10^5$ cm^{-3}, Shirley 2015).

CN can be formed through photodissociation of HCN, neutral-neutral reactions with various intermediary species involving carbon and nitrogen, and reactions with ionized carbon (Aalto et al. 2002; Boger & Sternberg 2005; Chapillon et al. 2012). Models of photon-dominated regions (PDRs) predict the abundance of CN to increase on the surfaces of molecular clouds, where the UV radiation field is strongest, with the abundance of HCN higher in the more shielded centres of molecular clouds (Boger & Sternberg 2005). Somewhat surprisingly, however, Wilson et al. (2023) found that the CN/HCN intensity ratio is relatively constant when compared with star formation rate surface density ($\Sigma_{\rm SFR}$) and gas surface density ($\Sigma_{\rm gas}$) in galaxies over a range of sub-kiloparsec spatial scales. Furthermore, the CN/CO and HCN/CO intensity ratios show a tight correlation, implying that the CN/CO intensity ratio can also be used to trace the dense gas fraction in galaxies (Wilson et al. 2023). Additional detailed studies of CN and HCN intensities and abundances are required to test the predictions of PDR models in galaxies.

There have been a large number of projects which have used the Atacama Large Millimeter/Submillimeter Array (ALMA) to observe CN ($N = 1 - 0$), hereafter CN ($1 - 0$), in spectral line surveys of starbursts and galaxies with active galactic nuclei (AGNs, e.g., Sakamoto et al. 2014; Harada et al. 2018; Martín et al. 2021; Saito et al. 2022b). CN ($1 - 0$) has been observed in local mergers and merger remnants (e.g., König et al. 2016; Sakamoto et al. 2017; Ueda et al. 2017, 2021; Ledger et al. 2021), the circumnuclear ring of the spiral galaxy M83 (Harada et al. 2019), and in starburst and AGN outflows (e.g., Sakamoto et al. 2014; Meier et al. 2015; Walter et al. 2017; Lutz et al. 2020; Saito et al. 2022b). Gas-rich early type galaxies have been detected in CN ($1 - 0$) (Young et al. 2021, 2022), and the line has been seen in absorption towards radio nuclei, AGNs, and bright cluster galaxies (Rose et al. 2019; Kameno et al. 2020; Baek et al. 2022). Observations of CN ($1 - 0$) with ALMA in multiple bright starbursts and

AGN have been compared with HCN $(1-0)$ and CO $(1-0)$ (Wilson 2018; Ledger et al. 2021; Wilson et al. 2023).

Additional observations of CN $(1-0)$ include spectral line surveys with the Nobeyama 45 m telescope (e.g., Nakajima et al. 2018; Takano et al. 2019) and the Large Millimeter Telescope (Cruz-González et al. 2020). CN $(1-0)$ was detected in molecular gas outflows in Mrk 231 (Cicone et al. 2020) with the IRAM PdBI telescope, and in nearby galaxies with the IRAM 30 m telescope (Henkel et al. 1998; Watanabe et al. 2014; Aladro et al. 2015). Higher transition lines of CN have been studied with ALMA in nearby galaxies (e.g., Nakajima et al. 2015; Saito et al. 2015; Rose et al. 2020; Ledger et al. 2021) and galaxies at redshifts 2.5-3.5 (Geach et al. 2018; Cañameras et al. 2021). For more discussion of previous observations of CN with single-dish and/or non-ALMA data (e.g., Aalto et al. 2002; Costagliola et al. 2011), we refer the reader to Wilson (2018).

Wilson (2018) explored the CN/CO ratio in nearby galaxies using archival Cycle 0 ALMA data and found significant CN/CO spatial variations within some galaxies, as well as global differences between individual galaxies. The galaxies ranged from nearby starbursts to ultra-Luminous and luminous infrared galaxies (U/LIRGs) and the line ratios were measured on kiloparsec scales. Wilson et al. (2023) measured the CN/CO line ratio in a sample of nearby galaxies, covering starbursts, Seyfert 2 galaxies with AGNs, and U/LIRGs. They found the CN/CO ratio also demonstrated variations between the galaxies in their sample and spatially within their galaxies. Both Wilson (2018) and Wilson et al. (2023) found that some ratio variations correlated spatially with regions of higher SFRs. Variations in CN/CO ratios were also found in a gas-rich elliptical (Young et al. 2022) and bright cluster galaxies (Rose et al. 2019). On more resolved scales in galaxies, Meier et al. (2015) found an enhanced CN/CO ratio in the inner nuclear region of NGC 253 compared with the outer disc. Cicone et al. (2020) measured total CN/CO line luminosity ratios in Mrk 231 and found they are enhanced by a factor of ~ 3 in the line wings of the outflow. They attribute this enhancement in the CN/CO ratio in the outflow to stronger UV radiation fields present in the gas, perhaps from the formation of massive stars in the outflow.

A major challenge of quantifying any trend in the CN/CO ratio in X-ray dominated regions (XDRs) is the limited spatial scales of most extragalactic observations in galaxies with an AGN. XDRs most strongly affect the gas properties in the innermost < 100 pc of the galaxy nuclei (Wolfire et al. 2022). Wilson (2018) found that the CN/CO ratio decreases in the vicinity of three of four AGNs in her galaxy sample. In contrast, Wilson et al. (2023) found an increase in the CN/CO ratio in the centres of NGC 7469 and NGC 1808, two galaxies with strong Seyfert nuclei. NGC 1068, a nearby Seyfert 2 galaxy, has also been shown to have an increasing CN/CO ratio near the AGN and the jet-driven molecular outflow (Saito et al. 2022b). It is clear that more work needs to be done to fully understand any trends in the CN/CO ratio in XDRs in galaxies.

U/LIRGs are ideal laboratories for studying the impact of radiation fields on the properties of molecular gas in galaxies (see e.g., Lonsdale et al. 2006 and Pérez-Torres et al. 2021). These galaxies have high infrared (IR) luminosity (L_{IR}) and are usually mergers of galaxies, starbursts, and contain AGNs (Sanders et al. 2003; Armus et al. 2009; Pearson et al. 2016). U/LIRGs have large fractions of dense molecular gas (Solomon et al. 1992; Gao & Solomon 2004; Privon et al. 2017; Sliwa et al. 2017), and the correlation between HCN line luminosity and SFR extends into this high-IR regime (Gao & Solomon 2004; Wu et al. 2005). Graciá-Carpio et al. (2008) found that the star formation efficiency of dense gas, $\mathrm{SFE_{dense}}$, is higher in U/LIRGs than normal galaxies, indicating that these galaxies are star forming engines that efficiently convert their large gas reservoirs into stars at extremely high rates. U/LIRGs can contain PDRs, XDRs, or a combination of both, and therefore are prime targets to study the CN/CO ratio in external galaxies.

The goal of this paper is to present an observational picture of the CN/CO intensity ratio in a comprehensive sample of U/LIRGs. We focus on galaxies which are nearby ($z < 0.05$), have $\mathrm{L_{IR}} > 10^{11}\ \mathrm{L_{\odot}}$, have starbursts, AGNs, or some mixture of the two, and have been observed with ALMA. Section 3.2 describes our sample selection and data processing procedures, including calibration, imaging, and analysis of 16 different archival ALMA projects. In Section 3.3, we discuss our measured line intensity ratios and compare them between a subset of ULIRGs and LIRGs. We summarize our conclusions in Section 3.4. We defer any comparisons of this ratio with Σ_{SFR} or PDR and XDR models to a future paper.

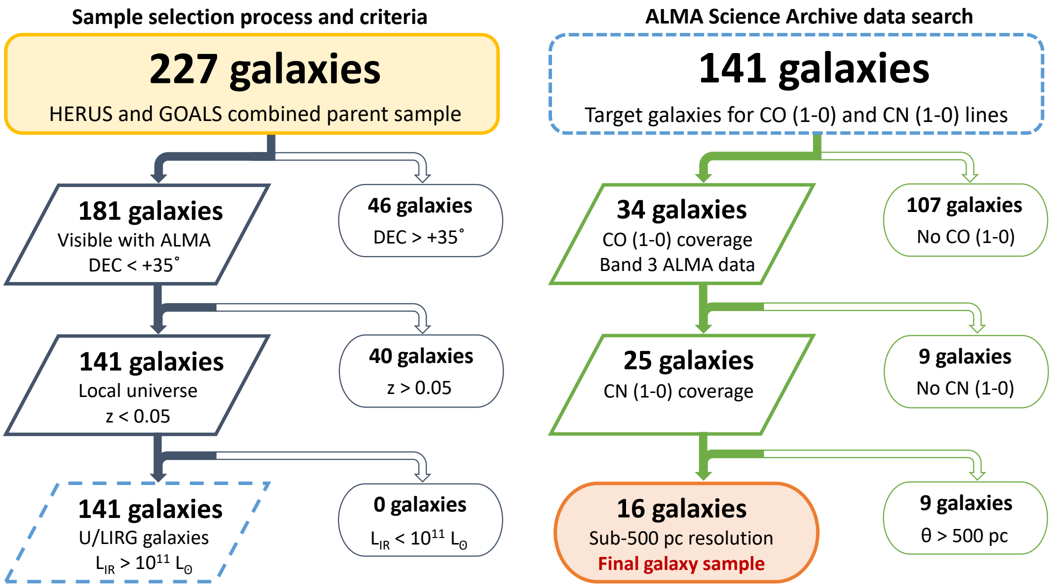

FIGURE 3.1: A graphical representation of the selection process to obtain our CN/CO ratio galaxy sample. Starting with the HERUS and GOALS parent surveys, we narrowed our sample based on the criteria of DEC < +35°, $z < 0.05$, and $L_{IR} > 10^{11}$ $L_\odot$ (left column in figure). We then searched the ALMA Science Archive on 2022 June 20, for potential galaxy targets that had both CO $(1-0)$ and CN $(1-0)$ lines with a physical resolution of $\theta < 500$ pc (right column in figure). From the 227 initial galaxy candidates, we obtained a final sample of 16 galaxies previously observed with ALMA.

3.2 Sample Selection and Data Analysis

In this section, we describe the methods by which we selected our sample of U/LIRGs and measured our intensity ratios. We describe the data calibration and image processing methods and discuss how we obtained our different data products. Finally, we summarize the various ways we measure our intensity ratios, which lead to the main results of this paper.

The lowest rotational line of CN, CN ($N = 1-0$), has two main hyperfine groupings with rest frequencies of ∼ 113.49 GHz and ∼ 113.17 GHz and quantum number designations of CN ($N = 1-0, J = 3/2-1/2$) and CN ($N = 1-0, J = 1/2-1/2$), respectively. The hyperfine groupings of CN ($N = 1-0$) are made up of nine individual hyperfine spectral lines (Skatrud et al. 1983), but at the turbulent line widths and velocity and spatial resolutions of extragalactic observations, these are typically blended into two larger groupings of five (brighter) and four (fainter) spectral lines[1]. Throughout this paper, we will denote the CN ($N = 1-0, J = 3/2 - 1/2$) and CN ($N = 1-0, J = 1/2 - 1/2$) lines as CN bright and CN faint, respectively.

3.2.1 The HERUS and GOALS U/LIRG surveys

For this archival project, we wanted to find as many nearby U/LIRGs as possible that were observed in both the CO (1 − 0) and CN (1 − 0) lines at sub-kiloparsec scales in public ALMA data. As our parent sample, we compiled a master list of galaxies combined from the HERschel Ultra Luminous InfraRed Galaxy Survey (HERUS, Pearson et al. 2016) and the Great Observatories All-Sky LIRG Survey (GOALS, Armus et al. 2009). The HERUS survey is a flux-limited sample of low-redshift ($z \leq 0.2$) ULIRGs identified from the *IRAS* Point Source Catalog Redshift (PSC-z) survey (Saunders et al. 2000) with 60 μm fluxes greater than 1.8 Jy (Pearson et al. 2016). The *Herschel* observations recovered nearly complete CO ladders of 43 ULIRGs, with the science goal of tracing different temperature components of the gas within PDR and XDR regions (Pearson et al. 2016). Of the 43 ULIRGs in our parent sample, 25 are unique to HERUS, while 18 are also covered in GOALS. The GOALS survey is a large collection of data from the *Spitzer Space Telescope*, the *Chandra X-ray Observatory*, the *Hubble Space Telescope*, and the *Galaxy Evolution Explorer* (Armus et al. 2009). A main science objective of GOALS is to describe the mechanisms responsible for the enhanced IR power generation in an unbiased representation (e.g., starbursts, AGNs, and mergers) of LIRGs (Armus et al. 2009). GOALS compiled observations of 202 low-redshift ($z < 0.088$) LIRGs, of which 18 are also covered in HERUS. The U/LIRGs observed in HERUS and GOALS are, by definition, galaxies with $L_{IR} > 10^{11}$ $L_\odot$. We therefore start with a sample of galaxies with $L_{IR} > 10^{11}$ $L_\odot$ (Fig. 3.1).

3.2.2 Sample selection criteria

From the HERUS and GOALS surveys, we obtained a combined parent sample of 227 potential U/LIRG targets for our CN/CO ratio study. In this section, we describe the criteria by which we narrowed down our target sample to 141 galaxies. Fig. 3.1 demonstrates the selection process visually.

[1] https://home.strw.leidenuniv.nl/~moldata/datafiles/cn-hfs.dat

We required our targets be visible with ALMA, which has an upper Declination (DEC) limit of +47° (see the ALMA Proposer's Guide [2]). To ensure that we targeted galaxies with optimal observing conditions and to limit the possibility of shadowing effects, we imposed a stricter requirement of DEC < +35°. We wanted to study the CN/CO ratio in nearby galaxies with sub-kiloparsec resolution (corresponding to a physical resolution representative of an ensemble of molecular clouds). To accomplish this resolution goal with ALMA, we imposed an upper redshift limit of $z = 0.05$, which corresponds to D $\sim$ 200 Mpc[3]. At this distance, a 1 arcsec ALMA beam corresponds to $\sim$ 1 kpc physical resolution.

3.2.3 The ALMA CO and CN galaxy sample

A list of the 141 galaxy targets was run through the ALMA Science Archive query tool on 2022 June 20. 46 of the 141 galaxies had public Band 3 data available, which were taken over ALMA Cycles 0-7. Of these 46 galaxies, 12 did not have spectral window coverage of the redshifted CO $(1-0)$ line. This further reduced our potential candidate galaxies to 34 (Fig. 3.1). Furthermore, 9 of the 34 galaxies did not have spectral window coverage of the redshifted brightest CN $(1-0)$ line, leaving 25 galaxies which had both CO and CN covered in Band 3 with ALMA (Fig. 3.1). We imposed an angular resolution limit to correspond to a physical scale of 500 pc. This requirement further reduced our potential candidates by nine galaxies (Fig. 3.1). Of the nine galaxies that were removed, five had CO and CN observed with 500 pc $< \theta <$ 1 kpc resolution, and four had CO and CN observed with $\theta >$ 1 kpc resolution.

After our extended sample selection process, we found 16 U/LIRGs with both CO $(1-0)$ and CN $(1-0)$ observed at $\theta <$ 500 pc resolution in the ALMA archive. 8 of the 16 galaxies are covered in HERUS, while all 16 galaxies are covered in GOALS. Table 3.1 lists the project codes which correspond to the archival ALMA data.

Our galaxy sample is comprised of 12 LIRGs but only 4 ULIRGs, which is likely not a statistically significant and representative sample of ULIRGs in the local Universe.

[2] G. Privon et al. 2022, ALMA Cycle 9 Proposer's Guide, ALMA Doc. 9.2 v1.4; https://almascience.eso.org/documents-and-tools/cycle9/alma-proposers-guide.

[3] The redshift cut removed 40 galaxies from our sample. 3 galaxies near the threshold redshift value with $z \gtrapprox 0.05$ (D $\gtrapprox$ 200 Mpc) were found to have archival CO and CN data with sub-kiloparsec resolution (IRAS F14378-3651, IRAS 19542+1110, and IRAS F01364-1042); however, these galaxies were removed from the sample list due to the CO and CN coverage criteria described in Section 3.2.3.

TABLE 3.1: Archival ALMA Cycle 1-6 projects with both CO $(1-0)$ and CN $(1-0)$ observations in nearby U/LIRGs.

Galaxy[a]	CO and CN project code	ALMA data reference
IRAS 13120-5453	2015.1.00287.S	Sliwa et al. (2017)
Arp 220	2015.1.00167.S	Brown & Wilson (2019)
IRAS F05189-2524	2012.1.00306.S	Lutz et al. (2020)
IRAS F10565+2448	2019.1.01664.S	PI: J. Wang
NGC 6240	2015.1.00003.S	Saito et al. (2018)
IRAS F18293-3413	2015.1.01191.S	Saito et al. (2020)
NGC 3256	2018.1.00223.S	Ueda et al. (2021)
NGC 1614	2013.1.00991.S	König et al. (2016)
	2013.1.01172.S	Saito et al. (2016)
NGC 7469	2013.1.00218.S	Wilson et al. (2019)
	2017.1.00078.S	Izumi et al. (2020)
NGC 2623	2015.1.01191.S	Brown & Wilson (2019)
NGC 3110	2013.1.01172.S	Kawana et al. (2022)
ESO 320-G030	2016.1.00263.S	Pereira-Santaella et al. (2020)
NGC 1068	2012.1.00657.S	PI: S. Takano
	2018.1.01684.S	Saito et al. (2022b)
NGC 5104	2015.1.01191.S	PI: Z. Zhang
NGC 4418	2016.1.00177.S	Lutz et al. (2020)
NGC 1365	2015.1.01135.S	Zabel et al. (2019)

Note.
[a]The galaxies are listed in order of decreasing IR luminosity.

We have compared our small sample of ULIRGs with those in HERUS (Pearson et al. 2016) in terms of redshift and $L_{\rm IR}$. We are not representative of the HERUS survey's redshift distribution as we have selected only those ULIRGs within $z < 0.05$. However, our population of ULIRGs is representative of the lower half of IR luminosities covered by the HERUS sample of ULIRGs (e.g., $\log(L_{\rm IR}) < 12.3$).

In our results discussion, we compare our population of LIRGs with our population of ULIRGs as independent samples, acknowledging that future work comparing galaxies with their distribution of IR luminosities is forthcoming and needed for our small statistical sample of galaxies (Ledger et al., in preparation).

Excluded ALMA data sets

We only consider data from ALMA Cycles 1-6. There were no corresponding projects which met our criteria with ALMA Cycle 7 or later dates at the time of searching the archive. We removed the only Cycle 0 project which met our selection criteria, project code 2011.0.00525.S, with observations of NGC 3256. The corresponding Cycle 6 observations for NGC 3256 are of higher spatial resolution and sensitivity and can be better calibrated than the Cycle 0 data. Wilson (2018) measured the (CN bright)/CO ratio for NGC 3256 using the archival Cycle 0 data and we compare with her results in Section 3.3.2.

We use only project code 2015.1.00167.S for Arp 220, although two other projects exist in the ALMA archive (2015.1.00113.S and 2017.1.00042.S). We ignore these two projects as they are of significantly higher angular resolution (physical scales of ~ 10 pc), and therefore we would need significant degradation of the data to match our target scale of 500 pc.

3.2.4 ALMA data calibration and imaging

In this section, we present an overview of the calibration, reduction, and imaging processes for our ALMA data. Data reduction and calibration were performed using Common Astronomy Software Applications (`CASA`, McMullin et al. 2007) and the PHANGS-ALMA pipeline v3 (Leroy et al. 2021). Many of the relevant imaging parameters are provided in Table 3.2.

TABLE 3.2: Data reduction and imaging parameters.

Galaxy[a]	Native CO (1 − 0) beam (arcsec × arcsec, PA in degrees)	Smoothed round beam[b] (arcsec)	Channel width (ΔV) CO (1 − 0) (km s^{-1})	CN (1 − 0)	Sensitivity per channel CO (1 − 0) (mJy beam^{-1})	CN (1 − 0)	Pixel size[b] (arcsec)
IRAS 13120-5453	0.7 × 0.64, 1	0.72	20.0	20.0	1.06	1.06	0.36
Arp 220	0.79 × 0.47, 12	1.17	20.32	20.3	1.21	1.50	0.58
IRAS F05189-2524	0.45 × 0.42, −56	0.55	20.32	20.64	0.36	0.72	0.28
IRAS F10565+2448	0.36 × 0.26, −37	0.52	20.32	20.3	0.38	0.76	0.26
NGC 6240	0.58 × 0.57, −44	0.89	20.0	20.0	1.32	1.24	0.44
IRAS F18293-3413	0.81 × 0.57, −85	1.2	24.14	24.51	2.88	4.31	0.6
NGC 3256	1.63 × 1.45, 78	2.34	19.69	23.22	2.55	1.15	1.17
NGC 1614	0.85 × 0.53, 90	1.49	17.78	23.22	1.9	2.97	0.74
NGC 7469	0.44 × 0.30, −55	1.46	15.24	20.64	1.98	2.55	0.73
NGC 2623	1.04 × 0.86, 1	1.34	19.05	24.51	1.9	3.37	0.67
NGC 3110	1.72 × 1.35, −86	1.8	17.78	23.22	1.38	2.0	0.9
ESO 320-G030	0.39 × 0.34, −29	2.5	17.78	23.22	2.52	3.86	1.25
NGC 1068[c]	3.92 × 3.67, −74	7.38	22.23	23.23	10.17	3.05	3.69
NGC 5104	0.78 × 0.58, 61	1.14	19.05	24.51	2.73	5.45	0.57
NGC 4418	1.67 × 1.28, 81	2.83	15.24	20.64	1.13	1.21	1.42
NGC 1365	1.85 × 1.43, 84	5.76	19.05	24.51	10.71	11.18	2.88

Notes.
[a]The galaxies are listed in order of decreasing IR luminosity.
[b]Both the pixel and smoothed beam size for each galaxy are set by the target resolution of 500 pc.
[c]We note that the resolution of NGC 1068 was tapered to a larger beamsize during cleaning to reduce the amount of post-process smoothing required. The original synthesized resolution of the dataset is 0.43 arcsec × 0.38 arcsec (Saito et al. 2022a,b).

Calibration

We were generously provided with calibrated *uv* measurement sets for NGC 7469 (only project code 2013.1.00218.S, Wilson et al. 2023) and Arp 220 (Brown & Wilson 2019). Similarly, we already had calibrated data for IRAS 13120-5453 (Ledger et al. 2021), NGC 1068 (Saito et al. 2022a,b), and NGC 6240 (Klimi, private communication).

To calibrate the remaining ALMA data, relevant projects were downloaded using scripts generated from the ALMA Science Archive[4]. In late 2022 June (data for IRAS F10565+2448 was downloaded and calibrated at a later date, after its public release). The individual project sets were calibrated using the 'ScriptForPI.py' `PYTHON` script and specificed `CASA` version in the calibration script (except for projects 2013.1.00991.S and 2013.1.01172.S, where version 4.7.2 was used for calibration instead of the recommended `CASA` version).

[4]https://almascience.nao.ac.jp/aq/

Imaging

Following calibration, we performed continuum subtraction and imaging using the PHANGS-ALMA pipeline v3 (Leroy et al. 2021). We already had images for IRAS 13120-5453 (Ledger et al. 2021) and NGC 6240 (Klimi, private communication) at the target angular resolution, and as a result these galaxies were not reduced with the pipeline. Processed data cubes (produced using the PHANGS-ALMA pipeline v3) for NGC 1068 were kindly provided by the project PIs at the target resolution (Saito et al. 2022a,b).

The PHANGS-ALMA pipeline reduces the calibrated data by joining together data for each galaxy from multiple measurement sets and project codes before performing continuum subtraction with `CASA`'s `uvcontsub` task on line-free channels. To obtain the best continuum subtraction, we specified the CO $(1-0)$ line and both CN $(1-0)$ hyperfine groupings to be excluded as channels with line emission. The spectral resolution of each datacube was determined as an integer multiplication of the original channel width. We targeted a channel width of ~ 20 km s^{-1} for all galaxies (Table 3.2) to increase the sensitivity for the often weak emission from the CN $(1-0)$ lines.

Most of the default PHANGS-ALMA pipeline v3 parameters were used for imaging the calibrated and continuum subtracted data. For the cleaning procedure, we set the default weighting to Brigg's (Briggs 1995) with robust = 0.5, and the primary beam was limited to > 20 per cent. For the CN $(1-0)$ line, we produced data cubes with a large spectral width to simultaneously image the two main hyperfine groupings around rest frequencies of 113.490970 GHz and 113.170492 GHz in the same data cube. Therefore, our final image products consist of a CO $(1-0)$ cube and a CN $(1-0)$ cube which contains both hyperfine groupings. We note that we did not recover both CN $(1-0)$ lines in NGC 1365, as the faint line was not covered in the spectral window set up.

Although the PHANGS-ALMA pipeline v3 has the ability to produce a variety of further data products, we did not use the pipeline for data processing after producing the initial data cubes. Instead, any additional reduction processes were performed on the data cubes using `CASA` version 6.5.0.15 and the `CASA` tasks `imsmooth`, `imsubimage`, `imregrid`, `imrebin`, `imstat`, and `exportfits`. These steps included: smoothing the cubes to the target beam resolution in arcsec (corresponding to 500 pc), extracting a primary beam slice at the channel with peak CO intensity for correction of the moment

0 maps, and rebinning or regridding the images to minimum Nyquist sampled pixel size of 250 pc (Table 3.2).

3.2.5 Data products

CO (1 – 0) line products

Integrated intensity maps for the CO (1 – 0) line were created using the Sun moment map method (Sun et al. 2018, 2020). The Sun method uses an expanding mask technique to find signal in the calibrated data cubes. Three-dimensional noise cubes are created and used to measure the RMS noise ($\sigma_{\rm RMS}$) for signal-free parts of the CO (1 – 0) line cubes in each pixel; the mean $\sigma_{\rm RMS}$ for each galaxy is listed in Table 3.2. Initial signal masks are then defined by selecting pixels which have positive CO (1 – 0) line emission and which have a signal-to-noise (S/N) ratio of at least 4 over two neighbouring channels. Finally, the mask expands to include pixels out to a lower S/N threshold of 2 (Rosolowsky & Leroy 2006; Sun et al. 2018, 2020).

We produced integrated intensity (moment 0) maps in K km s^{-1} units for the CO (1 – 0) line cubes and corrected these by the primary beam using the Astropy Spectral Cube package (Ginsburg et al. 2019). We also made moment 1 (intensity-weighted velocity) and moment 2 (spectral line width) maps for the CO (1 – 0) line to use in CN processing (Section 3.2.5). Uncertainties on these maps were calculated by taking the mean RMS noise in each pixel from the three-dimensional noise cubes ($\sigma_{\rm RMS}$) and multiplying this by the number of channels ($N_{\rm chan}$) with signal and the channel width (ΔV), using

$$\sigma_{\rm pix} = \sigma_{\rm RMS} \times \sqrt{N_{\rm chan}} \times \Delta V. \tag{3.1}$$

The resulting maps were used to estimate the uncertainty on the measured CO (1 – 0) fluxes and luminosities for each galaxy (Section 3.2.5; Table 3.3).

In this paper, we do not convert the CO intensities to molecular gas surface densities ($\Sigma_{\rm mol}$) or masses (M_{H_2}), as is often done using an $\alpha_{\rm CO}$ conversion factor (Bolatto et al. 2013). The typical conversion factor that is used for U/LIRGs is lower by roughly a factor of 5 compared with normal spirals, discs of galaxies, or the Milky Way, and would hold especially true in the CO bright central regions (Downes & Solomon 1998). We expect that the commonly accepted U/LIRG conversion factor, $\alpha_{\rm CO} = 1.088$ $M_\odot$ (K km

TABLE 3.3: CN (1 − 0) and CO (1 − 0) total integrated intensities and luminosities calculated using equation (3.2).

Galaxy[a]	$S_{\mathrm{CO}\,(1-0)}$ (Jy km s^{-1})	$L_{\mathrm{CO}\,(1-0)}$[b] (K km s^{-1} pc^2)	$S_{\mathrm{CN}\,(1-0)}$ bright[c] (Jy km s^{-1})	$L_{\mathrm{CN}\,(1-0)}$ bright[b] (K km s^{-1} pc^2)	$S_{\mathrm{CN}\,(1-0)}$ faint[c] (Jy km s^{-1})	$L_{\mathrm{CN}\,(1-0)}$ faint[b] (K km s^{-1} pc^2)	N[d] (pixels)	Distance[e] (Mpc)
IRAS 13120-5453	206 ± 10	86 ± 4	35 ± 2	15 ± 1	21 ± 2	9.3 ± 0.9	506	137
Arp 220	569 ± 28	87 ± 5	51 ± 3	8.0 ± 0.5	25 ± 2	3.9 ± 0.3	489	81.1
IRAS F05189-2524	23 ± 1	18 ± 1	2.0 ± 0.3	1.8 ± 0.3	1.0 ± 0.3	1.1 ± 0.3	174	188
IRAS F10565+2448	86 ± 4	70 ± 4	7 ± 1	6.1 ± 0.5	4.0 ± 0.5	3.6 ± 0.5	656	194
NGC 6240	236 ± 12	60 ± 3	20 ± 2	5.3 ± 0.6	12 ± 2	3.3 ± 0.6	396	106
IRAS F18293-3413	902 ± 45	125 ± 6	48 ± 6	6.9 ± 0.8	23 ± 5	3.3 ± 0.7	954	77.2
NGC 3256	1686 ± 84	79 ± 4	41 ± 2	2.0 ± 0.1	21 ± 1	1.0 ± 0.1	883	44.3
NGC 1614	357 ± 18	38 ± 2	54 ± 4	6.0 ± 0.4	31 ± 3	3.4 ± 0.3	608	67.9
NGC 7469	359 ± 18	37 ± 2	36 ± 3	3.7 ± 0.3	19 ± 2	2.0 ± 0.2	766	66
NGC 2623	129 ± 6	21 ± 1	9 ± 2	1.5 ± 0.3	4 ± 2	0.8 ± 0.3	186	83.4
NGC 3110	271 ± 14	38 ± 2	7 ± 2	1.0 ± 0.3	3 ± 2	0.4 ± 0.3	790	77.8
ESO 320-G030	292 ± 15	18 ± 1	34 ± 3	2.1 ± 0.2	17 ± 2	1.1 ± 0.1	225	50.7
NGC 1068	2768 ± 138	13 ± 1	174 ± 9	0.85 ± 0.04	72 ± 4	0.35 ± 0.02	209	13.97
NGC 5104	172 ± 9	28 ± 1	12 ± 3	2.0 ± 0.6	5 ± 4	0.9 ± 0.6	324	84.6
NGC 4418	121 ± 6	3.6 ± 0.2	10 ± 1	0.31 ± 0.02	4.0 ± 0.5	0.11 ± 0.02	140	35.3
NGC 1365	3399 ± 170	31 ± 2	116 ± 16	0.25 ± 0.01	-	-	786	19.57

Notes.
[a]The galaxies are listed in order of decreasing IR luminosity.
[b]All given luminosity values have been divided by a factor of 1×10^8.
[c]The CN ($N = 1-0, J = 3/2-1/2$) and CN ($N = 1-0, J = 1/2-1/2$) lines are denoted as CN bright and CN faint, respectively
[d]The number of pixels with CO (1 − 0) line detections.
[e]All luminosity distances were converted from redshifts with Ned Wright's (Updated) Cosmology Calculator adopting WMAP 5-year cosmology with $H_0 = 70.5$ km s^{-1} Mpc^{-1}, $\Omega = 1$, $\Omega_m = 0.27$ in the 3K CMB frame, except for NGC 7469 (SN type Ia distance is from Ganeshalingam et al. 2013) and NGC 1068 and NGC 1365 (tip of the red giant branch distance measures are from Anand et al. 2021). We note that any uncertainties from distance estimates are less relevant when considering line ratios.

$\mathrm{s^{-1}\ pc^2)^{-1}}$ (which includes a factor of 1.36 to account for Helium), is appropriate for the galaxies in our sample. U/LIRGs have high star formation rate surface densities, molecular gas surface densities, and are highly centrally concentrated (Solomon et al. 1992; Downes & Solomon 1998; Lonsdale et al. 2006; Pérez-Torres et al. 2021). If some portion of the discs of our U/LIRG sample has a different $\alpha_{\rm CO}$, this would account for a small fraction of the total percentage of CO flux and produce a small effect in global measurements.

CN $(1-0)$ line products

To measure the intensities of the weaker CN $(1-0)$ lines, we used a spectral shuffle and stack method, similar to that described in e.g., Schruba et al. (2011) and Leroy et al. (2016). Fig. 3.2 demonstrates the applied shuffle-stack method. We spatially masked the CN image cubes to include only pixels where we have emission in the CO moment 0 maps, since we do not expect any weaker CN emission where there is no CO emission. The CN spectrum in each pixel was then shifted (the shuffe method) by the CO velocity from the moment 1 map and masked to only include signal within a spectral width of 3× the CO linewidth ($\sigma_{\rm CO}$) from the moment 2 map. In each pixel, the CN emission was then integrated to obtain an intensity in K km $\mathrm{s^{-1}}$ units. After completing this process in each pixel, we had an integrated intensity map for each of the CN bright and CN faint lines. These maps include pixels with weak emission, as our shuffle method includes any CN emission (regardless of S/N) found within the $3\sigma_{\rm CO}$ linewidth. Both the CN bright and CN faint lines in our data become comparable to the total linewidth of the stronger CO emission after blending the individual hyperfine structure lines within each grouping (e.g., Fig. 3.3d). We also create uncertainty maps for the CN lines using equation (3.1), and use these values for estimating the uncertainty on the measured CN $(1-0)$ fluxes and luminosities (Section 3.2.5; Table 3.3) and applying any subsequent S/N cuts. The CN uncertainty is also used for determining upper limits on the (CN bright)/CO ratio when binning by CO intensity (Section 3.2.5).

Our final data products include moment 0 integrated intensity maps, uncertainty maps, and total integrated spectra for the CN bright, CN faint, and CO lines in each galaxy (see e.g., Fig. 3.3 and Appendix 3.A).

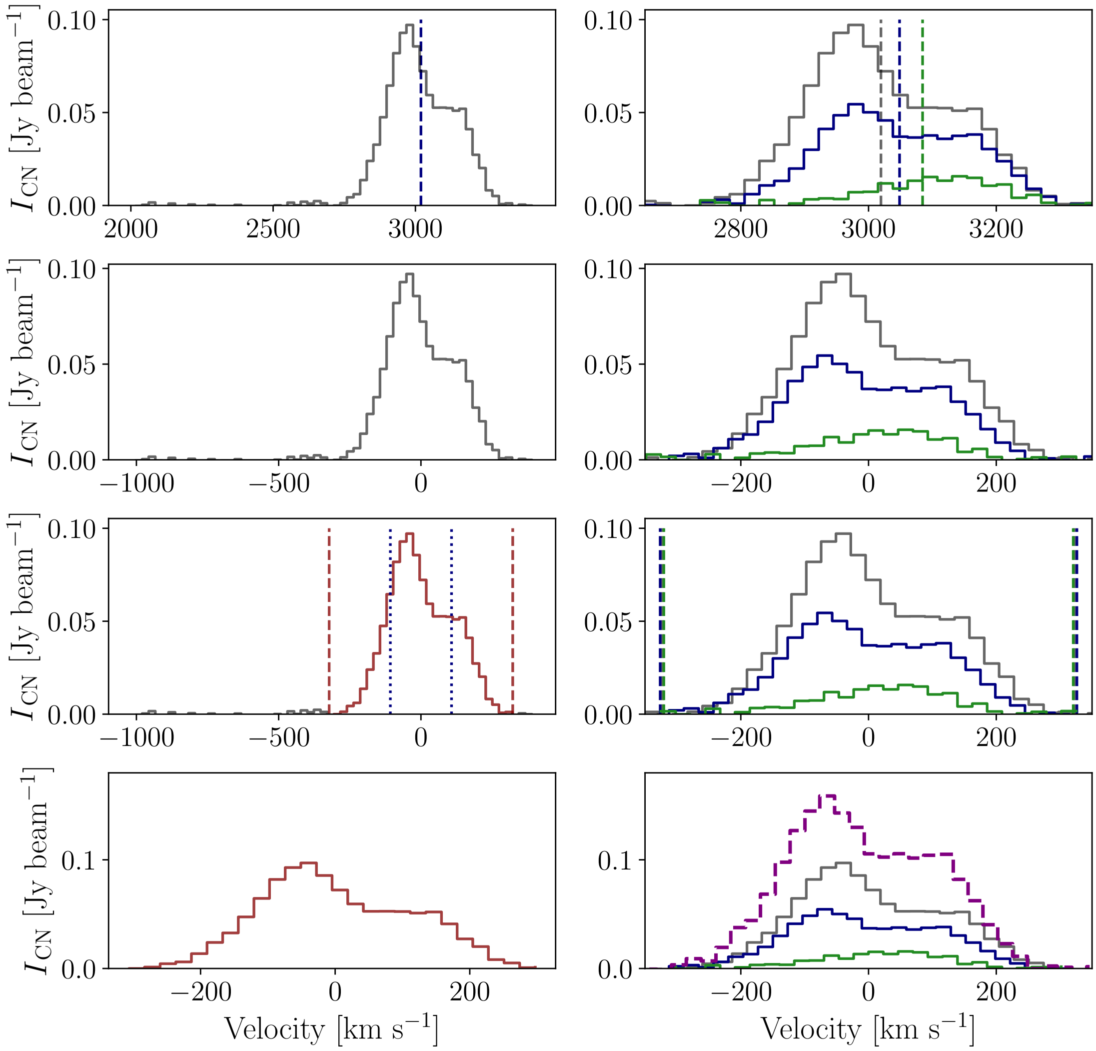

FIGURE 3.2: This figure illustrates an example of the shuffle-stack process for obtaining the moment 0 maps and the total integrated spectra for the CN bright and CN faint lines in ESO 320-G030. Left column: This column shows an example of the shuffle and integration of the CN bright line in the strongest pixel. From top to bottom, we show the native CN velocity spectrum, the spectrum that has been shifted by the peak central velocity of the CO line, the spectrum overplotted by red dashed lines that show the width of integration (3× the CO line width, which is shown as the blue dotted lines), and the spectrum to be integrated in this pixel. Right column: This column shows the shuffle and stack method for three example pixels. The top three figures are the same as the left column, but for the three pixels. The bottom plot shows the sum of the three stacked individual spectra as the magenta dashed line, which are integrated as part of the global spectrum.

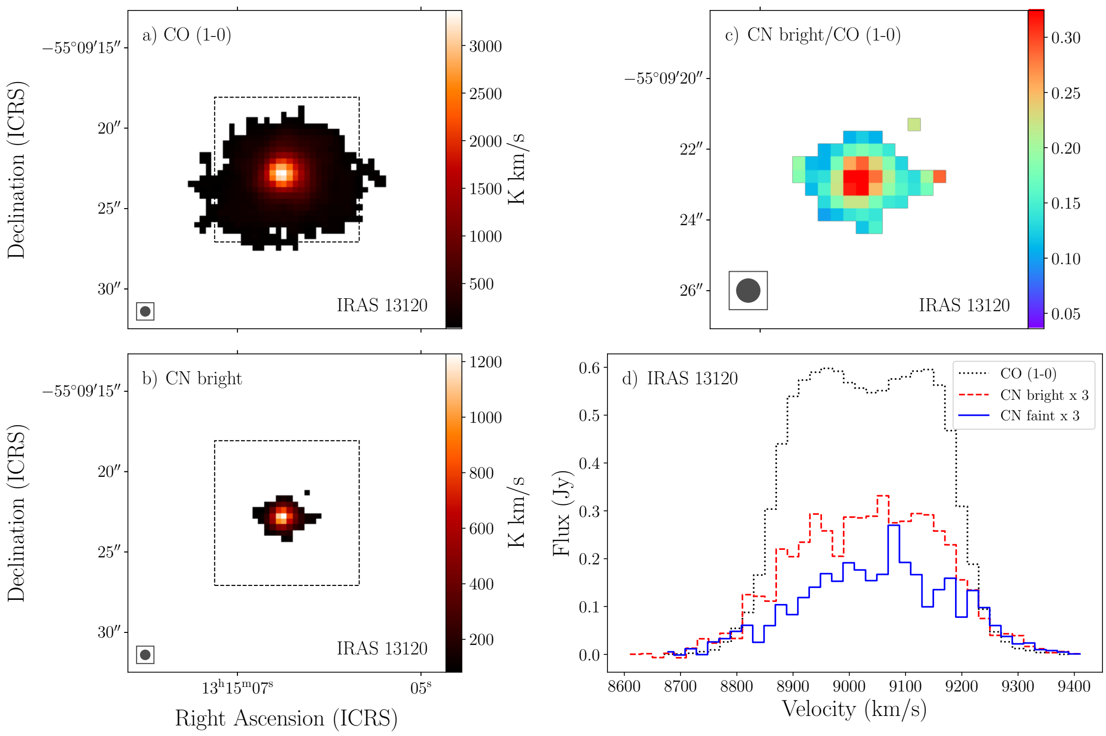

FIGURE 3.3: This figure shows the moment 0 and (CN bright)/CO intensity ratio maps in K km s^{-1} units in IRAS 13120, as well as the global spectra. The circle in the bottom left corner of each panel denotes the size of the beam smoothed to 500 pc. (a) The total integrated intensity of the CO $(1-0)$ line. The dashed square indicates the region in (c). (b) The total integrated intensity of the CN bright line. The pixels included here have an S/N of $> 6\sigma$ and $> 3\sigma$ in the CN bright and CN faint lines, respectively. (c) The (CN bright)/CO intensity ratio. The colour bar is clipped at the mean value plus or minus 80 per cent. (d) The total integrated spectra of the CO line (black dotted), CN bright line (red dashed), and CN faint line (blue). Both CN lines have been multiplied by a factor of 3 for demonstration purposes.

Measured fluxes, luminosities, and ratio maps

The flux values for the CO (1 − 0) line were calculated directly from the integrated intensity maps. In each galaxy, we summed the intensities from all pixels with CO emission. To measure the fluxes for the CN (1 − 0) lines, we stacked the spectra from each pixel and obtained a total integrated spectrum, which we then integrated to obtain the CN bright and CN faint line fluxes (Fig. 3.2). This method significantly improved our S/N for the CN lines, and allowed us to detect weaker CN emission and better obtain the true global values of our measured intensity ratios.

Line luminosities were subsequently calculated using equation (3) from Solomon & Vanden Bout (2005):

$$L_{\rm mol} = 3.25 \times 10^7 \frac{{D_{\rm L}}^2}{(1+z)^3} \frac{1}{{\nu_{\rm mol}}^2} S_{\rm mol} \Delta v. \tag{3.2}$$

We used the measured flux value and its uncertainty for each molecule as $S_{\rm mol}\Delta v$ (Jy km s^{-1}), with the corresponding line frequency, $\nu_{\rm mol}$ (GHz). Galaxy distances, $D_{\rm L}$ (Mpc), are listed in Table 3.3. We adopted WMAP 5-year cosmology (H_0 = 70.5 km s^{-1} Mpc^{-1}, $\Omega = 1$, and $\Omega_{\rm m} = 0.27$) in the cosmic microwave background (CMB) frame. Uncertainties were estimated on the line luminosities assuming all uncertainty comes from the fluxes (no uncertainty in $D_{\rm L}$, z, and $\nu_{\rm mol}$). Any distance uncertainties are less relevant when considering line ratios.

Ratio maps were created for (CN bright)/CO and (CN bright)/(CN faint) lines by dividing the individual moment maps. To avoid any low S/N pixels that were still included in the shuffle-stack creation of the CN moment maps, we spatially masked the CN bright and CN faint moment maps to include pixels with $> 6\sigma$ and $> 3\sigma$ emission in each spectral feature, respectively. This S/N threshold was chosen for each feature from the expected 2-to-1 (CN bright)/(CN faint) ratio that would come from optically thin CN emission in local thermodynamic equilibrium (LTE, Skatrud et al. 1983; Wang et al. 2004; Shirley 2015; Tang et al. 2019). Our main observational results, e.g. the CN and CO moment 0 maps, (CN bright)/CO ratio map, and total integrated spectra for all three lines, are combined and presented in four panel plots (Fig. 3.3 and Appendix 3.A), where only pixels with emission from all three lines have been included. (CN bright)/(CN faint) ratio maps for all galaxies are shown in Appendix 3.B.

We do not apply any correction for inclination angle of individual galaxies to our measured intensities. 13 of the 16 U/LIRGs in our sample are in some merger stage (see e.g. Stierwalt et al. 2013), and therefore an inclination angle is difficult to interpret (a comparison of our measured ratios with merger stage is deferred to a future paper; Ledger et al., in preparation). The galaxies which are not mergers are NGC 4418, ESO 320-G030, and NGC 1365 (Stierwalt et al. 2013). For reference, the inclination angles of these three galaxies are $i = 62°$ for NGC 4418 (Sakamoto et al. 2013), $i = 43°$ for ESO 320-G030 (Pereira-Santaella et al. 2016), and $i = 40°$ for NGC 1365 (Sakamoto et al. 2007).

CO (1 – 0) intensity binning

We also measure the (CN bright)/CO intensity ratios by binning pixels by the intensity of the CO (1 – 0) line. We split the range of CO intensities in logarithmic space into 15 CO intensity bins, spaced by $\sim 10^{0.25}$ K km s^{-1}. Choosing 15 bins allows for a minimum of eight bins in each galaxy. The first bin is equal to or less than $10^{0.5}$ K km s^{-1}, and the final bin is equal to or greater than $10^{3.75}$ K km s^{-1}. For the pixels in each bin, we measure the total integrated CO (1 – 0) intensity and shuffle-stack to get the total integrated CN (1 – 0) intensity.

Bešlić et al. (2021) and den Brok et al. (2021, 2022) perform a similar binning analysis when stacking into Galactocentric radial bins and CO (2-1) intensity bins. Similar to den Brok et al. (2022), we also identify upper limits on the binned intensities of the CN bright line if they are detected below a 3σ level. The results from binning and plots of the CO intensity binned ratio for each galaxy are discussed in Section 3.3.3.

Although we do not explicitly convert to molecular gas surface densities in this work, the reader can convert our CO intensity bins to Σ_{mol} bins [M$_\odot$ pc^{-2}] by multiplying by the ULIRG conversion factor: $\alpha_{\mathrm{CO}} = 1.088$ M$_\odot$ (K km s^{-1} pc^2)$^{-1}$.

3.2.6 Measuring the CN and CO intensity ratios

We measured global, peak, and spatially averaged (CN bright)/CO and (CN bright)/(CN faint) intensity ratios for each galaxy. The measured ratios are listed in Table 3.4.

(i) **(CN bright)/CO global ratios:** Global ratio values are measured using the total integrated intensities in Jy km s^{-1} of each spectral line and then converting to K km s^{-1}. For CO, we sum the detected pixels in the integrated intensity map. For CN bright, we

TABLE 3.4: Intensity ratios in K km s^{-1} of CN and CO in 16 U/LIRGs.

Galaxy[a]	(CN bright)/CO peak ratio	(CN bright)/CO global ratio	(CN bright)/CO spatial average[b]	(CN bright)/(CN faint) global ratio	(CN bright)/(CN faint) spatial average[b]	log(L_{IR})[c] ($L_\odot$)	Type of AGN[d]
IRAS 13120-5453	0.35 ± 0.01	0.17 ± 0.01	0.18 ± 0.01	1.64 ± 0.01	1.55 ± 0.03	12.28	Obscured
Arp 220	0.07 ± 0.01	0.09 ± 0.01	0.26 ± 0.02	2.07 ± 0.01	2.16 ± 0.08	12.21	Obscured
IRAS F05189-2524	0.26 ± 0.01	0.10 ± 0.01	0.20 ± 0.01	1.74 ± 0.01	1.73 ± 0.06	12.16	Seyfert 2
IRAS F10565+2448	0.22 ± 0.01	0.08 ± 0.01	0.15 ± 0.01	1.70 ± 0.01	1.63 ± 0.03	12.07	None
NGC 6240	0.10 ± 0.01	0.08 ± 0.01	0.16 ± 0.02	1.62 ± 0.01	1.78 ± 0.07	11.85	Obscured
IRAS F18293-3413	0.13 ± 0.01	0.05 ± 0.01	0.12 ± 0.01	2.14 ± 0.01	1.80 ± 0.05	11.79	None
NGC 3256	0.06 ± 0.01	0.02 ± 0.01	0.05 ± 0.01	1.99 ± 0.01	2.07 ± 0.04	11.75	Obscured
NGC 1614	0.17 ± 0.01	0.15 ± 0.01	0.20 ± 0.01	1.76 ± 0.01	1.72 ± 0.03	11.65	LINER
NGC 7469	0.28 ± 0.01	0.10 ± 0.01	0.27 ± 0.02	1.88 ± 0.01	1.73 ± 0.02	11.59	Seyfert 1
NGC 2623	0.13 ± 0.01	0.07 ± 0.01	0.13 ± 0.01	2.06 ± 0.01	1.88 ± 0.06	11.59	LINER
NGC 3110	0.07 ± 0.01	0.02 ± 0.01	0.07 ± 0.01	2.32 ± 0.01	1.64 ± 0.05	11.35	None
ESO 320-G030	0.17 ± 0.01	0.11 ± 0.01	0.24 ± 0.03	2.02 ± 0.01	2.00 ± 0.04	11.35	None
NGC 1068	0.08 ± 0.01	0.06 ± 0.01	0.07 ± 0.01	2.44 ± 0.01	2.75 ± 0.07	11.29	Seyfert 2
NGC 5104	0.09 ± 0.01	0.07 ± 0.02	0.11 ± 0.01	2.15 ± 0.02	1.99 ± 0.07	11.21	None
NGC 4418	0.12 ± 0.01	0.08 ± 0.01	0.09 ± 0.01	2.81 ± 0.01	2.58 ± 0.08	11.16	Obscured
NGC 1365[e]	0.05 ± 0.01	0.03 ± 0.01	0.05 ± 0.01	-	-	11.08	Obscured

Notes.
[a]The galaxies are listed in order of decreasing IR luminosity.
[b]Spatial averages are calculated from the intensity ratio maps as the mean pixel value and the uncertainties are given by jackknife sampling of the mean. The spatial averages are measured on maps with the pixels masked with $> 6\sigma$ and $> 3\sigma$ detections in the CN bright and CN faint lines, respectively.
[c]The log(L_{IR}) values are taken from GOALS (Armus et al. 2009) and we corrected them to our luminosity distances (as listed in Table 3.3).
[d]We classify the type of AGN based on previous literature as an obscured AGN (obscured), an optically identified AGN (Seyfert 1, Seyfert 2, or LINER), or no documented evidence for an AGN (none). For further discussion see Section 3.3.3. Galaxies with an obscured AGN: IRAS 13120 (Teng et al. 2015), Arp 220 (Sakamoto et al. 2017), NGC 6240 (Iwasawa et al. 2011), NGC 3256 southern nucleus (Sakamoto et al. 2014), NGC 4418 (Ohyama et al. 2019), and NGC 1365 (Swain et al. 2023). Galaxies with an optically classified AGN: IRAS F05189 (Smith et al. 2019), NGC 1614 (König et al. 2013), NGC 7469 (Liu et al. 2014), NGC 2623 (Aalto et al. 2002), and NGC 1068 (Saito et al. 2022a,b). Galaxies with no conclusive evidence for an AGN: IRAS F10565 (Iwasawa et al. 2011), IRAS F18293, NGC 3110 (Espada et al. 2018), NGC 5104, and ESO 320 (González-Alfonso et al. 2021).
[e]We only report (CN bright)/CO ratios because the spectral window for the NGC 1365 ALMA data did not cover the CN faint line.

integrate the shuffle-stacked spectral line. This approach takes advantage of the better S/N of the CN lines obtained through our shuffle-stacking method.

(ii) **(CN bright)/CO peak ratios:** To obtain the (CN bright)/CO peak ratio values, we measure the integrated intensity of each line using only the pixels in the strongest CO $(1-0)$ intensity bin (see the binning method described in Section 3.2.5). Note this is the ratio measured at the peak CO emission, and not necessarily the maximum (CN bright)/CO ratio in a given galaxy.

(iii) **(CN bright)/CO spatial averages:** The spatially averaged ratio values are obtained from averaging the pixels in the S/N matched moment maps, which may include uncertainties due to the S/N matching process (e.g., CO is masked using the Sun method and CN bright is masked at $> 6\sigma$).

(iv) **(CN bright)/(CN faint) global ratios and spatial averages**: The (CN bright)/(CN faint) global and spatial average ratios are measured in the same way as the (CN bright)/CO ratios, with CN bright and CN faint masked at $> 6\sigma$ and $> 3\sigma$, respectively. The spatially averaged ratios use the (CN bright)/(CN faint) S/N matched maps, which are shown in Fig. 3.25 in Appendix 3.B.

A brief note on Arp 220: The individual pixels of Arp 220 are not highly reliable because of varying RMS values across the data cube. However, we anticipate that the global values obtained will be trustworthy as they are calculated from multiple pixels and will average out the noise fluctuations. We do not consider absorption effects in our analysis, which have been seen previously in Arp 220 (see e.g. Ueda et al. (2022), although we do find subtle absorption signatures in the spectra of the CO and CN lines. The individual pixel data points for Arp 220 are not included in Figs. 3.4, 3.5, or 3.6, but we have quoted their values in Tables 3.4, 3.5, and 3.6. We recreated these three figures including the pixels in Arp 220 and provide them in Appendix 3.C.

3.3 The CN and CO Intensity Ratios in U/LIRGs

3.3.1 CN is more optically thin in LIRGs than ULIRGs

The (CN bright)/(CN faint) intensity ratio

We measure the (CN bright)/(CN faint) ratio in 16 U/LIRG galaxies using a global ratio calculated from comparing the total integrated intensities of the CN $(N = 1-0, J =$

$3/2 - 1/2$) and CN ($N = 1 - 0, J = 1/2 - 1/2$) hyperfine groupings. Additionally, we calculate a spatially averaged ratio using S/N matched ratio maps (Fig. 3.25). The ratios are presented in Table 3.4. On average, the (CN bright)/(CN faint) ratio we measure is lower when using the spatial averaging method than when calculating a global ratio from the shuffle-stacked spectra. This comparison implies we are picking up more bright relative to faint CN emission when using the stacking process. The uncertainty when calculating the spatially averaged ratio is higher than for the global ratios, in part because we have reduced the number of pixels used in calculating the spatial averages due to the S/N matching of the CN bright ($> 6\sigma$ cut) and CN faint ($> 3\sigma$ cut) lines. Using the integrated global stacked spectra, we measure (CN bright)/(CN faint) ratios ranging from $1.61 - 2.80$ in our galaxy sample. Using spatial averaging, we measure (CN bright)/(CN faint) ratios ranging from $1.55 - 2.75$. The overall trend of ULIRGs having lower (CN bright)/(CN faint) ratios than LIRGs and the range of ratio values are similar between the two methods.

Fig. 3.4 compares the luminosity of the CN bright line with the luminosity of the CN faint line in 14 of our 16 galaxies. NGC 1365 is not included, since the CN faint line was not observed in this galaxy. Arp 220 was excluded because we do not trust individual pixels because of varying RMS values across the data cube due to poor quality data (see Section 3.2.6); a version including Arp 220 is given in Fig. 3.28 in Appendix 3.C. We have used line luminosities in Fig. 3.4 instead of intensities to remove distance dependencies when comparing the ratio between galaxies.

The CN bright and CN faint lines should have a 2:1 brightness ratio for optically thin emission in LTE conditions (see e.g. Skatrud et al. 1983). To adjust for this, we use $> 6\sigma$ and $> 3\sigma$ S/N cuts for the CN bright and CN faint lines, respectively, in Fig. 3.4. The majority of individual pixels scatter around the 2:1 line; however, at higher line luminosities, there are a significant number of pixels that lie between the 1:1 dotted line and 2:1 dashed lines, indicating CN is becoming more optically thick in these regions.

Fig. 3.5 shows histograms of the (CN bright)/(CN faint) ratio after grouping the galaxies into ULIRG and LIRG samples. In Fig. 3.5, lower (CN bright)/(CN faint) ratios tend to be found in ULIRGs toward the left in the figure, matching the results from Fig. 3.4. Table 3.5 provides the mean, mode, and 16th, 50th and 84th quartiles of the histogram values for each galaxy and the combined values for the LIRG and ULIRG distributions.

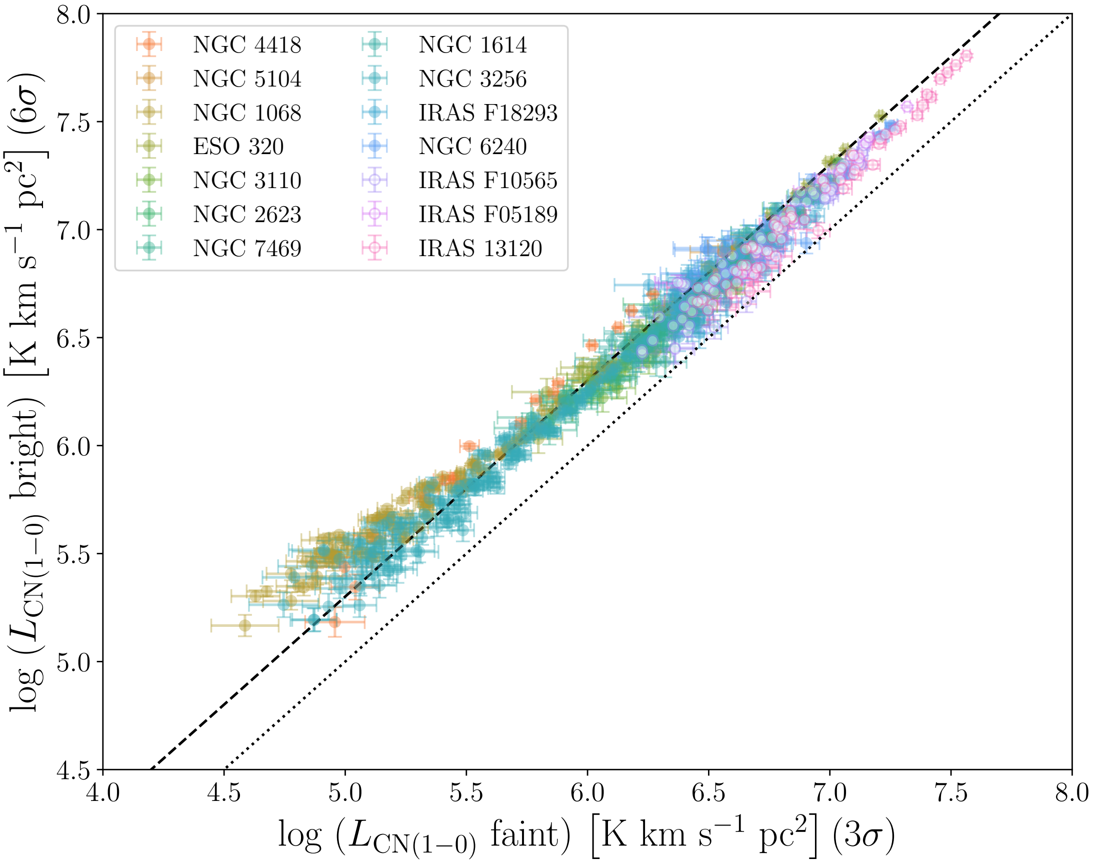

FIGURE 3.4: This figure compares the CN bright and CN faint lines on a pixel-by-pixel basis for 14 of the 16 galaxies in our sample. The (CN bright)/(CN faint) intensity ratio is lower in ULIRGs than LIRGs, implying that CN emission in more optically thick in ULIRGs. NGC 1365 is not included because the CN faint line is not covered by the spectral windows in the ALMA data. Data points from Arp 220 are not included due to uncertain pixels, but an example including this galaxy can be found in Fig. 3.28 in Appendix 3.C. Uncertainties on individual pixels are calculated from equation (3.1). Both pixel values and their uncertainties have been converted from fluxes to luminosities using equation (3.2). The pixels for the CN bright and CN faint lines are show with S/N cuts of $> 6\sigma$ and $> 3\sigma$, respectively. Pixels have been colourized by galaxy. Open circles are ULIRG galaxies. Closed circles are LIRG galaxies. The black-dotted and black-dashed lines represent 1:1 and 2:1 luminosity ratios, respectively. The colours for individual galaxies match those in Figs. 3.7 and 3.9.

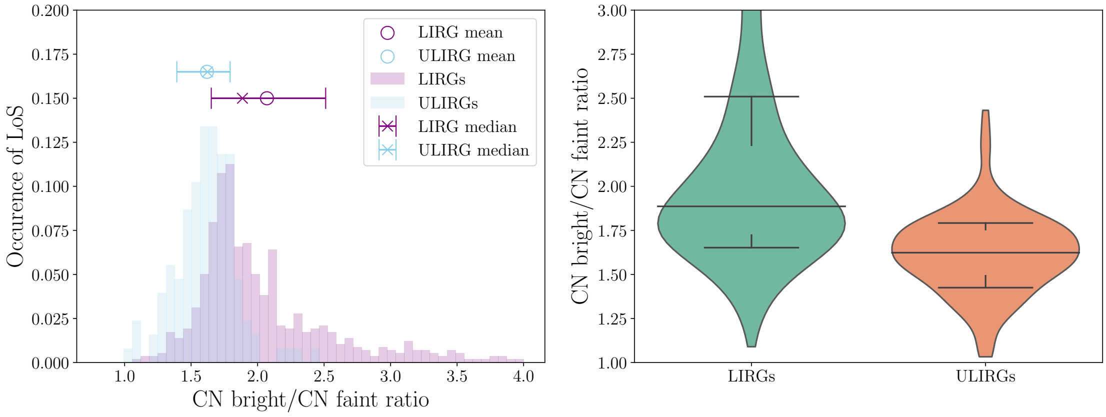

FIGURE 3.5: This figure shows the histograms of the (CN bright)/(CN faint) ratio after splitting the sample into pixels from ULIRGs and LIRGs. The median and mean (CN bright)/(CN faint) intensity ratios are lower in ULIRGs than LIRGs. Data points from Arp 220 are not included, but an example including this galaxy can be found in Fig. 3.26 in Appendix 3.C. Left panel: The y-axis shows the number of pixels with the specific ratio value, and the x-axis gives the ratio in a linear scale. The blue and violet histograms correspond to the ULIRG and LIRG data points, respectively. The open circles are the mean values of each distribution. The cross represents the median value, while the error bars extend to the 16$^{\text{th}}$ and 84$^{\text{th}}$ percentiles. A decreasing (CN bright)/(CN faint) ratio corresponds to an increasing optical depth. Right panel: Violin plots of the (CN bright)/(CN faint) intensity ratio in ULIRGs (orange) compared with LIRGs (green). The black lines correspond to the 16$^{\text{th}}$, 50$^{\text{th}}$, and 84$^{\text{th}}$ percentiles. The y-axis gives the (CN bright)/(CN faint) ratio in a linear scale.

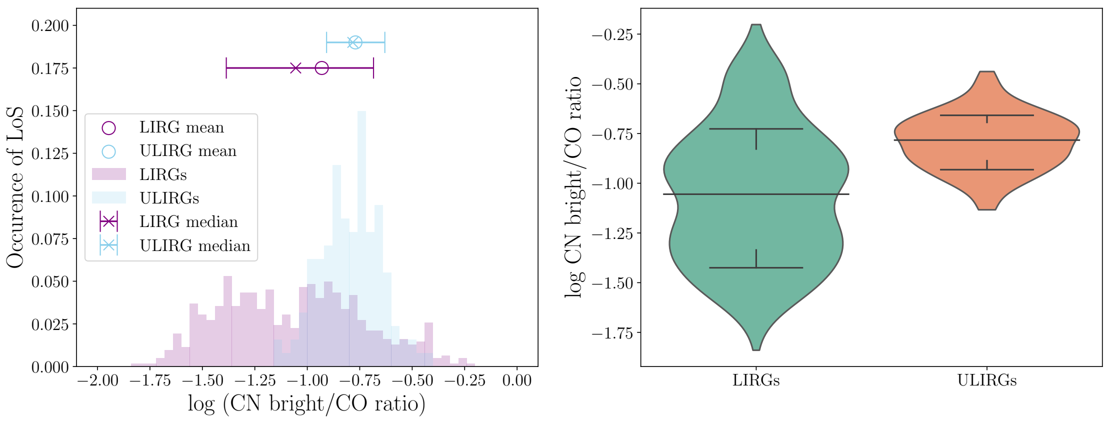

FIGURE 3.6: This figure shows the histograms of the (CN bright)/CO ratio after splitting the sample into pixels from ULIRGs and LIRGs. The (CN bright)/CO intensity is higher in ULIRGs than LIRGs; however, there is more spread in the ratio in LIRGs compared with ULIRGs. Data points from Arp 220 are not included, but an example including this galaxy can be found as Fig. 3.27 in Appendix 3.C. Left panel: The y-axis shows the number of pixels with the specific ratio value, and the x-axis gives the (CN bright)/CO ratio on a logarithmic scale. The blue and violet histograms correspond to the ULIRG and LIRG data points, respectively. The open circles are the mean values of each distribution. The cross represents the median value, while the error bars extend to the 16$^{\text{th}}$ and 84$^{\text{th}}$ percentiles. Right panel: Violin plots of the (CN bright)/CO intensity ratio in ULIRGs (orange) compared with LIRGs (green). The black lines correspond to the 16$^{\text{th}}$, 50$^{\text{th}}$, and 84$^{\text{th}}$ percentiles. The y-axis gives the (CN bright)/CO ratio on a logarithmic scale.

Estimating CN optical depths

The (CN bright)/(CN faint) intensity ratio can be used to estimate CN optical depth (Skatrud et al. 1983; Wang et al. 2004; Tang et al. 2019). We observe CN (1 – 0) line widths in excess of 100 km s^{-1}, which is sufficient to blend the hyperfine components of the nine individual CN lines which make up the two larger hyperfine groups. As a result, the optical depths we estimate are average τ values representative of the total integrated CN lines, and not opacities of individual hyperfine components or line peak opacities. We use the median ratio values from Table 3.5 to estimate the CN optical depth in ULIRGs compared with LIRGs. Under the initial assumption that the CN lines are optically thin and in LTE, we use equation (1) from Tang et al. (2019) to estimate the optical depth as

$$\frac{I_{\text{CN bright}}}{I_{\text{CN faint}}} = \frac{1 - e^{-\tau_1}}{1 - e^{-\tau_2}}. \tag{3.3}$$

τ_1 and τ_2 are the optical depths of the CN bright and CN faint lines, respectively, and $\tau_1 = 2\tau_2$ (Skatrud et al. 1983). Using the median (CN bright)/(CN faint) ratios from Table 3.5, we estimate the average CN optical depth to be $\tau = 0.96$ and $\tau = 0.23$ in ULIRGs and LIRGs, respectively. We note that CN is more optically thick in ULIRGs than LIRGs for our sample, although we only have three ULIRGs included in our analysis. Looking at Table 3.5, the trend is that galaxies with lower IR luminosities (L_{IR}) have lower CN optical depths, with (CN bright)/(CN faint) ratios closer to 2.

There are two galaxies with (CN bright)/(CN faint) > 2, NGC 1068 and NGC 4418, for which using this calculation method would mean $\tau \ll 1$. We attribute these high ratios to possible S/N matching issues, underestimated emission from the CN faint line, non-LTE effects in the excitation of the CN fine structure distribution, possible line blending effects, or the complicated influence of an AGN, which can be found in both galaxies.

CN opacities have been previously estimated in four nearby starburst galaxies. Henkel et al. (1998) observed CN in M82 using the IRAM 30m telescope and measured the (CN bright)/(CN faint) ratio to be ~ 2.33, implying optically thin CN emission. IC 342 was found to have optically thick CN emission, with a ratio of ~ 1.45 (Henkel et al. 1998) and an estimated optical depth of 4.09 (Nakajima et al. 2018). Wang et al. (2004) observed NGC 4945 with the Swedish-ESO Submillimeter Telescope. The authors found a (CN

TABLE 3.5: (CN bright)/(CN faint) intensity ratio distributions.

	(CN bright)/(CN faint) ratio			
Galaxy[a,b]	Mean[c]	16th-50th-84th[th]	Mode[d]	N^e
All ULIRGs	1.62 ± 0.02	1.39 – 1.62 – 1.79	1.5	127
IRAS 13120-5453	1.56 ± 0.03	1.36 – 1.58 – 1.75	1.5	53
Arp 220	2.17 ± 0.08	1.38 – 2.02 – 3.01	1.8	114
IRAS F05189-2524	1.74 ± 0.06	1.56 – 1.72 – 1.87	1.5	16
IRAS F10565+2448	1.64 ± 0.03	1.43 – 1.64 – 1.81	1.5	58
All LIRGs	2.07 ± 0.02	1.65 – 1.89 – 2.51	1.7	587
NGC 6240	1.79 ± 0.07	1.54 – 1.71 – 2.12	1.6	27
IRAS F18293-3413	1.81 ± 0.05	1.38 – 1.87 – 2.14	1.3	53
NGC 3256	2.08 ± 0.04	1.74 – 1.89 – 2.48	1.7	175
NGC 1614	1.73 ± 0.03	1.57 – 1.69 – 1.91	1.6	77
NGC 7469	1.74 ± 0.02	1.61 – 1.72 – 1.84	1.7	67
NGC 2623	1.89 ± 0.06	1.72 – 1.82 – 2.11	1.7	13
NGC 3110	1.65 ± 0.05	1.44 – 1.65 – 1.9	1.6	19
ESO 320-G030	2.01 ± 0.04	1.85 – 2.0 – 2.15	1.9	32
NGC 1068	2.76 ± 0.07	2.02 – 2.55 – 3.49	2.1	103
NGC 5104	2.00 ± 0.07	1.89 – 2.0 – 2.11	1.8	4
NGC 4418	2.59 ± 0.08	2.42 – 2.66 – 2.8	2.7	17

Notes.
[a]The galaxies are listed in order of decreasing IR luminosity.
[b]NGC 1365 is not included in this table because the CN faint line is not covered by the spectral windows in the ALMA data. Arp 220 is not included in the calculation of the 'All ULIRGs' values because the individual scatter points are not trustworthy.
[c]The uncertainty on the mean was calculated using jackknife resampling.
[d]The mode is the most common value in each histogram when dispersed in 50 bins ranging from 0.0 to 5.0.
[e]The number of points in the histogram for each galaxy as defined by the number of pixels seen in the spatial (CN bright)/(CN faint) ratio maps in Appendix 3.B. These ratio maps show pixels with $> 6\sigma$ and $> 3\sigma$ detections in the CN bright and CN faint lines, respectively.

TABLE 3.6: (CN bright)/CO intensity ratio distributions.

	(CN bright)/CO ratio			
Galaxy[a]	Mean[b]	16^{th}-50^{th}-$84th^{th}$	Mode[c]	N^d
All ULIRGs[e]	0.17 ± 0.01	0.12 – 0.16 – 0.22	0.17	127
IRAS 13120-5453	0.17 ± 0.01	0.12 – 0.16 – 0.23	0.12	53
Arp 220	0.22 ± 0.02	0.07 – 0.14 – 0.42	0.06	114
IRAS F05189-2524	0.21 ± 0.01	0.17 – 0.21 – 0.24	0.18	16
IRAS F10565+2448	0.15 ± 0.01	0.1 – 0.15 – 0.19	0.18	58
All LIRGs	0.12 ± 0.01	0.04 – 0.09 – 0.19	0.04	623
NGC 6240	0.15 ± 0.02	0.1 – 0.12 – 0.14	0.09	27
IRAS F18293-3413	0.11 ± 0.01	0.09 – 0.11 – 0.14	0.09	53
NGC 3256	0.05 ± 0.01	0.03 – 0.04 – 0.06	0.03	175
NGC 1614	0.19 ± 0.01	0.14 – 0.17 – 0.25	0.15	77
NGC 7469	0.25 ± 0.01	0.11 – 0.24 – 0.38	0.36	67
NGC 2623	0.13 ± 0.01	0.12 – 0.13 – 0.14	0.12	13
NGC 3110	0.07 ± 0.01	0.06 – 0.07 – 0.1	0.06	19
ESO 320-G030	0.24 ± 0.03	0.12 – 0.19 – 0.38	0.09	32
NGC 1068	0.08 ± 0.01	0.04 – 0.06 – 0.11	0.03	103
NGC 5104	0.11 ± 0.01	0.09 – 0.11 – 0.13	0.09	4
NGC 4418	0.09 ± 0.01	0.05 – 0.08 – 0.11	0.06	17
NGC 1365	0.05 ± 0.01	0.04 – 0.06 – 0.07	0.03	36

Notes.
[a]The galaxies are listed in order of decreasing IR luminosity.
[b]The uncertainty on the mean was calculated using jackknife resampling.
[c]The mode is the most common value in each histogram when dispersed in 50 bins ranging from 0.0 to 1.5.
[d]The number of pixels that are detected in all three spectral features, CN bright ($> 6\sigma$), CN faint ($> 3\sigma$), and CO.
[e]Arp 220 is not included in the calculation of the 'All ULIRGs' values because the individual scatter points are not trustworthy.

bright)/(CN faint) ratio of ∼ 1.58 and a moderate CN optical depth of 1.09. Similarly, Tang et al. (2019) used ALMA to measure a ratio of 1.68 and an optical depth of 0.8 in NGC 4945.

Henkel et al. (2014) measure the (CN bright)/(CN faint) ratio to be 1.55 in the starburst nucleus of NGC 253 using the IRAM 30m (with a peak temperature ratio of ∼ 1.96). From the ratio, Henkel et al. (2014) calculate a moderate optical depth of 0.5. Tang et al. (2019) measure a (CN bright)/(CN faint) ratio of 1.58 with ALMA in NGC 253, corresponding to an optical depth of 1.1. Their results suggest that the CN emission is becoming optically thick in NGC 253. In contrast, Meier et al. (2015) use ALMA to measure a (CN bright)/(CN faint) ratio of ∼ 2 in the inner disc of NGC 253, concluding that CN is optically thin. They found that their observed CN emission is strongest near the star forming regions of NGC 253 and the origin of the molecular outflow. Nakajima et al. (2018) quote an optical depth 0.39 in NGC 253, also suggesting a moderate to low optical depth in the central starburst, in agreement with Meier et al. (2015).

CN opacities have also been measured in three U/LIRGs. Henkel et al. (2014) observed Mrk 231 and found an integrated intensity ratio for (CN bright)/(CN faint) of ∼ 2, but do not quote an optical depth. Cicone et al. (2020) measure the CN $(1-0)$ line in the molecular outflows of Mrk 231 and found a (CN bright)/(CN faint) intensity ratio of ∼ 1.83. The measured (CN bright)/(CN faint) ratios in Mrk 231 are higher than the average values we find for the ULIRGs in our sample, suggesting this galaxy has more optically thin CN emission. Tang et al. (2019) used ALMA to observe CN $(1-0)$ in NGC 1068 and found a (CN bright)/(CN faint) ratio of 1.7 and an optical depth of 0.7. Nakajima et al. (2018) estimated an optical depth of 1.42 in NGC 1068. In contrast, we measure a (CN bright)/(CN faint) ratio of 2.44 in NGC 1068, suggesting optically thin emission. Differences in our methods for recovering CN emission using the shuffle-stack method could lead to this discrepancy for NGC 1068. König et al. (2016) measured a (CN bright)/(CN faint) integrated intensity ratio of 1.89 in NGC 1614, while we measure a ratio of 1.75 in NGC 1614 using the shuffle-stack method. Our conclusions agree with König et al. (2016) that CN emission will be moderately optically thin in this galaxy.

In summary, previous measures of CN optical depth in galaxies suggest that CN $(1-0)$ can indeed be used as an optically thin gas tracer for most cases, although moderate optical depths have been measured in some systems. Our analysis indicates a trend towards higher CN optical depths in ULIRGs relative to LIRGs, but we also observe variations between individual galaxies.

3.3.2 (CN bright)/CO is higher in ULIRGs compared with LIRGs

The (CN bright)/CO intensity ratio

Using the integrated global stacked spectra, we measure (CN bright)/CO ratios ranging from 0.02 to 0.17 in our galaxy sample. Using spatial averaging, we measure (CN bright)/CO ratios ranging from 0.047 to 0.26. For both methods, we find that ULIRGs have higher (CN bright)/CO ratios than LIRGs. The spatially averaged (CN bright)/CO ratios tend to be higher than the global ratios. We attribute these higher ratios to the $> 6\sigma$ S/N cut used for the CN bright line when creating the (CN bright)/CO ratio maps, which removes some of the pixels which have weaker CN bright emission relative to the CO emission. The fact that CN emission is weaker relative to CO was also considered in Wilson (2018), who used S/N matching between the two lines to avoid misinterpreting the (CN bright)/CO ratio because of the different line strengths and detection effects. We argue that our global ratio is a better representation of the true global (CN bright)/CO ratio than the spatially averaged ratios in our galaxies.

Fig. 3.6 shows histograms of the (CN bright)/CO ratio after grouping the galaxies into ULIRG and LIRG samples. Table 3.6 provides the mean, mode, and 16th, 50th and 84th quartiles of the histogram values for each galaxy and the combined values for the LIRG and ULIRG distributions (measured without Arp 220). By showing the distribution of pixel values rather than a single global ratio value for each galaxy, Fig. 3.6 demonstrates the complicated nature of the (CN bright)/CO ratio in galaxies. We conclude that the (CN bright)/CO ratio tends to be higher on average in ULIRGs (median value of 0.16) compared with LIRGs (median value of 0.09); however, the spread in the ratio values from the 16^{th} to 84^{th} percentiles is significantly larger in LIRGs ($0.04 - 0.19$) compared with ULIRGs ($0.12 - 0.22$).

Fig. 3.7 shows the (CN bright)/CO ratio histogram distributions for the individual galaxies in our sample, organized by increasing IR luminosity. Fig. 3.7 demonstrates that the ULIRGs have more compact distributions than the LIRGs. The larger scatter in the LIRGs can be attributed to differences in galaxy morphologies, less extreme ratio conditions found in galaxy discs which we can identify in certain systems, and the presence of a starburst/AGN in some galaxies. LIRGs with a smaller range of (CN

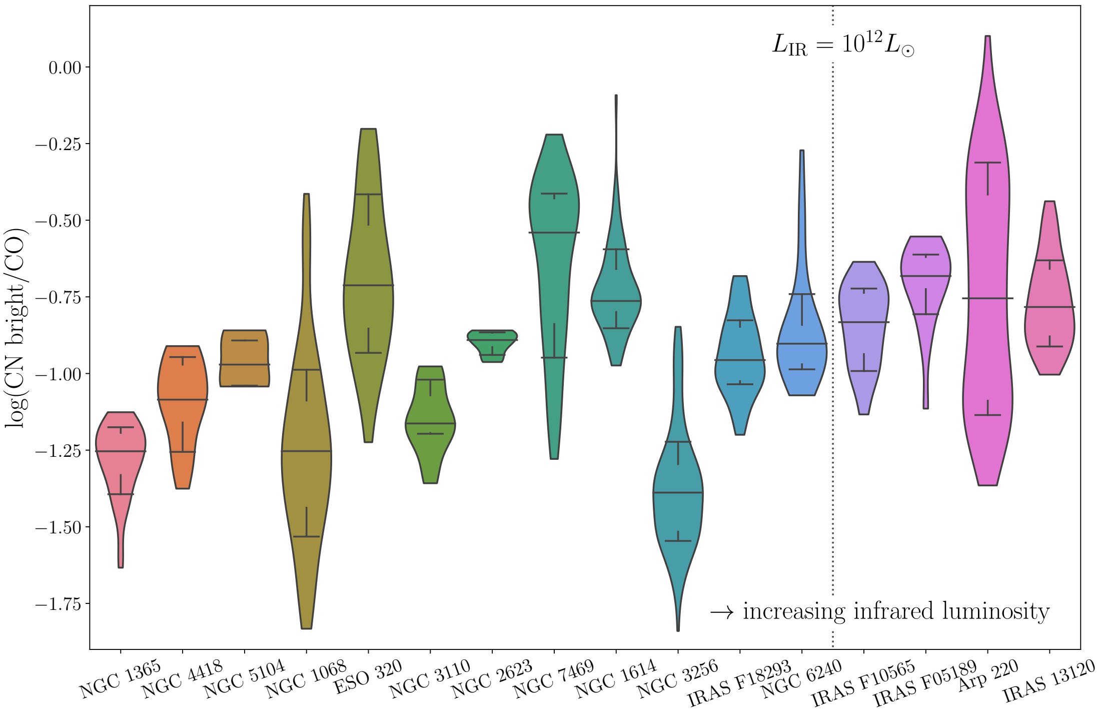

FIGURE 3.7: This figure shows the log-scale histograms of the CN bright/CO ratio as violin plots for each galaxy in our sample. There is a large spread in the (CN bright)/CO intensity ratio in our sample of LIRGs due to varying galaxy morphologies and types. The (CN bright)/CO intensity ratio is higher and has less spread on average in our ULIRG sample compared with the LIRGs. The violin plots are a visual way of representing the area-weighted averages from Table 3.4. The galaxies are organized in increasing order of IR luminosity from left to right. The black lines correspond to the 16$^{\mathrm{th}}$, 50$^{\mathrm{th}}$, and 84$^{\mathrm{th}}$ percentiles. Only pixels detected in the CO, CN bright > 6σ, and CN faint > 3σ lines are considered. Arp 220 is included but it should be noted that the individual scatter points are less trustworthy. The colours for individual galaxies match those in Figs. 3.4 and 3.9.

bright)/CO ratios are found to have accompanying compact ratio maps (compact in an absolute physical sense relative to the matched 500 pc resolution; Appendix 3.A). Three of our four ULIRGs (IRAS 13120, IRAS F05189, and IRAS F10565) also have compact ratio maps.

Our galaxy sample is quite heterogeneous, with many galaxies in various merger stages and hosting AGNs, starbursts, or some combination of the two. There is a range of $\sim$ 1.5 dex in IR luminosity between our galaxies, and they span distances between 10 and 200 Mpc. As such, it can be complicated to disentangle the physical origins of the variations observed in our (CN bright)/CO intensity ratios (Table 3.4). We plan to explore the variations in our observed (CN bright)/CO intensity ratio as a function of e.g. IR luminosity, C[II] luminosity, merger stage, and AGN fraction, in future work (Ledger et al., in preparation).

(CN bright)/CO ratios in previous observations of comparable galaxies

In general, our measured (CN bright)/CO intensity ratios and their variations agree with those previously observed in U/LIRG or starburst systems. Meier et al. (2015) measured a (CN bright)/CO ratio of 0.11 in the inner nuclear disc of NGC 253 compared with 0.035 in the outer nuclear disc. This result matches what we have seen for our starburst systems, where (CN bright)/CO appears to be stronger in the nuclear regions of galaxies and decreases in the less extreme disc regions. However, as NGC 253 is not an LIRG, we can only roughly compare the trends of our ratio values with what we might expect in the starburst nucleus of this galaxy. Wilson (2018) measured a global ratio of 0.05 in NGC 253 at kiloparsec scales, which is likely averaging out the variations seen on resolved scales.

Wilson (2018) carried out a study of the (CN bright)/CO intensity ratio using Cycle 0 ALMA data in a sample of eight galaxies with starbursts and AGN, including four LIRGs and one ULIRG. The four LIRGs (AM 2246-490, NGC 3256, VV 114, and AM 1300-233) have (CN bright)/CO ratios ranging 0.02 – 0.14 when using S/N matching between the lines[5]. This wide range of values is comparable with the global ratio range we find for our LIRG sample, which spans from 0.02 to 0.15. The one shared LIRG

[5] The S/N matching method used in Wilson (2018) involved iterating on different S/N cuts for the CN and CO lines to minimize the impact of the different line strengths on the measured line ratios. For exact details on the S/N matching performed, we refer the reader to Wilson (2018).

between our samples is NGC 3256, and we both find a global (CN bright)/CO ratio of ~ 0.02. The ULIRG (AM 2055-425) has a ratio of 0.07, which is comparable to the global ratios found in Arp 220 (0.09 ± 0.02), IRAS F05189-2524 (0.10 ± 0.04), and IRAS F10565+2448 (0.08 ± 0.02). Our work builds on the observed CN/CO ratio study performed in Wilson (2018) by adding four additional ULIRGs and eleven additional LIRGs. Further, we use newer ALMA data (Cycles 1-6) to measure the CN/CO intensity ratios on resolved as well as global scales, and include the CN faint line in our analysis.

Cicone et al. (2020) observed both CN and CO emission in the molecular outflow of Mrk 231. The authors measured the total CN/CO line luminosity ratio to be ~ 0.21, but found that the ratio is enhanced by a factor of ~ 3 to 0.70 and 0.9 in the blue and redshifted line wings of the outflow, respectively. They attribute this enhancement of the CN/CO ratio to stronger UV radiation fields present in the gas, perhaps from the formation of massive stars in the outflow. Wilson et al. (2023) measured the global (CN bright)/CO intensity ratio in a sample of four LIRGs, three of which overlap with our galaxy sample (IRAS 13120, NGC 7469, and NGC 3256). The global ratios measured by Wilson et al. (2023) are 0.176, 0.103, and 0.045 in IRAS 13120, NGC 7469, and NGC 3256, respectively. Our global ratios of 0.17 and 0.10 agree with their results for IRAS 13120 and NGC 7469, but our global ratio in NGC 3256 is lower (0.02). However, our spatially averaged (CN bright)/CO intensity ratio of 0.05 is in agreement for NGC 3256. Wilson (2018), Cicone et al. (2020), and Wilson et al. (2023) found higher (CN bright)/CO ratios towards regions with higher SFRs in U/LIRGs. Future work measuring the star formation rate surface densities in our galaxy sample will allow us to directly compare any trends of CN/CO with SFR and UV radiation field.

3.3.3 CN emission is stronger in galaxy nuclei than extended discs

We look for resolved variations in the CN/CO intensity ratio in individual galaxies by binning the pixels in each galaxy into 15 CO intensity bins (Section 3.2.5). Fig. 3.8 shows a compilation of the (CN bright)/CO intensity ratios versus CO intensity in each galaxy in our sample, distinguishing detected and non-detected pixels using a $> 3\sigma$ detection limit for the CN bright line. The CO intensity binning is effectively a rough 'gas surface density binning', since CO intensity can be converted to a gas surface density (for Fig. 3.8, use an $\alpha_{\rm CO} = 1.088$ M$_\odot$ (km s^{-1} pc^2)$^{-1}$; Bolatto et al. 2013). Binning by CO intensity also mimics a rough radial trend, with the higher intensity bins corresponding

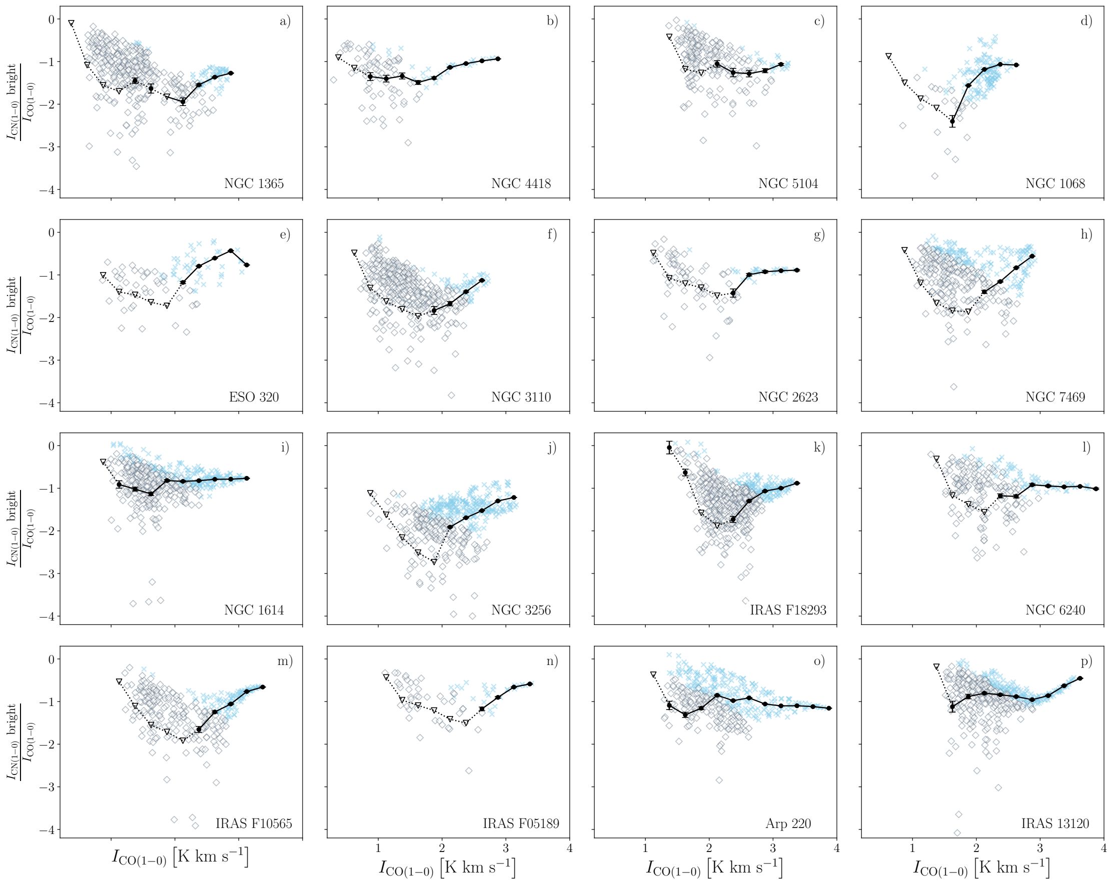

FIGURE 3.8: This figure shows the flat or gently increasing trend in the log-scale (CN bright)/CO intensity ratios with CO intensity (K km s^{-1} units). The large round connected symbols represent the binned values in the CO intensity bins with $> 3\sigma$ detections in the CN stacked spectra (see Section 3.2.5). The open triangles represent the CO intensity binned pixels which correspond to $< 3\sigma$ detections in the stacked CN bright spectra. The detected bins are connected by solid lines, while the non-detected binned data points are connected by dotted lines. The uncertainties on the binned data points are from equation (3.1). The faint blue scattered crosses represent the individual pixels detected in CN with $> 3\sigma$, while the grey open diamonds are the pixels with $< 3\sigma$.

to nuclear regions of galaxies and the lower bins being in the extended disc regions. We see that there is a flat or gently rising trend of (CN bright)/CO for higher CO intensity bins which holds for most galaxies in our sample. In some galaxies, particularly the ULIRGs, we see a factor of 2 or 3 increase in the (CN bright)/CO intensity ratio from the lowest CO intensity bin to the highest.

The trends seen in Fig. 3.8 can be compared with the (CN bright)/CO global and peak ratios in Table 3.4. The peak ratio represents the (CN bright)/CO ratio in the pixels found in the highest CO intensity bin, which roughly corresponds to the nuclear region of each galaxy. For most galaxies which exhibit higher peak ratios than global ratios, the (CN bright)/CO ratio gently rises with increasing CO intensity. When we compare these galaxies with the corresponding (CN bright)/CO ratio maps, we see that CN bright and CO are both spatially extended. The extended emission from both lines indicates that we are able to compare the ratio in the nuclear region of the galaxy with the extended disc, where the CN bright emission is weaker and the (CN bright)/CO ratio is lower. Galaxies that have (CN bright)/CO global ratios comparable with their peak ratios (e.g. NGC 1614 and NGC 5104), are those where the CN bright emission is compact but the CO is extended. This trend may indicate that the galaxies have a compact, dense core and CN bright emission is concentrated in the galaxy nucleus and therefore we do not resolve any trends with CO intensity.

Fig. 3.9 summarizes our comparison of the (CN bright)/CO ratio in the peak CO intensity bin compared with the global value in our entire galaxy sample. For every galaxy in our sample except Arp 220, the global (CN bright)/CO intensity ratio is lower than the ratio measured in the peak CO intensity bin. The average global (CN bright)/CO intensity ratio in our entire sample is 0.08 ± 0.01, a factor of 2 lower than the peak average of 0.15 ± 0.02.

Does (CN bright)/CO trace the position of a nuclear starburst or AGN?

The trend of increasing (CN bright)/CO intensity ratio in the nuclear regions of our galaxy sample matches the prediction that CN emission should increase in a PDR (Boger & Sternberg 2005). Galactic nuclei of U/LIRGs tend to be starburst dominant (Lonsdale et al. 2006), indicating that most nuclear regions in these galaxies are large PDRs. Meier et al. (2015) also found a higher (CN bright)/CO intensity ratio in the starburst centre of NGC 253 compared with the surrounding disc. For galaxies in our sample which do not host an AGN, we argue that the increase in the peak (CN bright)/CO ratio is a result of increased starburst-driven PDRs. Future work will compare the (CN bright)/CO intensity ratio maps with maps of surface density of star formation rates, so we can more directly compare the (CN bright)/CO ratio with the physical driver of star formation.

A more complicated influence in the nuclear regions of some of our galaxy sample is the presence of an AGN. An AGN will create a localized region of enhanced X-ray emission (an XDR) which will significantly impact the physical and chemical properties of the molecular gas (Meijerink et al. 2007). The typical scale of influence of an AGN is roughly 50 – 100 pc (see e.g. Izumi et al. 2020). The prediction from XDR models in Meijerink et al. (2007) is that there will be an increased CN/HCN abundance ratio due to the enhanced X-ray emission, and so we might expect a similar (CN bright)/CO intensity ratio increase in an XDR as in a PDR. Wilson et al. (2023) found evidence which supports this claim, with an increased ratio in the centres of two Seyfert nuclei galaxies NGC 7469 and NGC 1808. Additionally, Saito et al. (2022b) show an increasing CN/CO ratio near the AGN in NGC 1068 and the jet-driven molecular outflow. In contrast, Wilson (2018) found that the global (CN bright)/CO ratio decreased in the vicinity of three of the four AGNs in her galaxy sample, which is contrary to XDR model predictions (Meijerink et al. 2007).

In Table 3.4, we classify each of our 16 galaxies according to the type of AGN documented in the literature. There is no conclusive evidence for an optically identified or obscured AGN in 5 of our 16 galaxies: IRAS F10565, IRAS F18293, NGC 3110, NGC 5104, and ESO 320. Five galaxies in our sample have strong, optically defined AGN: IRAS F05189, NGC 1614, NGC 7469, NGC 2623, and NGC 1068. IRAS F05189 is optically classified as a Seyfert 2 (Smith et al. 2019). NGC 1068 is a Seyfert 2 AGN with a jet-driven molecular outflow (Saito et al. 2022a,b). NGC 7469 has a strong nuclear type-1 AGN (Liu et al. 2014), with a sphere of influence of ~ 3 pc with $M_{\rm BH} = 1.06 \times 10^7 M_\odot$ (Peterson et al. 2014), and a central XDR (Izumi et al. 2020). NGC 1614 (König et al. 2013) and NGC 2623 (Aalto et al. 2002) are both classified as LINERs.

Six galaxies in our sample have obscured or embedded AGN: IRAS 13120, Arp 220, NGC 6240, the southern nucleus of NGC 3256, NGC 4418, and NGC 1365. IRAS 13120 has been optically classified as a Seyfert 2 AGN (Véron-Cetty & Véron 2010); however, it is likely that the AGN is inactive, heavily obscured, and Compton-thick ($N_{\rm H} > 10^{24}$ cm^{-2}, Teng et al. 2015). The two nuclei of Arp 220 are heavily obscured (Sakamoto

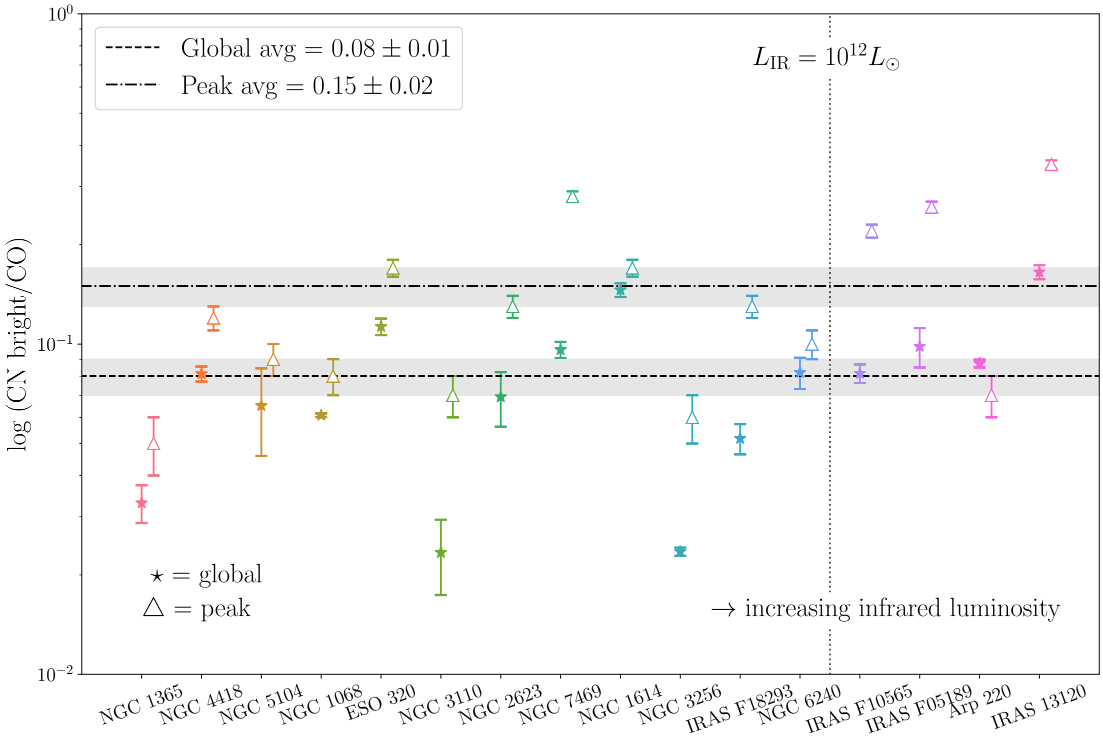

FIGURE 3.9: This figure shows the log-scale global and peak intensity (CN bright)/CO ratios in our sample of galaxies. The (CN bright)/CO intensity ratio at the CO intensity peak is higher in each galaxy compared with the global value. The CO intensity peak, and therefore peak ratio, roughly lines up with the nuclear region of each galaxy.The galaxies are organized in increasing order of IR luminosity from left to right. Closed star symbols give the global intensity ratio as measured from the total CN bright and CO integrated spectra (Table 3.4). Closed triangles give the peak intensity ratio as measured in the highest CO intensity bin (Section 3.2.5; Fig. 3.8. The dashed and dot-dashed black lines give the mean values for the global and peak intensity ratios, respectively. The uncertainties include the 5 per cent flux uncertainty on Band 3 observations with ALMA.

et al. 2017; Scoville et al. 2017), but the presence of an AGN has been inferred from X-ray (Paggi et al. 2017) and gamma-ray (Yoast-Hull et al. 2017) observations. NGC 6240 is heavily obscured (Iwasawa et al. 2011) and has two separated AGNs (Saito et al. 2018). The southern nucleus of NGC 3256 has an embedded, dormant AGN (Sakamoto et al. 2014), with evidence from both IR and X-ray emission (Ohyama et al. 2015) and observations of a jet-driven outflow (Sakamoto et al. 2014; Brunetti et al. 2021). An optical spectroscopic study of NGC 4418 found an enshrouded compact core with no luminous AGN (Ohyama et al. 2019). Finally, Swain et al. (2023) confirmed the presence of an obscured AGN in NGC 1365 using multiwavelength observations.

We find that 10 out of 11 galaxies in our sample that have well-documented AGN show an increase in the peak (CN bright)/CO intensity ratio relative to the global ratio (six of these galaxies show a significant increase within our uncertainties). The one galaxy of eleven which does not show an increase is Arp 220, which is thought to host two heavily obscured AGN in its merging nuclei, detected in X-rays (Paggi et al. 2017) and gamma rays (Yoast-Hull et al. 2017). The high column densities seen in this system (Sakamoto et al. 2017; Scoville et al. 2017) combined with our inability to resolve the two individual nuclear centres make this a challenging result to interpret in the general context of the impact of AGN on the (CN bright)/CO ratio.

Our work has offered significant evidence for the enhancement of the (CN bright)/CO intensity ratio in the galaxies with an AGN, which may be related to the increased X-ray emission dominating the nuclear regions of these galaxies. However, for most of our systems, the 500 pc resolution is not sufficient to disentangle competing AGN and starburst effects in the nuclear region and it may be difficult to identify any trends in (CN bright)/CO within an XDR. More highly resolved studies of individual systems with known AGN are required to conclusively compare our results with models of XDRs and PDRs in U/LIRGs. Future line ratio studies on 50-100 pc scales near known AGN would be beneficial for a more direct comparison with XDR models.

3.4 Conclusions

We have observationally quantified the CN ($N = 1-0$) / CO ($J = 1-0$) intensity ratio in a large selection of nearby U/LIRGs using the power of the ALMA archive. We measured the (CN bright)/CO and (CN bright)/(CN faint) intensity ratios in four

ULIRGs and twelve LIRGs, matching calibration, imaging, and data analysis techniques between galaxies. We have quantitatively and qualitatively compared our ULIRG and LIRG samples. Our main conclusions are as follows:

(i) Globally measured ratios using spectral stacking methods offer insight into the effect that spatial averaging has on intensity ratios due to S/N differences. We argue that our shuffle-stack method allows us to recover more weak CN emission and better recover the 'true' CN/CO intensity ratio in our galaxies.

(ii) The (CN bright)/(CN faint) intensity ratio is higher in LIRGs compared with ULIRGs. Converting this ratio into a CN optical depth indicates that CN is more optically thick in ULIRGs than LIRGs, although CN is optically thin or moderately thick in most cases. We measure the average optical depth to be $\tau \sim 0.96$ in ULIRGs and $\tau \sim 0.23$ in LIRGs.

(iii) Our measured (CN bright)/CO ratios are higher in ULIRGs than LIRGs. As we have a heterogeneous sample of 16 U/LIRG galaxies spanning various merger stages, AGN, and starburst contributions, we are unable to disentangle the exact physical origin of our observed line ratio variations. We plan to explore this physical origin and compare with global galactic properties in forthcoming work (Ledger et al., in preparation).

(iv) The (CN bright)/CO ratio shows more spread in LIRGs than ULIRGs, with the resolved ratio spanning a 16^{th}-84^{th} percentile range of 0.15 in LIRGs compared with 0.1 in ULIRGs. The global ratio values range from 0.02 to 0.15 in LIRGs and from 0.08 to 0.17 in ULIRGs. This difference is likely due to the larger range of galaxy types, morphologies, and components probed in LIRGs compared with the more compact ULIRGs.

(v) In 15 of our 16 galaxies, the (CN bright)/CO intensity ratio is higher in the peak CO intensity bin than the global value (only Arp 220 demonstrates a decrease in the peak ratio, and this may result from untrustworthy pixel effects when binning this galaxy). The average peak ratio is 0.15 ± 0.02, while the average global ratio is 0.08 ± 0.01. We argue that the increase in the (CN bright)/CO intensity ratio is a complicated combination of the presence of starbursts and/or AGN. In particular, six out of eleven galaxies which have well-documented AGN show a statistically significant increase in the (CN bright)/CO intensity ratio in the peak CO intensity bin relative to the global emission. Both optically defined AGN and obscured AGN have a similar impact on the ratio. This may be significant evidence that CN emission and/or abundance is enhanced by AGN. Future work on intensity ratios measured at < 100 pc is necessary to explore the impact an AGN on resolved scales.

We plan to compare our CN/CO intensity ratios star formation rate surface densities derived using radio continuum data in future work. We also plan to compare the global ratios with various parameters compiled in the GOALS survey for each galaxy, e.g., $L_{\rm IR}$, merger stage, AGN fraction, and [CII] luminosity (Ledger et al., in preparation).

Acknowledgements

We thank the anonymous referee for their detailed comments and revisions which improved the quality and content of this work.

This paper makes use of the following ALMA data:
ADS/JAO.ALMA#2012.1.00306.S,
ADS/JAO.ALMA#2012.1.00657.S,
ADS/JAO.ALMA#2013.1.00218.S,
ADS/JAO.ALMA#2013.1.00991.S,
ADS/JAO.ALMA#2013.1.01172.S,
ADS/JAO.ALMA#2015.1.00003.S,
ADS/JAO.ALMA#2015.1.00167.S,
ADS/JAO.ALMA#2015.1.00287.S,
ADS/JAO.ALMA#2015.1.01135.S,
ADS/JAO.ALMA#2015.1.01191.S,
ADS/JAO.ALMA#2016.1.00177.S,
ADS/JAO.ALMA#2016.1.00263.S,
ADS/JAO.ALMA#2017.1.00078.S,
ADS/JAO.ALMA#2018.1.00223.S,
ADS/JAO.ALMA#2018.1.01684.S, and
ADS/JAO.ALMA#2019.1.01664.S.

ALMA is a partnership of ESO (representing its member states), NSF (USA), and NINS (Japan), together with NRC (Canada), MOST and ASIAA (Taiwan), and KASI (Republic of Korea), in cooperation with the Republic of Chile. The Joint ALMA Observatory is operated by ESO, AUI/NRAO, and NAOJ. The National Radio Astronomy Observatory is a facility of the National Science Foundation operated under cooperative agreement by Associated Universities, Inc. Any ALMA specification details in this research has made use of G. Privon et al. 2022, ALMA Cycle 9 Proposer's Guide, ALMA Doc. 9.2 v1.4.

This research has made use of the NASA/IPAC Extragalactic Database (NED) which is operated by the Jet Propulsion Laboratory, California Institute of Technology, under contract with the National Aeronautics and Space Administration. The computing resources available at NAOJ were essential for this project. Data analysis was in part carried out on the Multi-wavelength Data Analysis System (MDAS) operated by the Astronomy Data Center (ADC), National Astronomical Observatory of Japan.

BL acknowledges partial support from an NSERC Canada Graduate Scholarship-Doctoral and an Ontario Graduate Scholarship. BL acknowledges funding for a 10-week Japan Society for the Promotion of Science (JSPS)-Mitacs summer research program which made this work possible. BL would like to thank Drs. Daisuke Iono and Toshiki Saito for hosting him at NAOJ and their guidance during the first months of this project. CDW acknowledges financial support from the Canada Council for the Arts through a Killam Research Fellowship. The research of CDW is supported by grants from the Natural Sciences and Engineering Research Council of Canada (NSERC) and the Canada Research Chairs program.

Software: This research has made use of the following software packages: `ASTROPY`, a community-developed core PYTHON package for astronomy (Astropy Collaboration et al. 2013, 2018, 2022), `CASA` (McMullin et al. 2007), `SciPy` (Virtanen et al. 2020), `MATPLOTLIB` (Hunter 2007), `NUMPY` (Harris et al. 2020), and `SPECTRAL-CUBE` (Ginsburg et al. 2019).

Data Availability

The derived data generated in this research will be shared on reasonable request to the corresponding author.

3.A Appendix: Galaxy images

The four panel plots of each galaxy are shown in decreasing order of the galaxy's IR luminosity. The four panels represent: (a) the moment 0 map for the CO line; (b) the

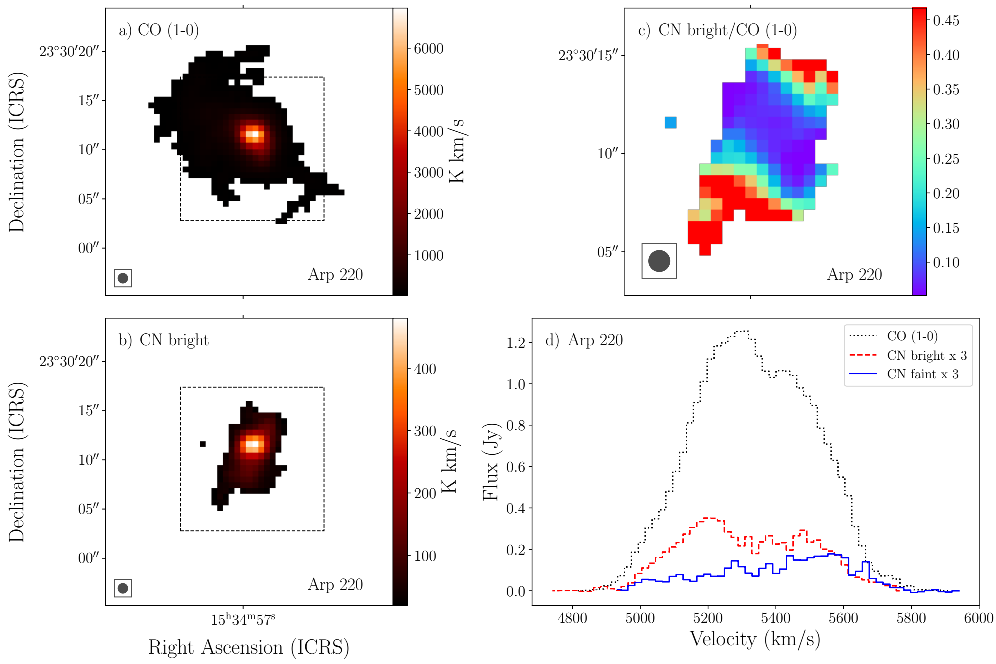

FIGURE 3.10: This figure shows an example of the moment 0 maps and (CN bright)/CO intensity ratio in K km s^{-1} units in Arp 220. The circle in the bottom left corner is the size of the beam smoothed to 500 pc. (a) The total integrated intensity of the CO (1-0) line. The dashed square indicates the region in (c). (b) The total integrated intensity of the CN bright line. The pixels included here have a S/N of $> 6\sigma$ and $> 3\sigma$ in the CN bright and CN faint lines, respectively. (c) The (CN bright)/CO intensity ratio. The colour bar is clipped at the mean value plus or minus 80 per cent. (d) The total integrated spectra of the CO line (black dotted), CN bright line (red dashed), and CN faint line (blue). Both CN lines have been multiplied by a factor of 3 for demonstration purposes.

moment 0 map for the CN bright line; (c) the (CN bright)/CO intensity ratio map; and (d) the total integrated spectra for each of the CN bright, CN faint, and CO lines. Refer to the discussion in Section 3.2.5 for more details and interpretation of individual plots. The maps included in this appendix section were used when measuring the spatially averaged (CN bright)/CO intensity ratios (Table 3.4).

3.B Appendix: (CN bright)/(CN faint) ratio maps

Fig. 3.25 shows a compilation of the (CN bright)/(CN faint) ratio maps in each galaxy in our sample. Each ratio map includes pixels with $> 6\sigma$ and $> 3\sigma$ detections in the

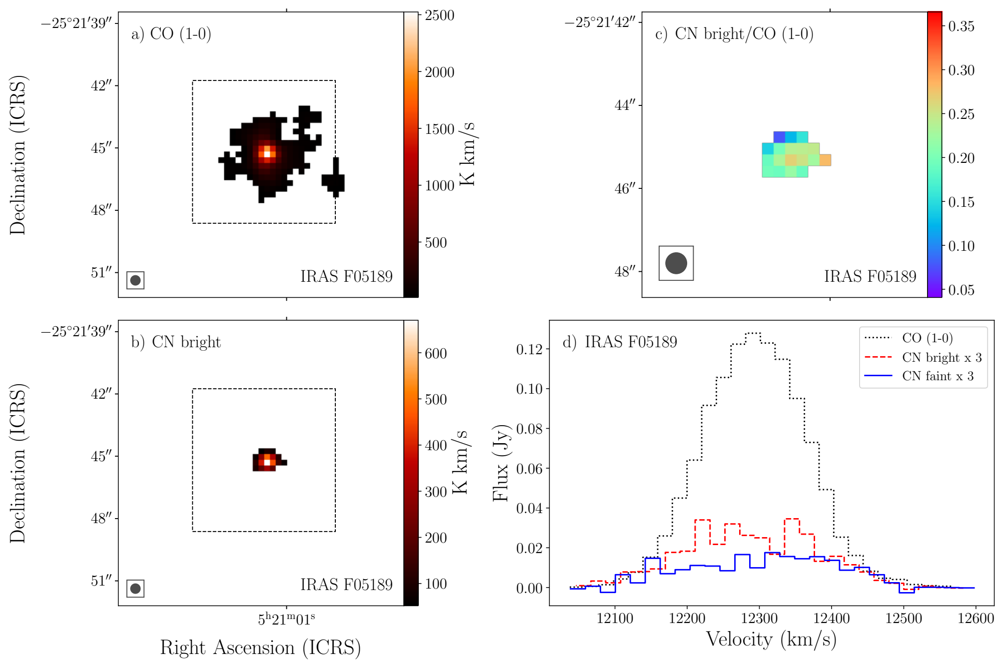

FIGURE 3.11: Moment maps, ratio maps, and spectra for IRAS F05189. See Figure 3.10 for more details.

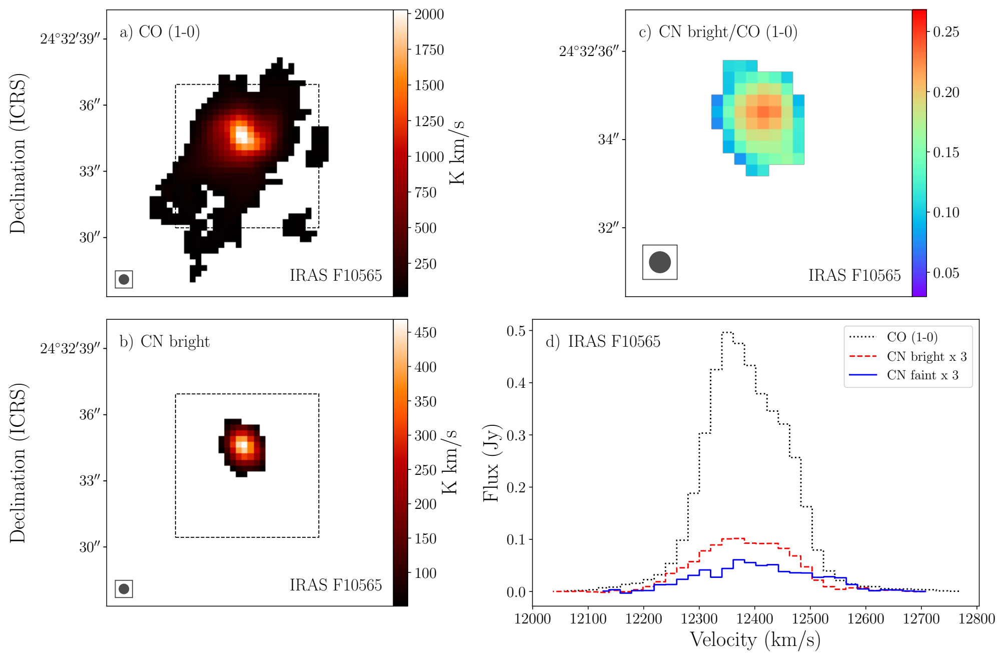

FIGURE 3.12: Moment maps, ratio maps, and spectra for IRAS F10565. See Figure 3.10 for more details.

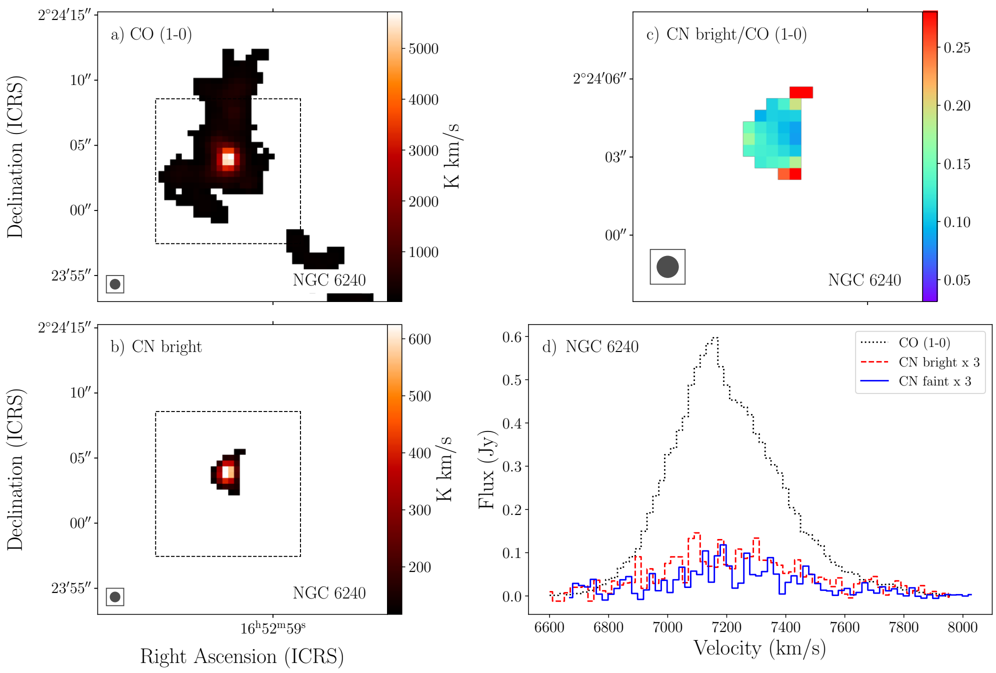

FIGURE 3.13: Moment maps, ratio maps, and spectra for NGC 6240. See Figure 3.10 for more details.

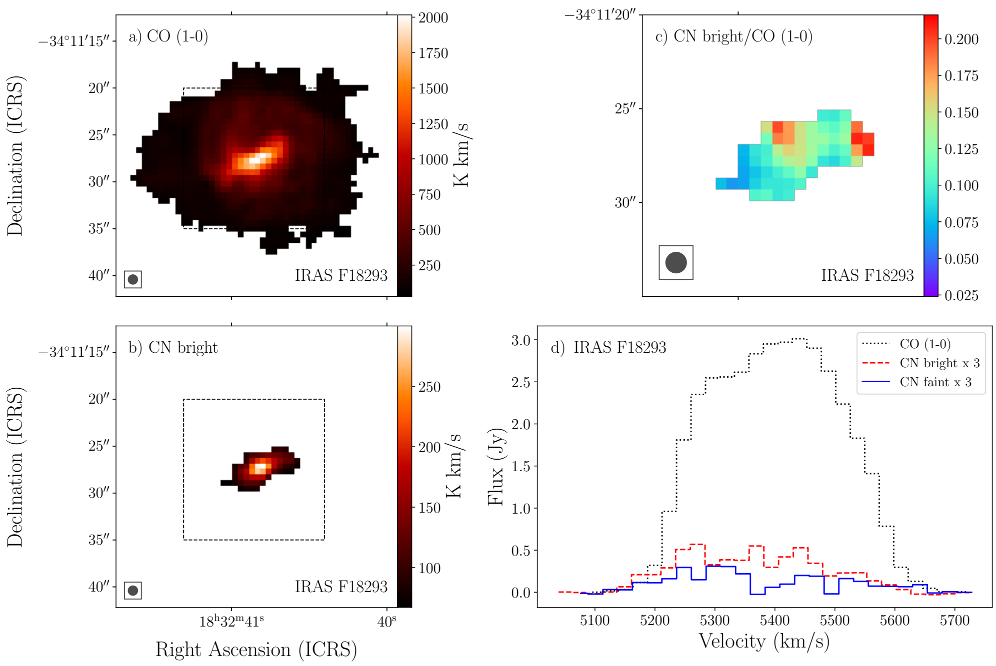

FIGURE 3.14: Moment maps, ratio maps, and spectra for IRAS F18293. See Fig. 3.10 for more details.

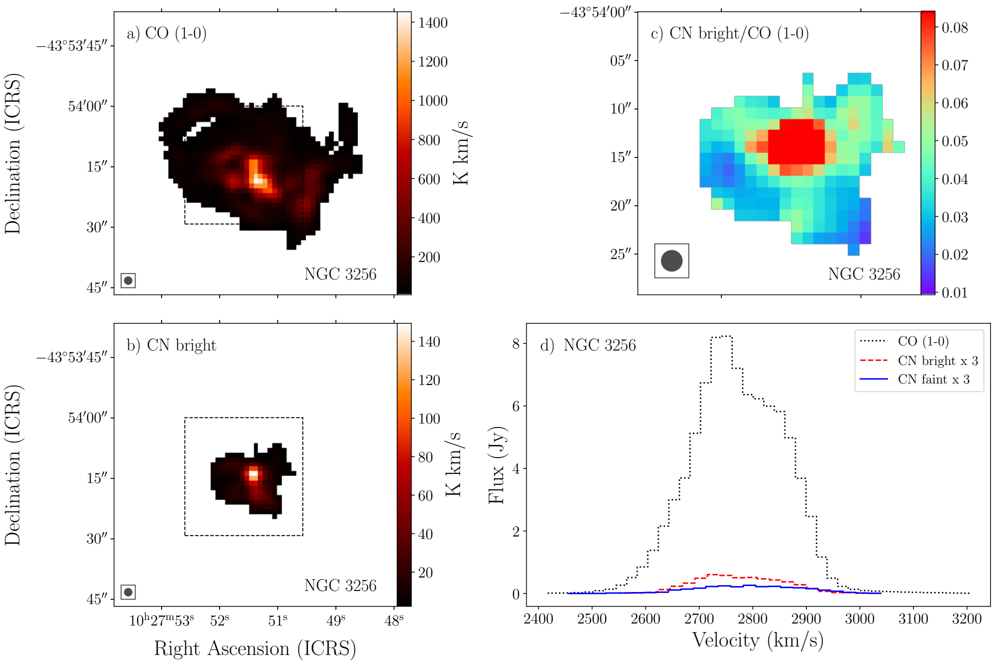

FIGURE 3.15: Moment maps, ratio maps, and spectra for NGC 3256. See Fig. 3.10 for more details.

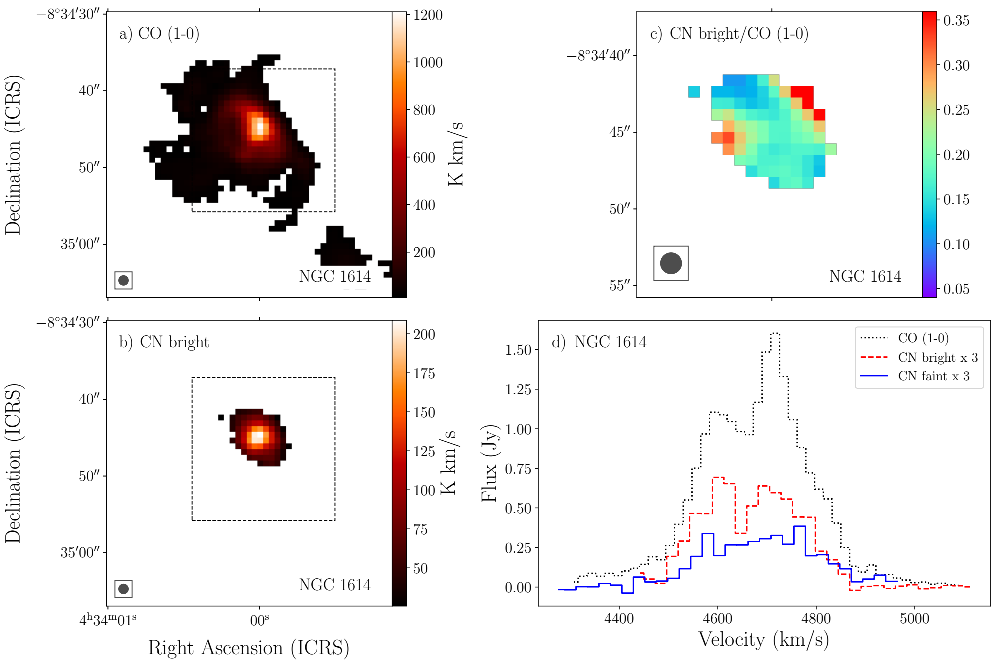

FIGURE 3.16: Moment maps, ratio maps, and spectra for NGC 1614. See Fig. 3.10 for more details.

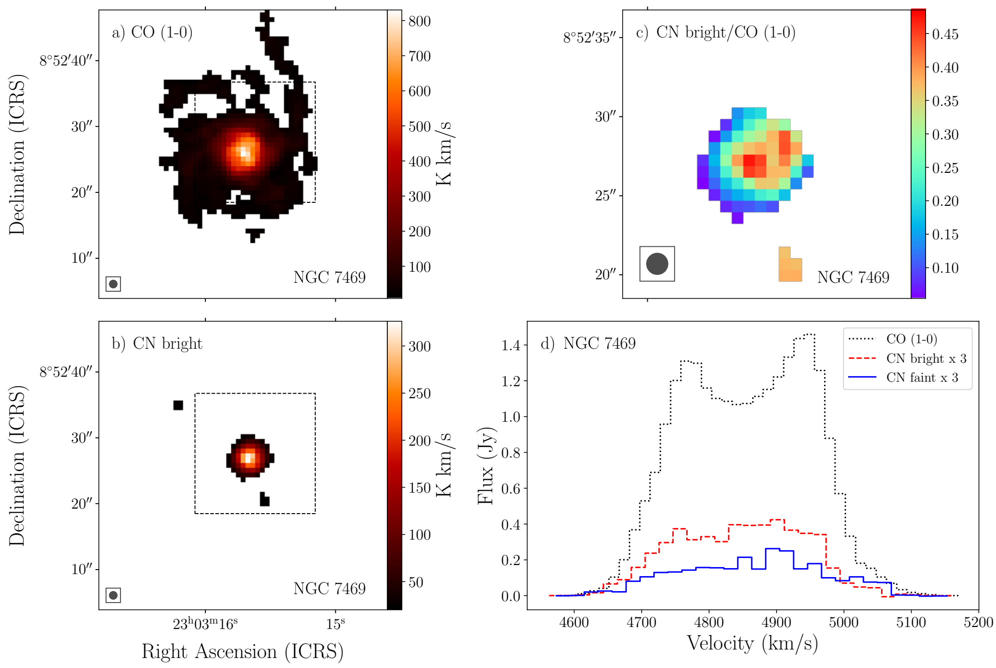

FIGURE 3.17: Moment maps, ratio maps, and spectra for NGC 7469. See Fig. 3.10 for more details.

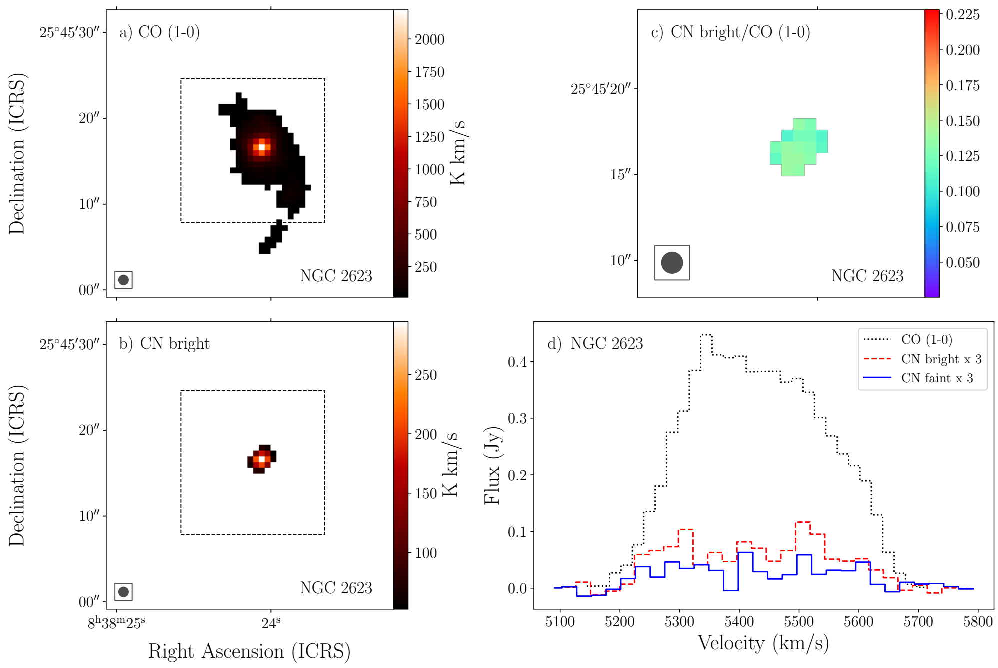

FIGURE 3.18: Moment maps, ratio maps, and spectra for NGC 2623. See Fig. 3.10 for more details.

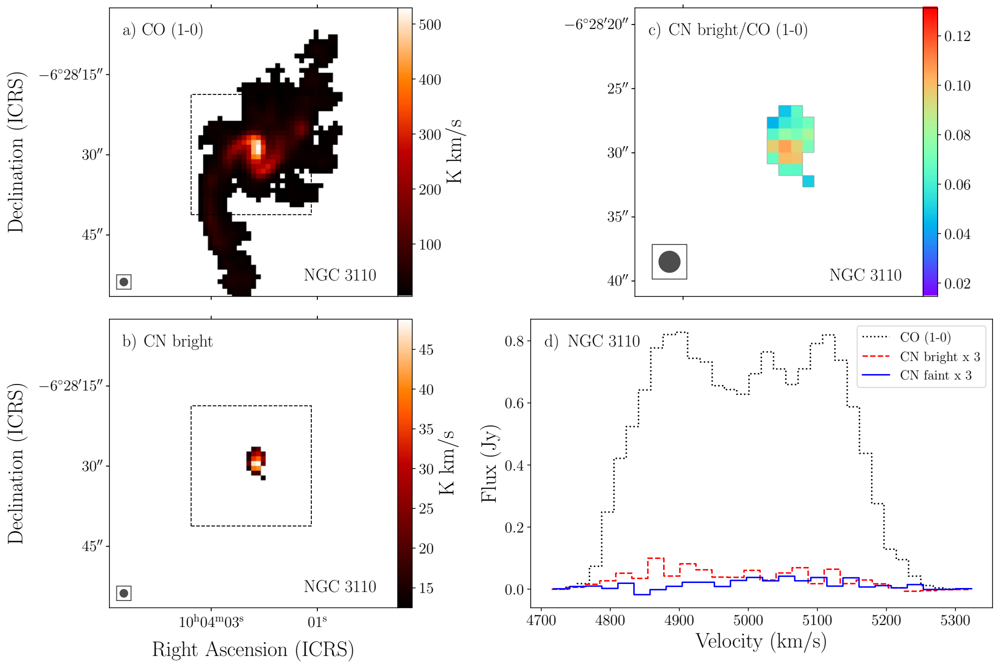

FIGURE 3.19: Moment maps, ratio maps, and spectra for NGC 3110. See Fig. 3.10 for more details.

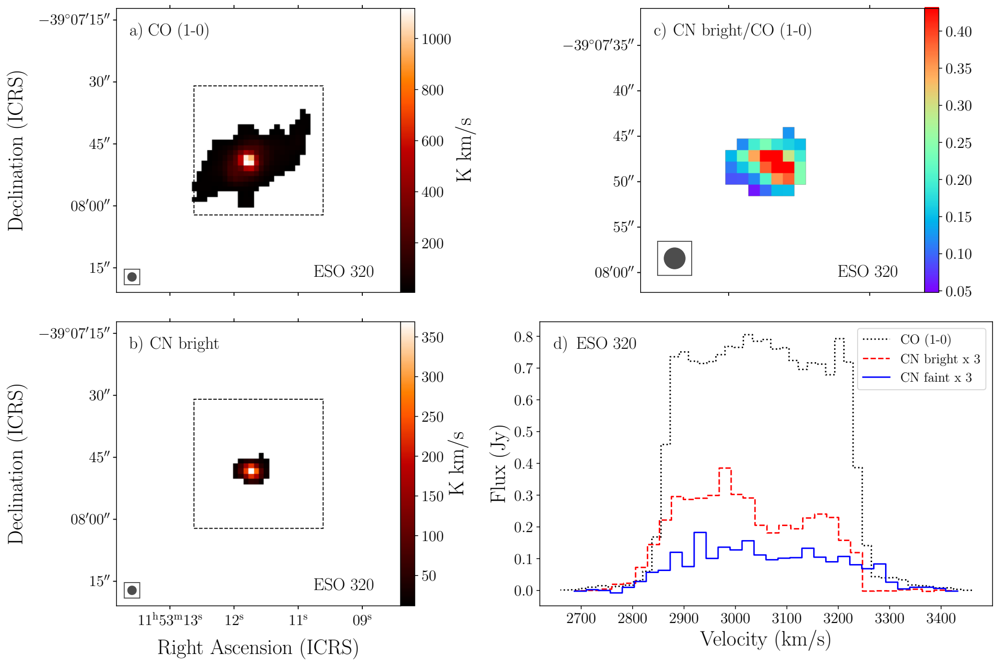

FIGURE 3.20: Moment maps, ratio maps, and spectra for ESO 320-G030. See Fig. 3.10 for more details.

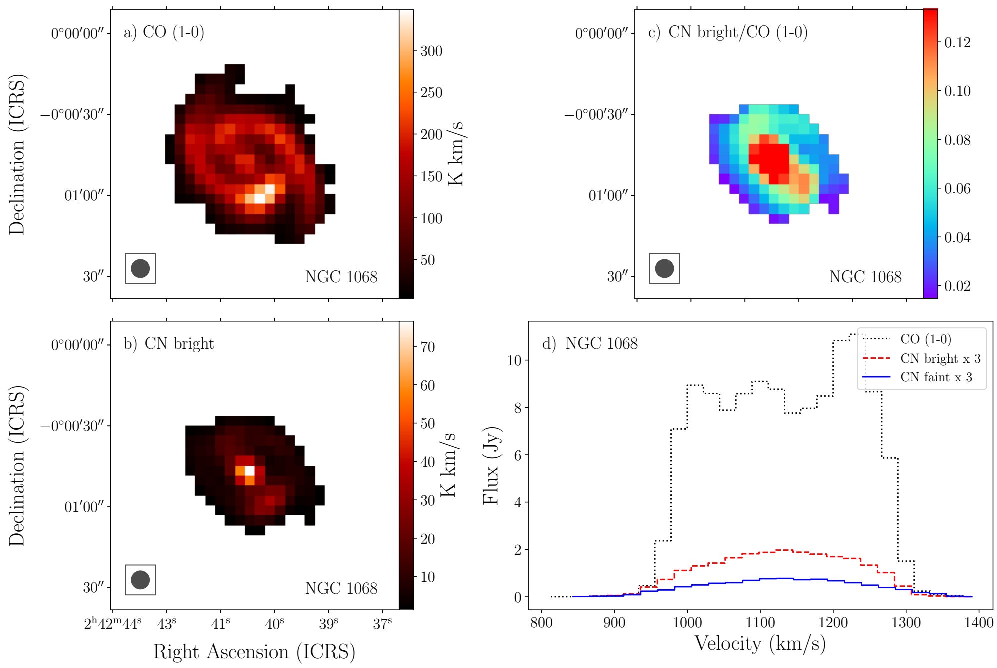

FIGURE 3.21: Moment maps, ratio maps, and spectra for NGC 1068. See Fig. 3.10 for more details.

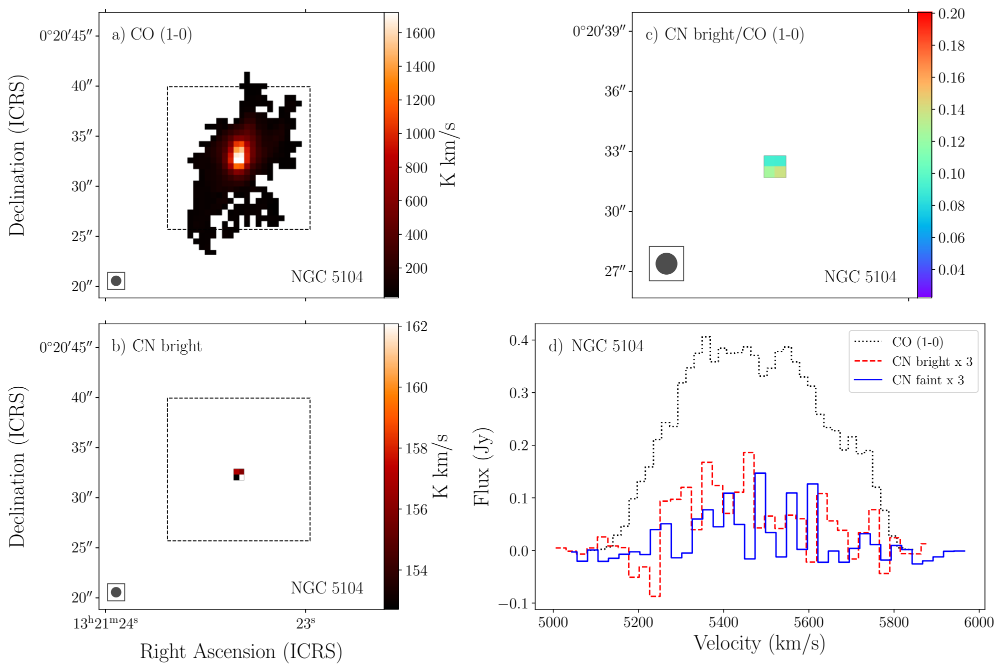

FIGURE 3.22: Moment maps, ratio maps, and spectra for NGC 5104. See Fig. 3.10 for more details.

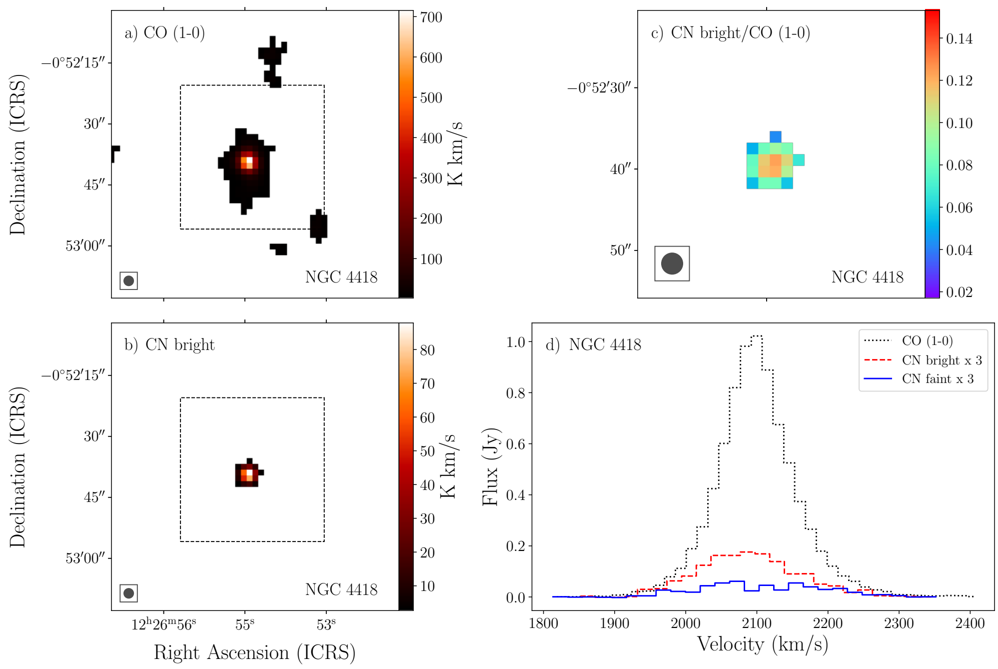

FIGURE 3.23: Moment maps, ratio maps, and spectra for NGC 4418. See Fig. 3.10 for more details.

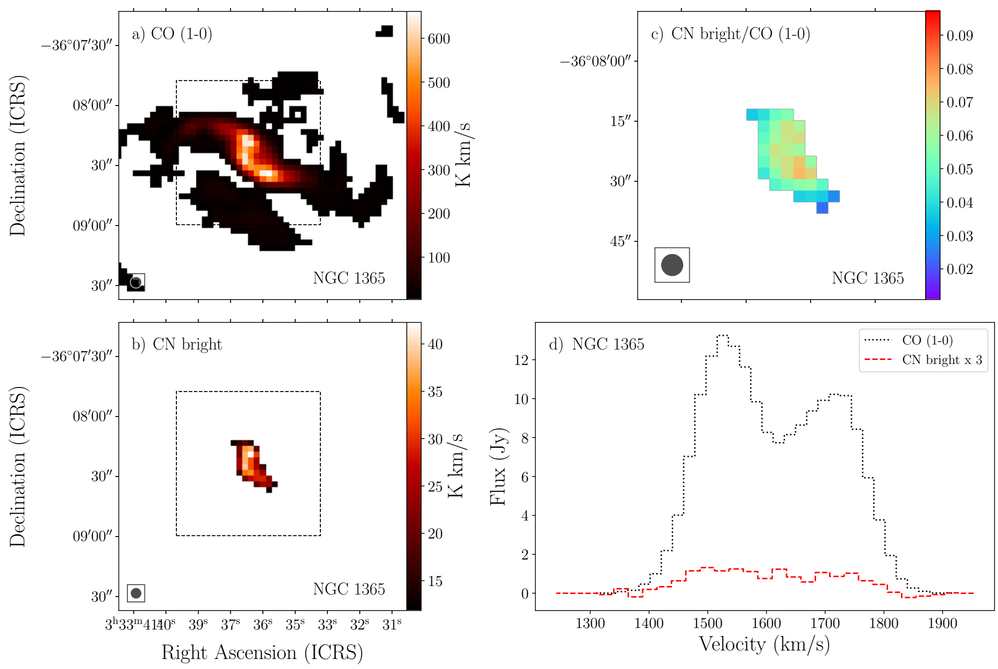

FIGURE 3.24: Moment maps, ratio maps, and spectra for NGC 1365. See Fig. 3.10 for more details.

CN bright and CN faint lines, respectively. The maps included in this appendix section were used when measuring the spatially averaged (CN bright)/(CN faint) intensity ratios (Table 3.4).

3.C Appendix: Figures including Arp 220

This appendix shows the effect of including Arp 220 in Figs. 3.4, 3.5, and 3.6. Individual pixels from Arp 220 were deemed untrustworthy due to variations in the noise throughout the cube, and as such we removed this galaxy from our results discussion when considering individual pixels within each galaxy. Fig. 3.26 includes the pixels from Arp 220 in the histogram of the (CN bright)/(CN faint) intensity ratio. The extension in the violin plot with combined ULIRG pixels to high ratio values is a result of the scatter of individual pixels within Arp 220. Fig. 3.27 includes the pixels from Arp 220 in the histogram of the (CN bright)/CO intensity ratio. The violin plot with combined ULIRG pixels has a larger spread because of the scatter of individual pixels within Arp 220. Fig. 3.28 describes the (CN bright)/(CN faint) luminosity ratio with the Arp 220 pixels overplotted in black. This figure clearly demonstrates the scatter of individual pixels within Arp 220.

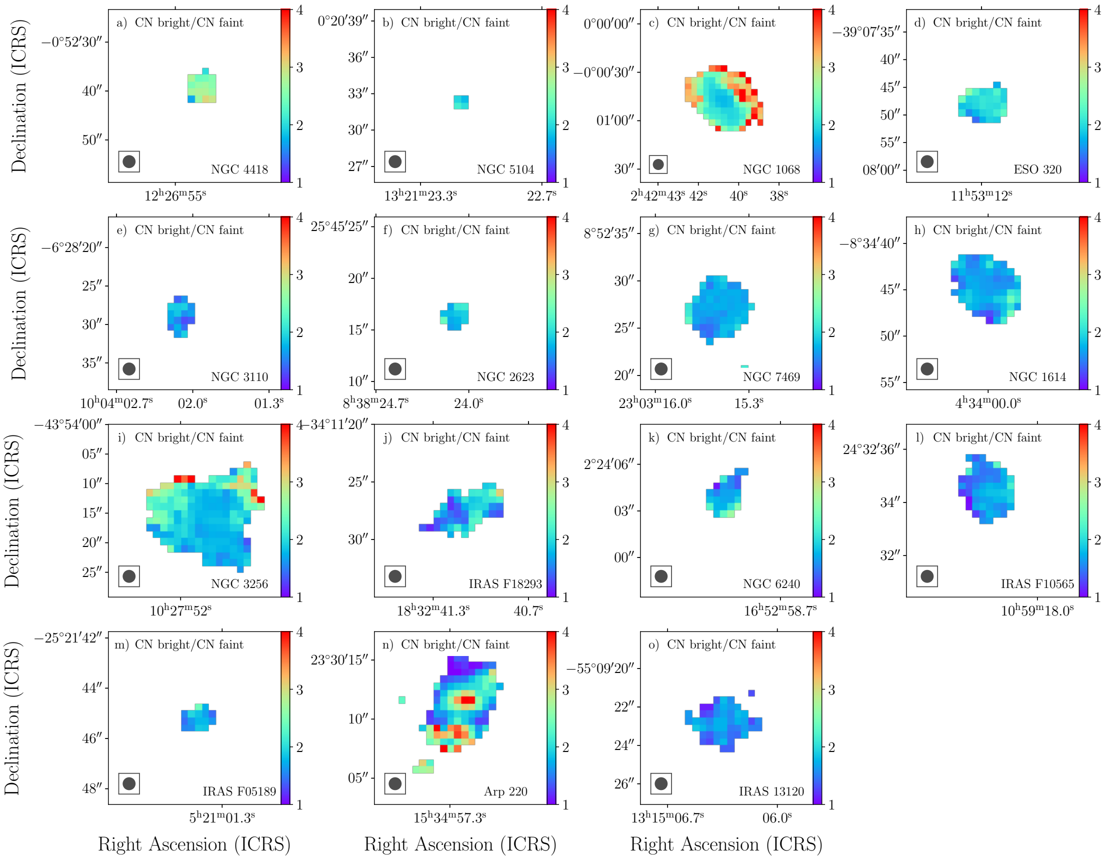

FIGURE 3.25: This figure shows the (CN bright)/(CN faint) intensity ratio in K km s^{-1} units. The circle in the bottom-left corner is the size of the beam smoothed to 500 pc. The colour bar in each panel is matched for easy comparison between galaxies. The pixels correspond to the CN bright and CN faint lines detected at $> 6\sigma$ and $> 3\sigma$, respectively. NGC 1365 is not shown because the observed spectral window did not cover the CN faint line.

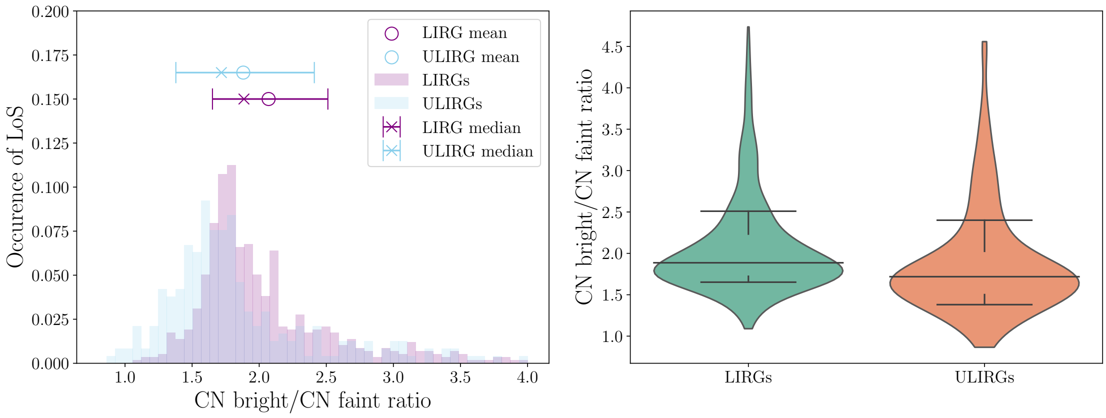

FIGURE 3.26: This figure shows the histograms of the (CN bright)/(CN faint) ratio after splitting the sample into pixels from ULIRGs and LIRGs. Data points from Arp 220 are included. We note that without the data from Arp 220, the ULIRG distribution only extends to a value of 2.5. Left panel: The y-axis shows the number of pixels with the specific ratio value, and the x-axis gives the ratio in a linear scale. The blue and violet bars correspond to the ULIRG and LIRG data points, respectively. The open circles are the mean values of each distribution. The cross represents the median value, while the error bars extend to the 16^{th} and 84^{th} percentiles. A decreasing (CN bright)/(CN faint) ratio corresponds to an increasing optical depth. Right panel: Violin plots of the (CN bright)/(CN faint) intensity ratio in ULIRGs (orange) compared with LIRGs (green). The black lines correspond to the 16^{th}, 50^{th}, and 84^{th} percentiles. The y-axis gives the (CN bright)/(CN faint) ratio in a linear scale.

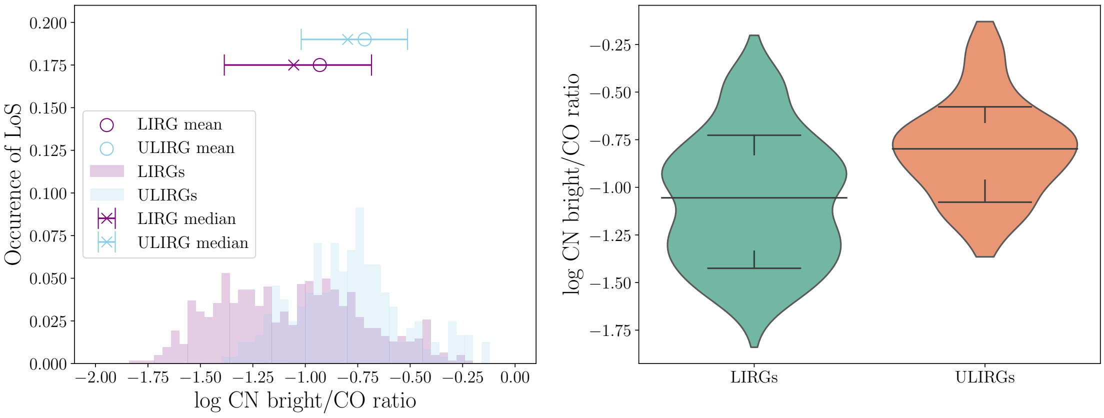

FIGURE 3.27: This figure shows the histograms of the (CN bright)/CO ratio after splitting the sample into pixels from ULIRGs and LIRGs. Data points from Arp 220 are included. We note that without the data from Arp 220, the spread in the ULIRG distribution is nearly a factor of 2 smaller. Left panel: The y-axis shows the number of pixels with the specific ratio value, and the x-axis gives the (CN bright)/CO ratio on a logarithmic scale. The blue and violet bars correspond to the ULIRG and LIRG data points, respectively. The open circles are the mean values of each distribution. The cross represents the median value, while the error bars extend to the 16^{th} and 84^{th} percentiles. Right panel: Violin plots of the (CN bright)/CO intensity ratio in ULIRGs (orange) compared with LIRGs (green). The black lines correspond to the 16^{th}, 50^{th}, and 84^{th} percentiles. The y-axis gives the (CN bright)/CO ratio on a logarithmic scale.

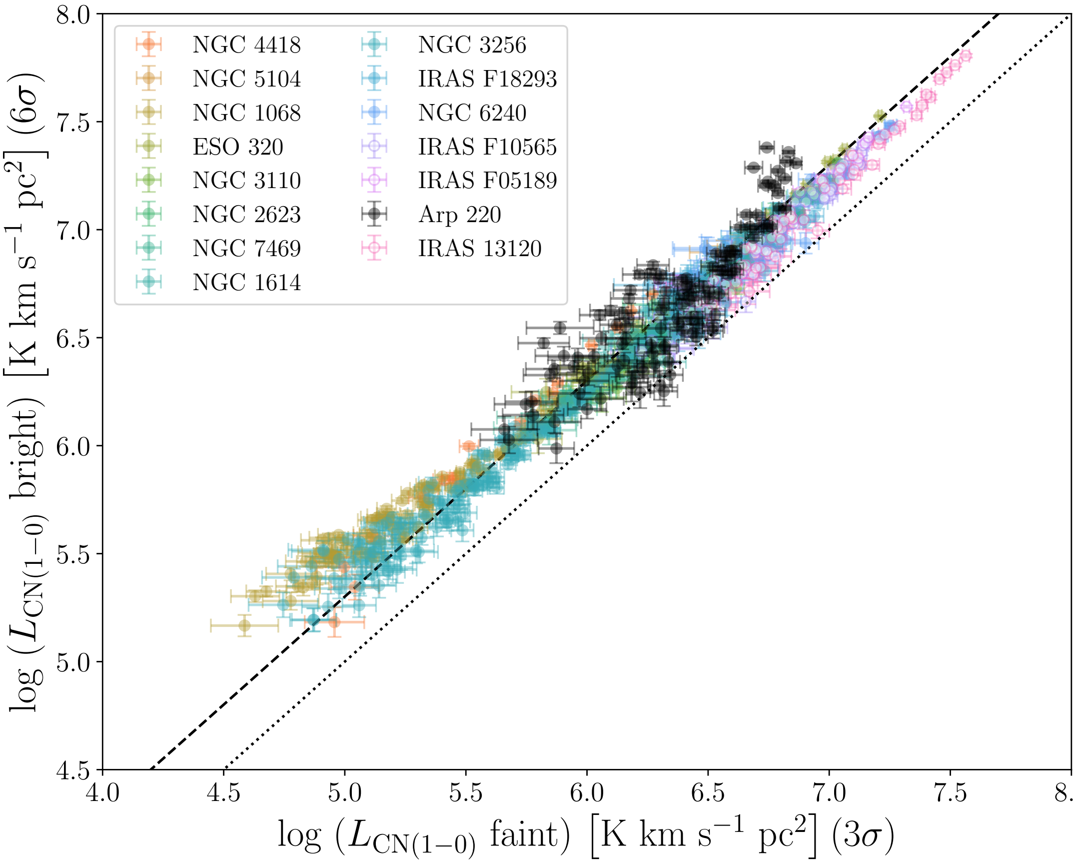

FIGURE 3.28: This figure compares the CN bright and CN faint lines on a pixel-by-pixel basis for 15 of the 16 galaxies in our sample. Uncertainties on individual pixels are calculated from equation (3.1). Both pixel values and their uncertainties have been converted from fluxes to luminosities using equation (3.2). The pixels for the CN bright and CN faint lines are show with S/N cuts of > 6σ and > 3σ, respectively. Pixels have been colourized by galaxy. Open circles are ULIRG galaxies. Closed circles are LIRG galaxies. The black dotted and black dashed lines represent 1:1 and 2:1 luminosity ratios, respectively. Data points from Arp 220 are highlighted in this figure as the black circles.

Bibliography

Aalto S., Polatidis A. G., Hüttemeister S., Curran S. J., 2002, A&A, 381, 783

Aladro R., et al., 2015, A&A, 579, A101

Anand G. S., et al., 2021, MNRAS, 501, 3621

Armus L., et al., 2009, PASP, 121, 559

Astropy Collaboration et al., 2013, A&A, 558, A33

Astropy Collaboration et al., 2018, AJ, 156, 123

Astropy Collaboration et al., 2022, ApJ, 935, 167

Baek J., Chung A., Edge A., Rose T., Kim J.-W., Jung T., 2022, ApJ, 932, 64

Bešlić I., et al., 2021, MNRAS, 506, 963

Boger G. I., Sternberg A., 2005, ApJ, 632, 302

Bolatto A. D., Wolfire M., Leroy A. K., 2013, ARA&A, 51, 207

Briggs D. S., 1995, in American Astronomical Society Meeting Abstracts. p. 112.02

Brown T., Wilson C. D., 2019, ApJ, 879, 17

Brunetti N., Wilson C. D., Sliwa K., Schinnerer E., Aalto S., Peck A. B., 2021, MNRAS, 500, 4730

Cañameras R., et al., 2021, A&A, 645, A45

Chapillon E., Guilloteau S., Dutrey A., Piétu V., Guélin M., 2012, A&A, 537, A60

Cicone C., Maiolino R., Aalto S., Muller S., Feruglio C., 2020, A&A, 633, A163

Costagliola F., et al., 2011, A&A, 528, A30

Cruz-González I., et al., 2020, MNRAS, 499, 2042

Downes D., Solomon P. M., 1998, ApJ, 507, 615

Espada D., et al., 2018, ApJ, 866, 77

Gallagher M. J., et al., 2018, ApJ, 858, 90

Ganeshalingam M., Li W., Filippenko A. V., 2013, MNRAS, 433, 2240

Gao Y., Solomon P. M., 2004, ApJ, 606, 271

García-Burillo S., Usero A., Alonso-Herrero A., Graciá-Carpio J., Pereira-Santaella M., Colina L., Planesas P., Arribas S., 2012, A&A, 539, A8

Geach J. E., Ivison R. J., Dye S., Oteo I., 2018, ApJ, 866, L12

Ginsburg A., et al., 2019, radio-astro-tools/spectral-cube: Release v0.4.5, Zenodo, doi:10.5281/zenodo.3558614

González-Alfonso E., et al., 2021, A&A, 645, A49

Graciá-Carpio J., García-Burillo S., Planesas P., Fuente A., Usero A., 2008, A&A, 479, 703

Harada N., Sakamoto K., Martín S., Aalto S., Aladro R., Sliwa K., 2018, ApJ, 855, 49

Harada N., Sakamoto K., Martín S., Watanabe Y., Aladro R., Riquelme D., Hirota A., 2019, ApJ, 884, 100

Harris C. R., et al., 2020, Nature, 585, 357

Henkel C., Chin Y. N., Mauersberger R., Whiteoak J. B., 1998, A&A, 329, 443

Henkel C., et al., 2014, A&A, 565, A3

Hunter J. D., 2007, Computing in Science & Engineering, 9, 90

Iwasawa K., et al., 2011, A&A, 528, A137

Izumi T., et al., 2020, ApJ, 898, 75

Jiménez-Donaire M. J., et al., 2017, MNRAS, 466, 49

Jones G. H., Clark P. C., Glover S. C. O., Hacar A., 2023, MNRAS, 520, 1005

Kameno S., et al., 2020, ApJ, 895, 73

Kawana Y., et al., 2022, ApJ, 929, 100

Kennicutt R. C., Evans N. J., 2012, ARA&A, 50, 531

König S., Aalto S., Muller S., Beswick R. J., Gallagher J. S., 2013, A&A, 553, A72

König S., Aalto S., Muller S., Gallagher J. S., Beswick R. J., Xu C. K., Evans A., 2016, A&A, 594, A70

Lada E. A., Bally J., Stark t. A., 1991, ApJ, 368, 432

Ledger B., Wilson C. D., Michiyama T., Iono D., Aalto S., Saito T., Bemis A., Aladro R., 2021, MNRAS, 504, 5863

Leroy A. K., et al., 2016, ApJ, 831, 16

Leroy A. K., et al., 2021, ApJS, 255, 19

Liu T., Wang J.-X., Yang H., Zhu F.-F., Zhou Y.-Y., 2014, ApJ, 783, 106

Lonsdale C. J., Farrah D., Smith H. E., 2006, Ultraluminous Infrared Galaxies. Springer, p. 285, doi:10.1007/3-540-30313-8_9

Lutz D., et al., 2020, A&A, 633, A134

Martín S., et al., 2021, A&A, 656, A46

McMullin J. P., Waters B., Schiebel D., Young W., Golap K., 2007, in Shaw R. A., Hill F., Bell D. J., eds, Astronomical Society of the Pacific Conference Series Vol. 376, Astronomical Data Analysis Software and Systems XVI. p. 127

Meier D. S., et al., 2015, ApJ, 801, 63

Meijerink R., Spaans M., Israel F. P., 2007, A&A, 461, 793

Nakajima T., et al., 2015, PASJ, 67, 8

Nakajima T., Takano S., Kohno K., Harada N., Herbst E., 2018, PASJ, 70, 7

Ohyama Y., Terashima Y., Sakamoto K., 2015, ApJ, 805, 162

Ohyama Y., Sakamoto K., Aalto S., Gallagher John S. I., 2019, ApJ, 871, 191

Onus A., Krumholz M. R., Federrath C., 2018, MNRAS, 479, 1702

Paggi A., et al., 2017, ApJ, 841, 44

Pearson C., et al., 2016, ApJS, 227, 9

Pereira-Santaella M., et al., 2016, A&A, 594, A81

Pereira-Santaella M., et al., 2020, A&A, 643, A89

Pérez-Torres M., Mattila S., Alonso-Herrero A., Aalto S., Efstathiou A., 2021, AAPR, 29, 2

Peterson B. M., et al., 2014, ApJ, 795, 149

Privon G. C., et al., 2017, ApJ, 835, 213

Rose T., et al., 2019, MNRAS, 489, 349

Rose T., et al., 2020, MNRAS, 496, 364

Rosolowsky E., Leroy A., 2006, PASP, 118, 590

Saito T., et al., 2015, ApJ, 803, 60

Saito T., et al., 2016, PASJ, 68, 20

Saito T., et al., 2018, MNRAS, 475, L52

Saito T., et al., 2020, MNRAS, 497, 3591

Saito T., et al., 2022a, ApJ, 927, L32

Saito T., et al., 2022b, ApJ, 935, 155

Sakamoto K., Ho P. T. P., Mao R.-Q., Matsushita S., Peck A. B., 2007, ApJ, 654, 782

Sakamoto K., Aalto S., Costagliola F., Martín S., Ohyama Y., Wiedner M. C., Wilner D. J., 2013, ApJ, 764, 42

Sakamoto K., Aalto S., Combes F., Evans A., Peck A., 2014, ApJ, 797, 90

Sakamoto K., et al., 2017, ApJ, 849, 14

Sanders D. B., Mazzarella J. M., Kim D. C., Surace J. A., Soifer B. T., 2003, AJ, 126, 1607

Saunders W., et al., 2000, MNRAS, 317, 55

Schruba A., et al., 2011, AJ, 142, 37

Scoville N., et al., 2017, ApJ, 836, 66

Shimajiri Y., et al., 2017, A&A, 604, A74

Shirley Y. L., 2015, PASP, 127, 299

Skatrud D. D., De Lucia F. C., Blake G. A., Sastry K. V. L. N., 1983, Journal of Molecular Spectroscopy, 99, 35

Sliwa K., Wilson C. D., Aalto S., Privon G. C., 2017, ApJ, 840, L11

Smith R. N., Tombesi F., Veilleux S., Lohfink A. M., Luminari A., 2019, ApJ, 887, 69

Solomon P. M., Vanden Bout P. A., 2005, ARA&A, 43, 677

Solomon P. M., Downes D., Radford S. J. E., 1992, ApJ, 387, L55

Stierwalt S., et al., 2013, ApJS, 206, 1

Sun J., et al., 2018, ApJ, 860, 172

Sun J., et al., 2020, ApJ, 901, L8

Swain S., Dewangan G. C., Shalima P., Tripathi P., Latha K. V. P., 2023, MNRAS, 520, 3712

Takano S., Nakajima T., Kohno K., 2019, PASJ, 71, S20

Tang X. D., et al., 2019, A&A, 629, A6

Teng S. H., et al., 2015, ApJ, 814, 56

Ueda J., et al., 2017, PASJ, 69, 6

Ueda J., et al., 2021, ApJS, 257, 57

Ueda J., Michiyama T., Iono D., Miyamoto Y., Saito T., 2022, PASJ, 74, 407

Usero A., et al., 2015, AJ, 150, 115

Vega O., Clemens M. S., Bressan A., Granato G. L., Silva L., Panuzzo P., 2008, A&A, 484, 631

Véron-Cetty M. P., Véron P., 2010, A&A, 518, A10

Virtanen P., et al., 2020, Nature Methods, 17, 261

Walter F., et al., 2017, ApJ, 835, 265

Wang M., Henkel C., Chin Y. N., Whiteoak J. B., Hunt Cunningham M., Mauersberger R., Muders D., 2004, A&A, 422, 883

Watanabe Y., Sakai N., Sorai K., Yamamoto S., 2014, ApJ, 788, 4

Wilson C. D., 2018, MNRAS, 477, 2926

Wilson C. D., Elmegreen B. G., Bemis A., Brunetti N., 2019, ApJ, 882, 5

Wilson C. D., Bemis A., Ledger B., Klimi O., 2023, MNRAS, 521, 717

Wolfire M. G., Vallini L., Chevance M., 2022, ARA&A, 60, 247

Wu J., Evans Neal J. I., Gao Y., Solomon P. M., Shirley Y. L., Vanden Bout P. A., 2005, ApJ, 635, L173

Wu J., Evans Neal J. I., Shirley Y. L., Knez C., 2010, ApJS, 188, 313

Yoast-Hull T. M., Gallagher John S. I., Aalto S., Varenius E., 2017, MNRAS, 469, L89

Young L. M., Meier D. S., Bureau M., Crocker A., Davis T. A., Topal S., 2021, ApJ, 909, 98

Young L. M., Meier D. S., Crocker A., Davis T. A., Topal S., 2022, ApJ, 933, 90

Zabel N., et al., 2019, MNRAS, 483, 2251

den Brok J. S., et al., 2021, MNRAS, 504, 3221

den Brok J. S., et al., 2022, A&A, 662, A89

4 | Building on the archives: Connecting the CN/CO intensity ratio with global galaxy properties in nearby U/LIRGs

This chapter represents an unchanged version of the paper *Building on the archives: Connecting the CN/CO intensity ratio with global galaxy properties in nearby U/LIRGs*, which has been submitted to the refereed journal, *The Astrophysical Journal*, for peer review and publication. The full reference, as of now, is as follows

Ledger B.[1], Wilson C. D.[1], Klimi O.[1], Torres-Albà N.[2,3,4], Saito T.[5], *submitted*

[1]*Department of Physics and Astronomy, McMaster University, 1280 Main St. W., Hamilton, Ontario L8S 4M1, Canada*
[2]*Department of Physics and Astronomy, Clemson University, Kinard Lab of Physics, Clemson, SC 29634, USA*
[3]*Department of Astronomy, University of Virginia, P.O. Box 400325, Charlottesville, VA 22904, USA*
[4]*GECO Fellow*
[5]*Faculty of Global Interdisciplinary Science and Innovation, Shizuoka University, 836 Ohya, Suruga-ku, Shizuoka 422-8529, Japan*

Abstract

We use the CN/CO intensity ratio to obtain the dense gas fraction, f_{dense}, for a sample of 16 Ultraluminous and Luminous Infrared Galaxies and compare f_{dense} with a suite of global galaxy properties. We find a significant correlation between f_{dense} and star formation rate calculated using both infrared luminosities and radio continuum, although there is significant scatter in each relation. We find no trend between global or peak f_{dense} and merger stage. We find no correlation between global f_{dense} and X-ray luminosity; however, the correlation becomes significant when we measure f_{dense} at the location of peak X-ray emission. Our interpretation is that the dense gas is co-localized with strong X-ray emission from an active galactic nuclei or strong central star formation.

Key words: galaxies: active – galaxies: interactions – galaxies: ISM – galaxies: nuclei – galaxies: starburst – galaxies: star formation

4.1 Introduction

Dense molecular gas plays a crucial role in connecting star formation and the interstellar medium (ISM) in galaxies. The dense phase of molecular gas is usually traced using hydrogen cyanide (HCN; Gao & Solomon 2004), while the bulk molecular gas is traced using carbon monoxide (CO; Bolatto et al. 2013). The dense gas fraction ($f_{\rm dense}$) in galaxies is typically estimated using the HCN/CO intensity ratio (e.g., Gao & Solomon 2004; García-Burillo et al. 2012). $f_{\rm dense}$ has been found to anti-correlate with the star formation efficiency (e.g., Usero et al. 2015; Jiménez-Donaire et al. 2019). Some studies suggest that this anti-correlation results from the conditions of the local environment (gas and stellar surface densities) and pressure in the molecular gas (Gallagher et al. 2018; Jiménez-Donaire et al. 2019; Neumann et al. 2023).

With their large gas reservoirs, high dense gas fractions, and high star formation rates (SFRs), Ultraluminous and Luminous Infrared Galaxies (U/LIRGs) are ideal laboratories in which to study molecular gas and star formation (Sanders & Mirabel 1996; Lonsdale et al. 2006; Pérez-Torres et al. 2021). They often host active galactic nuclei (AGN), with 40 – 50% of U/LIRGs having a Seyfert nucleus and strong AGN (Veilleux et al. 1995; Sanders & Mirabel 1996; Iwasawa et al. 2011). U/LIRGs often have significant hard X-ray emission from the AGN region, high-mass X-ray binaries (HMXBs), and other star formation properties (Pereira-Santaella et al. 2011; Iwasawa et al. 2011; Torres-Albà et al. 2018). X-rays can alter the physical and chemical properties of the ISM (e.g., Meijerink & Spaans 2005; Meijerink et al. 2007; Viti et al. 2014; Kawamuro et al. 2021) via negative AGN feedback and/or molecular gas destruction (Kawamuro et al. 2019, 2020, 2021). On the other hand, dense molecular gas is often associated with circumnuclear disks (CNDs) around AGN that supply gas for accretion onto central supermassive black holes (e.g., Izumi et al. 2016).

Recently, we have proposed that the cyanide radical (CN) can be used to trace the dense molecular gas (Wilson et al. 2023). Ledger et al. (2024), hereafter "Paper I", measured the CN/CO intensity ratio in a sample of 16 U/LIRGs. In this paper, we convert these intensity ratios to dense gas fractions and compare $f_{\rm dense}$ to global galaxy properties, such as SFR, merger stage, and hard X-ray luminosity. Section 4.2 describes our sample, data analysis, and the conversion of our measured quantities to physical properties (e.g., $f_{\rm dense}$ and SFR). Section 4.3 describes the correlations (or lack thereof) between $f_{\rm dense}$ and global galaxy properties, as well as our physical interpretation of the correlations. We summarize our conclusions in Section 4.4.

4.2 Data, Analysis, and Galaxy Properties

4.2.1 Galaxy sample

Paper I describes the selection process for our sample of 16 U/LIRGs. Briefly, the HERschel ULIRG Survey (HERUS; Pearson et al. 2016) and the Great Observatories All-Sky LIRG Survey (GOALS; Armus et al. 2009) were used as parent samples to identify nearby ($z < 0.05$) U/LIRGs that have both the CO $J = 1-0$ and CN $N = 1-0$ lines detected in the Atacama Large Millimeter/Submillimeter Array (ALMA) archive at $\theta < 500$ pc resolution. 11 of the 16 U/LIRGs in the sample have known AGN, and there are 4 ULIRGs and 12 LIRGs. The measured properties of the galaxies in our sample are listed in Tables 4.1 and 4.2, in order of decreasing infrared luminosity. For all our analysis, we use Ned Wright's (Updated) Cosmology Calculator adopting WMAP 5-year cosmology with $H_0 = 70.5$ km s^{-1} Mpc^{-1}, $\Omega = 1$, $\Omega_{\rm m} = 0.27$ in the 3K CMB frame.

4.2.2 ALMA data analysis

CO and CN lines

In this work, we consider CO ($J = 1-0$), hereafter "CO", and the brightest hyperfine grouping of the CN ($N = 1-0$) line, hereafter CN.[1] The ALMA data for the 16 galaxies span 20 unique ALMA project codes from observing Cycles 1-6. We refer the reader to Paper I for specific details of the steps taken to process the data systematically to ensure uniform analysis. For each galaxy, Paper I provides integrated intensity maps for CO and CN (in units of K km s^{-1}), a ratio map including only detected pixels in CO and both CN hyperfine groupings, and integrated spectra. In Figure 4.1, we compile the $I_{\rm CN}/I_{\rm CO}$ ratio maps for all 16 galaxies and adjust them to the same colour scale. The maps show the CN bright hyperfine grouping compared to CO, but include pixels detected only in

[1] This hyperfine grouping of CN has a rest frequency of $\sim$ 113.49 GHz and quantum number CN ($N = 1-0, J = 3/2-1/2$). Paper I discusses the fainter hyperfine grouping, CN ($N = 1-0, J = 1/2-1/2$), and its usefulness for determining CN optical depth.

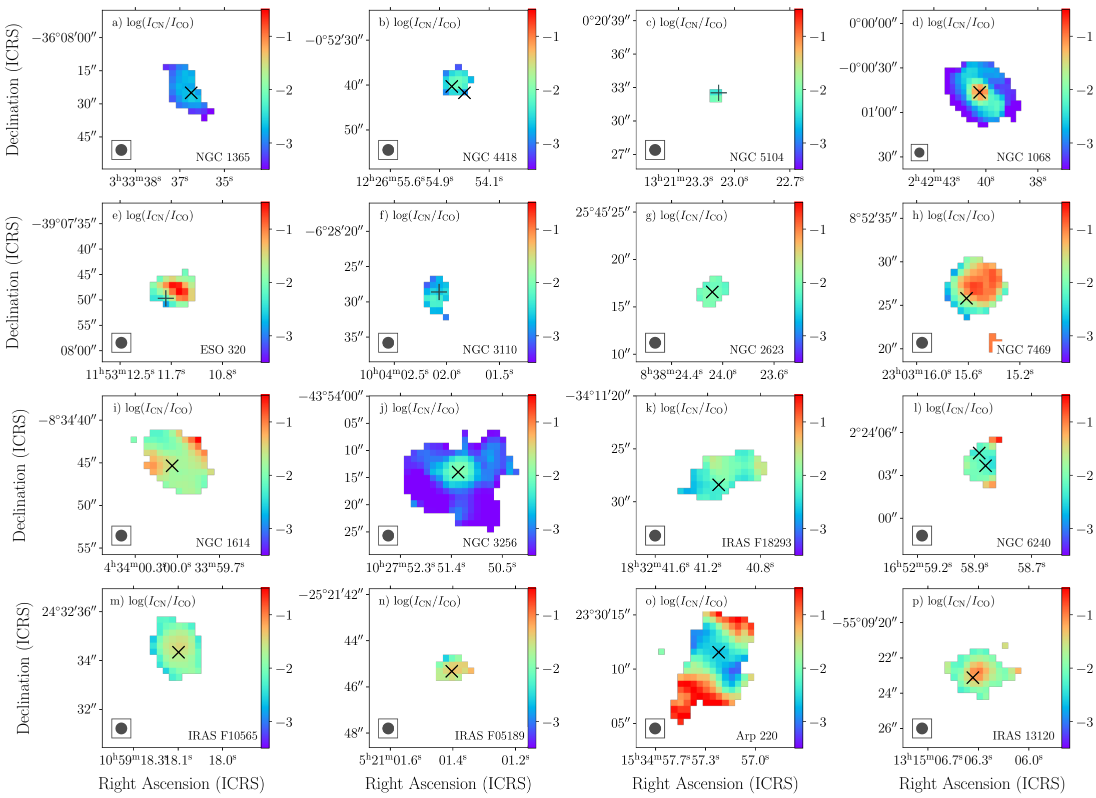

FIGURE 4.1: Log-scale $I_{\mathrm{CN}}/I_{\mathrm{CO}}$ ratio maps (K km s^{-1}) for the 16 galaxies in our sample, ordered by increasing infrared luminosity. The maps have 500 pc resolution with 250 pc pixels and the beam size is shown in the bottom left corner. Pixels shown here are detected in CO and both CN hyperfine groupings, but the measured ratio includes only the brightest CN hyperfine grouping (Ledger et al. 2024). Black crosses show the position of peak hard X-ray emission from *Chandra* observations, where NGC 4418 and NGC 6240 have two peaks. NGC 5104, ESO 320-G030, and NGC 3110, which were not observed by *Chandra*, have gray plus signs at the position of peak CO emission. In most galaxies, the hard X-ray peak roughly matches the peak CO and radio continuum emission.

CO and both CN hyperfine groupings. For the analysis in this paper, we consider the CO and CN cubes and the measured $I_{\rm CN}/I_{\rm CO}$ ratios from Paper I. For a comparison with single-dish $I_{\rm CN}/I_{\rm CO}$ global ratios, we refer the reader to Paper I or to Wilson (2018).

Radio continuum

We produced new radio continuum maps for 15 of our galaxies using Common Astronomy Software Applications (CASA, McMullin et al. 2007) and the Physics at High Angular resolution in Nearby GalaxieS (PHANGS)-ALMA pipeline v3 (Leroy et al. 2021) with CASA version 5.6.3. The continuum image for NGC 1068 is from Saito et al. (2022a,b). The continuum at a frequency of ~ 110 GHz was extracted from the calibrated ALMA data used in Paper I, masking out the spectral regions containing the CN and CO lines. Continuum emission at these frequencies is thought to be associated with free-free emission from recent star formation and is a useful tool for measuring the unobscured SFR (Section 4.2.4) in dusty galaxies like U/LIRGs (see e.g., Wilson et al. 2019). We smoothed the continuum images to a physical resolution of 500 pc and rebinned and regridded the data to match the CN and CO images with Nyquist sampled pixel sizes of 250 pc. Finally, the continuum maps were corrected by the primary beam. The global 110 GHz radio flux density and its uncertainty (Table 4.1) were measured within an aperture encompassing the emission seen in the integrated intensity.

4.2.3 Dense gas fractions

The dense gas fraction is typically calculated as

$$f_{\rm dense} = \Sigma_{\rm dense}/\Sigma_{\rm mol}, \tag{4.1}$$

where $\Sigma_{\rm dense}$ is the surface density of dense gas and $\Sigma_{\rm mol}$ is the surface density of molecular gas, both in units of $M_\odot$ pc^{-2}. $\Sigma_{\rm mol}$ is typically obtained from the CO $(1-0)$ intensity and a conversion factor, $\alpha_{\rm CO}$ (Bolatto et al. 2013). In disk galaxies, like the Milky Way, the canonical value is $\alpha_{\rm CO} = 4.35$, which includes a factor of 1.36 for Helium (Bolatto et al. 2013). In galaxies with high gas surface densities, like U/LIRGs, $\alpha_{\rm CO}$ tends to decrease (Downes et al. 1993; Solomon et al. 1992; Papadopoulos et al. 2012). The canonical value (including Helium) of $\alpha_{\rm CO} = 1.1$ (Bolatto et al. 2013) has recently been confirmed observationally by He et al. (2024).

TABLE 4.1: Dense gas and star formation properties for the U/LIRG sample.

Galaxy[a]	I_{CN}/I_{CO}[b] (global)	f_{dense} (global)	I_{CN}/I_{CO}[c] (at peak)	f_{dense} (at peak)	L_{IR}[d] ($L_\odot$)	SFR_{IR} ($M_\odot$ yr^{-1})	$S_{110\,GHz}$[e] (mJy)	$SFR_{110\,GHz}$[e] ($M_\odot$ yr^{-1})
IRAS 13120-5453	0.17	0.61	0.31	1.12	12.28	283.6	39.6 ± 2.2	634.0
Arp 220	0.09	0.32	0.07	0.25	12.21	241.4	46.6 ± 10.9	265.2
IRAS F05189-2524	0.10	0.36	0.27	0.97	12.16	215.2	2.5 ± 0.8	73.9
IRAS F10565+2448	0.08	0.29	0.22	0.79	12.07	174.9	3.1 ± 0.5	98.4
NGC 6240	0.08	0.29	0.11	0.40	11.85	105.4	11.3 ± 2.3	109.5
IRAS F18293-3413	0.05	0.18	0.11	0.40	11.79	91.8	18.9 ± 1.5	97.3
NGC 3256	0.02	0.07	0.14	0.50	11.75	83.7	38.2 ± 1.8	65.4
NGC 1614	0.15	0.54	0.20	0.72	11.65	66.5	11.5 ± 2.3	46.1
NGC 7469	0.10	0.36	0.22	0.79	11.59	57.9	19.1 ± 1.4	72.2
NGC 2623	0.07	0.25	0.13	0.47	11.59	57.9	7.8 ± 2.1	46.7
NGC 3110	0.02	0.07	0.07	0.25	11.35	33.3	6.3 ± 0.5	32.7
ESO 320-G030	0.11	0.40	0.12	0.43	11.35	33.3	12.0 ± 2.7	26.9
NGC 1068	0.06	0.22	0.39	1.40	11.29	29.0	129.5 ± 31.6	22.2
NGC 5104	0.07	0.25	0.09	0.32	11.21	24.1	3.3 ± 0.5	20.6
NGC 4418	0.08	0.29	0.12	0.43	11.16	21.5	11.8 ± 4.0	12.8
NGC 1365	0.03	0.11	0.07	0.25	11.08	17.9	31.5 ± 3.7	10.6

Notes: [a]Ordered by decreasing infrared luminosity.
[b]Global I_{CN}/I_{CO} ratios as measured in Paper I. Measurement uncertainties for the global I_{CN}/I_{CO} ratios include a 5% ALMA calibration uncertainty and are all ±0.01, except NGC 5104, which is ±0.02 because of the small number of detected pixels (Figure 4.1).
[c]I_{CN}/I_{CO} at the location of the peak hard X-ray emission from *Chandra*. For the three galaxies with no *Chandra* data (NGC 5104, ESO 320-G030, NGC 3110), we give I_{CN}/I_{CO} at the peak CO intensity. For the two galaxies with double X-ray peaks (NGC 4418, NGC 6240), we use the peak X-ray pixel which is closest to the location of the peak CO intensity. We estimate uncertainties of ±10% for I_{CN}/I_{CO} at peak because of using only a single pixel.
[d]Infrared luminosities from GOALS (Armus et al. 2009) scaled to the distances given in Table 4.2.
[e]Uncertainties on the radio continuum flux density were calculated as $\sigma_{RMS} \times \sqrt{N_{beam}}$, where σ_{RMS} is the RMS noise of the continuum map in Jy beam^{-1} and N_{beam} is the number of beams in the aperture used to measure $S_{110\,GHz}$. The 5% ALMA calibration uncertainty is not included here. $SFR_{110\,GHz}$ is not corrected for any dust contamination, synchrotron emission, or AGN impact (see Section 4.2.4).

Similarly, $\Sigma_{\rm dense}$ is obtained from the HCN $(1-0)$ intensity and a conversion factor, $\alpha_{\rm HCN}$. Gao & Solomon (2004) use a value of $\alpha_{\rm HCN} = 10$, which becomes $\alpha_{\rm HCN} = 13.6$ after including the Helium factor. The HCN conversion factor is also expected to decrease for U/LIRGs, but is much less constrained than the CO conversion factor (Gao & Solomon 2004).

For normal disk galaxies, the commonly used values of $\alpha_{\rm HCN} = 13.6$ and $\alpha_{\rm CO} = 4.35$ have a ratio of $\alpha_{\rm HCN}/\alpha_{\rm CO} \approx 3.1$. Following the discussion in Bemis & Wilson (2023), we apply a fixed ratio of $\alpha_{\rm HCN}/\alpha_{\rm CO} \approx 3.1$ for our U/LIRG sample, which combines with the U/LIRG value of $\alpha_{\rm CO} = 1.1$ to give $\alpha_{\rm HCN} \approx 3.5$ in U/LIRGs. The physical motivation for the decreased $\alpha_{\rm CO}$ in more extreme systems like U/LIRGs is that CO is optically thick and the gas temperature, density, and line width are all higher (Bolatto et al. 2013). All these factors together mean that there is less mass of gas for a given CO luminosity. Similar physical arguments should apply to HCN emission, which is also thought to be optically thick (e.g., Jiménez-Donaire et al. 2017) and higher temperatures, densities, and line widths are expected for HCN observations in U/LIRGs (Solomon et al. 1992; Gao & Solomon 2004; Graciá-Carpio et al. 2006; Privon et al. 2015; Imanishi et al. 2019).

Recently, Wilson et al. (2023) found a constant CN/HCN intensity ratio of $R_{\rm CN,HCN} = I_{\rm CN}/I_{\rm HCN} = 0.86 \pm 0.07$ (standard deviation of 0.2) for the CN (1-0) and HCN (1-0) lines in a sample of 9 nearby star-forming galaxies, which included 4 U/LIRGs. The physical scales discussed in Wilson et al. (2023) are $30-400$ pc, roughly comparable with our 500 pc resolution. We convert the CN intensity to HCN intensity using $R_{\rm CN,HCN}$ and refer the reader to Wilson et al. (2023) for further discussion on the similarities of CN and HCN as dense gas tracers. Thus, we calculate $f_{\rm dense}$ from the $I_{\rm CN}/I_{\rm CO}$ ratio using

$$f_{\rm dense} = \alpha_{\rm HCN}/\alpha_{\rm CO} \times 1/R_{\rm CN,HCN} \times I_{\rm CN}/I_{\rm CO}, \tag{4.2}$$

with $\alpha_{\rm HCN}/\alpha_{\rm CO} = 3.1$ and $R_{\rm CN,HCN} = 0.86$, so that $f_{\rm dense} = 3.6 \times I_{\rm CN}/I_{\rm CO}$.

4.2.4 Star formation rates

Since U/LIRGs contain large amounts of dust, infrared or radio emission must be used to obtain accurate SFRs. We calculate global SFRs using both global infrared luminosity and resolved radio continuum maps. The global infrared luminosities are taken from the original GOALS' publication (Armus et al. 2009) and have been corrected for our choice of cosmology and distance. We calculate SFR from infrared luminosity using

$$\log(\mathrm{SFR}) = \log(L_{\mathrm{IR}}) - \log(C_{\mathrm{IR}}), \tag{4.3}$$

where SFR is in $\mathrm{M}_\odot$ yr^{-1}, L_{IR} is the infrared luminosity in ergs s^{-1}, and $\log(\mathrm{C_{IR}}) = 43.41$ for L_{IR} covering the wavelength range $3 - 1100$ μm (Murphy et al. 2011; Kennicutt & Evans 2012). The resulting SFRs span $\sim 10 - 300$ $M_\odot$ yr^{-1} (Table 4.1). We note that while 11 of 16 of our sources have evidence of an AGN (Table 4.2), we have not corrected the L_{IR} emission for AGN contamination. Since AGN can contribute to the total infrared luminosity, we may overestimate the SFR in galaxies with AGN.

We use our resolved radio continuum images (Section 4.2.2) to obtain the global radio continuum flux density for our 16 galaxies (Table 4.1). We calculate the 110 GHz radio continuum luminosity as

$$L_\nu = 4\pi D_{\mathrm{L}}^2 (1+z)^{-1} S_{110\,\mathrm{GHz}}, \tag{4.4}$$

where z is the redshift, D_{L} is the luminosity distance, and $S_{110\,\mathrm{GHz}}$ is the observed flux density (Solomon & Vanden Bout 2005). We convert from radio continuum to SFR using the standard thermal-only equation (Murphy et al. 2011)

$$\mathrm{SFR} = 4.6 \times 10^{-28} \left(\frac{T_{\mathrm{e}}}{10^4\ \mathrm{K}}\right)^{0.45} \left(\frac{\nu}{\mathrm{GHz}}\right)^{0.1} L_\nu, \tag{4.5}$$

where SFR has units of $M_\odot$ yr^{-1} and L_ν has units of erg s^{-1} Hz^{-1}. T_{e} is the electron temperature, which we assume to be 10^4 K, and for the continuum we use $\nu = 110$ GHz. The SFR calculated from the radio continuum spans $\sim 10 - 650$ $M_\odot$ yr^{-1} (Table 4.1).

The 110 GHz emission from dusty systems may be contaminated by synchrotron or dust emission. Wilson et al. (2019) estimate that dust will contribute $10 - 15\%$ to the radio continuum for NGC 3256. Sakamoto et al. (2017) found a contamination of $\sim 40\%$ in the highly obscured western nucleus of Arp 220. It is difficult to quantify the specific dust contribution to our 110 GHz luminosities without spectral energy distribution fitting. We do not correct for any dust contamination, which may result in an overestimate of the SFRs calculated using the radio continuum.

Synchrotron emission is likely present in the galaxies in our sample which have strong AGN or Seyfert nuclei. We do not mask out the positions of the AGN in our global radio continuum flux density calculations as any AGN effect is blended with other radio continuum emission at our 500 pc resolution. As with dust contamination, any AGN contribution to the radio continuum may result in an overestimate of our SFRs.

4.2.5 Compiled global properties

The global properties that we have compiled to compare with the $I_{\rm CN}/I_{\rm CO}$ ratio are tabulated in Tables 4.1 and 4.2. The merger stages from Stierwalt et al. (2013) were assigned via visual inspection of IRAC 3.6 μm images and mid-infrared spectra. Our sample consists of 4 non-mergers, 3 pre-mergers, 1 mid-stage merger, and 8 late-stage mergers. In Paper I, we broadly classify the type of AGN found in each galaxy as obscured, optically identified (Seyfert 1, Seyfert 2, or LINER), or with no evidence of an AGN. We list the contribution from the AGN to the mid-infrared luminosities of our galaxies ($\rm AGN_{MIR}$) from Díaz-Santos et al. (2017) in Table 4.2.

The Galactic absorption-corrected hard X-ray luminosities, $L_{2\text{-}10\ \rm keV}$, were compiled from various sources. 6 of our galaxies were observed with *Chandra* by the GOALS team in C-GOALS I (Iwasawa et al. 2011) and an additional 7 galaxies were observed in C-GOALS II (Torres-Albà et al. 2018). Iwasawa et al. (2011) and Torres-Albà et al. (2018) both report hard X-ray luminosities in the $2-7$ keV bands and extrapolate to the $2-10$ keV band. Of the remaining 3 galaxies in our sample, NGC 5104 has no conclusive evidence for an AGN (González-Alfonso et al. 2021), but was detected by *NUSTAR* in hard X-rays thought to originate from star formation (Privon et al. 2020). Hard X-rays were detected in ESO 320-G030 by *XMM-Newton* (Pereira-Santaella et al. 2011) and this galaxy is also thought to not host an AGN (González-Alfonso et al. 2021). NGC 7469 has a well-known Seyfert 2 AGN that has been studied in hard X-rays (Blustin et al. 2003; Pereira-Santaella et al. 2011; Liu et al. 2014; Mehdipour et al. 2018). We use the absorption-corrected $2-10$ keV luminosity from Liu et al. (2014), which combined data from *XMM-Newton*, *Chandra*, *Suzaku*, and *Swift*.

For galaxies with *Chandra* data, the location of the hard X-ray peak is plotted as a black cross on the $I_{\rm CN}/I_{\rm CO}$ ratio maps in Figure 4.1. This hard X-ray peak corresponds to star forming regions, AGN, outflows, or a combination of these sources. The X-ray peak roughly lines up with the peak CO intensity and also with the peak radio continuum

TABLE 4.2: Global galaxy properties for the U/LIRG sample.

Galaxy[a]	Distance[b] (Mpc)	Merger stage[c]	$L_{2\text{-}10\,\mathrm{keV}}$[d] ($10^{41}$ erg s^{-1})	Reference[d]	AGN$_{\mathrm{MIR}}$[e]	Type of AGN[f]
IRAS 13120-5453	137	d	4.5	(1)	0.2	Obscured
Arp 220	81.1	d	0.68	(1)	0.29	Obscured
IRAS F05189-2524	188	d	130.0	(1)	0.67	Seyfert 2
IRAS F10565+2448	194	d	1.6	(1)	0.18	None
NGC 6240	106	d	21.0	(1)	0.29	Obscured
IRAS F18293-3413	77.2	c	0.94	(1)	0.17	None
NGC 3256	44.3	d	0.921	(2)	0.16	Obscured
NGC 1614	67.9	d	1.236	(2)	0.22	LINER
NGC 7469	66	a	148.0	(4)	0.44	Seyfert 1
NGC 2623	83.4	d	1.285	(2)	0.26	LINER
NGC 3110	77.8	a	0.87	(2)	0.23	None
ESO 320-G030	50.7	N	0.11	(3)	0.17	None
NGC 1068	13.97	N	1.015	(2)	1.0	Seyfert 2
NGC 5104	84.6	a	0.15	(5)	0.27	None
NGC 4418	35.3	N	0.019	(2)	0.62	Obscured
NGC 1365	19.57	N	2.889	(2)	0.51	Obscured

Notes: [a]Ordered by decreasing infrared luminosity.
[b]Luminosity distances as compiled in Paper I.
[c]Merger stages from Stierwalt et al. (2013), where "N" is a non-merger, "a" is a pre-merger, "c" is a late-stage merger, and "d" is a post-merger.
[d]Hard X-ray luminosities from (1) C-GOALS I, Iwasawa et al. 2011, (2) C-GOALS II, Torres-Albà et al. 2018, (3) Pereira-Santaella et al. 2011; (4) Liu et al. 2014; (5) Privon et al. 2020. The $L_{2\text{-}10\,\mathrm{keV}}$ values have been corrected for Galactic absorption in the original publications and scaled to the distances given here.
[e]AGN$_{\mathrm{MIR}}$ from Díaz-Santos et al. (2017). AGN$_{\mathrm{MIR}} > 0.2$ indicates a galaxy with an AGN that contributes significantly to the bolometric luminosity, while AGN$_{\mathrm{MIR}} < 0.2$ indicates a galaxy where the energetics are heavily dominated by star formation. See Díaz-Santos et al. (2017) for more details on the determination of AGN$_{\mathrm{MIR}}$ through the analysis of *Spitzer* spectra.
[f]From Paper I, where a literature search was used to classify AGN as obscured, optically identified (Seyfert 1, Seyfert 2, or LINER), or with no evidence of an AGN.

emission. Therefore, we use the location of the hard X-ray peak for our analysis and comparison of the I_{CN}/I_{CO} ratio at the "peak" (Table 4.1).

NGC 4418 and NGC 6240 have double X-ray peaks. In NGC 6240, these two X-ray peaks correspond to dual Compton-Thick AGN (Iwasawa et al. 2011). In NGC 4418, the galaxy has a single, heavily obscured AGN and the two X-ray peaks are likely two sides of the obscured AGN emission, with the true X-ray source located between these two peaks (Torres-Albà et al. 2018). For the galaxies with two X-ray peaks, we choose the X-ray peak which is closest to the peak CO intensity. For the 3 galaxies which have no *Chandra* data, we use the pixel corresponding to the peak CO intensity (shown as a gray plus sign in Figure 4.1).

4.3 Results

The results of our analysis include assumptions for the conversion factors of both CO and HCN in calculating f_{dense} and for converting the CN emission to HCN. We use both Spearman and Pearson rank coefficients to test the strength and significance of correlations between I_{CN}/I_{CO} and other quantities. There are only three significant correlations (p-values < 0.1 in one or both of the rank tests): global I_{CN}/I_{CO} and L_{IR}; global I_{CN}/I_{CO} and $L_{110\,\mathrm{GHz}}$; I_{CN}/I_{CO} at the peak pixel and $L_{2\text{-}10\,\mathrm{keV}}$.

4.3.1 Dense gas fraction and star formation rate

In Figure 4.2, we compare the observed I_{CN}/I_{CO} ratio to L_{IR} (top) and $L_{110\,\mathrm{GHz}}$ (bottom). We also include the conversion to the physical quantities f_{dense} and SFR. Both plots show positive correlations, although with significant scatter (L_{IR}: p-value < 0.08, Pearson R = 0.45; $L_{110\,\mathrm{GHz}}$: p-value < 0.05, Pearson R = 0.49). Although these are global I_{CN}/I_{CO} values, the scatter is likely a direct result of the internal variations observed in the resolved I_{CN}/I_{CO} ratio for the U/LIRG sample (see Figure 4.1), which has been averaged out in our global measurement (Ledger et al. 2024). Figure 4.3 compares the two SFR tracers; they are strongly correlated with a Spearman rank correlation coefficient of 0.96 and a p-value of $\ll 0.01$. This result agrees with previous observations that global radio continuum and IR emission are correlated for various galaxy luminosities and types (Liu & Gao 2010), including U/LIRGs (Yun et al. 2001).

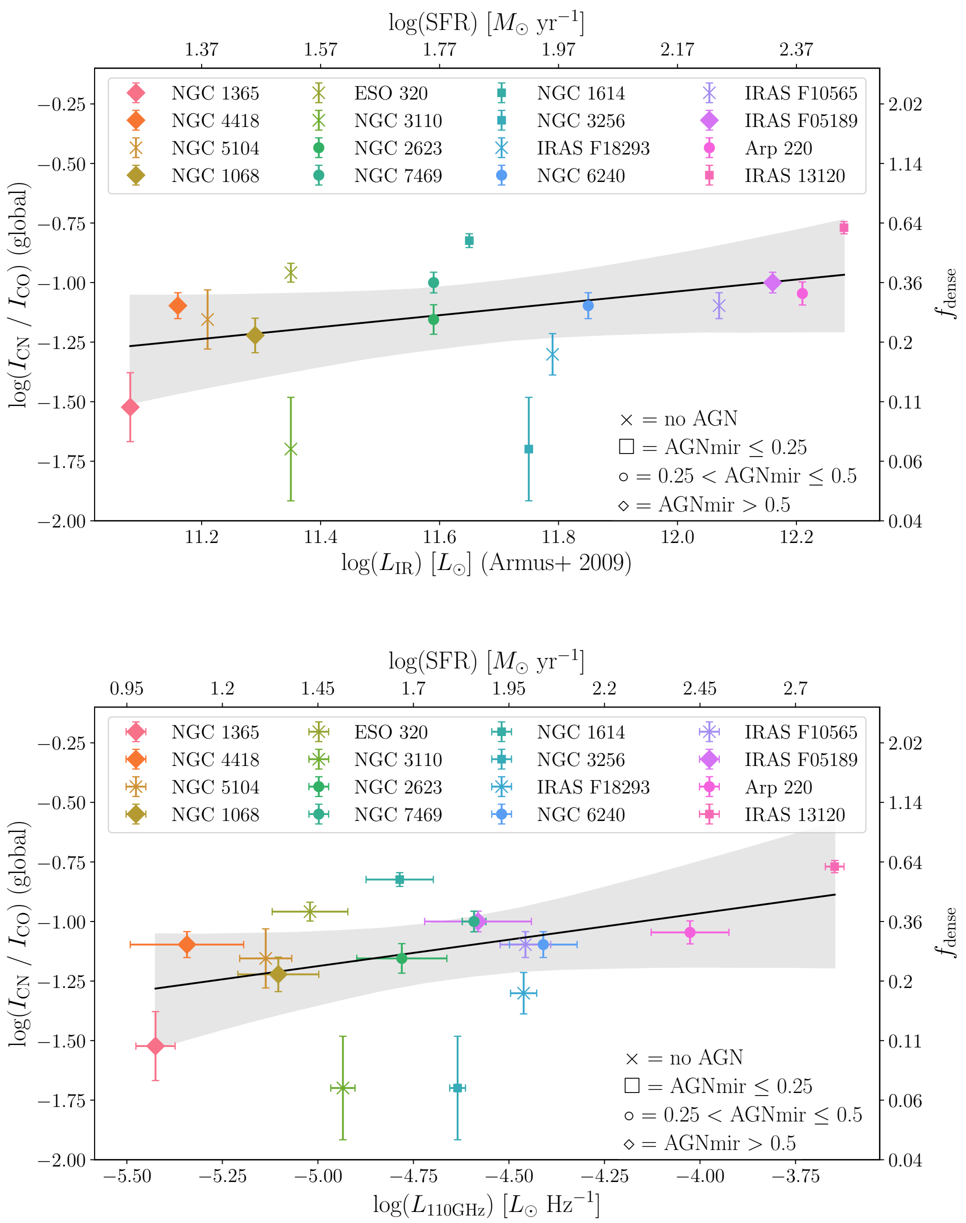

FIGURE 4.2: Global I_{CN}/I_{CO} and dense gas fraction (f_{dense}) versus L_{IR} (top), $L_{110\,GHz}$ (bottom), and the inferred star formation rates. SFR has a significant correlation with f_{dense} in U/LIRGs. Black solid lines show the best fit using `Linmix` with the 95% confidence interval in the shaded region. Galaxies with $AGN_{MIR} < 0.25$ are shown as square symbols, $0.25 < AGN_{MIR} < 0.5$ as circle symbols, $AGN_{MIR} > 0.5$ as diamond symbols (Díaz-Santos et al. 2017), and systems with no known AGN as crosses. The error bars shown for $L_{110\,GHz}$ do not include a 5% ALMA calibration uncertainty.

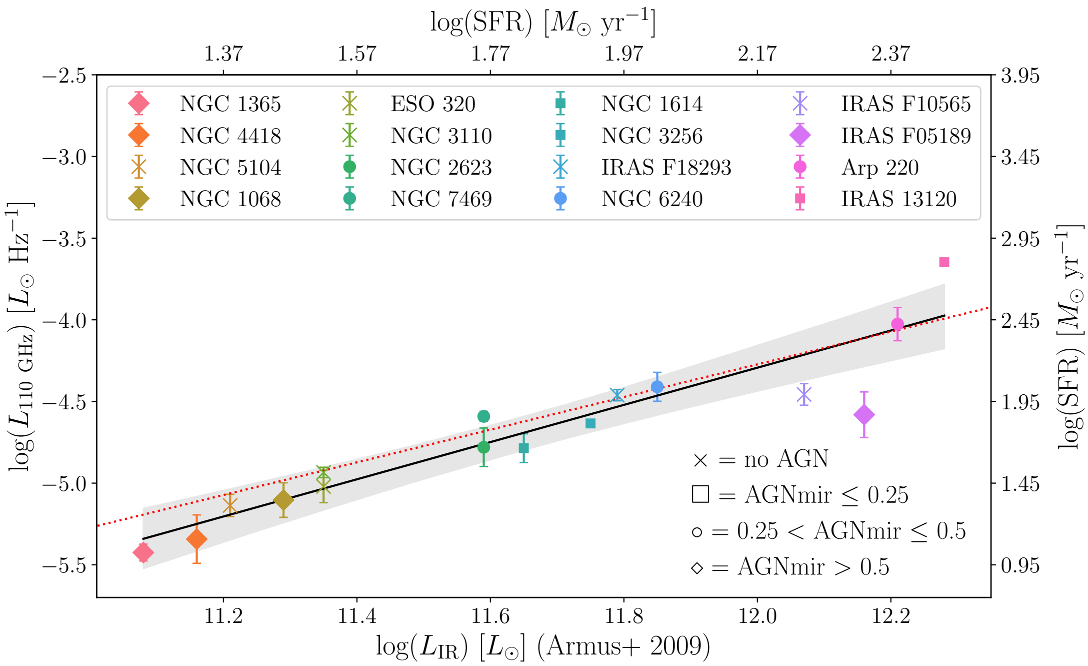

FIGURE 4.3: Global radio luminosity ($L_{110\text{ GHz}}$) versus global infrared luminosity ($L_{\rm IR}$). Both axes show the corresponding star formation rates calculated using Equations 4.3 and 4.5. The red dotted line shows the 1-to-1 ratio between the star formation rates and the black solid line is the fit to the data. Symbols are as described in Figure 4.2. There is a strong correlation (Spearman R=0.96, p-value $\ll$ 0.01) between these two star formation rate indicators.

Comparing I_{CN}/I_{CO} with L_{IR} and $L_{110\,GHz}$ probes the physical connection between f_{dense} and SFR. A significant, positive correlation between f_{dense} and SFR is consistent with previous work. Gao & Solomon (2004) first compared f_{dense} and SFR and found a weak correlation in their sample of U/LIRGs, but no correlation on the lower luminosity end in more normal disk galaxies. Both Graciá-Carpio et al. (2006) and Juneau et al. (2009) also found a positive correlation between f_{dense} (measured via HCN/CO) and L_{IR} with quite a large scatter in the relation, particularly toward the U/LIRG end. Juneau et al. (2009) compared observations and simulations of f_{dense} (based on Narayanan et al. 2008) and found that both show little to no correlation with lower L_{IR} values and then an increase in f_{dense} for higher L_{IR}. In a sample of roughly 20 merger remnants, Ueda et al. (2021) found a weak correlation between f_{dense} (via HCN/CO) and SFR (L_{IR}), particularly towards the higher end of L_{IR} values. Aalto et al. (1995), on the other hand, did not find a correlation between f_{dense} (via HCN/CO) and far-infrared emission in a sample of 11 interacting galaxies and mergers, 5 of which were LIRGs and the rest normal, star-forming galaxies. The presence of a weak correlation and a large scatter in f_{dense} with SFR persists in galaxies at higher redshift ($z > 1$, Gowardhan et al. 2017; Oteo et al. 2017).

4.3.2 Dense gas fraction and merger stage

We plot the I_{CN}/I_{CO} ratio (f_{dense}) versus merger stage in Figure 4.4. We also bin the data into "early" and "late" mergers, and "early" mergers are both non- and pre-mergers, while "late" mergers are mid- and late-stage mergers[2]. The mean I_{CN}/I_{CO} for "early" and "late" mergers are 0.07 ± 0.01 and 0.09 ± 0.02, respectively. Due to our small sample sizes, we use an Anderson-Darling (AD) test to compare the I_{CN}/I_{CO} ratio between the two samples (Scholz & Stephens 1987). The AD test shows that there is no statistical difference (p-value > 0.8) in the global I_{CN}/I_{CO} between "early" and "late" stage mergers. While galaxy simulations suggest that f_{dense} will increase in a galaxy during the merging process (Juneau et al. 2009; Moreno et al. 2019), Ueda et al. (2021) find no difference in f_{dense} with merger stage using observations in a sample of > 20 merger remnants. We similarly find no connection between f_{dense} and merger stage in our sample of U/LIRGs.

[2]Note that we have no "early mergers", as originally classifed as type 'b' in Stierwalt et al. (2013), in our sample.

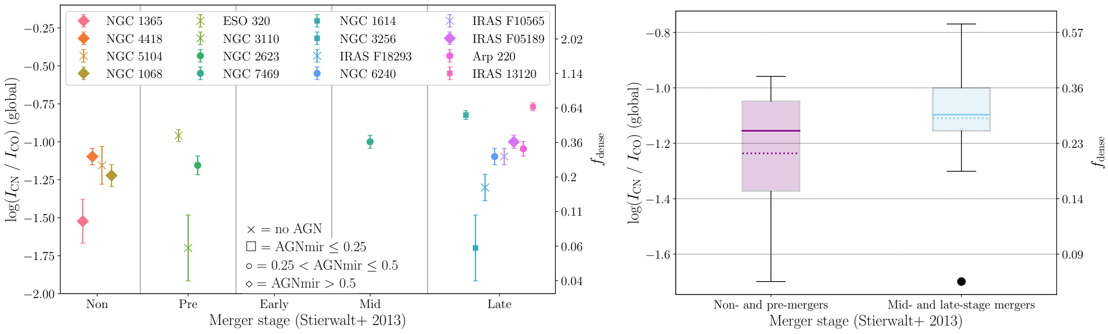

FIGURE 4.4: *Left*: Global I_{CN}/I_{CO} ratios (f_{dense}) versus merger stage from Stierwalt et al. (2013). There is no significant trend in f_{dense} with merger stage. Symbols are as in Figure 4.2. *Right*: Average global values show no statistical difference between f_{dense} in "early" (purple, left) and "late" (blue, right) merger stages. The boxes extend from the first to third quartiles of the data and the whiskers extend from the minimum to the maximum of the data, with the black circle an outlier in the sample of mid- and late-stage mergers (NGC 3256). The solid and dotted horizontal lines give the median and mean of the data, respectively.

The mean I_{CN}/I_{CO} ratio at the location of the peak X-ray emission for "early" and "late" mergers is 0.15 ± 0.04 and 0.17 ± 0.03, respectively; both values are larger than the mean global values. The results of an AD test suggest that there is no statistical difference (p-value > 0.5) in the I_{CN}/I_{CO} at the peak pixel between "early" and "late" stage mergers. Although some simulations show that interactions and merger events increase the amount of dense gas in the central kiloparsec region of galaxies (e.g., Cenci et al. 2024), we find no connection between f_{dense} and merger stage at the X-ray peak in our sample of U/LIRGs.

4.3.3 Dense gas fraction and hard X-ray luminosity

We compare the global I_{CN}/I_{CO} ratio with the global hard X-ray luminosity ($L_{2\text{-}10\,\mathrm{keV}}$) in Figure 4.5 (top). For galaxies with a confirmed AGN (see Table 4.2), the hard X-ray luminosity is likely to be strongly dominated by the AGN. The correlation between global I_{CN}/I_{CO} and $L_{2\text{-}10\,\mathrm{keV}}$ is not statistically significant (p-value > 0.37). Thus, we find no connection between f_{dense} and hard X-ray luminosities on global scales.

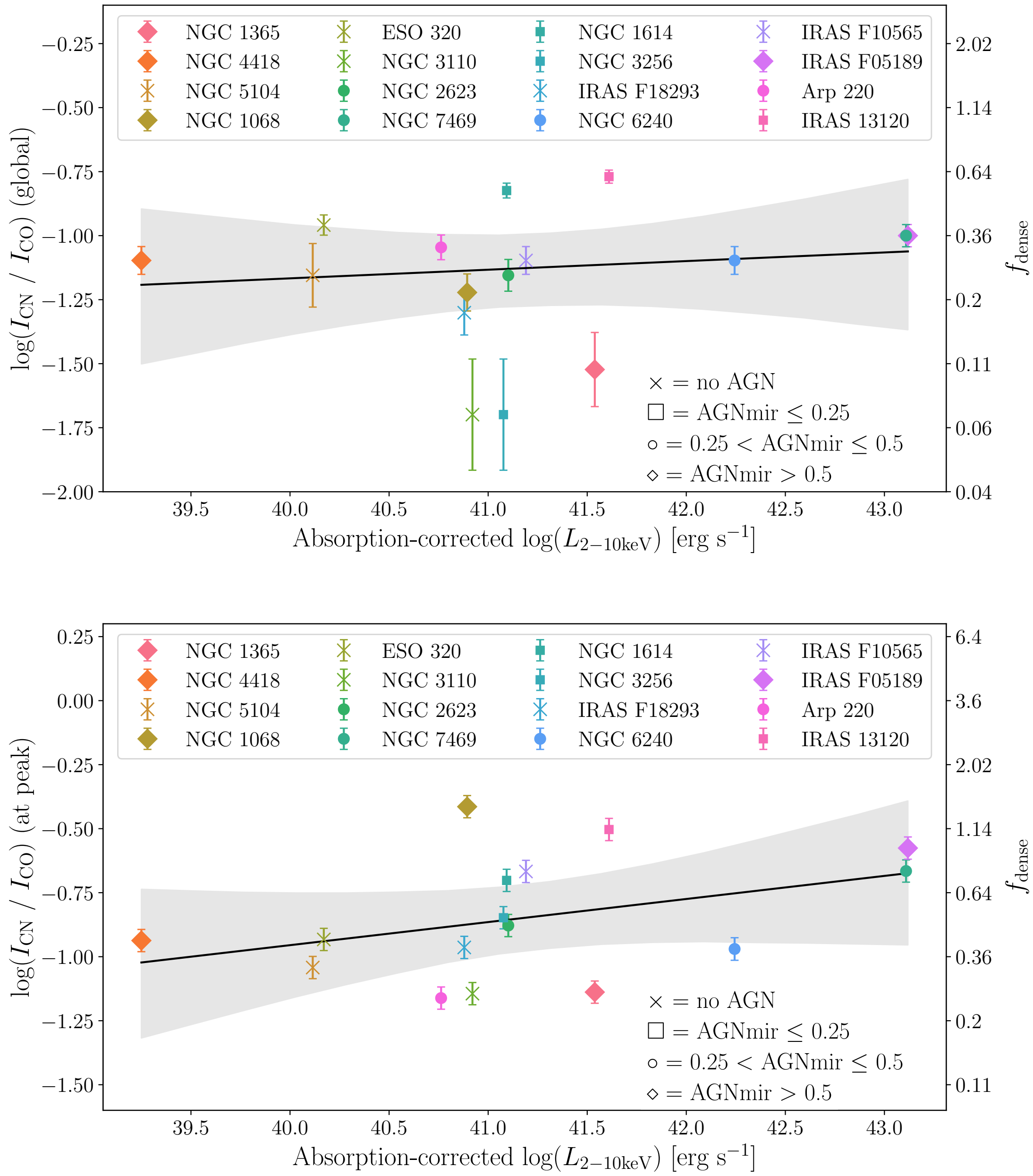

FIGURE 4.5: Global (top) and peak (bottom) $I_{\rm CN}/I_{\rm CO}$ ratios ($f_{\rm dense}$) versus hard X-ray luminosity ($L_{\text{2-10 keV}}$), including Linmix fits to the data. Although there is no discernible trend between global dense gas fraction and hard X-ray luminosity, there is a statistically significant correlation between dense gas fraction at the peak X-ray pixel and the hard X-ray luminosity.

The extent of X-ray emission and impact on gas properties is much more localized than, for example, star formation (e.g., Wolfire et al. 2022). Therefore, it is useful to explore the dense gas properties at the peak X-ray position rather than a global average. For many of our galaxies, the strong X-ray emission at the peak pixel is a result of concentrated X-ray emission and the "global" X-ray is practically the same as a "peak" X-ray. We find in all galaxies that $f_{\rm dense}$ increases at the peak X-ray pixel (near the galaxy nuclei) compared to the global value (except Arp 220, see Paper I). Resolved observations of nearby star-forming galaxies and U/LIRGs (including many overlapping with our sample) have also found multiple different dense gas tracers have increased emission in the centres relative to the disks (e.g., Meier et al. 2014; Xu et al. 2015; Privon et al. 2017; Li et al. 2024).

We compare $I_{\rm CN}/I_{\rm CO}$ at the peak X-ray pixel with the global $L_{2\text{-}10\,\rm keV}$ (Figure 4.5, bottom) and find a significant correlation between the two quantities (p-value < 0.09, Spearman R$= 0.44$), unlike the global $I_{\rm CN}/I_{\rm CO}$ comparison. We interpret this difference as a co-localization of higher $f_{\rm dense}$ and the source of the X-ray emission. Izumi et al. (2016) observed a positive correlation between HCN (1-0) emission ($\sim$ 200 pc scales) and $L_{2\text{-}10\,\rm keV}$ in 10 Seyfert galaxies and interpreted it as a correlation between dense gas mass and black hole accretion rate. The authors argued that the dense gas in the CNDs of the galaxies was helping to feed accretion onto the supermassive black holes. In contrast, using 20 – 50 keV hard X-rays, Kawamuro et al. (2021) observed lower $f_{\rm dense}$ with increasing X-ray luminosity in the central region of a sample of 26 galaxies at 100 – 600 pc resolution. We are likely not resolving any individual CNDs in our sample, but are instead seeing an unresolved increase in $f_{\rm dense}$ in the nuclear regions of our galaxies.

With higher resolution observations ($\sim$ 10 pc) of the Circinus galaxy, which hosts a strong Seyfert nuclei, Kawamuro et al. (2019) were able to find a spatial anti-correlation between dense gas and X-ray irradiated gas traced through highly ionized metal lines and argued X-rays were impacting the gas properties. In contrast, García-Burillo et al. (2010) found that the hard X-ray peak in *Chandra* data coincides with the position of their observed peak CN (2-1)/CO(1-0) intensity ratio in NGC 1068. They also found a positive correlation between their resolved CN/CO intensity ratio and hard X-ray luminosity, which they argue is a result of X-ray gas chemistry and an X-ray dominated region in this galaxy. We are not able to resolve the scales which would allow us to see the destructive impact that hard X-ray emission may have on molecular gas. Therefore, our analysis averages together the effect of any negative AGN feedback on the molecular gas and the existence of more dense gas in the centres of these galaxies.

For 2 galaxies in our sample, IRAS 13120 and NGC 1068, $f_{\rm dense} > 1$ at the X-ray peak. $f_{\rm dense} > 1$ means that there is more dense gas than there is total molecular gas, which is not physically possible. IRAS 13120 is the most luminous ULIRG in our sample, with the highest SFR of a few hundred $M_{\odot}$ yr^{-1}, and NGC 1068 has a powerful Seyfert 2 nucleus. It is likely in these two systems that additional physical or chemical conditions in the central regions near the X-ray peak pixel are increasing the CN emission relative to CO, e.g., through CN enhancement or CO destruction (c.f. Saito et al. 2022b). A similar strong enhancement of CN relative to CO was observed in the outflow of Mrk 231 (Cicone et al. 2020). In our simple calculation of $f_{\rm dense}$, we do not account for the unique excitation conditions and therefore we overestimate the peak $f_{\rm dense}$ in these galaxies.

4.4 Conclusions

We use the $I_{\rm CN}/I_{\rm CO}$ intensity ratio to estimate the dense gas fraction in a sample of 16 U/LIRGs and compare it to global galaxy properties such as SFR, merger stage, and hard X-ray luminosity. The correlations which are most statistically significant (p-values < 0.1) are global $f_{\rm dense}$ with SFR and $f_{\rm dense}$ at the X-ray peak pixel with hard X-ray luminosity. Our main conclusions are the following.

1. Using both infrared luminosity and radio continuum as SFR tracers, we find a significant correlation between global $f_{\rm dense}$ and SFR in our sample of U/LIRGs.

2. We find no correlation between $f_{\rm dense}$ and merger stage for global or peak values of $f_{\rm dense}$. This result agrees with previous observations showing little to no connection between dense gas and merger stage (Ueda et al. 2021), but is in conflict with simulations (Juneau et al. 2009; Moreno et al. 2019; Cenci et al. 2024).

3. We find a significant positive correlation between $f_{\rm dense}$ at the peak X-ray pixel and hard X-ray luminosity. This result suggests that dense gas and hard X-ray emission

are co-localized such that denser gas can foster AGN activation and growth (e.g., Izumi et al. 2016).

Future work with this sample will compare f_{dense} with resolved radio continuum continuum and star formation rate maps (Klimi et al. *in prep.*). This work will allow us to remove sites of AGN contamination and compare with previous resolved works in normal star-forming galaxies (e.g., Gallagher et al. 2018).

Acknowledgements

This paper makes use of the following ALMA data:
ADS/JAO.ALMA#2012.1.00306.S,
ADS/JAO.ALMA#2012.1.00657.S,
ADS/JAO.ALMA#2013.1.00218.S,
ADS/JAO.ALMA#2013.1.00991.S,
ADS/JAO.ALMA#2013.1.01172.S,
ADS/JAO.ALMA#2015.1.00003.S,
ADS/JAO.ALMA#2015.1.00167.S,
ADS/JAO.ALMA#2015.1.00287.S,
ADS/JAO.ALMA#2015.1.01135.S,
ADS/JAO.ALMA#2015.1.01191.S,
ADS/JAO.ALMA#2016.1.00177.S,
ADS/JAO.ALMA#2016.1.00263.S,
ADS/JAO.ALMA#2017.1.00078.S,
ADS/JAO.ALMA#2018.1.00223.S,
ADS/JAO.ALMA#2018.1.01684.S, and
ADS/JAO.ALMA#2019.1.01664.S.

ALMA is a partnership of ESO (representing its member states), NSF (USA), and NINS (Japan), together with NRC (Canada), MOST and ASIAA (Taiwan), and KASI (Republic of Korea), in cooperation with the Republic of Chile. The Joint ALMA Observatory is operated by ESO, AUI/NRAO, and NAOJ. The National Radio Astronomy Observatory is a facility of the National Science Foundation operated under cooperative agreement by Associated Universities, Inc. Any ALMA specification details in this research has made use of G. Privon et al. 2022, ALMA Cycle 9 Proposer's Guide, ALMA Doc. 9.2 v1.4[3].

This research has made use of the NASA/IPAC Extragalactic Database (NED) which is operated by the Jet Propulsion Laboratory, California Institute of Technology, under contract with the National Aeronautics and Space Administration. The computing resources available at NAOJ were essential for Paper I of this project. Data analysis was in part carried out on the Multi-wavelength Data Analysis System (MDAS) operated by the Astronomy Data Center (ADC), National Astronomical Observatory of Japan.

BL would like to thank Drs. Daisuke Iono and Toshiki Saito for hosting him at NAOJ and their guidance during the preparation of Paper I. BL acknowledges support from an NSERC Canada Graduate Scholarship-Doctoral. CDW acknowledges financial support from the Canada Council for the Arts through a Killam Research Fellowship. The research of CDW is supported by grants from the Natural Sciences and Engineering Research Council of Canada (NSERC) and the Canada Research Chairs program. NTA acknowledges support from NASA grants 80NSSC23K1611 and 80NSSC23K0484. TS acknowledges support from Japan Foundation for Promotion of Astronomy.

Facilities: ALMA, Chandra, IRAS, NUSTAR, Spitzer, Suzaku, Swift, and XMM-Newton.

Software: This research has made use of the following software packages: ASTROPY[4], a community-developed core PYTHON package for astronomy (Astropy Collaboration et al. 2013, 2018, 2022), CASA[5] (McMullin et al. 2007), MATPLOTLIB[6] (Hunter 2007), NUMPY[7] (Harris et al. 2020), RStudio[8] (R Core Team 2023), SciPy[9] (Virtanen et al. 2020), and SPECTRAL-CUBE[10] (Ginsburg et al. 2019).

[3]https://almascience.eso.org/documents-and-tools/cycle9/alma-proposers-guide
[4]https://www.astropy.org/
[5]https://casa.nrao.edu/
[6]https://matplotlib.org/
[7]https://numpy.org/
[8]https://posit.co/download/rstudio-desktop/
[9]https://scipy.org/
[10]https://spectral-cube.readthedocs.io/en/latest/

Bibliography

Aalto S., Booth R. S., Black J. H., Johansson L. E. B., 1995, A&A, 300, 369

Armus L., et al., 2009, PASP, 121, 559

Astropy Collaboration et al., 2013, A&A, 558, A33

Astropy Collaboration et al., 2018, AJ, 156, 123

Astropy Collaboration et al., 2022, ApJ, 935, 167

Bemis A. R., Wilson C. D., 2023, ApJ, 945, 42

Blustin A. J., et al., 2003, A&A, 403, 481

Bolatto A. D., Wolfire M., Leroy A. K., 2013, ARA&A, 51, 207

Cenci E., Feldmann R., Gensior J., Moreno J., Bassini L., Bernardini M., 2024, MNRAS, 527, 7871

Cicone C., Maiolino R., Aalto S., Muller S., Feruglio C., 2020, A&A, 633, A163

Díaz-Santos T., et al., 2017, ApJ, 846, 32

Downes D., Solomon P. M., Radford S. J. E., 1993, ApJ, 414, L13

Gallagher M. J., et al., 2018, ApJ, 858, 90

Gao Y., Solomon P. M., 2004, ApJ, 606, 271

García-Burillo S., et al., 2010, A&A, 519, A2

García-Burillo S., Usero A., Alonso-Herrero A., Graciá-Carpio J., Pereira-Santaella M., Colina L., Planesas P., Arribas S., 2012, A&A, 539, A8

Ginsburg A., et al., 2019, radio-astro-tools/spectral-cube: Release v0.4.5, Zenodo, doi:10.5281/zenodo.3558614

González-Alfonso E., et al., 2021, A&A, 645, A49

Gowardhan A., Riechers D. A., Daddi E., Pavesi R., Dannerbauer H., Carilli C., 2017, ApJ, 838, 136

Graciá-Carpio J., García-Burillo S., Planesas P., Colina L., 2006, ApJ, 640, L135

Harris C. R., et al., 2020, Nature, 585, 357

He H., Wilson C. D., Sun J., Teng Y.-H., Rosolowsky E., Bemis A. R., 2024, ApJ, 971, 176

Hunter J. D., 2007, Computing in Science & Engineering, 9, 90

Imanishi M., Nakanishi K., Izumi T., 2019, ApJS, 241, 19

Iwasawa K., et al., 2011, A&A, 529, A106

Izumi T., Kawakatu N., Kohno K., 2016, ApJ, 827, 81

Jiménez-Donaire M. J., et al., 2017, MNRAS, 466, 49

Jiménez-Donaire M. J., et al., 2019, ApJ, 880, 127

Juneau S., Narayanan D. T., Moustakas J., Shirley Y. L., Bussmann R. S., Kennicutt R. C. J., Vanden Bout P. A., 2009, ApJ, 707, 1217

Kawamuro T., Izumi T., Imanishi M., 2019, PASJ, 71, 68

Kawamuro T., Izumi T., Onishi K., Imanishi M., Nguyen D. D., Baba S., 2020, ApJ, 895, 135

Kawamuro T., Ricci C., Izumi T., Imanishi M., Baba S., Nguyen D. D., Onishi K., 2021, ApJS, 257, 64

Kennicutt R. C., Evans N. J., 2012, ARA&A, 50, 531

Ledger B., Saito T., Iono D., Wilson C. D., 2024, MNRAS, 527, 2963

Leroy A. K., et al., 2021, ApJS, 255, 19

Li F., Zhang Z.-Y., Wang J., Luo G., Lin L., Zhou J., 2024, MNRAS, 527, 531

Liu F., Gao Y., 2010, ApJ, 713, 524

Liu T., Wang J.-X., Yang H., Zhu F.-F., Zhou Y.-Y., 2014, ApJ, 783, 106

Lonsdale C. J., Farrah D., Smith H. E., 2006, Ultraluminous Infrared Galaxies. Springer, p. 285, doi:10.1007/3-540-30313-8_9

McMullin J. P., Waters B., Schiebel D., Young W., Golap K., 2007, in Shaw R. A., Hill F., Bell D. J., eds, Astronomical Society of the Pacific Conference Series Vol. 376, Astronomical Data Analysis Software and Systems XVI. p. 127

Mehdipour M., et al., 2018, A&A, 615, A72

Meier D. S., Turner J. L., Beck S. C., 2014, ApJ, 795, 107

Meijerink R., Spaans M., 2005, A&A, 436, 397

Meijerink R., Spaans M., Israel F. P., 2007, A&A, 461, 793

Moreno J., et al., 2019, MNRAS, 485, 1320

Murphy E. J., et al., 2011, ApJ, 737, 67

Narayanan D., Cox T. J., Shirley Y., Davé R., Hernquist L., Walker C. K., 2008, ApJ, 684, 996

Neumann L., et al., 2023, MNRAS, 521, 3348

Oteo I., et al., 2017, ApJ, 850, 170

Papadopoulos P. P., van der Werf P., Xilouris E., Isaak K. G., Gao Y., 2012, ApJ, 751, 10

Pearson C., et al., 2016, ApJS, 227, 9

Pereira-Santaella M., et al., 2011, A&A, 535, A93

Pérez-Torres M., Mattila S., Alonso-Herrero A., Aalto S., Efstathiou A., 2021, AAPR, 29, 2

Privon G. C., et al., 2015, ApJ, 814, 39

Privon G. C., et al., 2017, ApJ, 835, 213

Privon G. C., et al., 2020, ApJ, 893, 149

R Core Team 2023, R: A Language and Environment for Statistical Computing. R Foundation for Statistical Computing, Vienna, Austria, `https://www.R-project.org/`

Saito T., et al., 2022a, ApJ, 927, L32

Saito T., et al., 2022b, ApJ, 935, 155

Sakamoto K., et al., 2017, ApJ, 849, 14

Sanders D. B., Mirabel I. F., 1996, ARA&A, 34, 749

Scholz F. W., Stephens M. A., 1987, Journal of the American Statistical Association, 82, 918

Solomon P. M., Vanden Bout P. A., 2005, ARA&A, 43, 677

Solomon P. M., Downes D., Radford S. J. E., 1992, ApJ, 387, L55

Stierwalt S., et al., 2013, ApJS, 206, 1

Torres-Albà N., et al., 2018, A&A, 620, A140

Ueda J., et al., 2021, ApJS, 257, 57

Usero A., et al., 2015, AJ, 150, 115

Veilleux S., Kim D. C., Sanders D. B., Mazzarella J. M., Soifer B. T., 1995, ApJS, 98, 171

Virtanen P., et al., 2020, Nature Methods, 17, 261

Viti S., et al., 2014, A&A, 570, A28

Wilson C. D., 2018, MNRAS, 477, 2926

Wilson C. D., Elmegreen B. G., Bemis A., Brunetti N., 2019, ApJ, 882, 5

Wilson C. D., Bemis A., Ledger B., Klimi O., 2023, MNRAS, 521, 717

Wolfire M. G., Vallini L., Chevance M., 2022, ARA&A, 60, 247

Xu C. K., et al., 2015, ApJ, 799, 11

Yun M. S., Reddy N. A., Condon J. J., 2001, ApJ, 554, 803

5 | Summary and future work

Ultra-luminous and luminous infrared galaxies are some of the most extreme galaxy environments in the Universe. They have incredibly high gas surface densities and dense gas fractions compared with normal spiral galaxies. They are star-forming engines, with high star formation rate surface densities and starburst regions. U/LIRGs also contain AGN, which contribute to the energetics of the galaxy. They are often the result of galaxy mergers or interactions. Understanding the properties of dense molecular gas in U/LIRGs can help astronomers gain insight into what powers the energetic processes, either star formation or AGN related.

In this thesis, I have used the cyanide radical to measure the properties of dense molecular gas in a sample of U/LIRGs. I have included additional information from the molecules HCN and CO, and together created a picture which enhances our understanding of dense gas in these extreme systems. In Sections 5.1 and 5.2, I summarize the conclusions of this thesis and synthesize the discussion from Chapters 2, 3, and 4. I highlight future directions, open questions, and preliminary work measuring the CN/HCN abundance ratio in Sections 5.3 and 5.4.

5.1 Summary of this work

In Chapter 2, I describe a multi-transition line study of sub-kpc ALMA observations of two molecules: CN $N = 1 - 0$, $N = 2 - 1$, $N = 3 - 2$ and HCN $J = 1 - 0$, $J = 3 - 2$, $J = 4 - 3$. I investigate intensity ratios in starburst and AGN regions of a sample of three galaxies: the LIRGs NGC 3256 and NGC 7469 and the ULIRG IRAS 13120-5453. NGC 3256 is an active merger, with a strong starburst in the northern nucleus and a deeply embedded obscured AGN with molecular outflows in the southern nucleus. NGC 7469 is a Seyfert 2 galaxy with a circumnuclear disk surrounding a strong AGN. IRAS 13120-5453 is the second nearest bright ULIRG and a compact starburst with a Compton thick AGN. These three galaxies offer both starburst and AGN regions, allowing me to measure the CN and HCN intensity ratios in a variety of environments. I find enhanced HCN excitation in the nuclear region of NGC 7469 compared to its disk, suggesting that an XDR and shocks in outflows surrounding the AGN can heat the gas and increase HCN excitation. Enhanced HCN excitation is also observed in the starburst northern nucleus of NGC 3256, and to a greater extent, IRAS 13120-5453, suggesting higher SFR surface densities also impact the HCN excitation. I find that CN excitation is less impacted than HCN excitation in this galaxy sample. Finally, I find that, on resolved scales, there are variations in the CN (1 – 0)/HCN (1 – 0) intensity ratio that are localized to different environments within individual galaxies. This result suggests that while on global scales CN/HCN is relatively constant (Wilson et al. 2023), resolved observations of the two tracers in individual galaxies can lead to an understanding of starburst and AGN impact on dense gas properties and chemistry. I will briefly discuss follow up work I have planned to use the multiple transition lines to estimate CN and HCN abundance in these systems in Section 5.4.

In Chapter 3, I present the results of an archival ALMA study of CN $N = 1 - 0$ and CO $J = 1 - 0$ in a sample of 16 U/LIRGs on 500 pc scales. The U/LIRGs sample contains 4 ULIRGs and 12 LIRGs, is split into various merger stages including 4 non-mergers, 3 pre-mergers, 1 mid-stage merger, and 8 late-stage mergers, and has 11 out of 16 galaxies with an AGN. I spectrally resolve both hyperfine groupings of CN in my observations. I introduce a "shuffle-stack" method to enhance the detections of the weaker CN lines compared with the bright and optically thick CO intensity, such that I obtain a better estimate of the global CN/CO intensity ratio without introducing effects from the different intrinsic line brightnesses of the two molecules. I measure integrated intensities of CO and both CN hyperfine groupings and convert these to luminosities. Using the two CN hyperfine groupings, I measure CN optical depth and find that it is optically thin or moderately optically thick depending on the galaxy and region within a galaxy. On average, CN optical depth is higher in ULIRGs ($\tau \sim 0.96$) compared with LIRGs ($\tau \sim 0.23$). I compare the brightest hyperfine grouping of CN, CN bright, with CO intensity. CN bright/CO is higher in ULIRGs compared to LIRGs, although with more spread in the ratio measured in LIRGs (0.02 – 0.15) compared with ULIRGs (0.08 – 0.17). The range of values is likely related to the difference in galaxy morphologies, IR luminosities, and components probed in the LIRG sample. Finally, I find increase CN bright/CO intensity ratios in the peak CO intensity bin (0.15 ± 0.02) compared with the global galaxy average (0.08) in the entire sample. Additionally, the CN bright/CO intensity ratio is statistically significantly higher in six out of eleven galaxies which host an AGN. These results suggest that CN emission and/or abundance is enhanced in the nuclear regions of U/LIRGs, particularly near a starburst or an AGN.

In Chapter 4, I convert the observed CN/CO intensity ratios from Chapter 3 into measurements of dense gas fraction and compare them with global galaxy properties in the same sample of 16 U/LIRGs. From the literature, I compile SFRs estimated from IR luminosity, merger stage, and hard X-ray luminosity. I supplement these measurements with an estimate of SFR from radio continuum. I find that global dense gas fraction correlates with SFR as measured by both tracers. There is scatter in the relation and individual galaxies may deviate from the overall increasing trend of dense gas fraction with SFR. SFR_{IR} and $SFR_{110\,GHz}$ correlate well with a p-value $\ll 0.01$ and a Spearman rank coefficient of 0.96. I find that global dense gas fraction does not correlate with merger stage, which is in conflict with galaxy simulation results suggesting that dense gas fraction should increase throughout the merger process. Estimates of dense gas fraction in a statistically significant sample of galaxies sampling multiple merger stages will be critical in understanding how dense gas is affected by the merger process. Finally, I find that dense gas fraction at the location of peak X-ray emission correlates with hard X-ray luminosity, while global dense gas fraction does not. This result suggests a co-localization of dense gas with the source of hard X-rays in U/LIRGs, perhaps associated with a circumnuclear disk surrounding an AGN. Higher resolution observations targeting regions of high hard X-ray luminosities will be crucial in identifying if there is indeed a connection between X-ray emission and dense gas fraction.

The work in this thesis makes conclusions about the properties of dense molecular gas in U/LIRGs. I have shown that dense molecular gas can be different in ULIRGs compared with LIRGs, specifically in average properties like dense gas fraction and CN optical depth. CN and HCN excitation are different on resolved scales in U/LIRGs depending on region within a galaxy, particularly when co-localized with a starburst or an AGN. Combining these tracers for future observations in U/LIRGs will offer observers insight into the physical and chemical properties of dense molecular gas.

5.2 Implications

5.2.1 CN as a tracer of dense gas in galaxies

Wilson et al. (2023) conclude that CN can be used as a tracer of dense molecular gas in a similar way to the historically favoured HCN. The work in this thesis supports the use of CN as a dense gas tracer. Many observations of CN over the last few decades show that it is well-detected by ALMA in bright, star-forming systems. My work shows that CN has particularly strong emission in U/LIRGs, comparable with and at times exceeding HCN. Future observations can utilize the power of CN and the proximity of the frequency of the CN $N = 1-0$ transition to that of CO $J = 1-0$ when designing telescope proposals. For example, future proposals targeting CO $J = 1 - 0$ should aim to include the CN $N = 1-0$ in the spectral set up (if possible with the telescope design, e.g. with ALMA's spectral configurations) if it does not impact science goals. In this way, observations of CN will build over time in archived observations and a larger sample will be available simply from the frequency with which CO is targeted.

Chapter 3 of this thesis demonstrates the important of alternate data processing methods for molecular gas tracers which are not as bright as tracers like CO. In particular, if observers want to compare weaker gas tracers with brighter gas tracers, care has to be taken to not introduce bias in their results due to sensitivity differences. The "shuffle-stack" method I implement to measure global CN emission allows for a better comparison with CO emission and, in the end, a more accurate estimate of the global CN/CO intensity ratio and dense gas fraction in U/LIRGs. The method ensures that I compare similar physical scales and regions of the ISM when interpreting my results. This work shows the importance of the methods used to interpret physical properties in extragalactic systems and reducing the inherent observational biases that come with observing tracers with different line brightnesses and excitation.

I show in Chapter 3 that CN is generally optically thin and only moderately optically thick in U/LIRGs. This is an important result as it suggests that from the CN $N = 1 - 0$ transition alone observers can obtain an estimate of CN column density in the optically thin regions. The hyperfine structure of CN makes it a powerful observing tool for galaxies over other dense gas tracers like HCN, HCO^+, and CS. When optically thin, CN becomes a relevant tool for estimate the dense molecular gas mass in galaxies. I discuss the idea of an $\alpha_{\rm CN}$ conversion factor in Section 5.3.

5.2.2 Dense gas in ULIRGs compared with LIRGs

ULIRGs and LIRGs are both characterized by high molecular gas and star formation rate surface densities. Although qualititatively similar to first order, I have shown that there are subtle differences in the dense gas properties of LIRGs compare with ULIRGs. These differences are primarily intensity ratios in ULIRGs that are higher, on average, compared with LIRGs, which I attribute to the following galaxy conditions.

Global intensity ratios tend to be higher in ULIRGs compared to LIRGs. Despite nuclear or peak ratios having similar values between ULIRGs and LIRGs, the global ratios being higher in ULIRGs means that they are likely more compact and have a more constant intensity ratio in the galaxy as a whole compared with LIRGs. LIRGs may have certain regions where the conditions favour lower intensity ratios, e.g. disks with lower SFRs, which are then blended in with the higher ratios where star formation or AGN activity drives higher ratios. In particular, this can be seen in the larger spread of values in LIRGs compared with ULIRGs in the CN/CO intensity ratio violin plot in Figure 3.7.

Additionally, I find that CN is moderately optically thick in ULIRGs while it is more optically thin in LIRGs. This result indicates that if observers do plan to use CN to measure dense gas mass, resolving the hyperfine structure will be crucial in order to have an estimate of CN optical depth and ensure that it is not impacting any results. The higher optical depths are likely a result of the higher columns of molecular material seen in ULIRGs compared with LIRGs.

Despite some differences, I do find similarities between the properties of ULIRGs and LIRGs in how AGN and star formation tend to affect the excitation conditions of the dense molecular gas. Observers can use the relations between dense gas tracers and AGN/star formation in both ULIRGs and LIRGs to gain a full understanding of how XDRs and PDRs impact ISM properties.

5.3 Moving forward

This thesis answers a few questions about the usefulness of CN as a dense gas tracer and how dense gas properties differ between ULIRGs and LIRGs. Additional outstanding and open questions are also raised as a result of my conclusions and there is room for future work.

How does CN emission change in a larger, more homogeneous sample of normal galaxies compared with the results I have presented in this thesis in U/LIRGs? Most observations of CN in the past few decades have been conducted in brighter, star-forming systems where CN will be excited and easy to observe and detect. It is well established that dense gas is quite different in normal spiral galaxies compared with U/LIRGs (Baan et al. 2008; Juneau et al. 2009; Papadopoulos et al. 2012). Will observations of CN provide us with any additional benefits of comparing spirals and U/LIRGs? Is CN detectable in the quiescent disks of spiral galaxies, or is it confined to the denser regions of nuclear starbursts? Future work exploring the ALMA archive for observations which already target the spectral window of CN will provide details on the detectability of CN in normal galaxies and its merit as a dense gas tracer outside of star-forming systems.

Since CN tends to be optically thin, how will it function as a tracer of dense molecular gas mass? What are the possibilities of establishing an $\alpha_{\rm CN}$ conversion factor? Would $\alpha_{\rm CN}$ vary in similar ways to $\alpha_{\rm CO}$ and $\alpha_{\rm HCN}$? The hyperfine structure of CN provides valuable information about the molecular gas properties beyond other tracers. With sufficient spectral resolution and sensitivity, observations of a single transition allow for an estimate of optical depth and thus a more direct probe of column density and abundance. If CN can be used as an optically thin dense molecular gas mass tracer, this would be critical for measuring the mass of dense gas in galaxies. Existing projects which have observations of both CN and high-density gas mass calibrators like N_2H^+, which exist already in surveys of Milky Way molecular clouds like the Molecular Line Emission as a Tool for Galaxy Observations (LEGO) survey (Barnes et al. 2020), could be used to measure and calibrate $\alpha_{\rm CN}$.

How does dense gas fraction depend on merger stage? The results of this thesis in Chapter 4 show that there is no dependence of dense gas fraction on merger stage in a sample of 16 U/LIRGs, 12 of which are in some phase of a merger. This result confirms previous observations that dense gas properties are similar in a sample of > 20 merger remnants (Ueda et al. 2021). However, these observational conclusions are in conflict with simulations which predict that dense gas fraction should increase throughout the merger process (Juneau et al. 2009; Moreno et al. 2019; Cenci et al. 2024). While a sample of 16 galaxies is not statistically significant enough to make robust conclusions about the dense gas properties of mergers, it is clear that more observations are required to compare with predictions by simulations. Observations of dense gas tracers like HCN and CN in a statistically significant sample will be critical moving forward to understand how the merger process changes the dense molecular gas in galaxies.

Finally, an interesting result of this thesis is how hard X-ray luminosity correlates with dense gas fraction at the location of peak X-ray emission, but does not correlate with global dense gas fraction. Why is this the case? Are the observations in this thesis simply not at high enough resolution to disentangle the impact of X-rays on the molecular gas? Are the observations averaging together higher dense gas fractions seen in circumnuclear disks surrounding AGN (Izumi et al. 2016) with the dissociative impact of X-rays and X-ray chemistry which have been previously observed (Harada et al. 2013; Kawamuro et al. 2019, 2020, 2021)? High resolution observations of many molecular tracers are necessary to probe and confirm the physical and chemical impact of X-rays in regions surrounding AGN of galaxies.

5.4 Measuring the CN/HCN abundance ratio in NGC 3256, NGC 7469, and IRAS 13120-5453

In the final section of this thesis, I will share some preliminary results measuring CN and HCN abundances in NGC 3256, NGC 7469, and IRAS 13120-5453. These results are follow up work to Chapter 2 of this thesis. I use the multiple transition lines in radiative transfer models to measure molecular abundances, which will eventually be compared with chemical models incorporating UV and X-ray radiation fields.

In Figure 5.1 I show the HCN $(1-0)$ intensity maps for NGC 3256 (top), NGC 7469 (middle), and IRAS 13120-5453 (bottom). Details about the observations which made these integrated intensity maps are as described in Chapter 2 of this thesis. I highlight these maps here to define the individual regions where I will measure HCN (and CN) abundances. For all three galaxies, the left column shows the full intensity maps; the middle column shows the nuclear regions, defined by an area the size of the beam and centred on the peak 93 GHz radio continuum data (as found by Wilson et al. 2023); and the right column shows the non-nuclear region, defined by removing the pixels in an area with a radius twice the size of the beam.

I obtain the CN column densities using an LTE approximation (c.f. Tahani et al. 2016) and assuming the CN $N = 1-0$, $N = 2-1$, and $N = 3-2$ lines are optically thin. I have shown in this thesis that CN tends to be optically thin in U/LIRGs, and this holds true for these three galaxies with the CN $N = 1-0$ hyperfine ratios ~ 2. CN column densities are calculated using

$$\ln\left(\frac{N_u}{g_u}\right) = -\frac{1}{T}\frac{E_u}{k_B} + \ln\left(\frac{N_{tot}}{f}\right), \tag{5.1}$$

which expanded gives

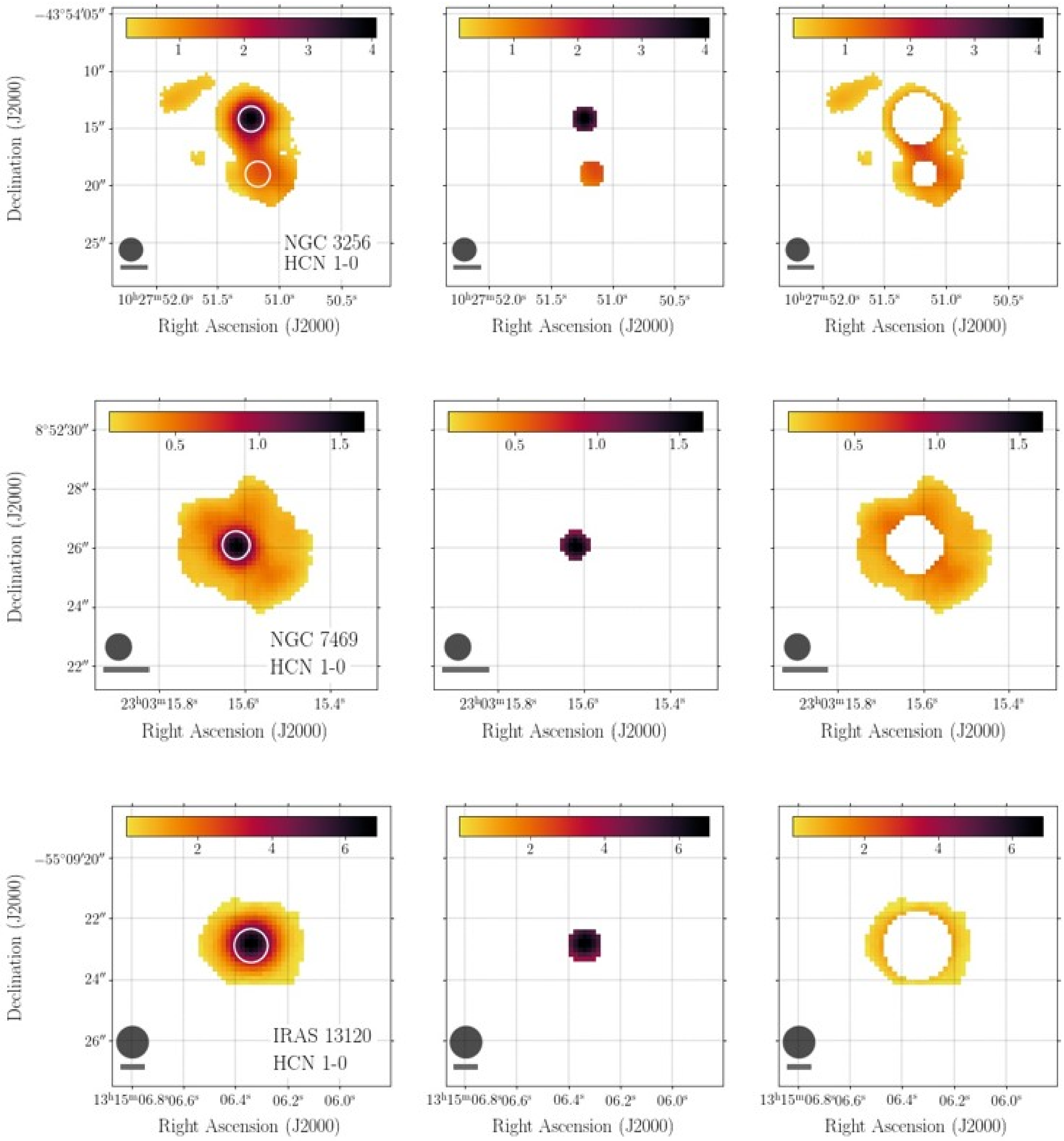

FIGURE 5.1: Integrated intensity maps (in K km/s) of the HCN $(1-0)$ line in each NGC 3256 (top row), NGC 7469 (middle row), and IRAS 13120-5453 (bottom row). The black circles in the bottom left corner indicate the beam size and the scale bar is 500 pc. The columns show the full intensity maps with nuclear regions in white circles the size of the beam (left), the nuclear region pixels (middle), and the non-nuclear region pixels (right).

$$\ln\left(\frac{8k_B\pi}{h\,c^3}\frac{\nu^2}{g_u\,A_{ul}}\int T_B dV\right) = -\frac{1}{T}\frac{E_u}{k_B} + \ln\left(\frac{N_{tot}}{f}\right), \tag{5.2}$$

where ν is the frequency of a given transition, A_{ul} is the coefficient of spontaneous emission, E_u is the energy, g_u is the degeneracy, T is the gas temperature, $N_{\rm tot}$ is the total column density, f is the partition function, and $\int TdV$ is the integrated intensity. By measuring N_u for each of the three CN lines, I then obtain excitation temperature and total CN column density from the slope and intercept of the fit to Equation 5.1, respectively.

I obtain the HCN column density in two different ways, since HCN is found to be optically thick in extragalactic systems (Jiménez-Donaire et al. 2017). I use the LTE approximation as described in the previous section and use Equation 5.1 to obtain estimates of excitation temperature and total HCN column density. I also use non-LTE radiative transfer modeling (van der Tak et al. 2007) and the Bayesian Likelihood Analysis tool PYRADEX (Kamenetzky et al. 2016) to obtain a more accurate estimate of the HCN column densities. I compare the column density estimates from each method in Figure 5.2 and I find higher HCN column densities using PYRADEX. This result suggests that an LTE approximation will underestimate HCN column densities due to the lines being optically thick. Future work will apply PYRADEX to the CN lines for a more similar abundance ratio comparison.

I compare the CN and HCN column densities, $N_{\rm CN}/N_{\rm HCN}$, measured via the LTE approximation in Figure 5.3. I use the LTE approximation for each molecule as I have not yet used the RADEX modeling to obtain CN column densities. CN always has higher column densities than HCN, $N_{\rm CN}/N_{\rm HCN} > 1$, with variations depending on the region and the galaxy. In NGC 3256, I find ratios of 4.5 ± 0.6, 3.2 ± 0.5, and 2.7 ± 0.4 in the northern nucleus, southern nucleus, and non-nuclear region, respectively. In NGC 7469, I find ratios of 3.2 ± 0.5 and 3.6 ± 0.5 in the nuclear and non-nuclear regions, respectively. In IRAS 13120, I find ratios of 3.9 ± 0.5 and 5.4 ± 0.8 in the nuclear and non-nuclear regions, respectively. Figure 5.3 shows that $N_{\rm CN}/N_{\rm HCN}$ correlates with $I_{\rm CN}/I_{\rm HCN}$.

These preliminary results show that there are some interesting differences in each of these three galaxies. The nuclear and non-nuclear regions of NGC 7469 have comparable $N_{\rm CN}/N_{\rm HCN}$ ratios, while the nuclear ratios are higher than the non-nuclear ratios in NGC

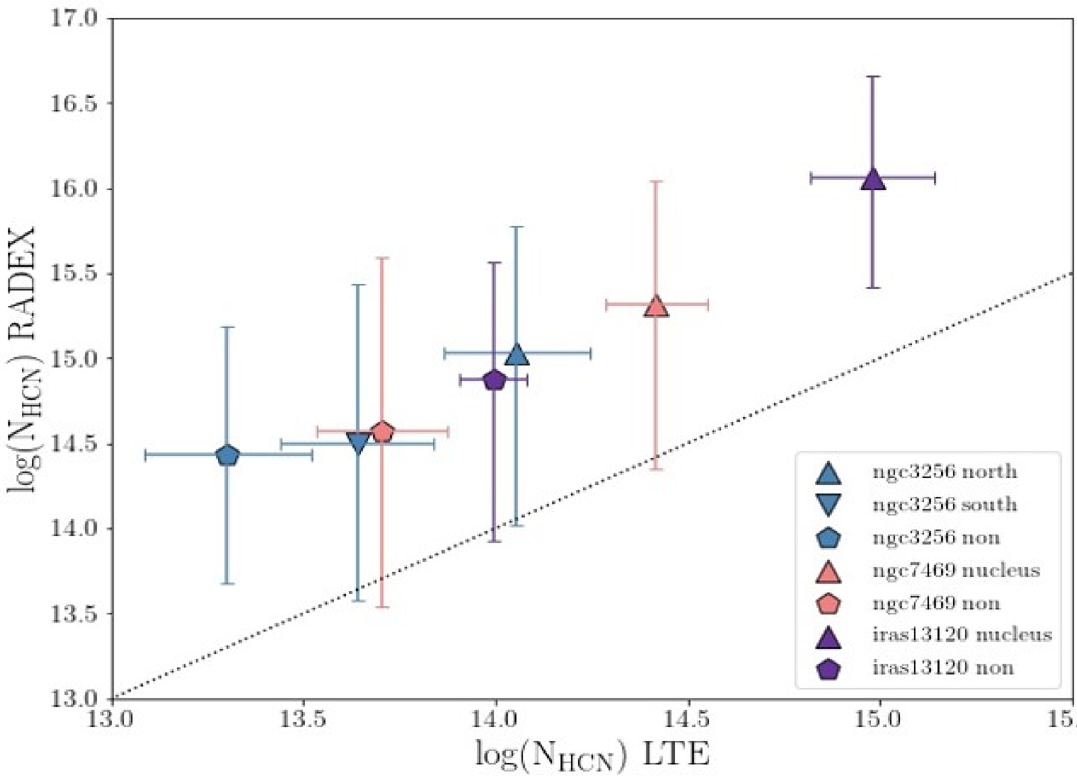

FIGURE 5.2: HCN column density calculated using an LTE approximation (x-axis) and non-LTE RADEX modeling using PYRADEX. The column densities measured via non-LTE methods are higher than the LTE approximation, suggesting that an LTE and optically thin approach underestimates the HCN column density in these three galaxies. The black dotted line shows a 1-to-1 ratio. The upward triangle symbols are the ratios in the northern nucleus of NGC 3256 and the nuclear regions of NGC 7649 and IRAS 13120-5453. The inverted triangle is the ratio in the southern nucleus of NGC 3256. The pentagon symbols are the ratios measured in the non-nuclear regions of each galaxy.

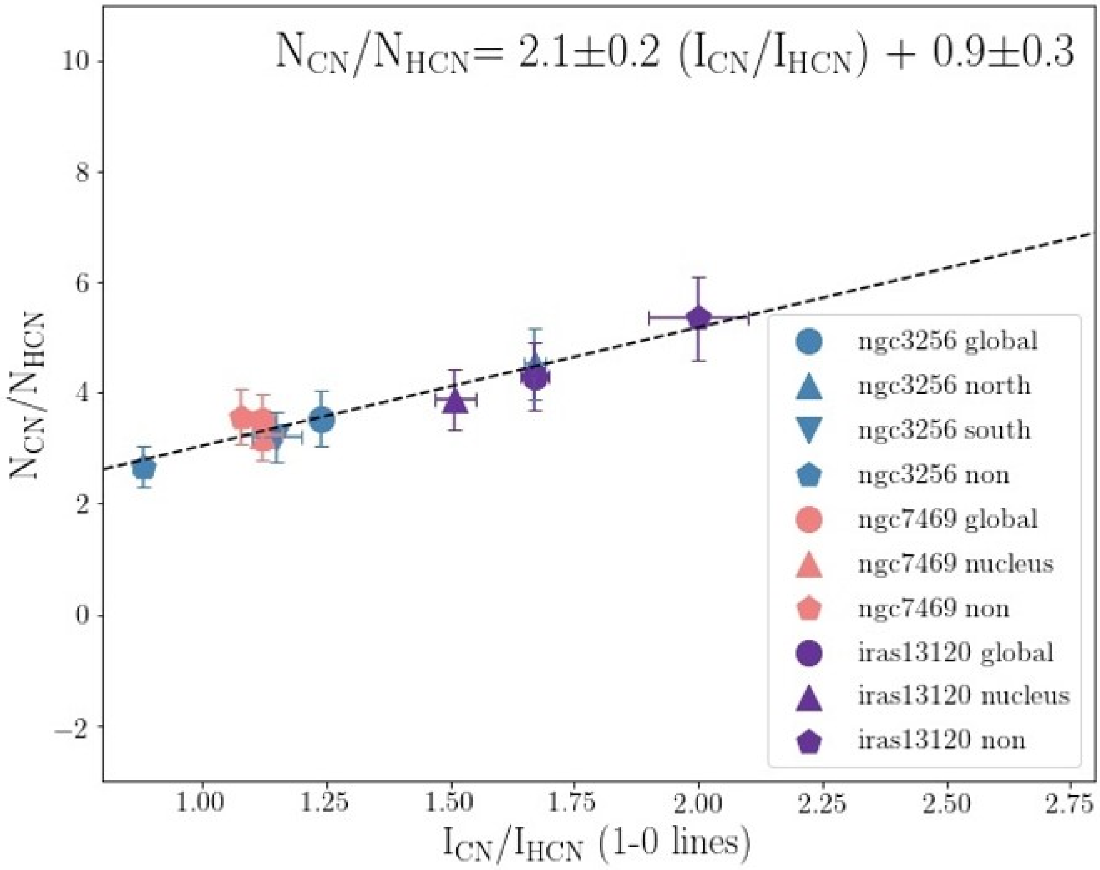

FIGURE 5.3: The CN/HCN column density ratio correlates with the CN/HCN intensity ratio as measured using the $(1-0)$ lines and an LTE approximation. The triangle and pentagon symbols are as described in Figure 5.2. The circle symbols represent the global measurements in each galaxy. The black dashed line indicates the fit to the data.

3256. There are differences in what is driving the column density ratio to higher values in the northern nucleus of NGC 3256 while maintaining a consistent value in NGC 7469. I speculate that there are X-ray chemistry effects in the nuclear region of NGC 7469 close to the Seyfert 2 nucleus. For example, Harada et al. (2013) found that CN will become HCN through high-temperature chemical reactions near an XDR.

Additionally, the positive correlation between N_{CN}/N_{HCN} and I_{CN}/I_{HCN} suggests that on resolved scales differences in the intensity ratio do trace abundance ratio differences. However, in this preliminary work I use an LTE and optically thin approximation for HCN, when it is not optically thin. Therefore, future work is necessary to estimate CN and HCN column densities both from non-LTE modeling. I plan to connect the results with chemical PDR and XDR models to compare my N_{CN}/N_{HCN} measurements with X-ray and UV radiation field strength and impact on molecular gas properties.

The results of this preliminary work demonstrate that there might be a connection between the CN/HCN abundance ratio and the CN/HCN intensity ratio. Further analysis will explore the physical and chemical drivers of this correlation, along with comparing the CN/HCN abundance ratio to chemical models.

Bibliography

Baan W. A., Henkel C., Loenen A. F., Baudry A., Wiklind T., 2008, A&A, 477, 747

Barnes A. T., et al., 2020, MNRAS, 497, 1972

Cenci E., Feldmann R., Gensior J., Moreno J., Bassini L., Bernardini M., 2024, MNRAS, 527, 7871

Harada N., Thompson T. A., Herbst E., 2013, ApJ, 765, 108

Izumi T., Kawakatu N., Kohno K., 2016, ApJ, 827, 81

Jiménez-Donaire M. J., et al., 2017, MNRAS, 466, 49

Juneau S., Narayanan D. T., Moustakas J., Shirley Y. L., Bussmann R. S., Kennicutt R. C. J., Vanden Bout P. A., 2009, ApJ, 707, 1217

Kamenetzky J., Rangwala N., Glenn J., Maloney P. R., Conley A., 2016, ApJ, 829, 93

Kawamuro T., Izumi T., Imanishi M., 2019, PASJ, 71, 68

Kawamuro T., Izumi T., Onishi K., Imanishi M., Nguyen D. D., Baba S., 2020, ApJ, 895, 135

Kawamuro T., Ricci C., Izumi T., Imanishi M., Baba S., Nguyen D. D., Onishi K., 2021, ApJS, 257, 64

Moreno J., et al., 2019, MNRAS, 485, 1320

Papadopoulos P. P., van der Werf P. P., Xilouris E. M., Isaak K. G., Gao Y., Mühle S., 2012, MNRAS, 426, 2601

Tahani K., et al., 2016, ApJ, 832, 12

Ueda J., et al., 2021, ApJS, 257, 57

Wilson C. D., Bemis A., Ledger B., Klimi O., 2023, MNRAS, 521, 717

van der Tak F. F. S., Black J. H., Schöier F. L., Jansen D. J., van Dishoeck E. F., 2007, A&A, 468, 627